Polyhedral Surfaces of Constant Mean Curvature

Konrad Polthier

Feb. 17, 2002

Contents

Preface

In differential geometry the study of smooth submanifolds with distinguished curvature properties has a long history and belongs to the central themes of this field. Modern work on smooth submanifolds, and on surfaces in particular, relies heavily on geometric and analytic machinery which has evolved over hundreds of years. However, non-smooth surfaces are also natural mathematical objects, even though there is less machinery available for studying them. Consider, for example, the pioneering work on polyhedral surfaces by the Russian school around Alexandrov [1], or Gromov's approach of doing geometry using only a set with a measure and a measurable distance function [48]. Recently, the application of discrete integrable systems to surface theory in the works of Bobenko and Pinkall [14] led to interesting results. Also in other fields, for example in computer graphics and numerics, we nowadays encounter a strong need for a discrete differential geometry of arbitrary meshes.

Here we focus on variational properties of general polyhedral curves and surfaces, and derive discrete differential operators and curvature properties which play the same role as differential operators on smooth manifolds. On polyhedral meshes, which are equipped with a piecewise flat metric, we define discrete analogues such as the Gauss and mean curvature, shortest and straightest lines, a Hodge-Helmholtz decomposition of vector fields, or study second order prob-

lems like the index of the discrete constant mean curvature surfaces. In several applications we demonstrate the practical importance of the discrete concepts, like the simulation of the geodesic flow or the analysis of vector field singularities. Further we derive new examples of complete discrete minimal surfaces, and we develop algorithms to compute constant mean curvature surfaces. Our discrete operators are applicable to a large class of polyhedral surfaces appearing in computer graphics and visualization, since we make only a few consistency assumptions on the mesh.

Among the main new results of the present work is the duality between conforming and non-conforming discrete minimal surfaces which now provides the theoretical justification of the conjugation algorithm by Pinkall and the author [88]. The result is of particular importance since many recent experimentally found constant mean curvature surfaces rely on this algorithm. The duality is proven in Chapter 4 based on non-conforming Laplace-Beltrami harmonic maps on surfaces, which are derived in Chapter 3. Also new is the work on the index of discrete constant mean curvature surfaces, and the first examples of complete discrete minimal surfaces which are critical for the discrete area functional - this is joint work with Rossman [95] (to appear in Crelle). In Chapter 7 we apply a Hodge-Helmholtz decomposition to the analysis of singularities of sampled vector fields which is a novel approach in visualization.

For a unified presentation of the discrete concepts we have integrated published results in Chapter 2 on straightest geodesics and the discrete geodesic flow (joint with Schmies [99][100]), in chapter 5 on the computation of constant mean curvature surfaces via minimal surfaces in $\mathbb{S}^3$, joint with Oberknapp [86], and in Chapter 8 on the smooth interpolation between adaptively refined meshes using hierarchical data structures, joint with Friedrich and Schmies [47]. This interpolation algorithm is an essential ingredient in practical applications of the discrete algorithms since many free-boundary value problems for constant mean curvature surfaces lead to multi-dimensional period problems. The introductory Chapter 1 provides the required syntax and some background material on polyhedral meshes.

Berlin, February 2002 Konrad Polthier

1
Introduction to Polyhedral Meshes

Polyhedral meshes belong to the most basic structures for the representation of geometric shapes not only in numerics and computer graphics. Especially the finiteness of the set of vertices and of their combinatorial relation makes them an ideal tool to reduce infinite dimensional problems to finite problems. In this section we will review the basic combinatorial and topological definitions and state some of their differential geometric properties.

In practice, a variety of different triangle and other polyhedral meshes are used. In this introduction we restrict ourselves to simplicial complexes, or conforming meshes, where two polygons must either be disjoint or have a common vertex or a common edge. That means, a polygon is not allowed to contain a vertex of another polygon in the interior of one of its edges. This restriction avoids discontinuity problems in the shape, so-called hanging nodes. Further, we restrict our discussion to piecewise linear meshes although many concepts extend to meshes with piecewise higher order polynomial order. Often it is too restrictive to work solely in the space of conforming triangulations, and, in later chapters, we will enlarge the function space to include discontinuous, non-conforming meshes as well.

In many situations a property of a polyhedral surface can be associated to depend either on the geometric shape or on the combinatorial respectively topological properties of the mesh. Therefore, it

is important to distinguish between the topology of a mesh and its geometric shape which is determined by the geometric position of the vertices. For example, assume that all points of a compact surface are collapsed to a single geometric position, then we would still like to derive the topological genus from the combinatorial properties of the surface. This forces us to introduce slightly more abstract definitions of polyhedral surfaces.

Introductions to polyhedral manifolds are given in most books on algebraic topology, for example by Munkres [82], in the book by Ziegler [120] on combinatorial aspects of polytopes, or by Bloch [12] on topological and differential geometric problems. But note, there are slight differences depending on the purpose. The standard approach in topology introduces simplices and simplicial complexes as embeddings into Euclidean space while we allow immersions with self-intersections. Good sources of applications of polyhedral manifolds to problems in differential geometry are also the books by A.D. Alexandrov and Zalgaller [1] and Reshetnyak [103].

1.1 Simplicial Complexes

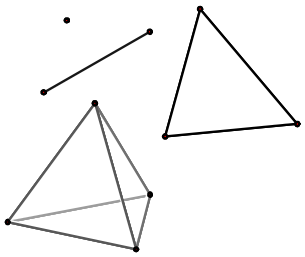

Low dimensional simplices.

We begin the introduction of polyhedral surfaces with a combinatorial point of view, that means, for the moment we do not care about the specific nature of points but consider them as abstract entities. In the combinatorial setup the most basic entities of polyhedral shapes are points, line segments, triangles, tetrahedrons, and their higher dimensional analogues, called simplices:

Definition 1 *Let $\mathfrak{V} = \{\mathfrak{v}_0, .., \mathfrak{v}_m\}$ be a finite set of $m+1$ abstract points. The (unordered) set $[\mathfrak{v}_0, .., \mathfrak{v}_m]$ is called a* combinatorial $m-$simplex*, or short, a* combinatorial simplex*. The number m is called the* dimension of the simplex*.*

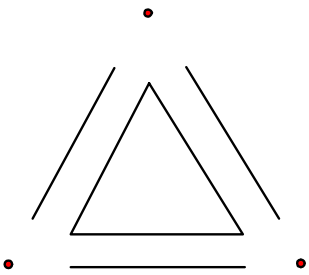

Faces of a triangle.

Definition 2 *A* face *f of a simplex $\sigma = [\mathfrak{v}_0, .., \mathfrak{v}_m]$ is a simplex determined by a non-empty subset of $\{\mathfrak{v}_0, .., \mathfrak{v}_m\}$. A $k-$face has $k+1$ points. A* proper *face is any face different from σ.*

For example, a $0-$simplex is a combinatorial point, a $1-$simplex is a line segment, a $2-$simplex is a triangle, and a $3-$simplex is a tetrahedron. There exist seven faces of a triangle $[\mathfrak{v}_0, \mathfrak{v}_1, \mathfrak{v}_2]$: the triangle itself $[\mathfrak{v}_0, \mathfrak{v}_1, \mathfrak{v}_2]$, its three edges $[\mathfrak{v}_0, \mathfrak{v}_1]$, $[\mathfrak{v}_1, \mathfrak{v}_2]$, $[\mathfrak{v}_2, \mathfrak{v}_0]$ and its three points $[\mathfrak{v}_0]$, $[\mathfrak{v}_1]$, $[\mathfrak{v}_2]$, where the last six faces are proper. A $0-$simplex has no proper face.

To perform the transition from combinatorics to geometry, we use the so-called standard simplex which serves as geometric representative associated to each combinatorial simplex:

Definition 3 *The* standard simplex $\Delta^m \subset \mathbb{R}^{m+1}$ *is the convex hull of the endpoints* $\{e_0, .., e_m\}$ *of the unit basis vectors in* $\mathbb{R}^m$ *which are given by* $e_i = (0, .., 0, 1, 0, .., 0)$. *Formally,*

$$\Delta^m = \left\{ \sum_{i=0}^{m} \lambda_i e_i \;\middle|\; 0 \leq \lambda_i \leq 1,\ \sum_{i=0}^{m} \lambda_i = 1 \right\}.$$

Note, the standard simplex not only is a set of points but includes the "interior" points. For example, the standard triangle Δ^2 in $\mathbb{R}^3$ is the planar triangle spanned by the three points $(1, 0, 0)$, $(0, 1, 0)$, $(0, 0, 1)$. Nevertheless, the standard simplex is simply a technical term. It provides the ground to formulate that any set of $m + 1$ points in a Euclidean space $\mathbb{R}^n$ defines a geometric simplex:

Definition 4 *A* geometric simplex $\sigma = [p_o, .., p_m]$ *is a set* $V = \{p_o, .., p_m\}$ *of* $m+1$ *points in* $\mathbb{R}^n$, *where* n *might be different from* m, *together with an affine map*

$$\varphi : \Delta^m \to convHull(p_0, .., p_m)$$
$$\varphi(e_i) = p_i.$$

The number m *is called the* dimension of the simplex.

The difference between an abstract and a geometric simplex is the existence of the geometric realization provided by the map φ, that means, the embedding of the simplex in a vector space.

Definition 5 *Let* $\mathfrak{V} = \{\mathfrak{v}_1, \mathfrak{v}_2, ..\}$ *be a set of abstract points. Then an* abstract simplicial complex K *is a set of simplices* S *formed by finite subsets of* $\mathfrak{V}$ *such that if* $\sigma \in S$ *is a simplex, then every subset* $\tau \subset \sigma$ *is also a simplex of* K.
If two, or more, simplices of K *share a common face, they are called* adjacent *or* neighbours. *The* boundary *of* K *is formed by any proper face that belongs to only one simplex, and its faces.*

The simplicial complex K formally represents the connectivity of a mesh, and its simplices represent the points, edges, triangles, and higher dimensional simplices. The number of points in a complex may be infinite. By associating the set of abstract points with geometric

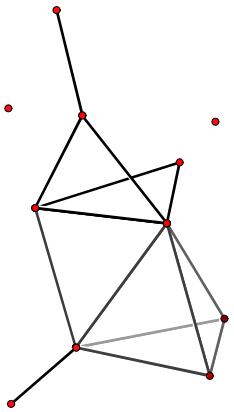

Simplicial Complex.

points in some $\mathbb{R}^n$ we obtain a geometric shape consisting of piecewise flat simplices. Note, the following definition does not require an embedding but allows that the geometric realization may have self-intersections. By allowing immersions this definition is non-standard in the sense of algebraic topology which usually requires embeddings.

Definition 6 *A* simplicial complex (K, V) *of an abstract simplicial complex K is a geometric realization uniquely given by*

1. *a set of geometric points $V = \{p_1, p_2, ..\} \subset \mathbb{R}^n$ with a bijection*

$$\Phi : \mathfrak{V} \to V$$
$$\mathfrak{v}_i \to p_i.$$

2. *for each $k-$simplex $\sigma = [p_{i_0}, .., p_{i_k}]$ an affine map from the standard simplex*

$$\varphi : \Delta^k \to convHull(p_{i_0}, .., p_{i_k})$$
$$\varphi(e_j) = p_{i_j}.$$

The above definitions ensure a strict separation between the combinatorial properties of a mesh specified by K and its geometric shape determined by V, which is also expressed by adding V to the notation of the simplicial complex (K, V). The gluing of abstract and geometric vertices is uniquely performed by the bijection Φ which relates the abstract points $\mathfrak{V}$ of K and the set of geometric points V. Any embedding of the abstract complex K into a Euclidean space induces a topology on the simplicial complex.

Definition 7 *The* underlying (topological) space $|K|$ *of a simplicial complex K immersed into $\mathbb{R}^n$ is the topological space consisting of the subset of $\mathbb{R}^n$ that is the union of all geometric realizations of simplices in K with the topology induced from any embedding of K.*

Important examples of simplicial complexes are simplicial disks and balls.

Definition 8 *A* simplicial n-ball B^n *is a simply connected simplicial complex such that $|B^n|$ is homeomorphic to the solid unit ball in $\mathbb{R}^n$, and a* simplicial n-sphere S^n *is homeomorphic to the boundary sphere of the solid unit ball in $\mathbb{R}^{n+1}$. For $n = 2$, B^2 is also called a* simplicial disk*, and S^2 is a* simplicial sphere*. For $n = 1$, S^1 is a* simplicial circle*.*

For example, an icosahedron is a simplicial sphere, and any simply closed polygon is a simplicial circle.

In some cases it makes sense to identify a simplicial complex (K, V) with its underlying set $|K|$ in a Euclidean space $\mathbb{R}^n$, for example, a polytope can always be recovered from its set of vertices. In the general case one should keep in mind that (K, V) has more the character of an immersion. For example, if the immersion of a polygonal circle intersects geometrically at a point shaping a figure-eight then it may still be a combinatorial respectively topological circle. Note that the topology of such a shape cannot be recovered solely from its shape.

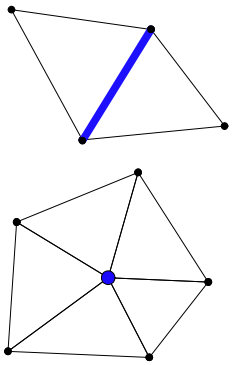

Star of an edge and a vertex.

Definition 9 *Let (K, V) be a simplicial complex. Then a subset $L \subset K$ is a* subcomplex *of K if L is a simplicial complex itself. For example, let $\sigma \in K$ be a simplex, then*

$$\operatorname{star} \sigma := \{\eta \in K \text{ that contains } \sigma, \text{ and all faces of } \eta\}$$

and

$$\operatorname{link} \sigma := \{\eta \in \operatorname{star} \sigma \mid \eta \cap \sigma = \emptyset\}.$$

are subcomplexes of K.

Simplicial surfaces extend the notion of a topological 2-manifold to the simplicial world.

Definition 10 *A* simplicial surface *S is a simplicial complex consisting of a finite set $\mathfrak{T}$ of triangles such that*

1. *Any point $p \in S$ lies in at least one triangle $T \in \mathfrak{T}$.*
2. *The star of each point $p \in S$ is a simplicial disk.*

Note, in the definition one may allow a denumerable set of triangles under the additionally assumption that the simplicial complex is locally finite, that is, the star of each vertex consists of a finite number of triangles.

A *polyhedral surface* is more general than a simplicial surface and may include flat faces with more than three vertices. The margin figure illustrates several pitfalls and degenerate situations which arise in practical implementations. First row shows two non-manifold situations. Second row is a hanging node where adjacent faces do not join a common edge. Third row shows a valid simplicial surface although the same edge belongs to four triangles. Care must be taken to avoid all these situations in practical implementations.

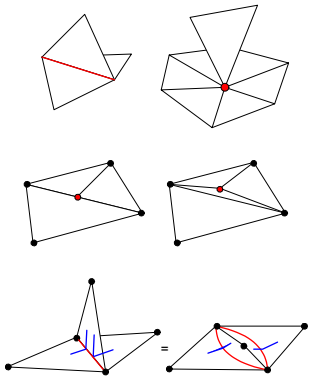

Degenerate situations and non-manifold surfaces.

Definition 11 *Let $M \subset \mathbb{R}^n$ be a topological surface. Then a simplicial surface S* triangulates *M if there exists a homeomorphism*

$$t : |S| \to M.$$

The simplicial complex S together with the homeomorphism t is called a triangulation *of M.*

Smooth surfaces and simplicial surfaces are related through the following theorem.

Theorem 12 *The following facts are true only for two-dimensional surfaces:*
(1) Any compact topological surface M in $\mathbb{R}^n$ can be triangulated, i.e. there exists a simplicial surface which triangulates M.
(2) If a topological surface is triangulated by two simplicial surfaces K_1 and K_2, then K_1 and K_2 have simplicially isomorphic subdivisions.

Often it is useful to enumerate the highest-dimensional simplices of a complex in a special way.

Definition 13 *The* shelling *of a simplicial ball B^n is a listing of its $n-$simplices $\{\sigma_1, .., \sigma_m\}$ such that for all $1 \leq k \leq m$ the subset $\{\sigma_1, .., \sigma_k\}$ is a simplicial ball.*

Any simplicial disk is shellable [79], but this result does not hold in higher dimensions. For example, see [107] for an unshellable subdivision of a tetrahedron.

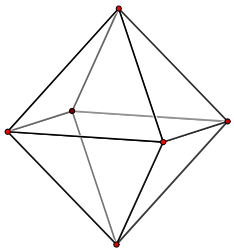

Octahedron

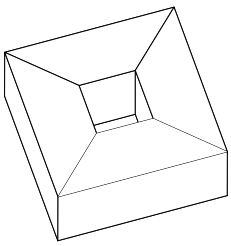

Cube with hole.

1.2 Topological Properties

Euler Characteristic and Genus

Certain properties of a polyhedral surface S do not depend on the combinatorial triangulation but are already determined by the topological properties of $|S|$. For example, let v denote the number of points, e the number of edges and f the number of faces of S. Then the *Euler characteristic* $\chi(S)$ is defined by

$$\chi(S) = v - e + f \tag{1.1}$$

For example, $\chi(\text{Octahedron}) = 2$ or $\chi(\text{Cube with hole}) = 0$. This counting procedure extends to higher dimensional simplicial complexes.

Definition 14 *Let K be a simplicial complex, and let $f_i(K)$ denote the number of $i-$simplices of a K. Then the* Euler-Poincaré characteristic *is defined as*

$$\chi(K) = \sum_{i \geq 0} (-1)^i f_i(K).$$

Note, that these concepts do not require a simplicial complex but extend to polyhedral complexes.

The Euler characteristic is a topological invariant. In higher dimensions the proof involves machinery from algebraic topology but for surfaces the invariance is easily shown: Let M be a compact topological surface with two different triangulations (K_1, t_1) and (K_2, t_2). Then we know that K_1 and K_2 have simplicially isomorphic subdivisions, and therefore have equal Euler number. But note, the inverse of this theorem is not true: if the Euler characteristics of two simplicial complexes K_1 and K_2 are the same then $|K_1|$ and $|K_2|$ need not be homeomorphic.

Therefore one speaks of the Euler characteristic of a compact 2-dimensional Riemannian manifold M, and which may be determined by an arbitrary triangulation $\mathfrak{T}$ of M. For example, $\chi(\text{Sphere}) = 2$, $\chi(\text{Torus}) = 0$ or $\chi(\text{Projective Plane}) = 1$.

Orientable compact surfaces may be classified by the genus, a different topological invariant. Simply speaking, a surface M with genus $g(M)$ is topologically equivalent, i.e. homeomorphic, to a sphere with g handles attached. For orientable surfaces the Euler characteristic and the genus are equivalent invariants with the relation

$$2 - 2g(M) = \chi(M). \tag{1.2}$$

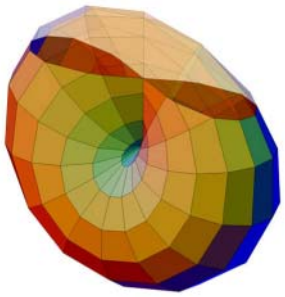

The cross cap is a realization of the projective plane.

If M is a triangulation without boundary then, counting multiplicities, each face contributes three edges and each edge belongs to two face which leads to

$$3f = 2e.$$

Therefore, on simplicial surfaces

$$\chi(M) = v - \frac{f}{2} = v - \frac{1}{3}e$$

we have roughly about two times more faces than vertices, and three times more edges than vertices.

Triangulations with Boundary

Many practical applications use triangulations with a boundary where each component is a simply connected closed polygon. The Euler characteristic helps to verify the combinatorics of triangulations in this context too. Let b be the number of boundary components of a triangulation, and assume all boundaries are pairwise disjoint, i.e. they have no vertex in common. Then the Euler characteristic $\chi(M)$ is defined as above and is a topological invariant of the manifold with boundary, i.e. M is homeomorphic to a compact surface with Euler characteristic $\chi(M) + b$ from which b discs are removed. In this case we associate to M the genus of its closed companion.

Let us note simple examples which can be used to verify the correctness of a triangulation:

1. Let M be a planar bounded triangulation with b boundary components. Then we have

$$2 - \chi(M) = b \tag{1.3}$$

since M can be closed to a sphere with $\chi(S^2) = 2$ by pasting with b simply connected faces.

2. In general, an oriented polyhedral surface M with genus g and with b missing disks has b boundary components and fulfills

$$2 - 2g - \chi(M) = b. \tag{1.4}$$

Note, that both identities provide an easy way to calculate the number of boundary components if the genus is known, or to validate a given mesh if the genus and the number of boundaries are known.

1.3 Distance and Metric

For metric measurements the interior of simplicial faces must be uniquely defined. Therefore, we prefer simplicial instead of polyhedral surfaces, or assure that we work with piecewise flat polygons. The metric of a surface may, for example, be induced from an immersion into a Euclidean space, or the metric may be defined in a more abstract way, say, by assigning a length to each edge which fulfills the triangle identity on each triangle. In a locally Euclidean metric the distance between two points is measured along curves whose length is measured segment-wise on the open edges and triangles:

Definition 15 *A curve γ on a simplicial complex M is called* rectifiable*, if for every simplex $\sigma \in M$ the part $\gamma_{|\sigma}$ is rectifiable w.r.t. to the smooth metric of σ. Then the* length *of γ is given by*

$$L(\gamma) := \sum_{\sigma \in M} L(\gamma_{|\mathring{\sigma}}). \tag{1.5}$$

as the sum of the lengths on each open simplex.

The area of a simplicial surface is defined in a similar way:

Definition 16 *Let M be a simplicial surface. Then we define*

$$\operatorname{area} M := \sum_{T \in M} \operatorname{area} M. \tag{1.6}$$

Most of our considerations apply to a more general class of length spaces. Each face may have an arbitrary metric as long as the metrics of two adjacent faces are compatible, i.e. if the common edge has the same length in both faces, and the triangle inequality holds.

In many practical applications simplicial complexes have a metric induced from an immersion into a Euclidean $\mathbb{R}^n$. For example, take a polyhedral surface in $\mathbb{R}^3$ and consider the two adjacent faces of an edge. Each face has the metric induced from $\mathbb{R}^3$, i.e. the length of any curve on a face is equal to the length of the same curve measured in $\mathbb{R}^3$. In this case, any neighbourhood of a point on the edge is isometric to a planar domain, since both faces can be unfolded to $\mathbb{R}^2$.

When considering the approximation of a smooth surface M with a sequence polyhedral surfaces $\{M_{h,i}\}$ one should be aware that higher order terms such as area may not need to converge as expected. The *Schwarz example* is a sequence of polyhedral surfaces which converges uniformly to a cylinder while the corresponding area grows to infinity.

1.4 Discrete Gauß Curvature

For a smooth surface S embedded into $\mathbb{R}^3$ the curvature measures the infinitesimal bending of the surface compared to the flat tangent plane. Instead of comparing the surface with the tangent plane, we can equally consider the turn of the normal vector along the surface. Formally, this is measured by the *Gauß map* $g : S \to \mathbb{S}^2$ which assigns to each point p on a surface S the tip of its normal vector $n(p)$ after it was parallel translated to the origin of $\mathbb{R}^3$, see Figure 1.1. The *total*

Gauß curvature $K(\Omega)$ of a domain $\Omega \subset S$ is then given by the area of its spherical image: $K(\Omega) = \operatorname{area} g(\Omega)$. The *Gauß curvature* $K(p)$ at a point p on S is defined as the limiting value

$$K(p) = \lim_{\varepsilon \to 0} \frac{\operatorname{area} g(U_\varepsilon(p))}{\operatorname{area} U_\varepsilon(p)} \tag{1.7}$$

for open neighbourhoods $U_\varepsilon(p)$ of radius less than ε of p. Note, if the surface S is twice differentiable, then the Gauß curvature can be expressed in terms of the partial derivatives of the metric tensor of S as product $K(p) = \kappa_1(p)\kappa_2(p)$ of the two principal curvatures at p.

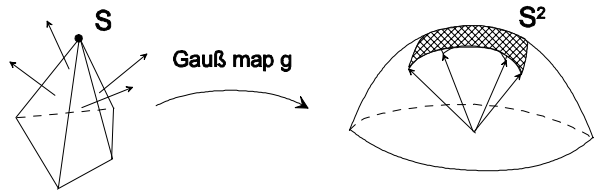

FIGURE 1.1. The Gauß map assigns to each point $p \in S$ of a surface its normal vector $n(p) \in \mathbb{S}^2$. At edges and vertices of a polyhedral surface the image of the Gauß map is the spherical convex hull of the normal vectors of adjacent faces.

The Gauß curvature of a general manifold is a central intrinsic property of the geometry and is fully determined by the Riemannian metric. It influences, for example, the parallel translation of tangent vectors along curves of the manifold.

On a polyhedral surface, the discrete Gauß curvature is concentrated at the isolated vertices since all other points on the surface have a neighbourhood isometric to a planar Euclidean domain with zero curvature. But at vertices the limit value in Equation 1.7 will not exist unless the surface is planar. Therefore it is more appropriate to work with the concept of total Gauß curvature in the polyhedral case.

On a polyhedral surface, the neighbourhood of a vertex is isometric to a cone. Before defining a discrete Gauß curvature we study simplicial cones in more detail. Metrically, each cone is characterized by the total vertex angle:

Definition 17 *Let S be a polyhedral surface and $p \in S$ a vertex. Let $\{f_1, \ldots, f_m\}$ be the set of faces of* $\operatorname{star} p$*, and let θ_i be the vertex angle of the face f_i at the vertex p, see Figure 1.2. Then the* total vertex

angle $\theta(p)$ *is given by*

$$\theta(p) = \sum_{i=1}^{m} \theta_i(p). \tag{1.8}$$

Interior points p of a face or of an open edge have a neighbourhood which is isometric to a planar Euclidean domain, and we define $\theta(p) = 2\pi$ *in these cases.*

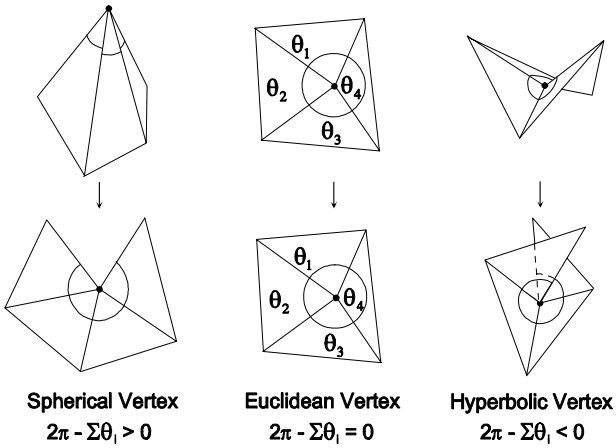

FIGURE 1.2. Classification of vertices on a polyhedral surface according to the excess of the vertex angle, and their unfolding to a planar domain.

All points of a polyhedral surface can be classified according to the sign of the *vertex angle excess* $2\pi - \theta(p)$:

Definition 18 *A vertex p of a polyhedral surface S with total vertex angle* $\theta(p)$ *is called* Euclidean, spherical, *or* hyperbolic *if its angle excess* $2\pi - \theta(p)$ *is* $= 0$, > 0, *or* < 0. *Respectively, interior points of a face or of an open edge are always Euclidean.*

The neighbourhood of a vertex can be isometrically unfolded to a (partial or multiple) covering of a part of the Euclidean plane. There exist three situations as shown in Figure 1.2 which metrically characterize the vertex. For example, the tip of a convex cone is a spherical vertex and a saddle point is hyperbolic. On the other hand, a spherical vertex need not be the tip of a convex cone. The isometric unfolding of sets of a polyhedral surface is a common procedure to study the geometry.

The vertex angles determine the discrete Gauß curvature directly in metrical terms of the polyhedral surface S.

Definition 19 *The discrete* Gauß curvature $K(p)$ *of an interior vertex p on a polyhedral surface S is defined as the vertex angle excess*

$$\begin{aligned} K(p) &= 2\pi - \theta(p) \\ &= 2\pi - \sum_{i=1}^{m} \theta_i(p). \end{aligned} \tag{1.9}$$

The discrete Gauss curvature of a boundary vertex is defined π.
The total Gauß curvature $K(S)$ *of the polyhedral surface S is the sum of the Gauß curvatures of all vertices of K*

$$K(S) = \sum_{p \in K^{(0)}} K(p).$$

An immediate consequence is that Euclidean vertices have curvature $K = 0$, spherical vertices have $K > 0$, and hyperbolic vertices have $K < 0$. For example, the vertices of a cube each have Gauß curvature $\frac{\pi}{2}$.
As a justification of this first definition of a discrete curvature term, let us note the following remarkable consequence. The total Gauß curvature, above derived from the local geometric properties of the vertex stars, is related to the Euler characteristic and, therefore, has a global topological significance for the polyhedral surface.

Theorem 20 (Simplicial Gauß-Bonnet) *Let S be a compact polyhedral surface in $\mathbb{R}^n$. Then*

$$K(S) = 2\pi\chi(S).$$

Proof. First we triangulate S without affecting either side of the equation. Since S is compact without boundary we then have

$$3f = 2e$$

where v, e, f denotes the number of vertices, edges and faces of the surface S. Therefore

$$\begin{aligned}\sum_{p\in K^{(0)}} K(p) &= \sum_{p\in K^{(0)}} (2\pi - \sum_{\sigma\in \operatorname{star} p^{(2)}} \theta(p,\sigma)) \\ &= 2\pi v - \sum_{\sigma\in \operatorname{star} p^{(2)}} \sum_{p\in K^{(0)}} \theta(p,\sigma) \\ &= 2\pi v - \pi f \\ &= 2\pi v - 2\pi e + 2\pi f \\ &= 2\pi\chi(S).\end{aligned}$$

□

In Chapter 2 the theorem is extended to bounded regions on surfaces by including the geodesic curvature of the simplicial boundary curve, see Theorem 42. We postpone this more general result until we have introduce the notion of discrete geodesic curvature of curves on polyhedral surfaces.

Minimizing the Gauß Curvature

We consider the Plateau problem for the Gauß curvature which starts with a given boundary curve γ and looks for a disk or punctured higher genus patch spanned by γ which minimizes the Gauß curvature. By the smooth version of Gauß-Bonnet [25], the total Gauß curvature of any spanned patch M can be estimated from below by the total curvature of γ:

$$\int_M K da = 2\pi\chi(M) - \int_\gamma \kappa_g ds \geq 2\pi\chi(M) - \int_\gamma \kappa ds \tag{1.10}$$

since the geodesic curvature is always smaller than the curvature of a curve $0 \leq \kappa_g \leq \kappa$.
Therefore, in the smooth situation a curvature minimizing patch M can be immediately constructed:

1. create a small strip along γ which is tangent to the osculating plane and which has zero width along segments with vanishing curvature.
2. arbitrarily extend the strip to a patch with assumed genus.

The tangency condition ensures that within the strip the geodesic curvature of γ is pointwise equal to its curvature, and we obtain equality in Equation 1.10, i.e. M is curvature minimizing.

In the smooth case the ambiguity of the extension of the strip to the interior can be removed by looking for a curvature minimizing cone over the curve, at least up to some extend. Let p be the center of the cone connected with straight lines to γ. Assume $\gamma(t)$ is parametrized by arclength. Let $b := p-\gamma-\langle p-\gamma, \gamma'\rangle \gamma'$ be parallel to the binormal vector along γ of the current cone, then the total geodesic curvature is given by

$$\int_0^\ell \kappa_g dt = \int_0^\ell < \gamma", \frac{b}{|b|} > dt.$$

It is maximized by variation of p in direction of the gradient

$$\frac{d}{dp}\int_0^\ell \kappa_g dt = \int_0^\ell \frac{1}{|b|}\left(\gamma'' - < \gamma", \frac{b}{|b|} > \frac{b}{|b|}\right) dt.$$

In the polyhedral case we start with a polygonal curve γ_h and given mesh connectivity, say by an initial surface $M_{h,0}$. Then it is generally not possible to find a strip with the combinatorics induced by $M_{h,0}$ such that γ_h has vanishing discrete normal curvature. But minimizing the Gauß curvature of the polyhedral surface will lead to a polyhedral immersion which approximates best the osculating plane along the boundary.

Let p be an interior vertex of the polyhedral surface and θ_i the vertex angle at p of a triangle Δ_i with edges $c_i = a_i - b_i$ and such that a_i,b_i emanate from p. Then the gradient of the vertex angle θ_i is given by

$$\begin{aligned}\nabla_p \theta_i &= \frac{\sin^2\theta_i}{\operatorname{area}\Delta_i}\left(\frac{a_i+b_i}{2} + \frac{1}{2}\cot\theta_i J c_i\right)\\ &= \frac{\sin^2\theta_i}{\operatorname{area}\Delta_i}(M_i - p)\end{aligned}$$

where M_i is the center of the circumcircle. Similarly, if q is a vertex adjacent to p, and θ the vertex angle at p then we have

$$\nabla_q \theta = \sum_{\Delta \in \operatorname{star} pq} \frac{J_\Delta (p-q)}{|p-q|^2}.$$

Summarizing, we obtain:

Lemma 21 *The gradient of the polyhedral Gauß curvature is given by*

$$\nabla_p K(p) = \sum_i \frac{\sin^2\theta_i}{\operatorname{area}\Delta_i}(p - M_i)$$

and

$$\nabla_q K(p) = \sum_{\Delta \in \operatorname{star} pq} \frac{J_\Delta(q-p)}{|q-p|^2}.$$

where M_i is the center of the circumcircle.

These equations suffice to apply the conjugate gradient method for minimizing the Gauß curvature of M_h.

1.5 Grids in Numerics and Graphics

Over the recent years an enormous effort went into the design of efficient grids in numerics and computer graphics. Adaptive grids and hierarchical representations became very important in numerical applications, and are nowadays complemented with subdivision surfaces in computer graphics modeling packages. Among the current issues is the construction of specialized encodings for efficient data compression.

This section recalls some important types of meshes used in numerical computations and computer graphics. The choice of a suitable grid depends on a number of criteria such as the shape of the domain, the type of the numerical method, or even the hardware, for example, to support parallelization of algorithms.

Structured grids tessellate a rectangle $[x_{\min}, x_{\min}] \times [y_{\min}, y_{\min}] \subset \mathbb{R}^2$ into regular quadrilaterals of the same size $h = (h_x, h_y)$. The grid Ω_h

$$\Omega_h = \left\{ (x_i, y_j) \;\middle|\; \begin{array}{ll} x_i = x_{\min} + ih_x & i \in [0, m-1] \\ y_j = y_{\min} + jh_y & j \in [0, n-1] \end{array} \right\}$$

is implicitly determined by the two extremal vertices $(x_{\min}, y_{\min})$ and $(x_{\max}, y_{\max})$ and the number of subdivisions (m, n). *Multiblock grids* use several structured grids at possibly different resolutions to cover the different regions of the domain. *Multigrids* and *sparse grids* are hierarchical representations which allow a considerable reduction of the number of grid points.

Parametric grids are obtained as images of other grid types under a continuous map Φ and thus are suitable for the discretization of more general domains. Important examples of parametric maps are Möbius maps and the Schwarz-Christoffel map, both are angle-preserving, i.e. conformal maps. Circle packings, remarkably applied by Thurston and others to problems with three-manifolds, are nowadays a promising concept in practical implementations, for example, for the flat-

tening of rather the general surfaces [64]. See also the variational characterization by Bobenko and Springborn [15].

Unstructured or irregular grids may consist of arbitrary non-overlapping polygons. Such grids are determined by a set of points, i.e. the vertices of the polygons,

$$P = \{P_0, P_2, ..., P_9\}$$

and connectivity information where each polygon is given as an ordered list of its vertices, or more efficient, of its vertex indices

$$\begin{aligned} E_0 &= \{0,1,2\} \\ E_1 &= \{2,1,3,4\} \\ E_2 &= \{5,6,1,3\} \\ E_3 &= \{3,6,7,8,9,4\}. \end{aligned}$$

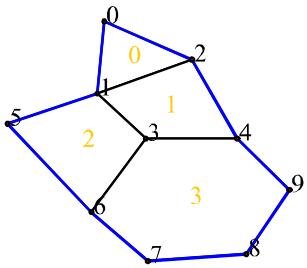

Unstructured Grid.

Many other information of a structured grid may be stored in order for faster access of information, or to clarify ambiguous situations. For example, a list of neighbour faces which have common edge with the current face. The following neighbour array has for each element E_i a list of indices of adjacent elements N_i where $N_i[j]$ denotes the element adjacent to the edge $E_i[j+1]E_i[j+2]$ of E_i (indices are modulo number of vertices of E_i).

$$\begin{aligned} N_0 &= \{0,1,2\} \\ N_1 &= \{2,3,-1,0\} \\ N_2 &= \{3,1,-1,-1\} \\ N_3 &= \{-1,-1,-1,-,1,1,2\}. \end{aligned}$$

In Chapter 8 we will introduce a hierarchical representation of irregular grids which allows a continuous interpolation between adaptively refined irregular meshes. This solves the interpolation problem in animations and for a set of adaptive geometries which depend on one or more parameters.

The *winged edge format* was introduced by Baumgart [11] as a redundancy free representation format to store polyhedral meshes of faces with an arbitrary and varying number of edges. It is an edge-based format where each edge contains references to two vertices P_1 and P_2, and references E_1 respectively E_2 to an adjacent edge on each of the two neighbouring faces. Boundary edges have one empty edge reference. It is assumed that each face has a unique orientation provided by an orientation of its edges. Therefore, faces are implicitly given by following the E_1 or E_2 reference of an arbitrary known edge of the

face. Note, the orientation of each individual face does not require that the whole surface is oriented.

Compared to the unstructured grid representation introduced above the winged edge format basically requires the same amount of storage: let E be the number of edges and F be the number of faces. In the winged edge format each edge has four integer references which leads to a storage of size $4E$. By the relation $3F = 2E$ for triangular meshes, the amount $4E$ is equal to $6F$ for irregular meshes which store 3 vertex references and 3 links to adjacent faces per face.

Non-manifold meshes may have more than two faces sharing an edge. In this case both the winged-edge format as well as the surface mesh format fail unless additional information is supplied.

Progressive meshes introduced by Hoppe [61] are based on vertex-split and edge-collapse operations for adaptive refinement and coarsening. In recent years these data types have been very popular in computer graphics especially since they allow topology changes. They are a special class of *multi-resolution grids* or *hierarchical grids* which store different levels of resolution of a shape. Often a smooth transition between different hierarchical resolutions is incorporated in the data structure. *Normal meshes* [54] were designed to describe shapes locally as graph over a coarser resolution of the same mesh. This technique is especially suitable for *subdivision surfaces* or multi-resolution surfaces obtained from a wavelet decomposition where the finer resolutions are obtained algorithmically.

The fast and incremental transmission of shapes over low-bandwidth connections plays an increasing role nowadays. Here specialized representations of meshes allow a compressed encoding. For example, the algorithm by Taubin and Rossignac [115], which is incorporated into the MPEG-4 standard, encodes the triangles connectivity with less more than $1-2$ bits compared to 96 bits used in the index based representation mentioned above.

1.5.1 Delaunay Triangulation

In numerics and visualization long thin triangles are often avoided since their occurrence may spoil the numerical error and lead to artefacts in rendered images. This is mainly due to the fact that linear interpolation of values given at the vertices of such a triangle may not have a good approximation property in the center. Although in some cases long thin triangles are appropriate, like in the cylindrical shape in the figure, we make the following Definition.

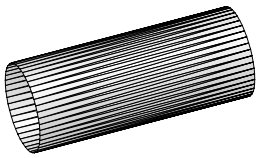

Cylinder with thin triangles.

Definition 22 *Let P be the set of vertices of a triangulation T and $A(T) = (\alpha_1, \alpha_2, ...)$, $\alpha_i \leqslant \alpha_j$ if $i < j$, the angle vector of all vertex angles in T. Then the triangulation T is called* angle-optimal *if for all triangulations T' the angle vector $A(T)$ is lexicographically larger than $A(T')$ $(A(T) > A(T'))$, i.e. there exists an index i such that*

$$\alpha_j = \alpha'_j \text{ for all } j<i, \text{ and } \alpha_i > \alpha'_i.$$

The lexicographic order of an angle vector of a triangulation can be increased by successive operations called *edge-flips*. This technique also avoids the computation of vertex angles.

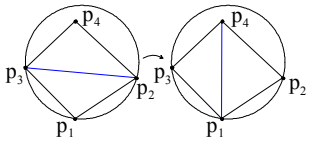

Edge flip criterium.

Lemma 23 *Consider two adjacent coplanar triangles with vertices p_1, p_2, p_3 and p_2, p_3, p_4 and common edge p_2, p_3. If p_4 lies inside the circumcircle through p_1, p_2, p_3 then the angle-vector can be increased by exchanging edge p_2, p_3 with edge p_1, p_4 (*edge flip*). Furthermore, if the four points lie on a common circle, then both diagonal edges are fine.*

Proof. Thales theorem allows to restrict the proof to a most symmetric situation from which the lemma follows by checking angles.
Let $a = (a_1, a_2)$ be the coordinates of four vertices of a planar, convex quadrilateral $\{a, b, c, d\}$, then it is easy to check that the edge bd must be flipped if and only if

$$\det \begin{pmatrix} a_1 & a_2 & a_1^2 + a_2^2 & 1 \\ b_1 & b_2 & b_1^2 + b_2^2 & 1 \\ c_1 & c_2 & c_1^2 + c_2^2 & 1 \\ d_1 & d_2 & d_1^2 + d_2^2 & 1 \end{pmatrix} > 0$$

For non-planar quadrilaterals in space a possible criterion is: the edge bd must be flipped if

$$\alpha + \delta > \beta + \gamma.$$

□

Definition 24 *A planar triangulation T of a point set P is* Delaunay *if the circumcircle of each triangle does not contain any point of P in its interior. This condition for being Delaunay is called the* sphere test.

Obviously, any Delaunay triangulation is edge-optimal, and Lawson [72] showed that an edge-optimal triangulation is a Delaunay triangulation. Any angle-optimal triangulation is edge-optimal and therefore a Delaunay triangulation, and Delaunay triangulations are angle-optimal, if no four adjacent vertices of P lie on a circle. If four vertices

of P lie on a circle then, at least, the Delaunay triangulation maximizes the minimum angle over all triangulations of P. Since any two triangulations of a planar point set can be transformed into each other [71], one can convert any initial triangulation to a Delaunay triangulation with the following edge swapping algorithm of Lawson [72]:

Algorithm 25 (Lawson 1977) *Let P be a given planar point set and a triangulation T'. Then the triangulation can be converted to a Delaunay triangulation T by a finite number of edge-flips, and T maximizes the minimal angle. Furthermore, if no four vertices of P lie on a common circle then T is angle-optimal.*

This algorithm is ensured to terminate since the number of possible angles in a triangulation is finite and in each edge flip the minimal angle is increased. We call such a triangulation edge-optimal. The algorithm is rather slow but stable and easy to implement.

Remark 26 *There should be some caution when using edge flips on non-planar surfaces in 3d space. On curved surfaces edge-flips may easily lead to degenerate situation even if care is taken on the valence of vertices. For example, the torus shown in the side figure is converted into a degenerate shape using a few edge-flips.*

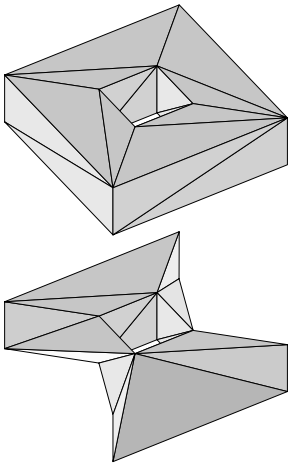

A 3d geometry may degenerate through edge flips.

If there is no initial triangulation of a point set P then there exist different algorithms for the direct construction of a Delaunay triangulation. For example, the algorithm of Watson [118] is based on inserting a point in an already existing Delaunay triangulation

1. Construct a triangle which covers the convex hull of the given point set P. This single triangle is a simple Delaunay triangulation, and it will be removed later.
2. Insert a point of P in the existing triangulation and make the triangulation again Delaunay.
3. If all points of P have been inserted then remove the original triangle, otherwise continue with step 2.

The crucial work is done in step 2. If the new vertex lies inside a triangle then the triangle is split into three new triangles and the three old edges must be legalized. If the new vertex lies on an edge, then both triangles are bisected and the four old edges must be legalized. Of course, the legalization must be continued if edges are flipped. A further optimization considers sorting the point set P.

It is possible to build the Delaunay triangulation of a set of n points in $\mathbb{R}^d$ in $O(n \log n + n^{\lceil \frac{d}{2} \rceil})$ expected time. The second term is the maximum number of possible simplices. In practice, the running time is much faster. A brute force algorithm starts with a simplex whose vertices are "at infinity", and adds a new vertex at each step while maintaining the Delaunay property through edge flips.

It should be noted that the Delaunay triangulation of a point set P contains interesting subgraphs, for example, the *minimum spanning tree* of P which connects all points of P with a set of edges of minimum total length.

1.5.2 Voronoi Diagrams

The Voronoi diagram of a set of points $P \subset \Omega \subset \mathbb{R}^d$ is a partitioning of Ω into cells where each cell c_i consists of the set of points $q \in \mathbb{R}^d$ which are closest to p_i. Finding a Voronoi diagram is often also called the Post Office Problem. A good introduction is the book by de Berg et al. [28] on computational geometry.

A promising strategy for tessellating the domain Ω with a given set of points P might associate to each point p a catchment area $V(p)$ of points closer to p than to any other point of P. For example, if P is the locations of good suppliers and Ω the region with people demanding goods, then for each supplier p the Voronoi region $V(p)$ is the area where people most efficiently go to location p for shopping. Formally,

Definition 27 *If P is a point set in a domain Ω and $p \in P$. Then the* Voronoi region $V(p) \subset \Omega$ *is*

$$V(p) = \left\{ r \in \Omega \,\middle|\, d(p,r) = \min_{q \in P} d(q,r) \right\}.$$

The Voronoi diagram $V(P)$ *consists of the boundaries of all Voronoi regions $V(p)$ with $p \in P$.*

The boundaries of all Voronoi regions are the Voronoi graph of the Voronoi diagram. Each interior point on an edge of the Voronoi graph has the same distance to exactly two points p, q of P, and it is closer to p and q than to any other point in P. Each vertex v of the Voronoi graph is the midpoint of the circumcircle of n points $p_1, p_2, p_3, .., p_n$ of P where n is the number of edges at v, respectively the number cells at v, and the circumcircle contains no point of P in its interior. If all vertices of the Voronoi graph have valence 3 then each triple (p_1, p_2, p_3) is a Delaunay triangle.

Theorem 28 *Let $V(P)$ be the Voronoi diagram of a planar point set P and let $\{p_i, p_j, p_k\} \subset P$ represent three sites.*

1. *A point q is a vertex of the Voronoi diagram $V(P)$ if and only if its largest empty circle $C(q)$ contains three or more points of P on its boundary.*
2. *The bisector between two sites p_i and p_j is an edge of the diagram if and only if there exists a point q on the bisector such that the circle $C(q)$ with center q through p_i and p_j contains no other point of P in its interior and on its boundary.*

The best algorithms to compute the vertices of the Voronoi diagram of a set of n-sites P spend $O(n \log n)$ time.
The Delaunay graph of a point set P is a triangulation dual to the Voronoi diagram, and each edge of the Voronoi diagram is the mid-perpendicular of a Delaunay edge connecting both sites.

1.5.3 $\alpha-$Shapes

$\alpha-$shapes were introduced in the plane by Edelsbrunner et al. [40] in 1983 to provide a continuous transition from the set of vertices through a growing shape to the convex hull. The original definition was later extended to three-dimensional space [41]. Let P be a set of points and T its Delaunay triangulation. Each simplex $\sigma \in T$ is assigned a size $s(\sigma)$ which is the radius of the smallest sphere enclosing σ. σ is called conflict-free if the smallest sphere does not contain any other point of P other than the vertices of σ.

Definition 29 *The* $\alpha-$shape *of a point set P with $\alpha \in \mathbb{R}_0^+$ is a subcomplex $\sum_\alpha$ of the Delaunay triangulation T consisting of all simplices $\sigma \in T$ with size $s(\sigma) < \alpha$ and which are conflict-free, as well as all their subsimplices.*

The $0-$shape consists of the set P of all vertices, and the $\infty-$shape consists of the convex hull of P. If P is finite then the family of $\alpha-$shapes is finite too.

1.6 Finite Element Spaces

Piecewise polynomial functions on simplicial surfaces conceptually fall into the category of finite element spaces. Here we briefly recall

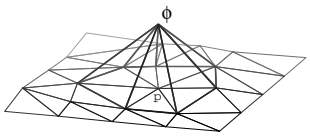

Basis function on manifold.

the most basic functions space relevant for our later work. See the books [27][21] for an introduction.

Definition 30 *On a simplicial surface M_h we define the function space S_h of* conforming finite elements*:*

$$S_h := \left\{ v : M_h \to \mathbb{R}^d \;\middle|\; v \in C^0(M_h) \text{ and } v \text{ is linear on each triangle} \right\}$$

S_h is a finite dimensional space spanned by the Lagrange basis functions $\{\varphi_1, .., \varphi_n\}$ corresponding to the set of vertices $\{p_1, ..., p_n\}$ of M_h, that is for each vertex p_i we have a function

$$\begin{gathered} \varphi_i : M_h \to \mathbb{R},\ \varphi_i \in S_h \\ \varphi_i(p_j) = \delta_{ij} \quad \forall i, j \in \{1, .., n\} \\ \varphi_i \text{ is linear on each triangle} \end{gathered} \tag{1.11}$$

where $\{p_1, ..., p_n\}$ is the set of interior vertices of M_h. Then each function $u_h \in S_h$ has a unique representation

$$u_h(p) = \sum_{j=1}^{n} u_j \varphi_j(p) \quad \forall\, p \in M_h$$

where $u_j = u_h(p_j) \in \mathbb{R}^d$. The function u_h is uniquely determined by its nodal vector $(u_1, ..., u_n) \in \mathbb{R}^{dn}$.

Sometimes we will also use piecewise higher-order polynomial representations described in a similar way with different basis functions. Note that any component function of a function $v \in S_h$ has bounded Sobolev H^1 norm.

1.6.1 Non-Conforming Finite Elements

In our later investigations the following space of non-conforming finite elements, see [27][21] for a detailed discussion, plays an important role. Since these spaces include discontinuous functions their use is often titled as a *variational crime* in the finite element literature. In our settings, non-conforming functions naturally appear as the correct spaces for our later considerations on constant mean curvature surfaces.

Definition 31 *For a simplicial surface M_h, we define the space of* non-conforming finite elements *by*

$$S_h^* := \left\{ v : M_h \to \mathbb{R}^d \;\middle|\; \begin{array}{l} v_{|T} \text{ is linear for each } T \in M_h, \text{ and} \\ v \text{ is continuous at all edge midpoints} \end{array} \right\}$$

The space S_h^* is no longer a finite dimensional subspace of $H^1(M_h)$ as in the case of conforming elements, but S_h^* is a superset of S_h. Let $\{m_i\}$ denote the set of edge midpoints of M_h, then for each edge midpoint m_i we have a basis function

$$\begin{array}{c} \psi_i : M_h \to \mathbb{R} \quad \psi_i \in S_h^* \\ \psi_i(m_j) = \delta_{ij} \quad \forall\, i,j \in \{1,2,..\} \\ \psi_i \text{ is linear on each triangle.} \end{array} \tag{1.12}$$

The support of a function ψ_i consists of the (at most two) triangles adjacent to the edge e_i, and ψ_i is usually not continuous on M_h. Each function $v \in S_h^*$ has a representation

$$v_h(p) = \sum_{\text{edges } e_i} v_i \psi_i(p) \quad \forall\, p \in M_h$$

where $v_i = v_h(m_i)$ is the value of v_h at the edge midpoint m_i of e_i. Let $M_h \subset \mathbb{R}^m$ be a conforming triangulation with vertices $V = \{p_1, p_2, ...\}$ and edge midpoints $E = \{m_1, m_2, ...\}$. For a given triangle $t \in M_h$ with vertices $\{p_{t_1}, p_{t_2}, p_{t_3}\}$ and edge midpoints $\{m_{t_1}, m_{t_2}, m_{t_3}\}$ we have the following elementary correspondence

$$\frac{1}{2}\begin{pmatrix} 0 & 1 & 1 \\ 1 & 0 & 1 \\ 1 & 1 & 0 \end{pmatrix}\begin{pmatrix} p_{t_1} \\ p_{t_2} \\ p_{t_3} \end{pmatrix} = \begin{pmatrix} m_{t_1} \\ m_{t_2} \\ m_{t_3} \end{pmatrix} \tag{1.13}$$

respectively

$$\begin{pmatrix} -1 & 1 & 1 \\ 1 & -1 & 1 \\ 1 & 1 & -1 \end{pmatrix}\begin{pmatrix} m_{t_1} \\ m_{t_2} \\ m_{t_3} \end{pmatrix} = \begin{pmatrix} p_{t_1} \\ p_{t_2} \\ p_{t_3} \end{pmatrix}. \tag{1.14}$$

We will also use the term *non-conforming surface* to denote a simplicial surface where adjacent triangles are connected at the midpoint of their common edge but may be twisted. Further, the corresponding edges of two adjacent triangles must have the same length. Such surfaces may be considered as images of a non-conforming map from a simplicial surface, therefore, we often do not distinguish between a non-conforming surface and a non-conforming map.

2

Discrete Geodesics on Polyhedral Surfaces

Geodesics on smooth surfaces are the straightest and locally shortest curves. They generalize the concept of Euclidean straight lines and play a fundamental role in the study of smoothly curved manifolds. Two basic properties are responsible for their importance: first, the length minimization property provides a solution of the boundary value problem of connecting two given points on a manifold with a locally shortest curve. Second, geodesics solve the initial value problem which states, that from any point of a manifold there starts a unique geodesic in any direction. On smooth surfaces geodesics possess both properties simultaneously, in contrast to the situation on polyhedral surfaces as we will show in this section.

Here we will generalize the notion of geodesics to polyhedral surfaces which leads to the idea of *straightest curves* on two-dimensional polyhedral surfaces, as opposed to the concepts of locally shortest and quasi-geodesics. Such straightest geodesics will uniquely solve the initial value problem on polyhedral surfaces, and therefore allow to move uniquely on a polyhedral surface in a given direction along a straightest geodesic until the boundary is reached, a property not available for locally shortest geodesics. An application of straightest geodesics is the definition of parallel translation of vectors and higher order numerical integration methods for tangential vector fields. This allows the extension of Runge Kutta methods to polyhedral surfaces.

We consider polyhedral surfaces as two-dimensional simplicial complexes consisting of triangles. Each triangle has a flat metric and the common edge of two adjacent triangles has the same length in both triangles. The definition of a metric on the polyhedral surface only requires the specification of edge lengths and does not refer to an immersion of the surface in an ambient space. This intrinsic approach allows the definition of straightest geodesics, discrete geodesic curvature, vector fields, and parallel translation of vectors in terms of the geometric data of the surface, such as edge lengths, triangle angles, and discrete curvature properties.

Geodesics on polyhedral surfaces were intensively studied using different definitions. The Russian school of A.D. Alexandrov [1] defines geodesics on polyhedral surfaces as locally shortest curves which leads to important implications in the study of non-regular and regular differential geometry. But shortest geodesics cannot be extended as shortest curves across a spherical vertex with positive Gauß curvature as, for example, the vertex of a cube. Beyond a hyperbolic vertex with negative Gauß curvature there even exists a continuum of extensions. Therefore, shortest geodesics fail to solve the initial value problem for geodesics at vertices of a polyhedral surface.

A.D. Alexandrov also introduced the concept of *quasi-geodesics* which are limit curves of geodesics on a family of converging smooth surfaces. They form a wider class than shortest geodesics and were amongst others studied by Pogorelov [89] on convex polyhedral surfaces. A quasi-geodesic through a spherical vertex is a curve with right and left angles both less than π, and therefore an inbound direction has multiple extensions.

Shortest geodesics appear in many practical applications. For example, the optimal movement of a robot should have minimal length in its parameter space. Such discrete minimization problems are studied in computational geometry, see for example Dijkstra [33], Sharir and Schorr [113], and Mitchell et al. [78] for efficient algorithms on the computation of the shortest path in graphs and in polyhedral spaces with respect to the edge metric.

In section 2.1 we start with a review of geodesics on smooth surfaces, especially since some of their properties differ from those of geodesics on polyhedral surfaces. Straightest geodesics are defined in section 2.2 and discussed as solutions of the initial value problem. In section 2.3 we imbed the notion of straightest lines into the concept of discrete geodesic curvature of arbitrary curves on polyhedral surfaces. This general setting is more appropriate for our later discussions, and straightest geodesics turn out to be those class of curves

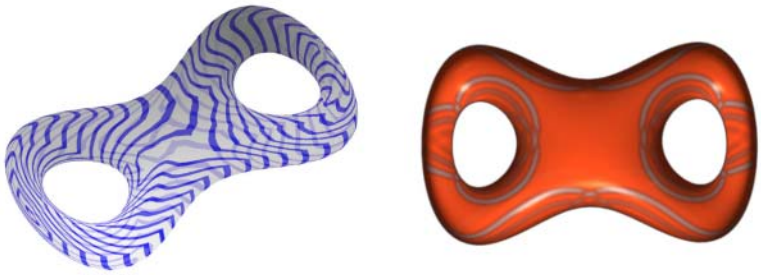

FIGURE 2.1. Combinatorial distance circles via Dijkstra (left) and geodesic flow via straightest geodesics (right).

with vanishing discrete geodesic curvature. As a validation of the definition we prove an extended version of the polygonal Gauß-Bonnet theorem which uses our notion of discrete geodesic curvature. In section 2.4 we apply the concept to the definition of parallel translation of tangential vector fields and in section 2.4.1 we generalize Runge Kutta methods to the numerical integration of ordinary differential equations on polyhedral surfaces.

The techniques described in this chapter have been applied, for example, in the simulation of a fire front on a surface [75] by Lee et al., or in the simulation of surface flows in the video *Geodesics and Waves* [101]. The numerics were originally developed for the study of magnetic fields on aircrafts within the visualization environment OORANGE [53], and now exist as a web-based JavaView application service [92][93]. The material in this section is a unified presentation of work by Polthier and Schmies [99] and [100].

2.1 Review of Smooth Geodesics

Geodesics on smooth surfaces can be characterized by different equivalent properties. The generalized properties on polyhedral surfaces will no longer be equivalent and lead to different classes of discrete geodesics. The following material can be found in many introductory text books on differential geometry, see for example [25].

Let M be a smooth surface and $\gamma : I = [a, b] \to M$ a curve parametrized over an interval I. To avoid accelerations tangential to the curve we assume arc length parametrization, i.e. the tangent vector has constant length $|\gamma'| = 1$. A curve γ is called *locally shortest* if it is a critical point of the length functional $L(\gamma_{|[a,b]}) := length(\gamma_{|[a,b]})$

with respect to variations tangential to M which leave the endpoints fixed. Formally, if $\phi : I \to T_\gamma M$ is a tangential vector field along γ with $\phi(a) = 0$ and $\phi(b) = 0$, then we have $\frac{\partial}{\partial \varepsilon} L(\gamma + \varepsilon\phi)_{|\varepsilon=0} = 0$. A critical point of the length functional is usually not a global minimizer compared to curves with the same endpoints.

On smooth manifolds the length minimizing property of geodesics can be reformulated as an ordinary differential equation for γ, namely $\gamma''(s)^{\tan \mathrm{M}} = 0$, the Euler-Lagrange equations of the variational problem.

The curvature $\kappa(s) = |\gamma''(s)|$ of a curve measures the infinitesimal turning of the tangent vector at every point $\gamma(s)$. For curves γ on surfaces $M \subset \mathbb{R}^3$, the curvature can be decomposed into the curve's bending in the normal direction n of the surface and its bending in the tangent space in direction of the binormal b. This decomposition leads to the definition of the geodesic curvature κ_g and the normal curvature κ_n of a curve:

$$\begin{aligned} \kappa^2(s) &= |\gamma''(s)|^2 \\ &= \left|\gamma''(s)^{\tan \mathrm{M}}\right|^2 + \left|\gamma''(s)^{\mathrm{nor\ M}}\right|^2 \\ &= \kappa_g^2(s) + \kappa_n^2(s). \end{aligned} \tag{2.1}$$

Here $\gamma''^{\tan \mathrm{M}}$ denotes the tangential and $\gamma''^{\mathrm{nor\ M}}$ the normal component of the second derivative. The geodesic curvature κ_g of a curve γ measures the tangential acceleration. If $\kappa_g = 0$ then the curve varies up to second order only in direction of the surface normal, therefore it is a *straightest curve* on the surface. The normal curvature κ_n is related with the bending of the surface itself and can be neglected from an intrinsic point of view.

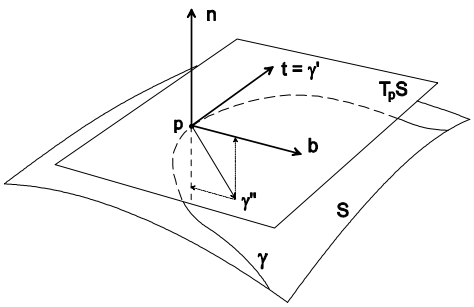

FIGURE 2.2. Geodesic and normal curvature of a curve on a smooth surface.

Summarizing, one characterizes smooth geodesics as follows:

Definition 32 *Let M be a smooth two-dimensional surface. A smooth curve $\gamma : I \to M$ with $|\gamma'| = 1$ is a* geodesic *if one of the equivalent properties holds:*

1. *γ is a locally shortest curve.*
2. *γ'' is parallel to the surface normal, i.e.*

$$\gamma''(s)^{tan\ M} = 0. \tag{2.2}$$

3. *γ has vanishing geodesic curvature $\kappa_g = 0$.*

In Section 2.2 we will consider geodesics on polyhedral surfaces and notice that the polygonal equivalents of the above properties lead to different notions of discrete geodesics.
For later comparison with the discrete case we mention two uniqueness properties of geodesics. The boundary value problem for geodesics usually has no unique solution, for example, there exists a locally shortest curve in any homotopy class. Instead, the initial value problem corresponding to Equation (2.2) has a unique solution which follows from the unique solvability of Lipschitz-continuous ordinary differential equations:

Lemma 33 *Let M be a smooth manifold. Then for any point $p \in \overset{\circ}{M}$ in the interior of M and any tangent direction $v \in T_pM$ the initial value problem*

$$\begin{aligned} \gamma''(s)^{tan\ M} &= 0 \\ \gamma(0) &= p \\ \gamma'(0) &= v \end{aligned} \tag{2.3}$$

has a unique solution $\gamma : [0, \ell) \to M$, where ℓ is the length of the maximal interval of existence.

2.2 Discrete Straightest Geodesics

The concept of shortest geodesics in graphs, polyhedral manifolds, and more general length spaces has been studied by a number of authors in different fields, see for example [33][78][1][2]. For applications related to vector fields, this concept has a central missing property,

namely, the initial value problem for geodesics is not uniquely solvable and, in some cases, has no solution: first, no shortest geodesics can be extended through a spherical vertex since it could be shortened by moving off the corner, and second, there exists a family of possible extensions of a geodesic as a shortest curve through a hyperbolic vertex: every extension with curve angles $\theta_l, \theta_r \in [\pi, \theta - \pi]$ is locally shortest where θ is the total vertex angle. See Lemma 37 and Figure 2.3.

Quasi-geodesics are a different approach introduced by A.D. Alexandrov (see the references to the original Russian literature in [1]) and later investigated by Pogorelov [89] and others. They are defined as limit sets of smooth geodesics when smooth surfaces approximate, for example, a polyhedral surface. On polyhedral surfaces quasi-geodesics are characterized by their fulfillment of the inequality $|\pi - \theta_l| + |\pi - \theta_r| - |2\pi - \theta_l - \theta_r| \geq 0$ at each point, where θ_l and θ_r are the two angles of the curve, and $\theta_l + \theta_r = \theta$ is the total vertex angle of the point. Compare Figure 2.3 for the notation. At hyperbolic vertices with $\theta > 2\pi$ the definition is identical to that for shortest geodesics, while at spherical vertices with $\theta < 2\pi$ curves with $\pi - \theta_l \geq 0$ and $\pi - \theta_r \geq 0$ are quasi-geodesics.

This approach to discrete geodesics on polyhedral surfaces concentrates on the property of a curve to be straightest rather than locally shortest. Both properties are equivalent for geodesics on smooth surfaces, as mentioned in Section 2.1, but locally shortest curves on polygonal surfaces do not allow a unique extension, for example, beyond spherical vertices of the surface. The original motivation for this study was to define a unique way to move straight ahead in a given direction on a polyhedral surface. Applications are, for example, the tracing of moving particles restricted to flow along a polyhedral surface, the solution of initial value problems on polyhedral surfaces related with given tangential vector fields, and the intrinsic generalization of numerical algorithms for ordinary differential equations to polygonal surfaces.

In the following definition we introduce straightest geodesics as a new class of discrete geodesics on polyhedral surfaces. This class has a non-empty intersection with the set of shortest geodesics, and it is a subset of quasi-geodesics.

Definition 34 *Let M_h be a polyhedral surface and $\gamma \subset M_h$ a curve. Then γ is a* straightest geodesic *on M_h if for each point $p \in \gamma$ the left and right curve angles θ_l and θ_r at p are equal, see Figure 2.3.*

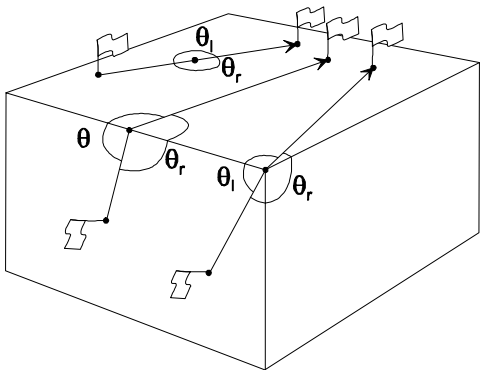

FIGURE 2.3. Notion of left and right curve angles θ_l and θ_r with $\theta_l + \theta_r = \theta$.

A straightest geodesic in the interior of a face is locally a straight line, and across an edge it has equal angles on opposite sides as shown in Figure 2.3. The definition of straightest geodesics on faces and through edges is identical to the concept of shortest geodesics but at vertices the concepts differ. Our definition fits into the more general discussion of discrete geodesic curvature of curves on a polyhedral surface which will be discussed in Section 2.3.

The following theorem shows the unique solvability of the initial value problem for straightest geodesics. To state the problem we start with the notion of a tangent vector on a polyhedral surface:

Definition 35 *Let M_h be a polyhedral surface and $p \in M_h$ a point. A* polyhedral tangent vector *v with base point p lies in the plane of an adjacent face and locally points into the face. The polyhedral tangent space T_pM_h consists of all polyhedral tangent vectors at p.*

We remark, that the polyhedral tangent bundle TM_h can be equipped with the structure of a topological vector bundle by introducing normalized angles as in Definition 43, but do not pursue this property here. Instead, we use the fact that polyhedral tangent vectors are characterized solely by intrinsic properties of the geometry rather than by reference to an ambient space.

Theorem 36 (Discrete Initial Value Problem) *Let M_h be a polyhedral surface and $p \in M_h$ a point with polyhedral tangent vector $v \in T_pM_h$. Then there exists a unique straightest geodesic γ with*

$$\begin{aligned} \gamma(0) &= p \\ \gamma'(0) &= v, \end{aligned} \tag{2.4}$$

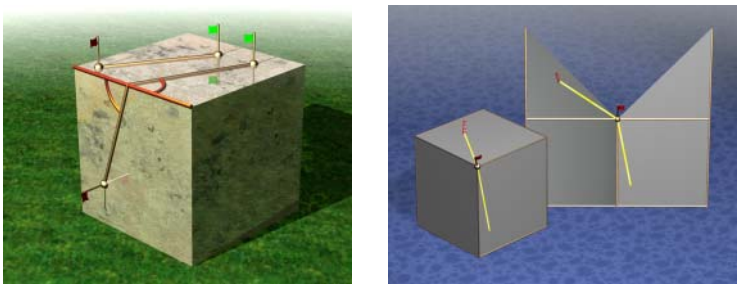

FIGURE 2.4. Straightest geodesics are defined to have equal angle on both sides at each point. On planar faces they are straight lines, and across edges they have equal angle on opposite sides. Straightest geodesics can be extended through polyhedral vertices, a property not available for shortest geodesics.

and the geodesic extends to the boundary of M_h.

Proof. There exists a face f of M_h which contains the initial point p and, for a small number $\varepsilon > 0$, the straight line $\gamma(t) := p + tv$ with $t \in [0, \varepsilon)$. γ is a straightest geodesic and a solution of Equation 2.4. If we extend γ beyond the small interval and γ reaches an edge or a vertex of M_h for larger values of t then Definition 34 of straightest geodesics uniquely defines how to extend γ beyond the edge or vertex. That is to proceed in that direction for which the left and right curve angles of γ at the vertex are equal. □

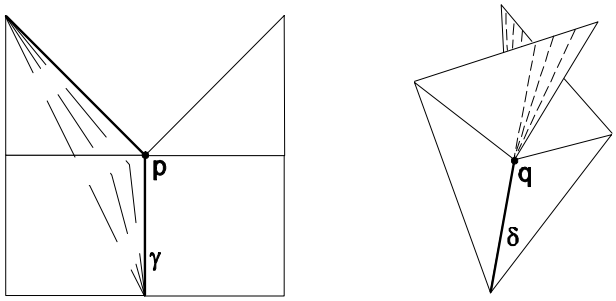

FIGURE 2.5. Locally shortest geodesics cannot be extended through a spherical vertex p and there exist multiple continuations at a hyperbolic vertex q.

The concepts of straightest and shortest geodesics differ on polyhedral surfaces. For example, as shown in the following lemma, the theorem above does not hold for locally shortest geodesics approach-

ing a spherical or hyperbolic vertex. As long as a geodesic γ does not meet a vertex of a polyhedral surface both concepts are equal and γ is both, straightest and locally shortest. The following lemma comprehends the differences:

Lemma 37 *On a polyhedral surface M_h the concepts of straightest and locally shortest geodesics differ in the following way (see Figure 2.5):*

1. *A geodesic γ containing no surface vertex is both straightest and locally shortest.*
2. *A straightest geodesic γ through a spherical vertex is not locally shortest. More general, there exists no locally shortest geodesic through a spherical vertex.*
3. *There exists a family of shortest geodesics γ_θ through a hyperbolic vertex with the same inbound direction. Only one of the shortest geodesics extends the inbound direction as straightest geodesic.*
4. *Straightest geodesics do not solve the boundary value problem for geodesics since there exist shadow regions in the neighbourhood of a hyperbolic vertex where two points cannot be joined by a straightest geodesic.*

Proof. Ad 1.) We unfold the faces met by the geodesic to an isometric strip of faces in the Euclidean plane. The geodesic γ is unfolded to a Euclidean straight line in the interior of the strip which is locally shortest and fulfills the angle condition of Definition 34.

Ad 2.) Let γ be a polygon through a spherical vertex with curvature $K > 0$. We unfold the adjacent faces to a planar domain by cutting along the outbound direction of γ. The image of γ in the plane has right and left vertex angles α and β such that $\alpha + \beta = \theta < 2\pi$. From this follows that either α or β is less than π, and therefore γ can be shortened by smoothing the corner on the side with smaller angle as shown on the left in Figure 2.5. As a consequence straightest geodesics through a spherical vertex are not locally shortest.

Ad 3.) A hyperbolic vertex has curvature $K < 0$. Let γ_0 be the unique straightest geodesic though the vertex which extends the inbound direction. We unfold the adjacent faces to a planar domain by cutting along the outbound direction of γ_0, then γ_0 has a curve angle $\frac{\theta}{2} = \pi - \frac{K}{2} > \pi$ at both sides of the corner. Assume a curve with the same inbound but a different outbound direction. Whenever both

angles between the inbound and outbound direction are bigger than or equal to π, we cannot locally shorten the curve. Therefore all such curves are locally shortest. □

Note, the equality of the concepts of shortest and straightest on the whole surface outside the set of vertices, which is a set of measure zero, should not lead to the conclusion that both concepts are equal in some weak sense. In contrast, it emphasises again the fact that the geometry of a polyhedral surface is concentrated at the vertices - like the Gauss curvature is concentrated at the vertices.

2.3 Discrete Geodesic Curvature

We define the notion of geodesic curvature of curves on piecewise linear surfaces. The major aim in mind is the later definition of parallel translation of vectors along arbitrary curves. As a by-product, the vanishing geodesic curvature gives another characterization of straightest geodesics. The definition will simplify to the known discrete curvature of polygons in the Euclidean plane. Further, a Gauß-Bonnet equation will hold in a more general case incorporating the discrete geodesic curvature of the boundary. In the following, we assume curves to be piecewise linear on faces with well-defined polyhedral tangent directions at the edges and vertices of the surface. Similar to the discrete Gauß curvature for surfaces, the discrete geodesic curvature is the equivalent of the total geodesic curvature of smooth surfaces.

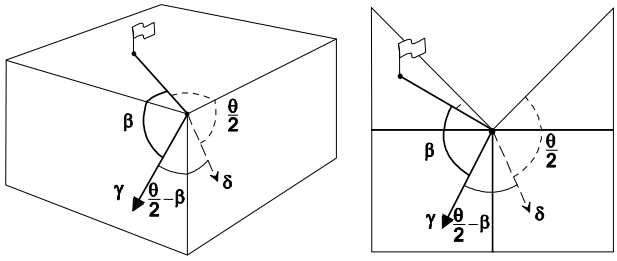

FIGURE 2.6. The discrete geodesic curvature of a curve γ is the normalized angle between γ and a discrete straightest geodesic δ.

Definition 38 *Let γ be a curve on a polyhedral surface M_h. Let θ be the total vertex angle and β one of the two curve angles of γ at p.*

Then the discrete geodesic curvature κ_g *of* γ *at* p *is given by*

$$\kappa_g = \frac{2\pi}{\theta}\left(\frac{\theta}{2} - \beta\right). \tag{2.5}$$

Choosing the other curve angle $\beta' = \theta - \beta$ *changes the sign of* κ_g.

Remark 39 *1.) Let* γ *be a polygon in the Euclidean plane and* $p \in \gamma$ *be a vertex with curve angle* β. *Then the discrete geodesic curvature equals the exterior angle* $\frac{\theta}{2} - \beta$, *i.e. the discrete curvature of* γ *at* p.
2.) Let M_h *be a polyhedral surface and let* γ *go straight in and directly go back from a vertex* $p \in M_h$, *i.e.* $\beta = 0$. *Then the geodesic curvature of* γ *at* p *is* $\kappa_g = \pi$, *i.e. it can be measured in the Euclidean face and without influence of the vertex angle* θ *at* p.
3.) Shortest geodesics through a hyperbolic vertex with total vertex angle $\theta > 2\pi$ *have a geodesic curvature* $\kappa_g \in \left[-\pi(1 - \frac{2\pi}{\theta}), \pi(1 - \frac{2\pi}{\theta})\right]$.

Using the notion of discrete geodesic curvature we obtain a new characterization of straightest geodesics since they have $\beta = \frac{\theta}{2}$ as bisector of the the total vertex angle θ.

Lemma 40 *Let* M_h *be a polyhedral surface and* $\gamma \subset M_h$ *a curve. Then* γ *is a straightest geodesic if and only if* γ *has vanishing discrete geodesic curvature.*

Straightest geodesics are natural generalizations of straight lines in Euclidean space. For example, geodesic triangles on surfaces can be defined as simply connected regions bounded by three straightest segments, and geodesic polygons as piecewise straightest curves.

The Gauß-Bonnet theorem relates the topology and geometry of a surface. It is a remarkable consequence of the definition of discrete geodesic curvature that this fundamental theorem still holds. In fact, one can even reverse the arguments and derive our formula for geodesic curvature from the requirement that the equation of Gauß-Bonnet should hold.

There have been different formulations of the Gauß-Bonnet theorem on polyhedral surfaces, each expressing the Euler characteristic $\chi(\Omega)$ of a domain Ω using different curvature terms. Among the first versions for compact polyhedral surfaces was Allendörfer and Weil [3]. Later Banchoff [4][5] related the discrete Gauß curvature with a polyhedral Morse theory on embedded polyhedra. Reshetnyak [103] covers polyhedral domain with boundary. He uses the Gauß curvature of interior vertices, and defines the curvature of the boundary curve by

$\kappa = \pi - \beta$, where β is the inner curve angle of the boundary. Implicitly he assumes Gauß curvature $K = 0$ at boundary vertices. In our approach we allow a non-vanishing Gauß curvature also at boundary vertices which allows an application of the theorem to a more general class of domains. In some sense, we split the boundary curvature in two components, a geodesic curvature of the boundary curve and a partial Gauß curvature, where the vertices $p \in \partial\Omega$ contribute to the total Gauß curvature of Ω. The following natural definition determines the contribution of boundary vertices to the total Gauß curvature of Ω. The contribution is proportional to the curve angle β:

Definition 41 *Let $\Omega \subset M_h$ be a domain on a polyhedral surface with boundary $\Gamma = \partial\Omega$. If $\theta(p)$ is the total vertex angle and $\beta(p)$ the inner curve angle at a vertex $p \in \Gamma$, then the* partial Gauß curvature $K_{|\Omega}$ *of Ω at p is proportional to β:*

$$K_{|\Omega}(p) = \frac{\beta}{\theta} K(p). \tag{2.6}$$

If $\beta = 0$ then the vertex has no partial Gauß curvature, and $\beta = \theta$ leads to a full contribution of the total Gauß curvature $K = 2\pi - \theta$ to Ω. In the following we simplify the notation by omitting the subindex $_{|\Omega}$.

Theorem 42 (Discrete Gauß-Bonnet) *Let M_h be a polyhedral surface and $\Omega \subset M_h$ a domain with boundary curve Γ and Euler characteristic $\chi(\Omega)$. Then the equation*

$$\sum_{p \in \bar{\Omega}} K(p) + \kappa_g(\Gamma) = 2\pi\chi(\Omega) \tag{2.7}$$

holds where the total Gauß curvature of Ω includes the partial Gauß curvature at boundary points. If Γ is piecewise straightest then the total geodesic curvature is the sum of the geodesic curvature at the vertices of Γ.

Proof. For the proof we use the version

$$\sum_{p \in \mathring{\Omega}} K(p) + \sum_{p \in \Gamma} (\pi - \beta(p)) = 2\pi\chi(\Omega)$$

proved by Reshetnyak [103] where only interior vertices of Ω contribute to the total Gauß curvature. Let $p \in \Gamma$ be a boundary vertex, then we have the splitting

$$K_{|\Omega}(p) - \kappa_g(p) = \pi - \beta(p)$$

which proves the assumption. Basically, Reshetnyak's version assumes Gauß curvature zero at boundary vertices while we make a finer distinction allowing non-zero Gauß curvature, i.e. allow to consider domains taken from a curved polyhedral surface. □

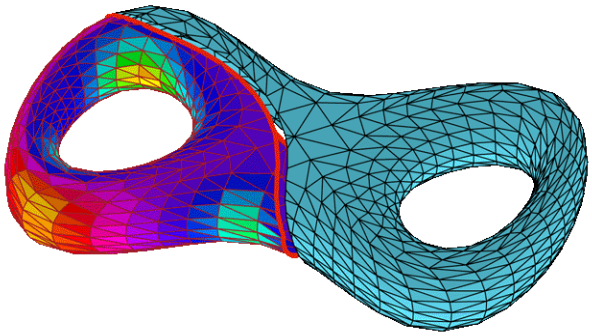

FIGURE 2.7. Polyhedral version of the Gauss-Bonnet theorem employing the notion of discrete geodesic curvature of the boundary curve.

The following sections provide some applications of the knowledge of discrete geodesic curvature.

2.4 Parallel Translation of Vectors

Numerical methods for the integration of ordinary differential equations rely on the possibility of parallel translation of vectors in the Euclidean plane. For example, higher order Runge-Kutta methods do several trial shots in a single integration step to compute the final shooting direction which is then translated to the current initial point. When transferring such integration methods to surfaces, it is necessary to compare vectors with different base points on the curved surface.

We use the notion of polyhedral tangent vectors formulated in Definition 35 and define an intrinsic version of parallel translation of vectors which uses no ambient space as reference. We start with two definitions of angles:

Definition 43 *Let M_h be a polyhedral surface and $p \in M_h$ a point with total vertex angle θ. The* Euclidean angle $\measuredangle(v, w)$ *between tangent vectors $v, w \in T_pM_h$ is the angle between corresponding vectors*

in the unfolded neighbourhood of p measured in $\mathbb{R}^2$, i.e. $\measuredangle(v,w) \in [-\frac{\theta}{2}, \frac{\theta}{2}]$. The normalized angle $\alpha(v,w)$ *is obtained by scaling:*

$$\alpha(v,w) := \frac{2\pi}{\theta}\measuredangle(v,w). \tag{2.8}$$

The Euclidean and normalized angles are identical except at vertices of the surface. In practical applications one measures the Euclidean angle, and then uses the normalized angle to avoid case distinctions at vertices of the surface. Usage of the normalized angle considerably simplifies statements, for example, on the sum of angles in a geodesic triangle:

Lemma 44 *Let Δ be a geodesic triangle on a polyhedral surface M_h whose edges are straightest segments. If α_1, α_2, and α_3 are the normalized angles of Δ then we have*

$$\alpha_1 + \alpha_2 + \alpha_3 - \pi = \int_\Delta K \tag{2.9}$$

where the Gauß curvature K on Δ includes the partial Gauß curvature along the edges of Δ.

Proof. Denote the Euclidean angles of Δ with β_i and the vertex angles with θ_i. Then the geodesic curvature of the boundary of Δ at one of its vertices of M_h is given by

$$\kappa_g = \frac{2\pi}{\theta}\left(\frac{\theta}{2} - \beta\right) = \pi - \alpha \tag{2.10}$$

and the assumption follows directly from the discrete Gauß-Bonnet equation (2.7). □

On polyhedral surfaces we can use the concept of straightest geodesics and normalized angles to define the parallel translation of vectors along geodesics and arbitrary other curves similar to the smooth case. For the definition, we use a formula which is well-known for curves on smooth surfaces.

Definition 45 *Let $\gamma : I \to M_h$ be a polygonal curve on a polyhedral surface M_h with $\gamma(0) = p$ and geodesic curvature κ_g. Let $v_0 \in T_pM_h$ be a tangent vector with normalized angle $\alpha(0) := \frac{2\pi}{\theta(p)}\measuredangle(v_0, \gamma'(0))$. Then v_0 uniquely extends to a* parallel vector field *v with $v(s) \in T_{\gamma(s)}M_h$ along γ with $v(0) = v_0$. $v(s)$ is defined by the normalized angle $\alpha(s)$ it encloses with $\gamma'(s)$:*

$$\alpha(s) = \alpha(0) + \int_0^s \kappa_g(t)dt. \tag{2.11}$$

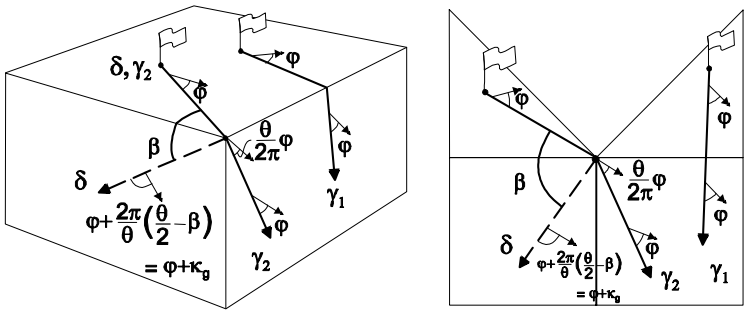

FIGURE 2.8. Parallel translation of vectors along straightest geodesics γ_1,γ_2 and an arbitrary curve δ.

Lemma 46 *Let $\gamma : I \to M_h$ be a parametrized straightest geodesic on a polyhedral surface M_h. A tangential vector field $v : I \to TM_h$ with $v(s) \in T_{\gamma(s)}M_h$ is a* parallel vector field *along γ if the normalized angle $\alpha(v(s), \gamma'(s))$ is constant.*

Another consequence follows directly from the Gauß-Bonnet formula 42:

Lemma 47 *Let $\gamma : [0, \ell] \to M_h$ be a polygonal curve on a polyhedral surface M_h enclosing a domain $\Omega \subset M_h$. Then the parallel translation of any vector around γ leads to a defect between the normalized angles*

$$\alpha(s) - \alpha(0) = 2\pi\chi(\Omega) - \sum_{p \in \bar{\Omega}} K(p)$$

where the total curvature includes the partial Gauß curvature of vertices on γ.

2.4.1 Geodesic Runge Kutta

The tracing of particles on a surface by integrating a given vector field with Euler or Runge Kutta methods requires an additional effort to keep the trace on the surface. For example, one may use local coordinate charts of a surface to transform the integration to a planar Euclidean domain. Here the metrical distortion between surface and Euclidean domain must be incorporated, and a preprocessing step to generate the charts and transitions between neighbouring charts is required.

If the vector field is given on a curved surface in an ambient space, say $\mathbb{R}^3$, then a usual tangent vector "points into the ambient space",

leading the numerical particle trace off the surface unless additional projection methods are employed.

The concepts of straightest geodesics and polyhedral tangent vectors offer an intrinsic access to solve these problems. In Euclidean methods, the vector $v|_{\gamma(s)}$ is interpreted as a tangent vector to the particle trace $\gamma(s)$, and the straight line through $\gamma(s)$ with direction $v|_{\gamma(s)}$ is the first order approximation of γ. The idea on surfaces is to use polyhedral tangent vectors defined in 35 and to replace the straight line with a straightest geodesic through $\gamma(s)$ and initial direction $v|_{\gamma(s)}$.

Algorithm 48 (Geodesic Euler Method) *Let M_h be a polyhedral surface with a polyhedral tangential vector field v on M_h. Let $y_0 \in M_h$ be an initial point, and $h > 0$ a possibly varying stepsize. For each point $p \in M_h$ let $\delta(t, p, v(p))$ denote the unique straightest geodesic through p with initial direction $v(p)$ and evaluated at the parameter value t. A single iteration step of the* geodesic Euler method *is given by*

$$y_{i+1} := \delta(h, y_i, v(y_i)). \tag{2.12}$$

This produces a sequence of points $\{y_0, y_1, ...\}$ on M_h which are connected by straightest geodesic segments of length h. For each $i \in \{0, 1, ...\}$ we define

$$\gamma(ih + t) := \delta(t, y_i, v(y_i)),\ t \in [0, h] \tag{2.13}$$

and obtain a piecewise straightest, continuous curve $\gamma : [0, \ell) \to M_h$ of some length ℓ such that each segment $\gamma_{|[ih,\ (i+1)h]}$ is a straightest geodesic.

The definition of the geodesic Euler method is intrinsic and no projection of the tangent vectors or tangent directions onto the surface are required during integration. If the original vector field is not a polyhedral tangential field then an initial generation of a polyhedral tangential vector field is required in a preprocessing step, however, this step is part of the formulation of the numerical problem and not of the integration method.

Using the concept of parallel translation it is straight forward to define higher order integration methods in a similar intrinsic way. For simplicity, we restrict to a 4-th order geodesic Runge Kutta method:

Algorithm 49 (Geodesic Runge Kutta Method) *Let M_h be a polyhedral surface with a polyhedral tangential vector field v on M_h. Let $y_0 \in M_h$ be an initial point, and let $h > 0$ a possibly varying stepsize. For each point $p \in M_h$ let $\delta(t, p, v(p))$ denote the unique*

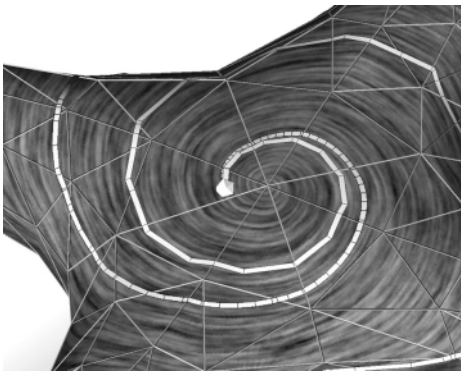

FIGURE 2.9. The two piecewise straightest geodesics are solutions computed with the geodesic Euler method (outer curve, stepsize h) and 4th order Runge Kutta method (inner curve, stepsize $4h$). Note, that the geodesic segments extend across triangle edges and vertices. Also, a comparison with the underlying flow shows the expected better approximation quality of the geodesic Runge Kutta method.

straightest geodesic through p with initial direction $v(p)$ and evaluated at the parameter value t. A single iteration step of the geodesic Runge Kutta method *is given by*

$$y_{i+1} := \delta(h, y_i, v_i) \tag{2.14}$$

where the direction v_i is a polyhedral tangent vector at y_i obtained as follows: we denote the parallel translation of vectors along a geodesic δ to $\delta(0)$ by $\pi_{|\delta}$ and iteratively define

$$\begin{aligned} v_i^1 &: = v(y_i) \\ v_i^2 &: = \pi_{|\delta_1} \circ v(\delta_1(\frac{h}{2}, y_i, v_i^1)) \\ v_i^3 &: = \pi_{|\delta_2} \circ v(\delta_2(\frac{h}{2}, y_i, v_i^2)) \\ v_i^4 &: = \pi_{|\delta_3} \circ v(\delta_3(h, y_i, v_i^3)) \end{aligned} \tag{2.15}$$

and

$$v_i := \frac{1}{6}(v_i^1 + 2v_i^2 + 2v_i^3 + v_i^4) \tag{2.16}$$

where the curves δ_i are straightest geodesics through y_i with initial direction v_i^j for $j \in \{1, 2, 3\}$.

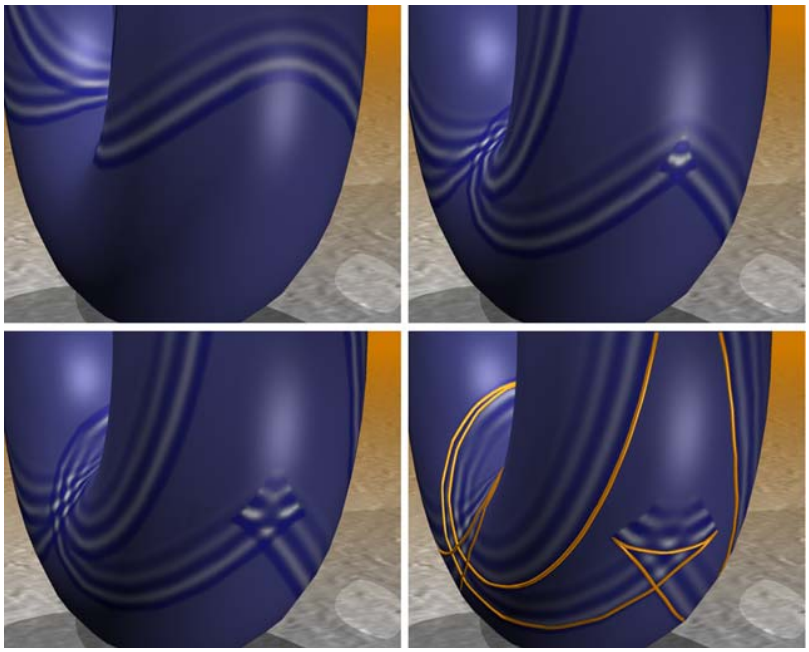

FIGURE 2.10. A point wave on a polyhedrally approximated torus initiated at top branches at the conjugate point in the form of a swallow's tail. Visualization of the interference uses branched texture maps.

2.5 Geodesic Flow

The study of geodesics and their behaviour under variations helps to understand the geometry of curved surfaces and general manifolds. In this section we will compute and visualize aspects of the geodesic flow on polyhedral surfaces, and discuss notions like injectivity radius and conjugate points. By postponing a formal definition for later we can introduce some of these terms by considering the evolution of a wave front. For example, if the front of a point wave on a surface evolves with unit speed, then the time of the first hit upon itself is equal to the *injectivity radius*, unless a previous branching of the front occurs – the branch point is called a *conjugate point*. Both items depend on the position of the center point of the wave.

In the following we solve two problems: First, the computation of the evolution of a point wave on a polyhedral surface. At each time the front of the wave is a topological circle on the surface, which may overlap and have singular points resulting from previous branchings

of the front. In a numerical step, each point of the front is moved a constant distance in orthogonal direction to the circle, i.e. a constant distance along the straightest geodesic normal to the circle at this point. In Section 2.5.2 we employ the concept of straightest geodesics on polyhedral surfaces to give a thorough definition of the evolution on polyhedral surface and describe its numerics.

The second problem is a visualization task to handle the branching and interference of a point wave evolving on a polyhedral surface. For the visualization of the evolving wave we use isometric texture maps to avoid metric distortions between texture space and the surface. Further, we extend these maps to include the multiple local coverings of parts of the surface by different layers of the wave which occur behind the injectivity radius and branch points. Branched texture maps are defined to combine the notion of global texture maps, that cover the whole surface, and local texture maps, which cover a subregion. Isometric texture maps on surfaces are intensively used, for example, in the line integral convolution technique in flow visualization [10].

FIGURE 2.11. A point wave branches at the vertices of a cube which are equivalents of conjugate points on smooth surfaces. The section behind a vertex is covered by three interfering texture layers while other parts are covered once. The zoom shows the triangles and texels on the surface.

The numerics and visualization ideas in this section easily extend to other applications besides the geodesic flow. For example, the evolution and interference of other wave fronts over flat or curved surfaces. More abstract, even the visualization of a homotopy of a curve, i.e. a one-parameter deformation, may be visualized using the interpretation as an evolving wave front.

Waves have been studied in computer graphics from different aspects. In the animation [77] Max used bump mapping to perturb the surface of water for simulating waves viewed from a distance. Fournier and Reeves [46] explicitly model waves using parametric surfaces which

allow simulation of detail structure such as waves curling over. The ideas presented in the next sections are the basis of the video Geodesics and Waves [101].

2.5.1 Circles on Surfaces and the Geodesic Flow

A *point wave* in the Euclidean plane starts at an origin p and evolves in concentric circles around p. In a particle model all particles of the wave front move with constant unit speed along radial rays away from the origin p if we neglect surface tension. At each time t the outer wave front forms a distance circle $\sigma(t)$ with center p and radius t.

For the construction of concentric circles on curved surfaces we use a similar picture. Particles of a wave front move along geodesic rays emanating from the origin p, therefore the circle at radius t consists of all points at distance t along a geodesic ray from p. It is one purpose of this section to compute, study, and visualize such distance circles. We start with a review of some facts on geodesic distance circles and their extension to polyhedral surfaces.

Evolution of Distance Circles and Point Waves

Geodesics on smooth surfaces and straightest geodesics on polyhedral surfaces uniquely solve the initial value problem for geodesics. That is, each geodesic is uniquely determined by an initial point and an initial direction. This property allows particles with an initial impulse to move on surfaces along geodesics assuming there is no additional tangential acceleration.

The set of geodesics unveils information about the underlying geometry of the surface. We define two geometric terms, cut locus and conjugate points, since both are used to characterize the behavior of distance circles, i.e. the branching and overlapping of point waves.

The set of geodesics emanating from a given point p is conveniently described by the exponential map.

Definition 50 *The* exponential map *at a point p on a smooth surface M associates to each tangent vector $v \in T_pM$ a point on a geodesic γ through $\gamma(0) = p$ with initial direction $\gamma'(0) = v$ as follows:*

$$\begin{array}{c} \exp_p : T_pM \to M \\ \exp_p(v) = \gamma(1) \end{array} . \tag{2.17}$$

Here $\gamma(1)$ is a point on γ at distance $|v|$ from p since γ runs at speed $|v|$.

The exponential map maps small circles around 0 in the tangent space T_pM to *distance circles* around p on M, that means, to circular curves on M where all points have the same geodesic distance to p. For a given vector $v \in T_pM$ the radial lines $\{rv \mid r \in \mathbb{R}\} \subset T_pM$, are mapped isometrically to a geodesic ray $\gamma(r) := \exp_p rv$.

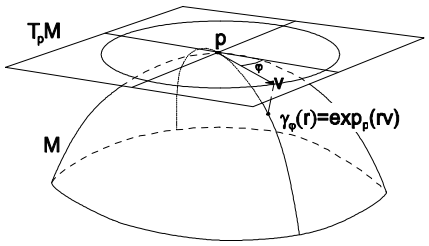

FIGURE 2.12. Exponential map of geodesics emanating at a point.

In this formalism it is straight forward to describe distance circles around a point p on a surface M. Let $V(0) \subset T_pM$ be a small neighbourhood of $0 \in T_pM$,then its image under the exponential map is a neighbourhood $U(p) := \exp_p V(0)$ of p. Using polar coordinates (r, φ) in the tangent space centered at 0, each vector $v := r \cdot (\cos\varphi, \sin\varphi) \in V(0)$ is uniquely determined by its coordinates (r, φ). Its image under the exponential map given by $\gamma_\varphi(r) := \exp_p r(\cos\varphi, \sin\varphi)$ induces a local polar coordinate system on $U(p)$on the surface.

Using the above definitions, the particle model of a wave front in the plane extends immediately to curved surfaces M. The particles of a wave front start at $p \in M$ and move with constant speed along geodesic rays emanating at p. If we normalize the speed to 1 then the wave front at a time t is a distance circle δ_t with radius t given by

$$\begin{aligned} \delta_t &: [0, 2\pi] \to M \\ \delta_t(\varphi) &:= \gamma_\varphi(t) \end{aligned} \tag{2.18}$$

In contrast to the Euclidean case, the wave front on a curved surface will usually self-intersect after some time t_0. There are two possible reasons for the intersection. First of all, if the surface is not simply connected and has a handle like a torus, then for each point p there exist two emanating geodesic rays, γ_{φ_1} and γ_{φ_2}, with $\varphi_1 \neq \varphi_2$ and a time t_0 such that $\gamma_{\varphi_1}(t_0) = \gamma_{\varphi_2}(t_0) =: q$ (both curves go around a different side of a handle). At such a point q the wave front hits upon itself and interferes. The time t_0 of the first hit of any two disjoint geodesic emanating from p is called the *injectivity radius* at p.

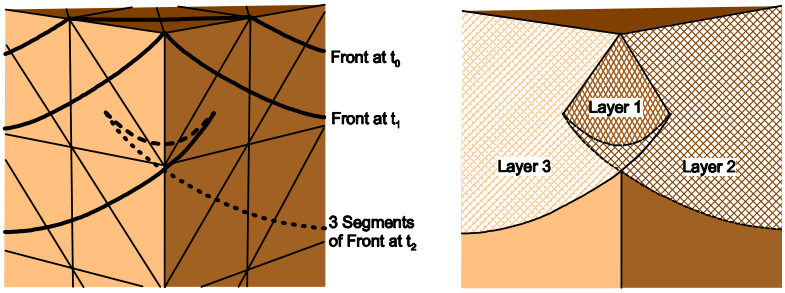

FIGURE 2.13. Front of a point wave branches at conjugates points in the form of a swallow's tail. Behind the vertex of a cube the wave splits in two layers, and a third new layer is generated at the conjugate point. All three layers start to interfere.

A second type of intersection occurs at so-called *conjugate points* of p. At conjugate points $q = \gamma_{\varphi_0}(r_0)$ the differential $\nabla \exp_p$ does not have maximal rank, i.e. $\partial/\partial\varphi \exp_p(r_0, \varphi_0) = 0$. Here, the wave front branches and nearby geodesics intersect shortly behind the conjugate point. The branching occurs in the form of a swallow's tail, see Figures 2.13 and 2.10. For $t > t_0$ the polar coordinates fail to be a coordinate chart.

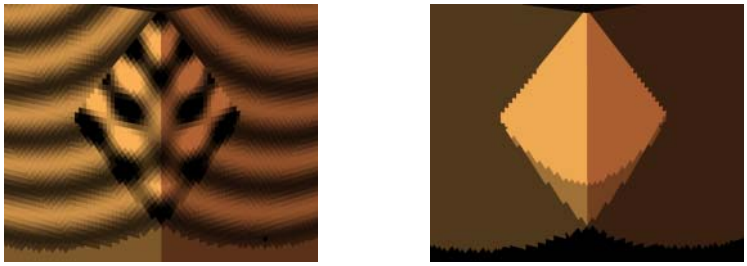

FIGURE 2.14. Interference of a point wave at the vertex of a cube and texture layers. The left picture shows the interference behavior of the wave at the vertex of a cube. The wave is stored as a branched texture map, where to each point on the surface a stack of texels is associated. In the right picture the surface texels are colored according to the height of the texture stack at each point.

2.5.2 Computing Discrete Distance Circles

In a practical algorithm for the computation of distance circles at a point p on a polyhedral surface we start with a topological polygonal circle $\sigma(0)$ such that all of its vertices lie at p. Each vertex $q \in \sigma(0)$ has a unit tangent vector associated to it, and therefore the circle $\sigma(0)$ at time $t_0 = 0$ is completely described by a set of pairs $(q_{i,0}, v_{i,0}), i = 1, .., n$. For the numerics, it is essential to distribute the tangent vectors equally spaced in angular direction since they determine the geodesic along which the particles $q_{i,0}$ will move.

In the numerical iteration step from time t_j to t_{j+1}, the circle $\sigma(t_{j+1})$ is obtained by computing for $i = 1, .., n$, the set of vertices and tangent vectors

$$\begin{aligned} q_{i,j+1} &= \gamma_{(q_{i,j},v_{i,j})}(1) \\ v_{i,j+1} &= \dot{\gamma}_{(q_{i,j},v_{i,j})}(1) \end{aligned} \tag{2.19}$$

where $\gamma_{(q_{i,j},v_{i,j})}$ is the straightest geodesic starting at $\gamma_{(q_{i,j},v_{i,j})}(0) = q_{i,j}$ with initial direction $\dot{\gamma}_{(q_{i,j},v_{i,j})}(0) = v_{i,j}$, compare Figure 2.15. It should be noted that $\gamma_{(q_{i,j},v_{i,j})}(0) = \gamma_{(p,v_{i,0})}(t_j)$, i.e. for fixed j all points $q_{i,j}$ lie on a distance circle with distance t_j to p.

Equation 2.19 is essentially the computation of a segment of a straightest geodesic for all vertices on the outer circle $\sigma(t_j)$. On the other hand, the distance between adjacent vertices on the same circle may grow exponentially with the radius (depending on the Gauss curvature of the covered region). Therefore, each timestep includes a refinement and coarsening step to maintain nearly constant distance between adjacent points on each circle. For the insertion of new vertices, say between $q_{i,j}$ and $q_{i+1,j}$, we connect both points by a geodesic segment and insert a new vertex on this geodesic. In practice, for a fixed t_j the circle $\sigma(t_j)$ is piecewise geodesic - a natural generalization of piecewise linear.

When a curve reaches a conjugate point it starts to form a swallow's tail with sharp edges. This does not irritate the algorithm since each vertex on the curve still has a vector attached which uniquely determines its further movement.

We remark that on a polyhedral surface each positively curved vertex is a conjugate point for all points in a small neighborhood. The resulting branching is similar to the branching at vertices of a cube which is studied in detail in Figures 2.13 and 2.11. When approximating a smooth geometry with a polyhedral surface, we suppress this type of local branching related to the discretization in favor of a global branching related to the shape of the smooth surface. We use

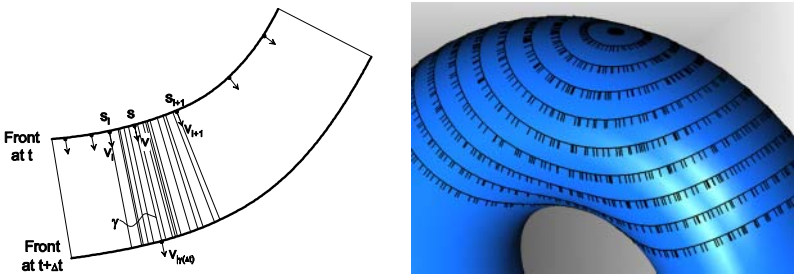

FIGURE 2.15. Set of distance circles with direction of movement (right). Left, the front at time $t + \Delta t$ is generated from the front at time t by computing geodesics with length Δt.

a manually selected threshold factor depending on the smoothness of the mesh to distinguish between local and global branching.

A direct visualization of the set of circles gives reasonable results only for a small number of circles, see Figure 2.15. In the following section we interpret the set of concentric circles as an evolving wave and use a resolution independent visualization based on texture map techniques.

2.5.3 Dynamic Computation of a Wave Texture

We divide the simulation of the wave in two major computational steps: first, the computation of the evolution of the wave front, which consists of geometric problems described in Section 2.5.2 and leads to a static set of concentric circles, i.e. a set of wave fronts. Second, the simulation of the actual flow by animating the set of wave fronts. The animation is not done on the original set of fronts but on the level of textures. From the set of fronts, i.e. a set of geometric curves on the surface, we produce a single branched texture map which associates to each base texel of the surface a stack of abstract texels. The final animation of the wave is obtained from the single branched texture map by imposing a periodic function, and without any new computation of the wave evolution.

The separation of the numerical step and the use of branched texture maps make the animation of a moving wave a very cheap computation once the branched texture maps have been created.

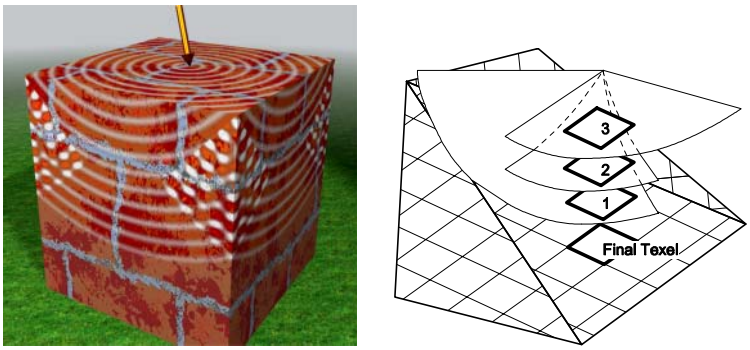

FIGURE 2.16. Point waves on surfaces develop singularities at so-called conjugate points where the wave branches. Right figure shows a stack of abstract texels of the branched texture map, each corresponding to one layer of the wave.

Generating the Branched Texture Map

The set of wave fronts $\sigma(t_j),\ j = 1, 2, ..$ computed in Section 2.5.2 are a discretization of the exponential map from T_pM_h to M_h. We store this information in a branched texture map data structure. First, we construct an isometric texture map covering M_h once with so-called base texels. Then we associate to each base texel of M_h an empty stack of abstract texels, as shown in Figure 2.16. The height of each stack is not known in advance and will vary from base texel to base texel depending on the number of layers covering the texel. Now we analyze the set of curves $\sigma(t_j)$, and whenever the front has flowed over a base texel we add a new abstract texel (α, t) to the stack of this base texel where α is the angle α and t is the time of the current wave front.

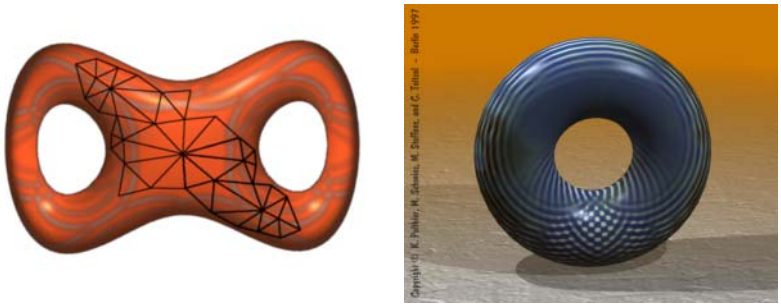

FIGURE 2.17. Evolution of distance circles under the geodesic flow on the (highly discretized) polyhedral model of a pretzel and a torus.

The task of generating the stack is simple if the maximal distance between two successive curves is smaller than half the diameter of the smallest texel on the surface, which can be easily controlled for isometric texture maps. Here we sample each wavefront which carries the necessary information about angle α and time t. To avoid aliasing effects it is essential to hit texels more frequently, say $4-8$ times, and finally store average values $(\bar{\alpha}, \bar{t})$.

Each sheet of the wave hitting a given base texel corresponds to exactly one abstract texel above the base texel. A serious problem is the detection of the sheet corresponding to the current hit. For polyhedral geometries, we avoid this problem by letting the front detect branch points from the vertex curvature and split. This allows us to assign to each front segment a unique level number which identifies each sheet.

But, when approximating smooth surfaces, we need to distinguish between the branch points of the smooth geometry and those induced by polyhedral vertices. In this case, we let each base texel reconstruct the necessary information for each circle, respectively geodesic, from the time and angle of the current hit. Let m_T be the midpoint of a base texel T with edge size δ and let each abstract texel have stored average values $(\bar{\alpha}, \bar{t})$. Assume a circle $\sigma(\alpha, t)$ hits the base texel at a point q corresponding to an angle α, then q belongs to the same layer of the abstract texel if

$$dist_M(m_T, q) \approx \left(\frac{d}{d\alpha}\sigma(\alpha, t)^2 \, (\alpha - \bar{\alpha})^2 + (t - \bar{t})^2 \right)^{\frac{1}{2}} \leq \frac{\delta}{\sqrt{2}}$$

for a threshold δ depending on the discretization of the flow.

In practice, we have a lower resolution in time direction and compute fewer wave fronts with distance of more than a few triangle diameters, and interpolate between successive fronts as indicated in the left image in Figure 2.15.

3

Conjugation of Discrete Harmonic Maps

Discrete harmonic maps appear as a basic model problem in finite element theory and differential geometry for the discretization of smooth concepts. Beyond that, discrete harmonic maps have a wide range of non-trivial applications in computer graphics, for example to smoothen noisy meshes, or in differential geometry to compute constant mean curvature surfaces.

Several discrete operators on simplicial surfaces are related with discrete harmonic maps. For example, the area gradient, the mean curvature, or the divergence operator on vector fields. The main topic of this section is the construction of pairs of conjugate discrete Laplace-Beltrami harmonic maps on polyhedral surfaces. We start to derive the definitions and properties of discrete harmonic maps in a geometric setting which will then allow us to develop other discrete geometric operators and to solve problems related to minimal and constant mean curvature surfaces in Chapters 4, 5 and 7.

Harmonic maps on surfaces also have practical importance, for example, we derive in Chapters 4 and 5 efficient numerical algorithms for solving free boundary value problems for unstable minimal surfaces and constant mean curvature surfaces. In the algorithms [88] and [86], the conjugate of a minimal surface is obtained via the conjugation of a discrete harmonic map. Conjugate harmonic maps are originally defined on the dual graph of the edge graph of the original

surface but one should consider them as non-conforming functions. The results of the present chapter provide a thorough understanding of the geometric constructions used in Pinkall and Polthier [88] and in Oberknapp and Polthier [86] by relating the discrete conjugation of surfaces to non-conforming finite element spaces.

Convergence of conforming harmonic maps has been shown by Tsuchiya [117]. As a more general result for surfaces, Dziuk and Hutchinson [37] obtained optimal convergence results in the H^1 norm for the finite element procedure of the Dirichlet problem of surfaces with prescribed mean curvature. Compare Müller et al. [81] for harmonic maps on planar lattices using the five-point Laplacian.

In a subsequent section we will apply the duality between discrete harmonic maps and their conjugates to define discrete conformal maps. We will extend a conformal energy proposed by Hutchinson [65] to the discrete spaces $S_h \times S_h^*$ and show that the discrete holomorphic maps have zero conformal energy, a property generically not available for conforming piecewise linear maps.

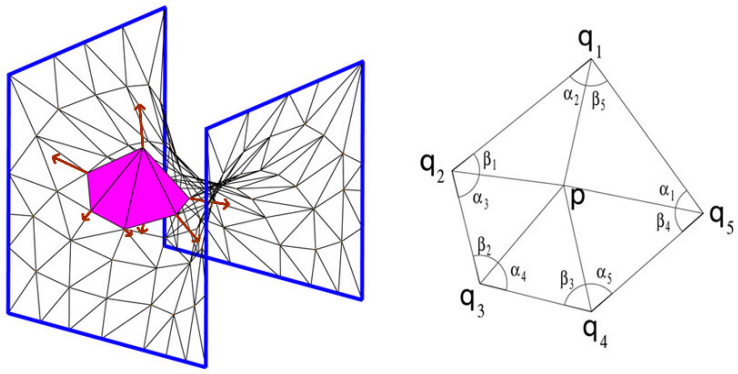

FIGURE 3.1. Discrete mean curvature vector on a polyhedral surface given as Laplace-Beltrami operator of the identity map from the surface to itself.

We start with a review of the Dirichlet problem of harmonic maps in Section 3.1 followed by the discretization using conforming Lagrange elements in Section 3.2. In Section 3.3 we discretize the same Dirichlet problem using the non-conforming Crouzeix-Raviart elements, and derive a pointwise expression of the discrete minimality condition. Section 3.4 contains the main results of this chapter, namely, identifying solutions in both finite element spaces as pairs of discrete conjugate harmonic maps. Applications of the results are given in Chapters

4 and 5 to the conjugation of discrete minimal and constant mean curvature surfaces.

3.1 Review of Smooth Harmonic Maps

On a Euclidean domain, the Laplace operator is given by the second partial derivatives

$$\Delta = \frac{d}{dx_1^2} + ... + \frac{d}{dx_n^2}.$$

Harmonic maps $u : \Omega \to \mathbb{R}$ on an open set Ω in $\mathbb{R}^n$ are solutions of the Laplace equation

$$\Delta u = 0 \text{ in } \Omega \tag{3.1}$$

which often appears with prescribed boundary conditions. Dirichlet conditions prescribe fixed boundary values in the form of a function g

$$u_{|\partial\Omega} = g \text{ on } \partial\Omega$$

and Neumann conditions prescribe the derivative of u in direction of the normal ν of the boundary

$$\partial_\nu u_{|\partial\Omega} = \mu \text{ on } \partial\Omega.$$

Dirichlet and Neumann boundary conditions may appear simultaneously on disjoint segments of the boundary.

The Laplace operator of vector-valued maps, and thereby the harmonicity of vector-valued maps, is defined component-wise on each coordinate function. For functions $u : M \to \mathbb{R}$ on a manifold M with a Riemannian metric g the Laplace-Beltrami operator Δ_g is a generalization of the Laplace operator. Assume normal coordinates on M and let $\{e_1, ..., e_n\}$ be the induced orthonormal frame in the tangent space of M, then

$$\Delta_g = \nabla_{e_1}\nabla_{e_1} + ... + \nabla_{e_n}\nabla_{e_n}.$$

Harmonic maps also appear as minimizers of the *Dirichlet energy*

$$E_D(u) = \frac{1}{2}\int_M |\nabla u|^2 \, dx \tag{3.2}$$

with Dirichlet conditions (or Neumann) at the boundary, since the Laplace equation 3.1 is the Euler-Lagrange equation of the Dirichlet energy. To see this, let $u(t) := u_0 + t\phi : M \to \mathbb{R}$ be any C^1-variation of

a function u_0 whose variation function has compact support $\phi_{|\partial M} = 0$. Then by differentiation and partial integration we obtain

$$\begin{aligned} \frac{d}{dt}_{|t=0} E_D(u(t)) &= \int_M < \nabla u, \nabla \phi > \\ &= -\int_M \Delta u \cdot \phi + \int_{\partial M} \partial_v u \cdot \phi \end{aligned}$$

where v is the exterior normal along ∂M. Since ϕ has compact support, the last integrand vanishes identically. Since the above equation holds for any C^1-variation we derive

$$\nabla E_D(u) = 0 \Longleftrightarrow \Delta u = 0$$

from the fundamental lemma of the calculus of variations. The minimizer $u_{\min}$ is unique since

$$\begin{aligned} E_D(u_{\min} + \phi) &= E_D(u_{\min}) + E_D(\phi, \phi) \\ &> E_D(u_{\min}) \quad \forall\, \phi_{|\partial M} = 0. \end{aligned}$$

3.2 Discrete Dirichlet Energy

There are different equivalent ways to introduce discrete harmonic maps. Here we use the characterization of harmonic maps as minimizers of the Dirichlet energy since this approach also provides an efficient numerical algorithm to solve the boundary value problems for discrete harmonic maps.

Definition 51 *Let M_h be a simplicial surface in $\mathbb{R}^m$ and S_h the set of polyhedral maps on M_h. Then the* Dirichlet energy *of a function $u_h \in S_h$ with $u_h : M_h \to \mathbb{R}^d$ is given by*

$$E_D(u_h) := \frac{1}{2} \sum_{T \in \mathfrak{T}_h} \int_T |\nabla u_h|^2 \, dx. \tag{3.3}$$

That is, the Dirichlet energy of u_h is the sum of the Dirichlet energies of the smooth atomic maps $u_{h|T}$ on each triangle T.

Now we consider critical points of the Dirichlet energy. For simplicity, we restrict to interior variations which keep the boundary values fixed.

Definition 52 *A* variation $\phi(t) \in S_h$, $t \in [0, \varepsilon)$, *is a family of functions differentiable in t such that each map $u_h \in S_h$ gives rise of a family of maps $u_h(t) \in S_h$ with*

$$u_h(t) = u_h + \phi(t)$$

Basically, a variation of a function $u_h \in S_h$ is a modification of its values at each vertex p_i of the triangulation M_h given by $u_h(t)(p_i) = u_h(p_i) + \phi(t)(p_i)$. For simplicity, we restrict to Dirichlet boundary conditions, that is, the variations $\phi(t)$ are zero along the boundary of M_h.

Definition 53 *A critical point u_h in S_h of the Dirichlet energy (3.3) in S_h with respect to Dirichlet boundary conditions is called a* discrete harmonic map.

In the following we derive an explicit representation of the Dirichlet energy of polyhedral maps and a system of equations for the discrete minimizers which characterize discrete harmonic maps.

Let $T = \{p_1, p_2, p_3\}$ be a triangle of a simplicial surface and oriented edges $\{c_1, c_2, c_3\}$ with $c_i = p_{i-1} - p_{i+1}$, and $\varphi_i : T \to \mathbb{R}$ be the Lagrange basis function at vertex p_i with $\varphi_i(p_j) = \delta_{ij}$. Then its gradient is

$$\nabla\varphi_{i|T} = \frac{1}{2\,\mathrm{area}\,T} J c_i, \tag{3.4}$$

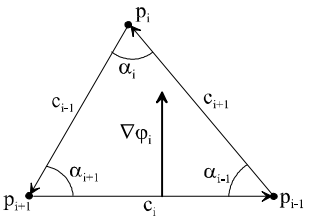

Gradient of basis function.

where J denotes rotation by $\frac{\pi}{2}$ oriented such that Jc_i points into the triangle. Note, that Equation 3.4 implies $\nabla\varphi_i = -\nabla\varphi_{i-1} - \nabla\varphi_{i+1}$. The basis functions have mutual scalar products given by

$$\begin{aligned} \langle \nabla\varphi_{i-1}, \nabla\varphi_{i+1} \rangle &= -\frac{\cot\alpha_i}{2\,\mathrm{area}\,T} \\ \langle J\nabla\varphi_i, \nabla\varphi_{i+1} \rangle &= \frac{1}{2\,\mathrm{area}\,T} \\ |\nabla\varphi_i|^2 &= \frac{\cot\alpha_{i-1} + \cot\alpha_{i+1}}{2\,\mathrm{area}\,T}. \end{aligned} \tag{3.5}$$

Since each function $u_h \in S_h$ has a representation

$$u_h(p) = \sum_{j=1}^{n} u_j \varphi_j(p) \quad p \in M_h,$$

where $u_j = u_h(p_j)$ denotes the function value of u_h at the vertex p_j of M_h, on a single triangle T the gradient of $u_{h|T} : T \longrightarrow \mathbb{R}^d$ is given by

$$\nabla u_{h|T} = \frac{1}{2\,\mathrm{area}\,T} \sum_{j=1}^{3} u_j J c_j. \tag{3.6}$$

Theorem 54 *Let M_h be a simplicial surface and S_h the set of continuous and piecewise linear functions on M_h. Then the discrete Dirichlet energy of any function $u_h \in S_h$ is given by*

$$E_D(u_h) = \frac{1}{4} \sum_{edges\ (x_i,x_j)} (\cot \alpha_{ij} + \cot \beta_{ij}) \left| u_h(p_i) - u_h(p_j) \right|^2 . \quad (3.7)$$

Further, the minimizer of the Dirichlet functional (3.3) is unique and solves

$$\frac{d}{du_i} E_D(u_h) = \frac{1}{2} \sum_{x_j \in n(x_i)} (\cot \alpha_{ij} + \cot \beta_{ij})(u_h(p_i) - u_h(p_j)) = 0 \quad (3.8)$$

at each interior vertex p_i of M_h. The first summation runs over all edges of the triangulation, and the second summation over all edges emanating from p_i. The angles α_{ij} and β_{ij} are vertex angles lying opposite to the edge (p_i, p_j) in the two triangles adjacent to (p_i, p_j).

Proof. Using the explicit representation (3.4) of the basis functions and the identity $\nabla\varphi_i = -\nabla\varphi_{i-1} - \nabla\varphi_{i+1}$, we obtain the Dirichlet energy of $u_{h|T}$:

$$\begin{aligned} E_D(u_{h|T}) &= \frac{1}{2} \int_T - \sum_{j=1}^{3} |u_{j+1} - u_{j-1}|^2 \left\langle \nabla\varphi_{j-1}, \nabla\varphi_{j+1} \right\rangle \\ &= \frac{1}{4} \sum_{j=1}^{3} \cot \alpha_j \left| u_{j+1} - u_{j-1} \right|^2 . \end{aligned}$$

Summation over all triangles of M_h and combining the two terms corresponding to the same edge leads to equation.

At each interior vertex p_i of M_h, the gradient of E_D with respect to variations of $u_i = u_h(p_i)$ in the image of u_h is obtained by partial differentiation and easily derived from

$$\frac{d}{du_i} E_D(u_h) = \int_\Omega \left\langle \nabla u_h, \nabla\varphi_i \right\rangle .$$

Since S_h is a finite dimensional space, the quadratic minimization problem for the Dirichlet energy has a unique solution u_h in S_h. □

The definition of the Dirichlet energy of vector-valued maps $F_h : M_h \to N_h \subset \mathbb{R}^d$ is in full coherence with the definition of Dirichlet energy of scalar-valued maps. Namely, if the map $F_h = (f_1, .., f_d)$ has component functions $f_i : M_h \to \mathbb{R}$ then we have

$$E_D(F_h) = \sum_{i=1}^{d} E_D(f_i)$$

since $|\nabla F_h|^2 = |\nabla f_1|^2 + .. + |\nabla f_d|^2$. Vector-valued harmonic maps are defined as critical values of the Dirichlet functional in the same way as in the scalar-valued case. Therefore, the balancing condition for scalar-valued harmonic maps directly gives a balancing formula for vector-valued discrete harmonic maps too.

The following definition includes more general boundary conditions. Neumann boundary conditions constrain the derivative of a function in direction of the exterior normal of the domain. Later we will make use of other boundary conditions which are useful for maps from a simplicial surface M_h to another surface N_h.

Definition 55 *A solution $u_h \in S_h$ of the Dirichlet problem (3.8) in S_h is called a* discrete harmonic map. *To include symmetry properties into this definition we allow in some cases also variation of boundary points:*

- *if a domain boundary segment and its corresponding image boundary segment are straight lines, then the interior boundary points may vary along the straight line in image space*
- *if both corresponding segments are planar symmetry curves restricted to planes we allow variation of interior boundary points in the image plane. This models also free boundary value problems*
- *in all other cases the image boundary points remain fixed.*

Remark 56 *At each vertex x_i Equation (3.8) can be geometrically interpreted as a balancing condition for the weighted edges emanating from the vertex x_i. The weight of each edge solely depends on the angles in the base surface M_h, i.e. the weights depend only on the conformal structure of M_h.*

Examples of Discrete Harmonic Maps

Simple examples of discrete harmonic maps are derived from the observation that on the integer grid $\mathbb{Z} \times \mathbb{Z}$ in $\mathbb{R}^2$ the interpolants of some smooth harmonic functions are discrete harmonic:

Example 57 *On a rectangular $\mathbb{Z} \times \mathbb{Z}$ grid in $\mathbb{R}^2$, which is triangulated by subdividing along either diagonal of each rectangle, the interpolating functions of*

$$\operatorname{Re} z, \operatorname{Re} z^2, \operatorname{Re} z^3, \text{ and } \operatorname{Im} z^4$$

are discrete harmonic maps, and so are the interpolants of some other polynomials.

Example 58 *On a rectangular $\mathbb{Z} \times \mathbb{Z}$ grid in $\mathbb{R}^2$, the weight of each diagonal is $\cot \frac{\pi}{2}$, and it vanishes independent of the chosen diagonal in each square. Therefore, at each grid point (i, j) only the discrete values of the* five-point stencil

$$\{(i,j),(i,j-1),(i-1,j),(i+1,j),(i,j+1)\} \quad i,j \in \mathbb{Z}$$

of the finite difference Laplacian contribute to the Dirichlet gradient.

The next example leads to discrete harmonic maps on a simplicial surfaces using linear maps:

Definition 59 *Let M_h be a polyhedral surface in $\mathbb{R}^m$. A map $u_h \in S_h(M_h)$ from M_h to $\mathbb{R}^d$ is called a* linear map *if u_h is the restriction $u_{|M}$ of a linear map $u : \mathbb{R}^m \to \mathbb{R}^d$, i.e.*

$$u_h = u_{|M} : M_h \to \mathbb{R}^d.$$

For example, any coordinate function $x_i : M_h \to \mathbb{R}$ on a polyhedral surface M_h is a linear map, and, more general, let $a \in \mathbb{R}^m$ be a constant vector, then

$$u_h(p) := \langle a, p \rangle \quad \forall\, p \in M_h$$

is linear.
On an arbitrary simplicial surface $M_h \subset \mathbb{R}^m$ the following geometric assumption on the underlying domain surface M_h leads to discrete harmonic functions:

Example 60 *A linear map $u_h : M_h \to \mathbb{R}^d$ on a polyhedral surface M_h is discrete harmonic if and only if M_h is a discrete minimal surface.*

Proof. Using the Lagrange basis functions $\varphi_i : M_h \to \mathbb{R}$ associated to each vertex p_i of M_h we have the representation

$$u_h(x) = \sum_{p_i \in M_h} u_h(p_i)\varphi_i(p), \quad p \in M_h.$$

The gradient of the Dirichlet energy can be transformed using the linearity of u_h

$$\begin{aligned}\frac{d}{du_i}E_D(u_h) &= \frac{1}{2}\sum_{j\in n(i)}\left(\cot\alpha_{ij}+\cot\beta_{ij}\right)\left(u_h(p_i)-u_h(p_j)\right)\\ &= u_h(\frac{1}{2}\sum_{j\in n(i)}\left(\cot\alpha_{ij}+\cot\beta_{ij}\right)\left(p_i-p_j\right))\\ &= u_h(\frac{d}{dp_i}E_D(\mathrm{id}_h\, M_h)).\end{aligned}$$

Therefore, u_h is a critical value of the Dirichlet energy if and only if the identity map of M_h is discrete harmonic. □

Mean Value Property and Maximum Principle

Among the two most important properties of smooth harmonic maps are the mean value property and the maximum principle.
Mean Value Property: let $p \in M$ and $U_\varepsilon(p)$ be a disk with radius ε around p. Then the value of a smooth harmonic function u at the center p is the average of the values along the boundary of the disk

$$u(p) = \frac{1}{2\pi\varepsilon}\int_{|q-p|=\varepsilon} u(q).$$

We obtain a discrete version for polyhedral maps if we replace the disk with a regular polygon.

Lemma 61 *Let u_h be a discrete harmonic map defined on the points $\{q_j\}$ of the link of a vertex p of a simplicial surface M_h. If the points $\{q_j\}$ form a regular not necessarily planar polygon with center p, then*

$$u_h(p) = \frac{1}{\#n(x)}\sum_{q_j\in n(p)} u_h(q_j)$$

is the center of mass of the surrounding function values $\{u_h(p_j)\}$.

Proof. All vertex angles appearing in Equation (3.8) are the same in a regular polygon. □
Maximum Principle: Since smooth harmonic maps solve an elliptic differential equation they satisfy a maximum principle. This means, in any open domain $U \subset M$ the maximum and minimum of u is attended at the boundary ∂U. In the discrete case, a similar statement for the star of a vertex does not hold in general, for example, it may fail if the spatial domain contains angles larger than 90 degrees.

Lemma 62 *Let u_h be a discrete harmonic map defined on a spatial domain of a simplicial surface M_h formed by the points $\{q_j\}$ around a vertex p. If the triangles around p are all acute, then $u_h(p)$ is bracketed by the convex hull of the points $\{u_h(q_j)\}$.*

Proof. From the local harmonicity condition (3.8) we see that $u_h(p)$ can be represented as a linear combination of the points $\{u_h(q_j\}$. Since all relevant angles are acute the weights of the $u_h(q_j)$ are in the interval $(0, 1)$, and $u_h(p)$ is a convex combination. □

The two previous lemmas do not hold if we allow more general domains. For example, if the domain contains obtuse triangles as in the following example, then neither the mean value nor the convex hull property may be valid.

The non-convexity of discrete harmonic maps will lead to interesting counterexamples of the maximum principle of minimal surfaces in Chapter 4. In practical applications, for example, when smoothing meshes with a Laplace filtering or mapping surfaces onto a planar domain, then one would often like to ensure convexity. In these case the mesh parametrization by Floater [45] might be a useful strategy since it ensures convexity.

3.3 Non-Conforming Harmonic Maps

Non-conforming maps on simplicial surfaces were introduced in Section 1.6.1 as another natural set of discrete maps. Let M_h be a simplicial surface then we state the Dirichlet energy in the space S_h^* as in the previous section.

Definition 63 *Let M_h be a simplicial surface in $\mathbb{R}^m$. Then the* Dirichlet energy *of a function $v_h \in S_h^*$ with $v_h : M_h \to \mathbb{R}^d$ is given by*

$$E_D(v_h) := \frac{1}{2} \sum_{T \in M_h} \int_T |\nabla v_h|^2 \, dx.$$

That is, the Dirichlet energy of v_h is the sum of the Dirichlet energies of the smooth atomic maps $v_{h|T}$ on each triangle T.

Now we consider critical points of the Dirichlet energy, and again, for simplicity, we restrict to interior variations which keep the boundary values fixed.

Definition 64 *A* variation *$\Psi(t) \in S_h^*$, $t \in [0, \varepsilon)$, is a family of functions differentiable in t such that each map $v_h \in S_h^*$ gives rise of a*

family of maps $v_h(t) \in S_h^*$ *with*

$$v_h(t) = v_h + \Psi(t)$$

Basically, a variation of a function $v_h \in S_h^*$ is a modification of its values at each edge midpoint m_i of the simplicial surface M_h given by $v_h(t)(m_i) = v_h(m_i) + \Psi(t)(m_i)$. For simplicity, we restrict to Dirichlet boundary conditions, that is, the variations $\Psi(t)$ are zero at midpoints of boundary edges of M_h.

Definition 65 *A critical point* v_h *in* S_h^* *of the Dirichlet energy (3.3) in* S_h^* *with respect to Dirichlet boundary conditions is called a* (non-conforming) discrete harmonic map.

Using the identities in an Euclidean triangle T with vertices $\{p_1, p_2, p_3\}$ and oriented edges $\{c_1, c_2, c_3\}$ with $c_i = p_{i-1} - p_{i+1}$, we obtain on T the following representation of the basis functions $\psi_i \in S_h^*$ corresponding to edge c_i :

$$\nabla\psi_i = -2\nabla\varphi_i = \frac{-1}{\operatorname{area} T} J c_i, \tag{3.9}$$

where $\varphi_i \in S_h$ is the conforming basis function corresponding to the triangle vertex p_i opposite to the edge c_i, and J is the rotation of an edge by $\frac{\pi}{2}$ such that Jc points in the opposite direction of the outer normal of the triangle.

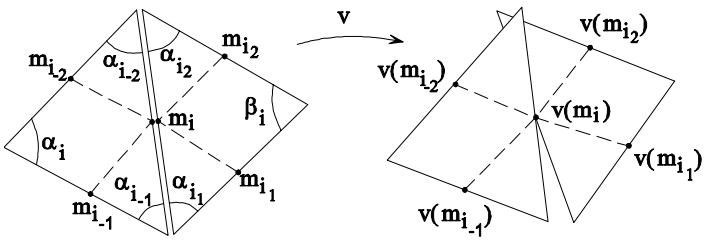

FIGURE 3.2. A non-conforming map is given by its values on edge midpoints.

Theorem 66 *Let* $v \in S_h^*$ *be a non-conforming function on a simplicial surface* M_h*. Then the Dirichlet energy of* v_h *has the explicit representation*

$$E_D(v) = \sum_{all\ edges\ c_i} \cot\alpha_i \left|v_{i-2} - v_{i-1}\right|^2 + \cot\beta_i \left|v_{i_1} - v_{i_2}\right|^2. \tag{3.10}$$

where $\{i_{-2}, i_{-1}, i_1, i_2, \}$ *denote subindices of adjacent edge midpoints as shown in Figure 3.2, and* v_{i_j} *denote the value* $v(m_{i_j})$*. The angles are measured on* M_h*.*

The unique minimizer of the Dirichlet functional on M_h *solves a system of equations such that at each edge midpoint* m_i *we have*

$$\begin{aligned} \frac{d}{dv_i} E_D(v) &= 2(\cot\alpha_{i_{-2}}(v_i - v_{i_{-1}}) + \cot\alpha_{i_{-1}}(v_i - v_{i_{-2}}) \\ &\quad + \cot\alpha_{i_1}(v_i - v_{i_2}) + \cot\alpha_{i_2}(v_i - v_{i_1})) \\ &= 0. \end{aligned} \tag{3.11}$$

Proof. Since $\nabla\psi_i = -2\nabla\varphi_i$, the representation of the Dirichlet energy is a consequence of the explicit representation for conforming elements (3.7). On a single triangle T,

$$\begin{aligned} E_D(v_{|T}) &= \frac{1}{2}\int_T -\sum_{j=1}^{3} |v_{j+1} - v_{j-1}|^2 \left\langle \nabla\psi_{j-1}, \nabla\psi_{j+1} \right\rangle \\ &= \sum_{j=1}^{3} \cot\alpha_j \, |v_{j+1} - v_{j-1}|^2 . \end{aligned}$$

The support of a component of the gradient of the Dirichlet energy consists of those two triangles adjacent to the edge corresponding to this variable. Equation (3.11) follows directly from the representation on a single triangle T with edges $\{c_1, c_2, c_3\}$ and $c_1 + c_2 + c_3 = 0$

$$\begin{aligned} \frac{d}{dv_i} E_D(v_{|T}) &= \int_T \left\langle \nabla v_{|T}, \nabla\psi_i \right\rangle = \frac{1}{\operatorname{area} T} \sum_{j=1}^{3} v_j \left\langle c_j, c_i \right\rangle \\ &= 2\cot\alpha_{i-1}(v_i - v_{i+1}) + 2\cot\alpha_{i+1}(v_i - v_{i-1}). \end{aligned}$$

by combining the expression for the two triangles in the support of ψ_i. □

3.4 Conjugate Harmonic Maps

Discrete harmonic maps have been well studied as a basic model problem in finite element theory, while the definition of the conjugate of a discrete harmonic map was not completely settled. In this section we are interested in pairs of discrete harmonic maps on a Riemann surface M which are both minimizers of the Dirichlet energy

$$E(u) = \frac{1}{2}\int_M |\nabla u|^2 \, dx,$$

and are conjugate, i.e. solutions of the Cauchy Riemann equations

$$dv = *du.$$

We note that generically such pairs do not exist in the space of piecewise linear conforming Lagrange finite elements S_h but the problem naturally leads to the space of piecewise linear non-conforming Crouzeix-Raviart elements S_h^*. S_h alone is too rigid to contain the conjugate of a generic discrete harmonic function.

We define the conjugate harmonic maps of discrete harmonic maps in S_h and in S_h^*. A smooth harmonic map $u : M \to \mathbb{R}$ on an oriented Riemannian surface M and its conjugate harmonic map $u^* : M \to \mathbb{R}$ solve the Cauchy-Riemann equations

$$du^* = *du$$

where $*$ is the Hodge star operator with respect to the metric in M. In the discrete version, we denote by J the rotation through $\frac{\pi}{2}$ in the oriented tangent space of M, and start with a locally equivalent definition as Ansatz:

Definition 67 *Let $u \in S_h$, respectively S_h^*, be a discrete harmonic map on a simplicial surface M_h with respect to the Dirichlet energies in S_h, respectively S_h^*. Then its conjugate harmonic map u^* is defined by the requirement that it locally fulfills*

$$\nabla u^*_{|T} = J\nabla u_{|T} \quad \forall \text{ triangles } T \in M_h. \tag{3.12}$$

The remainder of the section is devoted to prove that the discrete conjugate map is well-defined by showing the closedness of the differential $*du$, and to prove the harmonicity properties of its integral u^*.

To avoid case distinctions we represent each function with respect to the basis functions ψ_i of S_h^* such that on each triangle

$$u_{|T} = \sum_{i=1}^{3} u_i \psi_i,$$

where u_i is the function value of u at the midpoint of edge c_i. We use the same notation for $u^*_{|T}$, and obtain by Definition 3.12

$$\sum_{i=1}^{3} u_i^* \nabla \psi_i = \sum_{i=1}^{3} u_i J \nabla \psi_i. \tag{3.13}$$

Lemma 68 *Let T be a triangle with oriented edges $\{c_1, c_2, c_3\}$, $c_1 + c_2 + c_3 = 0$. A pair of linear functions u and u^* related by Equation (3.13), has values at edge midpoints related by*

$$\begin{pmatrix} u_3^* - u_1^* \\ u_3^* - u_2^* \end{pmatrix} = \begin{pmatrix} \cot\alpha_3(u_2 - u_1) + \cot\alpha_1(u_2 - u_3) \\ \cot\alpha_3(u_2 - u_1) + \cot\alpha_2(u_3 - u_1) \end{pmatrix} \tag{3.14}$$

Proof. The representation (3.9) of $\nabla\psi_i$ converts Equation (3.13) to

$$\sum_{i=1}^{3} u_i^* J c_i = \sum_{i=1}^{3} u_i c_i.$$

Using $-c_3 = c_1 + c_2$, we express the left side of the above equation as a vector in the span of $\{Jc_1, Jc_2\}$

$$(u_3^* - u_1^*)\, Jc_1 + (u_3^* - u_2^*)\, Jc_2 = \sum_{i=1}^{3} u_i c_i.$$

If the triangle T is nondegenerate, then the matrix (Jc_1, Jc_2) has rank 2, and scalar multiplication with c_1 and c_2 yields

$$\begin{pmatrix} u_3^* - u_1^* \\ u_3^* - u_2^* \end{pmatrix} = \frac{2}{\mathrm{area}(T)} \sum_{i=1}^{3} u_i \begin{pmatrix} \langle c_2, c_i \rangle \\ -\langle c_1, c_i \rangle \end{pmatrix},$$

which easily transforms to Equation (3.14). □

Now we consider a discrete harmonic map $u \in S_h$ and prove local exactness of its discrete conjugate differential.

Proposition 69 *Let M_h be a simply connected simplicial surface and $u \in S_h$ with $u : M_h \longrightarrow \mathbb{R}^d$ an edge continuous discrete harmonic function. Then the discrete Cauchy-Riemann equations (3.12) have a globally defined solution $u^* : M_h \longrightarrow \mathbb{R}^d$ with $u^* \in S_h^*$. Two solutions u_1^* and u_2^* differ by an additive integration constant.*

Proof. We define the discrete differential du^* of u^* such that on each triangle T

$$du^*_{|T} := *du_{|T}.$$

Since $u_{|T}$ is a linear map, the conjugate differential $du^*_{|T}$ is well defined and there exists a unique smooth solution $u^*_{|T}$ of the smooth Cauchy-Riemann equations on T, up to an additive constant. By Lemma 68, $u^*_{|T}$ is explicitly given in terms of $u_{|T}$ and T.

If $u \in S_h$ is a discrete harmonic map then it turns out that du^* is closed along closed paths on M_h that cross edges only at their

midpoints. Since du^* is closed inside each triangle, it is sufficient to prove closedness for a path γ in the vertex star of a vertex $p \in M_h$ such that $\gamma_{|T}$ linearly connects the midpoints of the two edges of T having p in common, see Figure 3.3. Let $\{m_1, .., m_k\}$ be the sequence

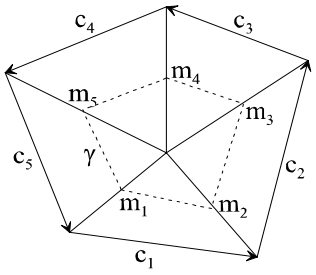

FIGURE 3.3. Dual edge graph γ around a vertex.

of edge midpoints determining γ. The edges $d_j := m_{j+1} - m_j$ of γ are parallel to c_j with $c_j = 2d_j$. We use Equation (3.14) in each triangle to derive

$$\begin{aligned} \int_\gamma du^* &= \sum_{j=1}^{k} \int_{\gamma_{|T_j}} *du_{|T_j} = \sum_{j=1}^{k} < J\nabla u_{|T_j}, d_j > \\ &= -\frac{1}{2} \sum_{j=1}^{k} < \nabla u_{|T_j}, Jc_j >= 0, \end{aligned}$$

since u is harmonic in S_h, see Equation (3.8). Therefore, du^* is closed along the dual edge graph through the edge midpoints of M_h, and $u^* \in S_h^*$ is globally defined on simply connected regions of M_h. $\square$
For a harmonic map $u \in S_h$, the following proposition proves harmonicity of the conjugate map $u^* \in S_h^*$.

Proposition 70 *Let $u \in S_h$ be a discrete harmonic map on a simplicial surface M_h and let $u^* \in S_h^*$ be a solution of the discrete Cauchy-Riemann equations (3.12) given by Proposition 69. Then u^* has the same Dirichlet energy as u, and u^* is discrete harmonic in S_h^*.*

Proof. Let u^* be the solution of the discrete Cauchy-Riemann equations (3.12) for a discrete harmonic map $u \in S_h$. Then we show that u^* is a critical point of the non-conforming Dirichlet energy in S_h^* by rewriting the Dirichlet gradient (3.11) of u^* in terms of values of u.

On a single triangle T with midpoint m_i on edge c_i, we note that

$$\left\langle J\nabla u_{|T}, \nabla\psi_i \right\rangle = \frac{2}{\operatorname{area} T}(u(m_{i-1}) - u(m_{i+1})) \;\forall i \in \{1,2,3\}, \quad (3.15)$$

which follows directly from $\nabla u = \sum_{j=1}^{3} u(m_j)\nabla\psi_j$ and

$$\left\langle J\nabla\psi_j, \nabla\psi_i \right\rangle = \begin{cases} 0 & j = i \\ \frac{2}{\operatorname{area}(T)} & j = i-1 \\ \frac{-2}{\operatorname{area}(T)} & j = i+1 \end{cases}.$$

Let $T_1 \cup T_2$ denote the two triangles forming the support of ψ_i as shown in Figure 3.4. Using Equation (3.15) we obtain

$$\begin{aligned} \frac{d}{du_i^*}E_D(u^*) &= \int_{T_1\cup T_2} \langle \nabla u^*, \nabla\psi_i \rangle \\ &= 2(u(m_{i_{-2}}) - u(m_{i_{-1}})) + 2(u(m_{i_1}) - u(m_{i_2})). \end{aligned}$$

Since u is linear we can rewrite the differences at edge midpoints as differences of u at vertices on the common edge of T_1 and T_2, and obtain

$$\frac{d}{du_i^*}E_D(u^*) = u(V_{j_{-1}}) - u(V_{j_{-2}}) + u(V_{j_2}) - u(V_{j_1}). \quad (3.16)$$

This equation relates the energy gradient of u^* to the function values at vertices of u. We emphasize the fact that the derivation of the equation does not use edge continuity of u, which will allow us to use 3.16 in the proof of Theorem 71. The right hand side of (3.16)

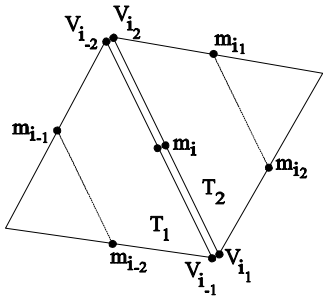

FIGURE 3.4. Notation of edge midpoints in pair of triangles.

vanishes if and only if

$$u_{|e_i \text{ in } T_1} = u_{|e_i \text{ in } T_2} + constant.$$

Therefore, the harmonicity of u^* follows from, and is equal to, the edge continuity of $u \in S_h$. $\square$

The following main theorem states the complete relationship between harmonic maps in S_h and S_h^*, and includes the previous propositions as special cases.

Theorem 71 *Let M_h be a simplicial surface in $\mathbb{R}^m$ and S_h respectively S_h^* the space of conforming respectively non-conforming maps from M_h into $\mathbb{R}^d$. Then we have the following duality of Laplace-Beltrami harmonic maps on M_h:*

1. *Let $u \in S_h$ be a minimizer of the Dirichlet energy in S_h. Then its conjugate map u^* is in S_h^* and is discrete harmonic.*

2. *Let $v \in S_h^*$ be a minimizer of the Dirichlet energy in S_h^*. Then its conjugate map u is in S_h and discrete harmonic.*

3. *Let $u \in S_h$, respectively S_h^*, be discrete harmonic in S_h, respectively. S_h^*. Then $u^{**} = -u$.*

Proof. 1. The first statement was proved in Propositions 69 and 70.

2. Let $v \in S_h^*$ given by $v = \sum v_i \psi_i$ be discrete harmonic. Along the lines of the proof for the corresponding Proposition 69 concerning S_h, we define $v^*_{|T}$ (up to an additive integration constant) as the well-defined integral of

$$dv^*_{|T} := *dv_{|T} \quad \forall\, T \in M_h,$$

which uniquely exists since $v_{|T}$ is linear. Using the same arguments as in the proof of Proposition 70 and $\nabla v^* = J \nabla v$, we derive an equation for v that is identical to Equation (3.16) for u :

$$\frac{d}{dv_i} E_D(v) = v^*(V_{j_{-1}}) - v^*(V_{j_{-2}}) + v^*(V_{j_2}) - v^*(V_{j_1}),$$

where V_{j_k} are vertices as denoted in Figure 3.4. Since v is harmonic, we can choose the integration constants of v^* such that v^* becomes edge continuous and lies in S_h.

The harmonicity property of v^* follows from the closedness of v. Let $v^* = \sum v_i^* \varphi_i \in S_h$, and then splitting $\nabla \psi_i = -\nabla \psi_{i_j} - \nabla \psi_{i_{j+1}}$ in

each triangle, we obtain

$$\begin{aligned}
\frac{d}{dv_i^*} E_D(v^*) &= \int_{M_h} \left\langle \nabla v^*, \frac{d}{dv_i^*} \nabla v^* \right\rangle = \int_{star(p_i)} \langle J\nabla v, \nabla \varphi_i \rangle \\
&= \sum_j \int_{T_{i_j}} \left\langle J\nabla v, -\frac{1}{2}(\nabla \psi_{i_j} + \nabla \psi_{i_{j+1}} \right\rangle \\
&= \sum_j \int_{T_{i_j}} \frac{1}{\operatorname{area} T_{i_j}} ((v_{i_{j+1}} - v_{i_{j-1}}) + (v_{i_{j-1}} - v_{i_j})) \\
&= \sum_j v_{i_{j+1}} - v_{i_j} = 0
\end{aligned}$$

since $v \in S_h^*$ is closed on the path around each vertex p_i. Therefore v^* is critical for the Dirichlet energy in S_h.

3. The third statement is a direct consequence of twice applying the $*$ operator twice, which rotates the gradient in each triangle by π in the plane of the gradient. □

Corollary 72 *The conjugation is a bijection between discrete Laplace-Beltrami harmonic maps in S_h and S_h^*, where each pair (u, v) fulfills the discrete Cauchy Riemann equations. Further, corresponding maps have the same Dirichlet energy.*

Proof. The proof of Theorem 71 and the previous propositions show that, for a pair (u, v) of harmonic conjugate functions $u \in S_h$ and $v \in S_h^*$, the harmonicity condition of u is equal to the closedness condition of v, and the closedness condition of u is equal to the harmonicity condition of v.

The equality of the Dirichlet energies follows directly from the Cauchy-Riemann equations. □

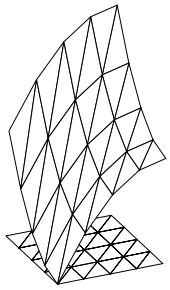

Discrete harmonic map
$u \in S_h$ interpolating $\operatorname{Re} z^2$

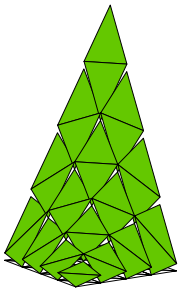

Conjugate harmonic $u^* \in S_h^*$
is a non-conforming map

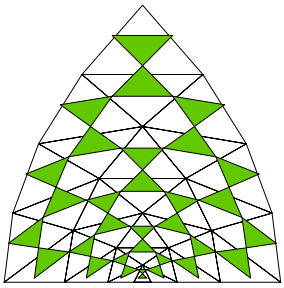

Holomorphic pair (u, u^*) and
exact solution as full grid

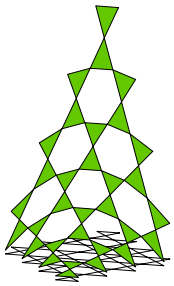

u^* applied to center
quarter of each triangle.

3.5 Minimizing with Conjugate Gradients

For completeness we will mention some of the numerical methods to practically solve the variational problems which we discussed so far. These methods apply to both the conforming and non-conforming meshes.

Let u_h be a map from a simplicial surface M_h satisfying a Dirichlet boundary value problem

$$\begin{aligned} u_h &: M_h \to \mathbb{R}^3 \\ u_{h|\partial M} &= \Gamma. \end{aligned}$$

With respect to the Lagrange basis functions, u_h is given

$$u_h(x) = \sum_{i=1}^{n} u_i \varphi_i(x).$$

Assume, we ordered the set vertices of M_h by interior and boundary vertices $\{p_1, .., p_I, p_{I+1}., p_{I+B}\}$. Then the harmonicity condition at each interior vertex p_j is

$$\begin{aligned}\frac{d}{du_j}E_D(u_h) &= \sum_{i=1}^{n} u_i \int_{M_h} \langle \nabla\varphi_i, \nabla\varphi_j \rangle \\ &= \sum_{i=1}^{I} u_i \int_{M_h} \langle \nabla\varphi_i, \nabla\varphi_j \rangle + \sum_{i=I+1}^{I+B} u_i \int_{M_h} \langle \nabla\varphi_i, \nabla\varphi_j \rangle \\ &= 0 \quad \forall\, j \in \{1, .., I\}\,.\end{aligned}$$

This system of equations is equivalent to a single matrix equation

$$Au = B$$

where $A = (a_{ji})$ is an IxI matrix, the so-called *stiffness matrix*, and $u = (u_i)$ and $B = (b_j)$ are I dimensional vectors with

$$\begin{aligned}a_{ji} &= \int_{M_h} \langle \nabla\varphi_i, \nabla\varphi_j \rangle \\ b_j &= \sum_{i=I+1}^{I+B} u_i \int_{M_h} \langle \nabla\varphi_i, \nabla\varphi_j \rangle\,.\end{aligned}$$

In praxis it is usually more efficient not solve the matrix system but employ a conjugate gradient method which is an iterative method with a fast convergence especially during the first iteration steps. See the comments of Brakke [18] who compared our method with other minimization algorithms built into the surface evolver.

The method *steepest descent* is an iterative method which incrementally reduces the energy by modifying the function u_h a small distance ε in direction of the negative of the energy gradient

$$\begin{aligned}u_0 &: = u_h \\ u_{i+1} &: = u_i - \varepsilon \nabla E_p(u_i).\end{aligned}$$

The *conjugate gradient method* is more efficient method where the direction vector is modified such that previous optimizations are not spoiled. It uses a sequence of *line minimizations*: given $p \in \mathbb{R}^n$, direction $n \in \mathbb{R}^n$ and an energy functional $E : \mathbb{R}^n \to \mathbb{R}$. Find a scalar λ that minimizes

$$E(p + \lambda n) \to \min,$$

and then replace p by $p + \lambda n$. If the energy functional is differentiable then an obvious choice for a direction is the gradient of E. Such a

gradient method can be more efficient by incorporating second order information which avoids spoiling of previous results.
The Taylor expansion around p gives

$$\begin{aligned} E(x) &= E(p) + \nabla E_p(x) + \frac{1}{2}\nabla^2 E_p(x,x) + \dots \\ &\approx c - bx + \frac{1}{2}x^t A x \end{aligned}$$

For a quadratic function E the gradient can be written as

$$\nabla E(x) = Ax - b.$$

How does the gradient change along some direction ν?

$$\partial_v \nabla E = A \cdot \partial_v x = Av$$

The idea of the conjugate gradient method can be summarized as follows: assume we have moved along some direction u to a minimum and now want to move along a new direction v. Then v shall not spoil our previous minimization, i.e. the change of the gradient shall be perpendicular to u:

$$0 =< u, \partial_v (\nabla E) >= uAv$$

The vectors u and v are called *conjugate directions* which can be constructed using the following Gram-Schmidt bi-orthogonalization procedure employed in the methods of Fletcher-Reeves and Polak-Ribiere [90][102].
Let A be a positive-definite, symmetric $n \times n$ matrix. Let g_0 be an arbitrary vector, and $h_0 = g_0$. For $i = 0, 1, 2, \dots$ define the two sequences of vectors

$$\begin{aligned} g_{i+1} &= g_i - \lambda_i A h_i \\ h_{i+1} &= g_{i+1} + \gamma_i h_i, \end{aligned} \tag{3.17}$$

where λ_i respectively γ_i are chosen to obtain mutually orthogonal vectors $g_{i+1} \cdot g_i = 0$ respectively mutually conjugate directions $h_{i+1} A h_i = 0$, that is:

$$\lambda_i = \frac{g_i \cdot g_i}{g_i A h_i} \qquad \gamma_i = -\frac{g_{i+1} A h_i}{h_i A h_i}.$$

If denominators are zero take $\lambda_i = 0$ resp. $\gamma_i = 0$. Then

$$g_i \cdot g_{i+1} = 0 \qquad h_i A h_j = 0 \qquad \forall i \neq j$$

and the bi-orthogonalization procedure has produced a sequence g_i where each g_i is orthogonal and each h_i is conjugate to its set of predecessors.

Generally, the Hessian matrix A is not known. In this case the following observation provides the essential hints. Assume E is a quadratic functional and we take

$$g_i := -\nabla E|_{p_i} \quad \text{for some point } p_i.$$

Then we proceed from p_i along the direction h_i to the local minimum of E which is located at some point p_{i+1}. If we set again $g_{i+1} := -\nabla E_{|p_{i+1}}$ then this vector g_{i+1} is exactly the vector which would have been obtained by the above Equations 3.17 but without the knowledge of the Hessian A. More precisely, the matrix A never needs to be computed.

Summarizing, the conjugate gradient method computes a set of directions h_i using only line minimizations, the evaluations of the energy gradient, and an auxiliary vector to store the recent vectors g_i. In praxis, further optimizations are obtained through pre-conditioning.

3.6 Discrete Laplace Operators

The discretization of the second order Laplace operator for smooth functions to simplicial meshes may be pursued in different ways. Depending on the structure of and information about the underlying mesh the Laplace operator may include more combinatorial or more geometric information. Here we review some basic combinatorial Laplacians and then relate them with the Laplace-Beltrami operator in the context of the functions spaces used in this chapter.

Combinatorial Laplacian

The purely combinatorial point of view ignores metric information like edge length or vertex angles of a mesh. All information about a combinatorial mesh is contained in its connectivity. For theoretical purposes it is convenient to express the connectivity in form of the adjacency matrix.

Definition 73 *Let $\{p_1, ..., p_n\}$ be the vertices of a mesh. Then the* adjacency matrix *A of the mesh connectivity is an $n \times n$ matrix given*

by

$$A_{ij} = \begin{cases} 1 & \text{if } p_i p_j \text{ is an edge} \\ 0 & \text{else} \end{cases}$$

The matrix A is sparse, and the sum of the $i-$th row respectively column is equal to the valence d_i of the vertex i. Note, in practical applications one would never explicitly store the full matrix.

Definition 74 *Let D be an $n \times n$ diagonal matrix with entries $d_{ii} := \frac{1}{d_i}$ where d_i is the valence of the vertex p_i, then the matrix*

$$\begin{aligned} L &: = \mathrm{id} - DA \\ L_{ij} &= \begin{cases} 1 & i = j \\ -\frac{1}{d_i} & \text{if } p_i p_j \text{ is an edge} \\ 0 & \text{else} \end{cases} \end{aligned}$$

is the combinatorial Laplacian *of the mesh, or short, the* mesh Laplacian.

Let e_i be the vector $(0, ..0, 1, 0, .., 0)$ with 1 at the $i-$th position which is associated to p_i. Then

$$Le_i = e_i - \frac{1}{d_i} \sum_{j \in n(i)} e_j$$

where $n(i)$ denotes the set of vertices adjacent to p_i excluding p_i.
Karni and Gotsmann [69] extend the mesh Laplacian in the framework of mesh compression to include distance information

$$GL(p_i) = p_i - \frac{\sum_{j \in n(i)} \frac{1}{|p_i - p_j|} p_j}{\sum_{j \in n(i)} \frac{1}{|p_i - p_j|}}.$$

Five-Point Laplacian

The five-point Laplacian is the $2d-$extension of the finite difference Laplacian on the real axis. Consider a real-valued function $f : \mathbb{R} \to \mathbb{R}$ on an interval of the real axis. Then the smooth Laplacian Δf is defined as second derivative of f. In the discrete case, let $\{u_i\}$ be a uniform knot vector on the axis, for example, $u_i := i$, then $f_h"(x_i)$ can be approximated using finite differences

$$\begin{aligned} f_h"(x_i) &= \frac{1}{2} \left(f_h'(x_i) - f_h'(x_i) \right) \\ &= \frac{1}{2} \left((f(x_{i+1}) - f(x_i)) - (f(x_i) - f(x_{i-1})) \right) \\ &= \frac{1}{2} \left(f(x_{i+1}) - 2f(x_i) + f(x_{i-1}) \right) \end{aligned}$$

This can be written in matrix representation

$$\Delta f_h = -Af_h$$

with $f = (f(x_0), f(x_1), ..)$ and the matrix

$$A = \frac{1}{2}\begin{pmatrix} 0 & & & & & & & & \\ -1 & 2 & -1 & & & & & & \\ & -1 & 2 & -1 & & & & & \\ & & & .. & & & & & \\ & & & & .. & -1 & 2 & 1 & \\ & & & & & & & & 0 \end{pmatrix}.$$

A smoothing operation of f can be performed by a so-called Gaussian filtering method

$$f_h^{j+1} := f_h^j + \lambda \Delta f_h^j$$

with a scalar factor $0 < \lambda < 1$. Other values of λ will enhance the variation of f. In matrix form we have

$$f_h^{j+1} = f_h^j - \lambda A f_h^j$$

Discrete Laplace-Beltrami Operator on Surfaces

Let M_h be a simplicial surface in $\mathbb{R}^m$. We now define the Laplace operator for piecewise linear functions in S_h respectively S_h^* similar to the derivation of the discrete Dirichlet energy. Since second derivatives are involved the discrete Laplace-Beltrami operator will be a function on the vertices respectively edge midpoints, and it will not extend as piecewise linear function over the whole triangulation.

Definition 75 *Let $u \in S_h$ be a map $u : M_h \to \mathbb{R}^d$ on a simplicial surface M_h with set of vertices V_h. Then the (total)* discrete Laplacian *$\Delta_h u(p) \in \mathbb{R}^d$ at each vertex $p \in V_h$ is defined as*

$$\Delta_h u(p) := -\int_{\text{star } p} \langle \nabla u, \nabla \varphi_p \rangle . \tag{3.18}$$

Similarly, let $u \in S_h^*$ be a non-conforming map then $\Delta_h^* : S_h^* \to V_h^*$ at an edge midpoint m is given by

$$\Delta_h^* u(m) := -\int_{\text{star } m} \langle \nabla u, \nabla \psi_m \rangle \tag{3.19}$$

with basis functions $\varphi_p \in S_h$ and $\psi_m \in S_h^*$.

In explicit notation we have at an interior vertex p and an interior edge midpoint m

$$\begin{aligned}\Delta_h u(p) &= -\frac{1}{2}\sum_{q_i\in n(p)}(\cot\alpha_i+\cot\beta_i)(u(p)-u(q_i))\\ \Delta_h^* u(m) &= -2(\cot\alpha_{-2}(u(m)-u(m_{-1}))+\cot\alpha_{-1}(u(m)-u(m_{-2}))\\ &\quad +\cot\alpha_1(u(m)-u(m_2))+\cot\alpha_2(u(m)-u(m_1)))\end{aligned}$$

where $\{q_i\}$ is the set of vertices on the link of p, and $\{m_i\}$ the set of vertices on the link of m in counter-clockwise order and vertex angles α_i opposite to m_i in each triangle.
In Chapter 7 we will see the relationship between the discrete Laplace-Beltrami operators and the divergence operators on vector fields.

3.7 Extension to Bezier Polyomials

Among the important concepts in CAD is the control polygon of piecewise polynomial curves and surfaces which provides an intuitive representation of the shape. For completeness we show how easily the previous concepts extend to a characterization of harmonicity in terms of the control polygon of Bezier triangles. Here we give the notion of the Dirichlet energy of polynomial maps of order n in terms of their Bezier control polygon.
Any polynomial $b^n : T \to \mathbb{R}^d$ is determined by a triangular Bezier control grid given by vertices $\{b_I\} \subset \mathbb{R}^d$. Using Bernstein basis functions and barycentric coordinates q on T the polynomial b^n has the representation

$$b^n(q) = \sum_{I=|n|} b_I B_I^n(q) \tag{3.20}$$

using the multi-index $I = (i, j, k)$ with $i + j + k = n$. A good introduction is the book by Farin [42].
For the derivation of the Dirichlet energy we denote the difference vector between two adjacent control points by

$$\Delta b_{I+e_j} := b_{I+e_{j+1}} - b_{I+e_{j-1}}.$$

Similarly we introduce a shortcut for difference of Bernstein polynomials

$$\Delta B^{n-1}_{I-e_j} := B^{n-1}_{I-e_{j+1}} - B^{n-1}_{I-e_{j-1}}.$$

Then we have

Lemma 76 *The Dirichlet energy of a Bezier polynomial $b^n : T \to \mathbb{R}$ be a Bezier polynom given by Equation 3.20 on a triangle $T \in \mathbb{R}^m$ is given by*

$$\frac{1}{2}\int_T |\nabla b^n|^2 = \sum_{j=1}^{3} \cot \alpha_j \sum_{\substack{|I|=|J| \\ =n-1}} \left\langle \Delta b_{I+e_j}, \Delta b_{J+e_j} \right\rangle B^n_{IJ} \tag{3.21}$$

where α_j are the vertex angles of the domain triangle T, $\{b_I\}$ the Bezier control points of the image, and coefficients

$$B^n_{IJ} := \int_{\Delta_n} B^{n-1}_I B^{n-1}_J dx,$$

integrated over a triangle Δ_n of area $\frac{n^2}{2}$, which depend on the chosen Bernstein basis B^n_I only, and not on b^n and T.

Proof. We define shortcuts

$$d_j := \frac{d}{du_j} \sum_{|I|=n} b_I B^n_I(u(x)) = n \sum_{|I|=n} b_j B^{n-1}_{I-e_j}(u(x)).$$

such that

$$\nabla b^n(u(x)) = \sum_{j=1}^{3} d_j \nabla u_j$$

and

$$|\nabla b^n(u(x))|^2 = \sum_{j=1}^{3} \left(d_j^2 |\nabla u_j|^2 + 2 d_{j-1} d_{j+1} \langle \nabla u_{j-1}, \nabla u_{j+1} \rangle \right). \tag{3.22}$$

Since

$$\sum_{j=1}^{3} \nabla u_j = 0$$

we have

$$\begin{aligned} |\nabla u_j|^2 &= |\nabla u_{j-1}|^2 + 2 \langle \nabla u_{j-1}, \nabla u_{j+1} \rangle + |\nabla u_{j+1}|^2 \\ &= -\langle \nabla u_{j-1}, \nabla u_j \rangle - \langle \nabla u_j, \nabla u_{j+1} \rangle . \end{aligned}$$

Inserting this into above Equation 3.22 leads to

$$|\nabla b^n(u(x))|^2 = -\sum_{j=1}^{3} (d_{j+1} - d_{j-1})^2 \langle \nabla u_{j+1}, \nabla u_{j-1} \rangle . \tag{3.23}$$

Using

$$\langle \nabla u_{j-1}, \nabla u_{j+1} \rangle = -\frac{\cot \alpha_j}{2 \operatorname{area} T}.$$

and

$$\begin{aligned} & \int_T (d_{j+1} - d_{j-1})^2 dx \qquad (3.24) \\ = \; & n^2 \int_T \left(\sum_{|I|=n-1} \Delta b_{I+e_j} B_i^{n-1}(u(x)) \right)^2 dx \\ = \; & n^2 \sum_{\substack{|I|=|J| \\ =n-1}} \left\langle \Delta b_{I+e_j}, \Delta b_{J+e_j} \right\rangle \int_T B_I^{n-1} B_J^{n-1} dx \end{aligned}$$

We replace the integration domain T with a triangle Δ_n of area $\frac{n^2}{2}$ such that $\frac{2 \operatorname{area} T}{n^2}$ is factored out and obtain the proposed equation. □

For each j the double sum contains pairwise scalar products for all parallel edges of the Bezier control net. The independent coefficients B_{IJ}^n and the right-hand integral can be precomputed and stored in a lookup table. They are totally symmetric with respect to any permutation inside I and J.

The Dirichlet energy is quadratic in the control points of the Bezier net. Let $b := (b_1, .., b_m)$ be a linear enumeration of all Bezier control points then one can setup a stiffness matrix S such that

$$E_D(b^n) =^t B \cdot S \cdot B.$$

The same matrix can be used for the Dirichlet gradient:

Lemma 77 *Let $E_D(b^n)$ be the Dirichlet energy of a Bezier polynom over a triangle T. By variation of a Bezier control point b_J we obtain the J-th component of the Dirichlet gradient*

$$\frac{d}{db_J} \int_T |\nabla b^n|^2 \, dx = 4 \sum_{j=1}^{3} \cot \alpha_j \sum_{|I|=n-1} \Delta b_{I+e_j} \int_{\Delta_n} B_I^{n-1} \Delta B_{J-e_j}^{n-1} dx.$$

Proof. Using a different numbering in Equation 3.24 we obtain

$$\begin{aligned} \int_T (d_{j+1} - d_{j-1})^2 dx &= n^2 \int_T \left(\sum_{|I|=n} b_I \Delta B_{I-e_j}^{n-1} \right)^2 dx \\ &= n^2 \sum_{|I|=|J|=n} b_I b_J \int_T \Delta B_{I-e_j}^{n-1} \Delta B_{J-e_j}^{n-1} dx \end{aligned}$$

which leads to

$$\begin{aligned}\frac{1}{2}\int_T |\nabla b^n(u(x))|^2\,dx &= \sum_{j=1}^{3}\cot\alpha_j \cdot \sum_{|I|=|J|=n} b_I b_J \int_{\Delta_n} \Delta B^{n-1}_{I-e_j}\Delta B^{n-1}_{J-e_j}\,dx \\ &= 4\sum_{j=1}^{3}\cot\alpha_j \sum_{|I|=n} b_I \int_{\Delta_n} \Delta B^{n-1}_{I-e_j}\Delta B^{n-1}_{J-e_j}\,dx.\end{aligned}$$

The proposed equation follows by inserting the Bezier representation of $\Delta B^{n-1}_{I-e_j}$. $\square$

4
Discrete Minimal Surface

Minimal surfaces are characterized by having least area compared to near-by surfaces with the same boundary. This variational property, which was the original interest in minimal surfaces, was soon relaxed to include unstable critical points as well. Equivalently, these surface can be geometrically characterized by having vanishing mean curvature.

Examples have played a central part in the development of the minimal surface theory and fruitfully complemented the theoretical research. In recent years many new examples were studied experimentally using elaborated calculations for the analytic continuation of complex functions and the integration of the Weierstraß representation formulas. Although these methods allow to compute any surface given by its Weierstraß representation, this analytic approach has the drawback that the Weierstraß formulas must be known in advance. Since the existence of many unstable minimal surfaces was mathematically proved indirectly via the so-called *conjugate surface construction* there was a strong need to develop a numerical scheme and actually compute the conjugate surface of a minimal surface [66][68].

The numerical method developed in [88] jointly with Pinkall was the first scheme to compute the conjugate of a numerically computed minimal surface. The key insight came from a new understanding of the geometric and variational properties of triangle nets. The method

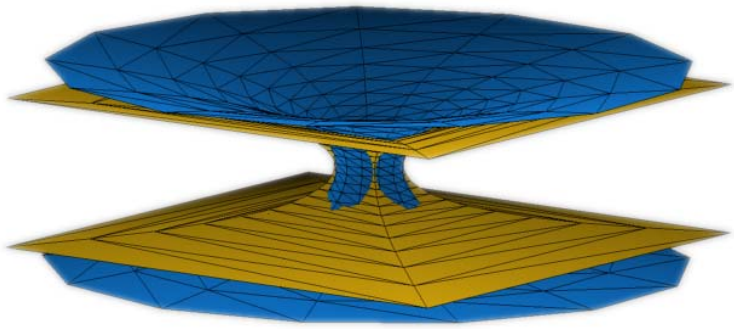

FIGURE 4.1. Asymptotic growth of two complete discrete catenoids depends on the dihedral symmetry.

was later extended in [86] jointly with Oberknapp to the computation of constant mean curvature surfaces via a conjugation of minimal surfaces in $\mathbb{S}^3$, compare Chapter 5.

The main theoretical result in this section is a new precise understanding of the variational properties of pairs of discrete conjugate minimal surfaces, which was not known in the original works, by working in the functions space of non-conforming triangle meshes. This chapter also introduces discrete minimal surfaces and derives their variational properties, we define the mean curvature normal as an operator on the discrete mesh.

Another important result is an explicit description some complete discrete minimal surfaces which were jointly discovered with Rossman [95]. For example, these descriptions allow to construct unstable discrete surfaces whose shape is given exact coordinates, a fact, which is particularly useful for the study of higher order properties like the index of minimal surfaces, see Chapter 6.

4.1 Review of the Smooth Variation of Area

Let $F : \Omega \to M \subset \mathbb{R}^3$ be a parameterized surface of a domain $\Omega \subset \mathbb{R}^2$. A variation of M is a family of surfaces given by a differentiable map

$$\begin{aligned} G : \Omega \times (-\varepsilon, \varepsilon) &\to \mathbb{R}^3 \\ G(x, 0) &= F(x) \quad x \in \Omega. \end{aligned}$$

The induced vector field on M

$$\begin{aligned} Y &: \Omega \to TM \\ Y(x) &= \frac{d}{d\varepsilon} G(x,\varepsilon)_{|\varepsilon=0} \end{aligned}$$

is called the *first variation* of G.

Lemma 78 *For a given surface M and a variation vector field Y the first variation of the area functional at M in direction of Y is defined by*

$$\delta \operatorname{area}(M,Y) := \frac{d}{d\varepsilon} \operatorname{area}(M_\varepsilon)_{|\varepsilon=0} \in \mathbb{R}$$

and given by

$$-\delta \operatorname{area}(M,Y) = \int_{\partial M} \langle Y, \nu \rangle \, ds + 2 \int_M \langle Y, N \rangle \, H dA \ ,$$

where ν is the outer normal along ∂M.

Proof. *see Hildebrandt et al. [32] or Lawson [73].* □

If $Y = \lambda N$ is a normal variation then the boundary component vanishes and we have

$$\delta \operatorname{area}(M,Y) = -2 \int_M \lambda H dA.$$

Further, if $\lambda \equiv 1$ and H is constant we obtain

$$H = -\frac{\delta \operatorname{area}(M,N)}{\operatorname{area}(M)}.$$

4.2 First Variation of the Discrete Area and Volume

A variation of a polyhedral surface is determined by a variation of its vertices with the same mesh connectivity. For simplicity we require a C^2 variation but often a differentiability of lower order is sufficient.

Definition 79 *Let $\mathcal{P} = \{p_1, ..., p_m\}$ be the set of vertices of a discrete surface M_h. A* variation *$M_h(t)$ of M_h is defined as a C^2 variation of the vertices p_i*

$$p_i(t) : [0, \epsilon) \to \mathbb{R}^d \quad \textit{so that} \quad p_i(0) = p_i \ \forall i = 1, .., m.$$

The straightness of the edges and the flatness of the triangles are preserved as the vertices move.
Formally, we have for each t that $p_i(t) \in S_h$ and $p_i(0) = id(M_h)$ is the identity map of M_h.

Up to first order a variation is given by a set of vectors $\mathcal{V} = \{v_1, ..., v_m\}$, $v_i \in \mathbb{R}^d$ defined on the vertices $\mathcal{P} = \{p_1, ..., p_m\}$ of M_h. Often we restrict a variation to interior vertices by assuming $v_i = 0 \in \mathbb{R}^d$ along the boundary, or add special constraints on the boundary of M_h. The vectors v_{p_j} are the *variation vector field* such that the variation has the form

$$p_j(t) = p_j + t \cdot v_{p_j} + \mathcal{O}(t^2), \tag{4.1}$$

that is, $p_j'(0) = v_{p_j}$. We define the vector $\vec{v} \in \mathbb{R}^{dm}$ by

$$\vec{v^t} = (v_1^t, ..., v_m^t). \tag{4.2}$$

In the following we will restrict to $d = 3$ which allows the use of a well-defined normal vector although many results hold in higher codimension too.
In the smooth situation, the variation at interior points is typically restricted to normal variation since the tangential part of the variation only performs a reparametrization of the surface. However, on discrete surfaces there is an ambiguity in the choice of normal vectors at the vertices, so we allow arbitrary variations. But we will later see in Chapter 6 (Section 6.5) that our experimental results can accurately estimate normal variations of a smooth surface when the discrete surface is a close approximation to the smooth surface.
In the following we derive the evolution equations for some basic discrete operators under variation $M_h(t)$ of a discrete surface M_h.
Recalling, that the area of a discrete surface is

$$\operatorname{area} M_h := \sum_{T \in \mathcal{T}} \operatorname{area} T,$$

where $\operatorname{area} M_h$ denotes the Euclidean area of the triangle T as a subset of $\mathbb{R}^3$.
At each vertex p of M_h, the gradient of area is

$$\nabla_p \operatorname{area} M_h = \frac{1}{2} \sum_{T=(p,q,r) \in \operatorname{star} p} J(r - q), \tag{4.3}$$

where J is rotation of angle $\frac{\pi}{2}$ in the plane of each oriented triangle T. The first derivative of the surface area is then given by the chain

rule

$$\frac{d}{dt}\operatorname{area} M_h = \sum_{p\in\mathcal{V}} \langle p', \nabla_p \operatorname{area} M_h\rangle. \tag{4.4}$$

The volume of an oriented surface M_h is the oriented volume enclosed by the cone of the surface over the origin in $\mathbb{R}^3$

$$\operatorname{vol} M_h := \frac{1}{6}\sum_{T=(p,q,r)\in M_h} \langle p, q\times r\rangle = \frac{1}{3}\sum_{T=(p,q,r)\in M_h} \langle \vec{N}, p\rangle \cdot \operatorname{area} T,$$

where p is any of the three vertices of the triangle T and $\vec{N} = (q-p)\times(r-p)/|(q-p)\times(r-p)|$ is the oriented normal of T. It follows that

$$\nabla_p \operatorname{vol} M_h = \sum_{T=(p,q,r)\in \operatorname{star} p} q\times r/6 \tag{4.5}$$

and

$$\frac{d}{dt}\operatorname{vol} M_h = \sum_{p\in\mathcal{P}} \langle p', \nabla_p \operatorname{vol} M_h\rangle. \tag{4.6}$$

Remark 80 *Note also that* $\nabla_p \operatorname{vol} M_h = \sum_{T=(p,q,r)\in\operatorname{star} p}(2\cdot\operatorname{area} T\cdot \vec{N} + p\times(r-q))/6$. *Furthermore, if* p *is an interior vertex, then the boundary of* $\operatorname{star} p$ *is closed and* $\sum_{T\in\operatorname{star} p} p\times(r-q) = 0$. *Hence the* $q\times r$ *in Equation 4.5 can be replaced with* $2\cdot\operatorname{area} T\cdot\vec{N}$ *whenever* p *is an interior vertex.*

4.3 Discrete Mean Curvature

The mean curvature vector on smooth surfaces provides a measure how much the surface area changes compared to near-by surfaces, that means, if a surface is moved at constant speed along the surface normal. In the polyhedral case we will use a similar approach to obtain a discrete version of the mean curvature vector. Similar to the definition of a discrete Gauß curvature the polyhedral mean curvature will measure the curvature of a small region. Later it will turn out that the mean curvature vector can be interpreted as the discrete Laplace-Beltrami operator on surfaces which was introduced in Chapter 3.

The area of a polyhedral surface is defined as the sum of the area of all elements. Let T be a triangle spanned by two edges v and w emanating from a vertex then its area is given by the relation $4\operatorname{area}^2 T = |v|^2|w|^2 - \langle v, w\rangle^2$. In the following we prefer an expression

of the area in terms of vertices and vertex angles of the surface. Let T be a triangle with vertices q_i and vertex angles α_i. Then

$$\operatorname{area} T = \frac{1}{4} \sum_{j=1}^{3} \cot \alpha_j \left| q_{j-1} - q_{j+1} \right|^2 .$$

For practical applications we derive a simple formula of the area gradient in intrinsic terms of the polyhedral mesh, see [88].

Lemma 81 *Let p be an interior vertex of a simplicial surface M_h. Then the gradient of the area with respect to variation of vertices can be expressed in the following cotangent formula*

$$\nabla_p \operatorname{area} M_h = \frac{1}{2} \sum_j (\cot \alpha_j + \cot \beta_j)(p - q_j). \tag{4.7}$$

Proof. The area gradient is the sum of the individual area gradients of all triangles containing p. In each triangle the area gradient of p is parallel to the height vector point toward p with length $|c|$. If c is the oriented edge opposite to p and J the rotation in the oriented plane of the triangle by $\frac{\pi}{2}$ then the gradient can be expressed by $\frac{1}{2}Jc$. Summing over all triangles containing p we obtain

$$\nabla_p \operatorname{area} M_h = \frac{1}{2} \sum_j Jc_i.$$

Using the explicit representation of Jc on a single triangle with edges $c = a - b$ and vertex angles α and β at the end points of c,

$$Jc = a \cot \alpha + b \cot \beta,$$

one obtains the proposed equation. □

This formula easily generalizes to non-manifold surfaces where, for example, three triangles join at a common edge.

If $M_h(t)$ is a variation of simplicial surfaces such that each vertex $p(t)$ is a differentiable function for $t \in (-\varepsilon, \varepsilon)$ then

$$\frac{d}{dt} \operatorname{area} M_h(t) = \sum_{p \in P} \left\langle p', \nabla_p \operatorname{area} M_h \right\rangle .$$

The mean curvature of a smooth surface measures the variation of area when changing to parallel surfaces in normal direction. In the discrete case there exists no unique normal vector, but, as first derived in [88], if we choose as normal vector the direction of the area gradient, then the following definition leads to a discrete mean curvature vector which has similar properties as the smooth mean curvature vector.

Definition 82 *The discrete mean curvature at the vertex p of a simplicial surface M_h is a vector-valued quantity*

$$\overrightarrow{H}(p) := \nabla_p \operatorname{area} M_h. \tag{4.8}$$

Note, this mean curvature operator is an integrated operator and measures the total mean curvature in the vicinity of a vertex. Therefore, when computing the total mean curvature of a surface one simply needs to sum up the mean curvature of all vertices instead of integrating over the surface. In this sense, the mean curvature is a measure at vertices similar to the (total) Gauss curvature introduced in Definition 19. Compare the definition of discrete mean curvature by Hsu, Kusner and Sullivan [63] in the experimental study of minimizers of the Willmore integral.

Another idea, which we just mention for completeness, is to define the mean curvature at edges instead of vertices based on the heuristic that the bending of a surface happens at edges. Here we will compare these two approaches.

Lemma 83 *Let e be an edge common to two triangles T_1 and T_2, and let m be an arbitrary point in the interior of e. If we bisect both triangles with edges from m and to the vertex opposite to e in each triangle then m becomes a vertex with four adjacent triangles. Then the area gradient at m*

$$\nabla_m \operatorname{area}(\operatorname{star} m) = \frac{|e|}{2}\sqrt{2+2\cos\theta}N_e$$

does not depend on the position of m within the edge but depends only on the dihedral angle θ of the edge, the length of the edge e and the angle bisecting unit normal vector N_e.

Proof. Denote the edges of the triangle T_i with $\{a_i, b_i, e\}$. Then $\operatorname{star} m$ consists of four triangles and we calculate the mean curvature normal at m:

$$\begin{aligned}\nabla_m \operatorname{area}(\operatorname{star} m) &= \frac{1}{2}\left(J_1 a_1 + J_1 b_1 + J_2 a_2 + J_2 b_2\right)\\ &= \frac{|e|}{2}\sqrt{2+2\cos\theta}N_e\end{aligned}$$

where θ is the edge angle and N_e is the angle bisecting unit normal along e. □

Since the area gradient is independent of the position of the point m on the edge we use the result of the previous lemma to define the mean curvature of an edge:

Definition 84 *Let e be an edge of a simplicial surface M_h. Then the mean curvature vector of the edge is defined by*

$$\overrightarrow{H}(e) = \frac{|e|}{2}\sqrt{2+2\cos\theta}N_e$$

where θ is the dihedral angle between the two triangle adjacent to e and N_e the angle bisecting unit normal vector. If e is a boundary edge, we set $\theta := 0$ and $N_e := Je$.

Note, the sign of the mean curvature is hidden in the definition of the normal vector N_e. If the surface is orientable then one could use a normal vector field and obtain a vector $H(e)$ whose sign is the sign of $< N_e, N >$.

Lemma 85 *Let M_h be a simplicial surface possibly with boundary, and let us denote all edges as interior which are not fully part of the boundary. Then we have*

$$\frac{1}{2}\sum_{e\in\partial M_h} Je = \sum_{e\in\mathring{M}_h} \overrightarrow{H}(e).$$

Proof. The contribution of each triangle, which does not contain a boundary edge, to the total mean curvature term is zero. The contribution of each boundary triangle to the total mean curvature term is equal to the contribution of the left hand side. □

The following lemma compares the vertex and edge based mean curvature notions.

Lemma 86 *Let $\Omega \subset M_h$ be a simply connected domain on a simplicial surface which is a subcomplex and whose boundary $\partial\Omega$ is an embedded circle. Then the total mean curvature of all interior points of Ω is equal to the force along the boundary, i.e.*

$$\sum_{p\in\mathring{\Omega}} \overrightarrow{H}(p) = \frac{1}{2}\sum_{e\in\partial\Omega} Je + \textit{contribution from vertices.}$$

where the right summation is taken over all edges e of the boundary.

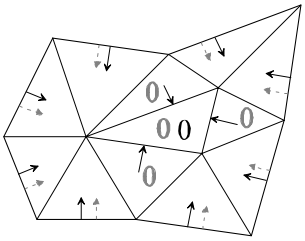

Total mean curvature.

Proof. The margin figure shows the contribution to the total interior mean curvature and the force along the boundary. The black arrows and zeros are the contribution of the edges to the total mean curvature of all interior vertices. The grey arrows and zeros is the contribution to the total mean curvature of all edges. □

Surface Tension as Force

An equivalent characterization of discrete minimal surfaces is possible by looking at the force which acts on the boundary of a soap film. As in the smooth case we assume at each vertex a tension respectively force. Here the force is assumed to be orthonormal to the edge of the link of a vertex and pointing in outward direction of the triangle.

Definition 87 *Let M_h be simplicial surface possibly with boundary. For each vertex $p \in M_h$ we define the* force $F(p)$ *as the sum of the area gradients of each triangle in* $\operatorname{star} p$

$$F(p) := -\sum_{T \in \operatorname{star} p} \nabla_p \operatorname{area} T.$$

Similar to the smooth case the total mean curvature of all interior vertices of a domain on a simplicial surface can be expressed as a boundary term.

Lemma 88 *Let M_h be a connected region on a simplicial surface. Then the total mean curvature of all interior points of S is equal to the total force along the boundary, i.e.*

$$\sum_{p \in \mathring{M}_h} \overrightarrow{H}(p) = \sum_{p \in \partial M_h} F(p).$$

Proof. The margin figure shows the contribution of vertex gradients of the different types of triangles to the total interior mean curvature and to the total force along the boundary.

First, the contribution of triangles with only interior or only boundary triangles is zero for mean curvature and for force. A triangle with one interior vertex contributes the same to the interior vertex as to the two boundary vertices, and a triangle with two interior vertices also has identical contributions. This proofs the statement. □

Therefore, the definition of a discrete minimal surface is equivalent to the vanishing of the total force of the star of each interior vertex, or more general.

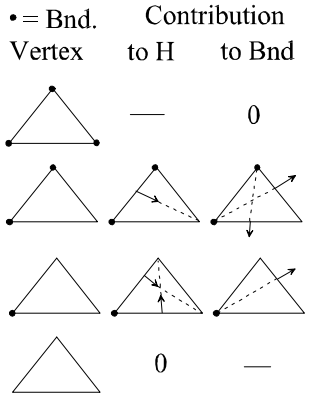

Contribution to force.

Corollary 89 *Let M_h be a simplicial surfaces. Then M_h is a discrete minimal surface if and only if the total force vanishes along the boundary of any connected region $\Omega \subset M_h$ vanishes.*

Proof. If M_h is minimal then the total interior mean curvature of any region Ω in M_h is zero and by Lemma 88 the total force of $\partial\Omega$ vanishes. The minimality of M_h follows from the vanishing of the force of the link of each vertex star. □

4.4 Properties of Discrete Minimal Surfaces

In the previous section we have introduced the notion of mean curvature vector as the gradient of the discrete area functional. Here we will study the critical values of the area functional in more detail, that is, surfaces with $H \equiv 0$.

Definition 90 *A simplicial surface M_h is a* discrete minimal surface *iff the discrete area functional of M_h is critical w.r.t. variations of any set of interior vertices. To include symmetry properties into this definition we sometimes allow a constraint variation of boundary points:*

- *if a boundary segment is a straight line, then its interior points may vary along the straight line*
- *if a boundary segment is a planar curve, then its interior points may vary within the plane*
- *in all other cases the boundary points always remain fixed.*

Note, the above definition is equivalent to saying that the area of M_h is critical with respect to variations of any interior vertex. The relaxed boundary constraints allow to simulate free boundary value problems, and to extend minimal surfaces by reflection.

Corollary 91 *A simplicial surface M_h is minimal if and only if at each interior vertex p*

$$\nabla_p \operatorname{area} M_h = \frac{1}{2} \sum_j (\cot \alpha_j + \cot \beta_j)(p - q_j) = 0 \qquad (4.9)$$

where $\{q_j\}$ denotes the set of vertices of $\operatorname{link} p$ *and α_j,β_j denote the two angles opposite to the edge pq_j. At boundary vertices on symmetry arcs the area gradient is constraint to be tangential to the straight line or to the plane.*

Proof. This equation follows directly from the representation of the area gradient as discrete mean curvature vector. □

The following properties of discrete minimal surfaces derived in [88] are similar to equivalent properties of harmonic maps.

Lemma 92 *Let M_h be a discrete minimal surface. If the star of an interior vertex p consists of congruent isosceles triangles then p lies in the center of mass of the vertices of its link.*

Proof. The weights in Equation 4.9 are all equal, therefore, p is the mean of its adjacent vertices $\{q_i\}$. □

The convex hull property for discrete minimal surfaces holds as long as the surface consists only of acute triangles.

Lemma 93 *Let M_h be a discrete minimal surface. If the star of an interior vertex p consists of acute triangles then p lies in the convex hull of its star.*

Proof. The weights in Equation 4.9 are all positive, therefore, p is a convex combination of its adjacent vertices $\{q_i\}$

$$p = \frac{\sum_j (\cot \alpha_j + \cot \beta_j) q_j}{\sum_j (\cot \alpha_j + \cot \beta_j)}$$

and lies within the convex hull of its link spanned by $\{q_i\}$. □

The previous lemma does not hold in a more general case. The following configuration is a counterexample to the maximum principle and the convex hull property of discrete minimal surfaces. Its construction in [95] jointly with Rossman is based on the existence of obtuse triangles. See also the model at [96] which contains an interactive applet to analyze the dependence on the boundary configuration.

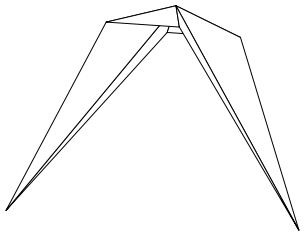

Counterexample to the maximum principle of discrete minimal surfaces. The center vertex lies outside the convex hull of its link.

The counterexample is a special configuration of the 1−parameter family of discrete minimal surfaces:

```
<points>
    <p>-u 0 -u </p>
    <p> u 0 -u </p>
    <p>-1 1 0 </p>
    <p> 1 1 0 </p>
    <p>-1 -1 0 </p>
    <p> 1 -1 0 </p>
    <p> 0 0 h(u)</p>
</points>
<faces>
    <f>0 6 2</f>
    <f>6 3 2</f>
    <f>6 1 3</f>
    <f>0 4 6</f>
    <f>4 5 6</f>
    <f>5 1 6</f>
```

</faces>

The parameter u varies in $(0, \infty)$ and the function $h(u)$ determines the vertical height of the center vertex. For $u \in [0, 2]$ the central vertex lies within the convex hull of the boundary after minimization. The remarkable fact is that this property does not hold for $u > 2$ when the minimum position of the central vertex is outside the convex hull of the boundary. The model in the margin figure corresponds to the parameter value $u = 5$.

Note, since the identity map of a discrete minimal surface is a discrete harmonic map, this example also demonstrates that the mean value property and convex hull property of discrete harmonic maps do not hold. Further note, that both properties hold in special situations where either all triangles are equilateral or have all vertex angles in $[-\frac{\pi}{2}, \frac{\pi}{2}]$ degrees. In this example, the center vertex lies on the convex hull exactly at $u = 2$ which is the situation when the first vertex angle becomes $\frac{\pi}{2}$. Increasing u further leads to an increasing angle.

Note that the discrete maximum principle does hold for the five-vertex Laplacian defined over a the special rectangular $\mathbb{Z} \times \mathbb{Z}$ grid [21].

4.5 Computing Discrete Minimal Surfaces

A direct minimization of the area functional is a non-linear problem because of the angle terms in Equation 4.9. Another effect, which may spoil numerical convergence, is the invariance of the area functional with respect to reparametrizations of the image surface. This may lead to tangential motions in an area minimization procedure.

The following observation leads to an effective method for area minimization which in fact minimizes the Dirichlet energy in an iteration process. This method was first employed by Dziuk [36] for the mean curvature flow and later used in the context of discrete minimal surfaces by Pinkall and Polthier [88]. For a smooth map $F : M \to \mathbb{R}^3$ from a Riemann surface M we have the estimate

$$\operatorname{area} F(M) \leq \frac{1}{2} \int_M |\nabla F|^2 \, dx =: E_D(F)$$

with equality iff F is a conformal map. Following a proposal of Hutchinson [65] we call the difference

$$E_C(F) := E_D(F) - \operatorname{area} F(M)$$

the *conformal energy* of the map F since for a Euclidean (x, y)-domain M one has

$$E_C(F) = \frac{1}{2} \int_\Omega |JF_x - F_y|^2 , \tag{4.10}$$

where J is the rotation by $\frac{\pi}{2}$ in the oriented tangent plane, is a natural measure of failure for a map to be conformal. In the following we will introduce a discrete analogue of these relationships.

Lemma 94 *The gradient of the Dirichlet energy of the identity map* id *of a simplicial surface M_h is equal to the area gradient, that is, at any interior vertex $p \in M$ we have*

$$\nabla_p \operatorname{area} M = \nabla_p E_D(\mathrm{id}).$$

Proof. The statement follows directly by applying the previous theorem to the id map and comparing its Dirichlet gradient with the area gradient of M_h. □

Corollary 95 *A simplicial surface M_h is minimal if and only if the identity map* $\mathrm{id}_h : M_h \to M_h$ *is discrete harmonic.*

As a consequence, we have a simplicial equivalent for the conformal energy of smooth maps given in Equation 4.10.

Definition 96 *Let $F_h : M_h \to N_h$ be a map between two simplicial surfaces, then its discrete conformal energy is given by*

$$E_C(F_h) := \operatorname{area} F_h(M_h) - E_D(F_h). \tag{4.11}$$

Corollary 97 *Let $F_h : M_h \to N_h$ be a map between two simplicial surfaces, then the discrete conformal energy and its gradient are given by*

$$\nabla_{F_h(p)} E_C(F_h) = \frac{1}{2} \sum_{p_j \in n(p_i)} (\Delta\alpha_{ij} + \Delta\beta_{ij})(F_h(p_i) - F_h(p_j)) \tag{4.12}$$

with the shortcuts

$$\begin{aligned} \Delta\alpha_{ij} &: = \cot\overline{\alpha_{ij}} - \cot\alpha_{ij} \\ \Delta\beta_{ij} &: = \cot\overline{\beta_{ij}} - \cot\beta_{ij} \end{aligned}$$

where α, β denote vertex angles on M_h and $\overline{\alpha}, \overline{\beta}$ denote vertex angle on N_h.

Proof. The statement directly follows from the definition of the discrete conformal energy

$$\nabla_{F_h(p)} E_C(F_h) = \nabla_{F_h(p)} \operatorname{area} F_h(M_h) - \nabla_{F_h(p)} E_D(F_h).$$

and inserting the above representations of area and Dirichlet gradients. □

Note, a map has vanishing conformal energy if and only if angles of domain and image triangles are equal. But critical values of the conformal energy are much less constraint. For example, Hutchinson [65] noticed that minimizing the conformal energy leads to nice triangulations since it avoids decreasing the surface area which occurs when minimizing the Dirichlet energy.

The following algorithm uses a sequence of Laplace-Beltrami harmonic maps. In short, let M_0 be an initial simplicial surface and let a sequence of simplicial surfaces $\{M_i\}$ be defined as images of a sequence of maps

$$\begin{aligned} F_i &: M_i \to M_{i+1} \\ \Delta_g F_i &= 0 \\ \partial F_i(M_i) &= \Gamma \end{aligned}$$

which are Laplace-Beltrami harmonic with respect to the metric g of M_i. If the limit surface $M := \lim M_i$ exists then the limit function $F : M \to M$ is harmonic and conformal, therefore, $F(M)$ is minimal.

The algorithm makes essential use of the fact that minimizing the Dirichlet energy also minimizes the surface area in first order. The major advantages of minimizing the Dirichlet energy compared to minimizing surface are, first, that the minimization process has a unique solution, and, second, that tangential motions can be ignored during the first iterations. Compare the comments of Brakke on this issue [19].

Algorithm 98 *Solve the boundary value problem for discrete minimal surfaces (either Dirichlet or Neumann conditions):*

1. *Choose an arbitrary initial surface M_0 with boundary $\partial M_0 = \Gamma$ as the first approximation of M, set i to 0.*
2. *Let M_i be a surface with boundary Γ, then compute the surface M_{i+1} as minimizer of the Dirichlet energy*

$$\int_{M_i} |\nabla(F_i : M_i \to M_{i+1})|^2 = \min_{M, \partial M = \Gamma} \int_{M_i} |\nabla(F : M_i \to M)|^2 .$$

This uniquely defines a Laplace-Beltrami harmonic function F_i whose image $F_i(M_i) = M_{i+1}$ will be taken as the domain surface in the next iteration.

3. *Set i to $i+1$ and continue with step 2, for example, until $|area(M_i) - area(M_{i+1})| < \epsilon$.*

In practice, this algorithm converges very fast during the first iteration steps. It slows down if the surface is close to a critical point of the area functional probably because then the area gradient no longer approximates a "good" surface normal. In any case, if the algorithm converges to a non-degenerated surface then the limit is discrete minimal. The next convergence statement shown in [88] is merely a theoretical observation than having use in practical applications since the degeneracy assumption can hardly be ensured in advance.

Proposition 99 *The algorithm converges to a solution of the problem, if no triangles degenerate.*

Proof. The condition "no triangles degenerate" means that we assume all triangle angles for all surfaces of the sequence to be uniformly bounded away from 0 to π. From the construction the sequences $\{area(M_i)\}$ and$\{E_D(f_i : M_i \to M_{i+1})\}$ are monotone decreasing:

$$\begin{aligned} area(M_i) = E_D(id_{|M_i}) &\geq E_D(f_i : M_i \to M_{i+1}) \\ &= area(M_{i+1}) + E_C(f_i) \\ &\geq E_D(id_{|M_{i+1}}) = area(M_{i+1}) \end{aligned}$$

If no triangles degenerate we minimize in a compact set of surfaces. Therefore, a subsequence of $\{M_i\}$ converges uniformly to a limit surface M with respect to the norm assumed in the space of surfaces.

Since the identity map of the limit surface M is discrete harmonic the area gradient of M vanishes everywhere, that means M is discrete minimal. □

Other Methods for Solving the Plateau Problem

The Plateau problem looks for a minimal surface M spanned by a given boundary curve $\Gamma \subset \mathbb{R}^3$. As an overview we mentioned three popular methods to compute a numerical solution.

Minimal graph: If the surface is known to be a graph over a plane, then there exists a scalar valued function z over a planar domain

$\Omega \subset \mathbb{R}^2$ with boundary $\partial\Omega$

$$\begin{aligned} z &: \Omega \to \mathbb{R} \\ z_{|\partial\Omega} &= g_1 \text{ or} \\ \partial_v z_{|\partial\Omega} &= g_2 \end{aligned}$$

where g_1 are prescribed Dirichlet boundary values, or g_2 are Neumann boundary conditions which prescribe the directional derivative of z in direction of the outer normal along $\partial\Omega$. Such a graph is area minimizing w.r.t. to variations with compact support if it fulfills a nonlinear elliptic partial differential equation, the minimal surface equation

$$(1 + z_y^2)z_{xx} + 2z_x z_y z_{xy} + (1 + z_y^2)z_{xx} = 0$$

Mean curvature flow allows to gradually decrease surface area. Let $M(t)$ with $\partial M(t) = \Gamma$ be a 1-parameter family of C^2 surfaces which is differentiable in t. Then $M(t)$ flows by mean curvature if it fulfills the following parabolic partial differential equation

$$\begin{aligned} \frac{d}{dt}M(t) &= H(t) \cdot N(t) \\ \frac{d}{dt}M(t) &= \Delta_g M \end{aligned}$$

where $H(t)$ is the mean curvature and $N(t)$ the surface normal of $M(t)$. If the flow does not run into a singularity and if it stops, then this limit surface is minimal.

4.6 Conjugate Pairs of Discrete Minimal Surfaces

Here we combine the results on non-conforming meshes of Chapter 3 and on simplicial minimal surface to derive the variational properties of pairs of discrete conjugate minimal surfaces.

Review of Smooth Minimal Surfaces

Among the fundamental observations in the theory of smooth minimal surfaces was the fact that each minimal surface comes in a family of minimal surfaces, the so-called *associate family* or *Bonnet family*. The simplest and most known example is the associate family which

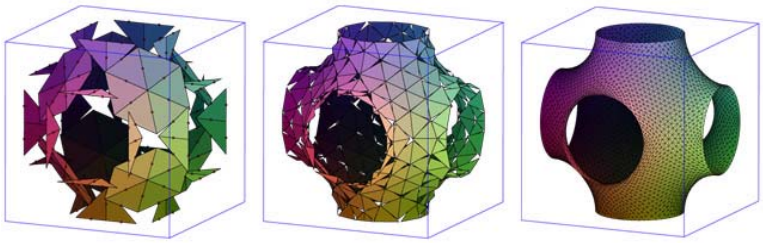

FIGURE 4.2. Free-boundary value problem of Schwarz P-surface in a cube solved via discrete conjugate surface construction. Even the very coarse resolution of the non-conforming mesh gives qualitatively good results.

transforms the catenoid C into the helicoid H, both are given by

$$C(u,v) = \begin{pmatrix} \cos v \cosh u \\ \sin v \cosh u \\ u \end{pmatrix}, \qquad H(u,v) = \begin{pmatrix} \sin v \sinh u \\ -\cos v \sinh u \\ v \end{pmatrix}.$$

Their associate family $F^\varphi(u,v)$ consists of all minimal surfaces given by

$$F^\varphi(u,v) = \cos\varphi \cdot C(u,v) + \sin\varphi \cdot H(u,v).$$

The surface $F^{\frac{\pi}{2}}$ is called the *conjugate surface* of F^0, or, more general, pairs F^φ and $F^{\varphi+\frac{\pi}{2}}$. $F^\pi = -F$ is a point mirror image of F^0.

A more appropriate notation of the associate family follows from the representation of minimal surfaces as complex curves in $\mathbb{C}^3$. Recall the basic fact in minimal surface theory that the three coordinate functions $F = (f_1, f_2, f_3)$ of a minimal surface $F : \Omega \subset \mathbb{R}^2 \to \mathbb{R}^3$ are harmonic maps if F is a conformal parameterization. Therefore, there exist three conjugate harmonic maps f_i^* which describe another minimal immersion $F^* = (f_1^*, f_2^*, f_3^*) : \Omega \subset \mathbb{R}^2 \to \mathbb{R}^3$. If we introduce complex coordinates $z = u + iv$ in Ω then combination of both maps to a holomorphic curve $F + iF^* : \Omega \to \mathbb{C}^3$ with holomorphic coordinate functions gives a family of immersion.$F^\varphi = \mathrm{Re}(e^{-i\varphi} \cdot (F + iF^*)$ called the associate family of F respectively F^*. In the above example the introduction of complex coordinates leads to the following representation of the associate family of catenoid and helicoid given by

$$F^\varphi(z) = \mathrm{Re}(e^{-i\varphi} \cdot (C(z) + i \cdot H(z)) = \mathrm{Re}(e^{-i\varphi} \cdot \begin{pmatrix} \cosh z \\ -i \sinh z \\ z \end{pmatrix}).$$

The following theorem summarizes the most important properties of the associate family of smooth minimal surfaces without proof.

Theorem 100 *Let $C, H : \Omega \to \mathbb{R}^3$ be a pair of conformally parametrized conjugate minimal surfaces. Then the associate family $F^\varphi : \Omega \to \mathbb{R}^3$ has the following properties:*

1. *All surfaces F^φ of the associate family are minimal and isometric.*
2. *The surface normals at each point $F^\varphi(u,v)$ is independent of φ.*
3. *The partial derivatives fulfill the following correspondence:*

$$\begin{aligned} F^\varphi_u(u,v) &= \cos\varphi \cdot C_u(u,v) - \sin\varphi \cdot C_v(u,v) \\ F^\varphi_v(u,v) &= \sin\varphi \cdot C_u(u,v) + \cos\varphi \cdot C_v(u,v) \end{aligned} ,$$

   in particular, the partials of a conjugate pair C and H satisfy the Cauchy-Riemann equations:

$$\begin{aligned} C_u(u,v) &= H_v(u,v) \\ C_v(u,v) &= -H_u(u,v) \end{aligned} .$$

   This relation can be written in a compact form $dH = *dC$ using the Hodge $*$ operator.
4. *If a minimal patch is bounded by a straight line, then its conjugate patch is bounded by a planar symmetry line and vice versa. This can be seen in the catenoid-helicoid examples, where planar meridians of the catenoid correspond to the straight lines of the helicoid.*
5. *Since at every point the length and the angle between the partial derivatives are identical for the surface and its conjugate (i.e. both surfaces are isometric) we have as a result, that the angles at corresponding boundary vertices of surface and conjugate surface are identical.*

The last two properties are most important for the later conjugate surface method.

Review of the Conjugate Surface Construction

Over the last decade the conjugate surface method has been established as one of the most powerful techniques to construct new minimal surfaces with a proposed shape in mind. One of the major drawbacks of the method is the so-called period problem which often prevents a rigorous existence proof of the examples. In these situation

where theoretical techniques fail up to now, a numerical approach is required to allow experiments.

The major obstacle for a numerical simulation of the conjugate surface method is the fact, that the minimal surfaces are usually unstable. Currently, the conjugation method based on discrete minimal surfaces is the only numerical method to compute the conjugate of a polyhedral minimal surface with satisfactory results.

4.6.1 Discrete Conjugate Minimal Surface

In this section we develop the notion of the conjugate and the associate family of a discrete minimal surface. In [88] the discrete conjugation algorithm is based the concept of discrete harmonic maps, but the method did not unveil the variational properties of the conjugate surface. In the following we first show the area minimality of the conjugate discrete minimal surface, and second, describe a practical algorithm by reformulating the conjugation method of [88] in terms of the conjugation of harmonic maps using conforming and non-conforming functions derived in Chapter 3.

Currently, the method [88] seems to be the only method to allow the conjugation of a numerically computed discrete minimal surface with reasonable results. The main difficulties are to provide accurate C^1 information, which is required for the conjugation, from numerically obtained minimal surfaces.

The remaining part of this section shows that the conjugate minimal surface is well-defined, and derives some important properties. Most results follow from properties of the conjugate harmonic coordinate functions.

Let us remind some properties of the differential of a polyhedral map $F : M_h \to \mathbb{R}^d$ where either $F \in S_h$ or $F \in S_h^*$. At each point $p \in M_h$ the differential $dF_{|p} : T_pM_h \to T_{F(p)}F(M_h)$ is given by

$$dF_{|p}(v) = \begin{pmatrix} \langle \nabla_p f_1, v \rangle \\ .. \\ \langle \nabla_p f_d, v \rangle \end{pmatrix} \quad \forall\, v \in T_pM_h$$

if $F = (f_1, .., f_d)$ are the coordinate functions. A map F is said to be harmonic if all coordinate functions are harmonic with respect to the metric of M_h. Recalling the definition of the Hodge $*$ operator directly leads to the following definition by applying the operator on the component functions. We say, that a simplicial surface M_h is in S_h respectively S_h^* if the triangulation is edge continuous respectively edge-midpoint continuous.

Definition 101 *Let $F = (f_1, .., f_d) : M_h \to \mathbb{R}^d$ be a simplicial map in S_h or S_h^*. The Hodge star operator is defined by*

$$*dF_{|p}(v) := \begin{pmatrix} *df_{1|p}(v) \\ .. \\ *df_{d|p}(v) \end{pmatrix} = \begin{pmatrix} \langle J\nabla_p f_1, v\rangle \\ .. \\ \langle J\nabla_p f_d, v\rangle \end{pmatrix} \forall\, v \in T_pM_h$$

where J is the rotation by $\frac{\pi}{2}$ in the oriented tangent space of each triangle of M_h with respect to the metric in M_h.

For example, if $F = \mathrm{id} : M_h \to M_h$ is the identity map of a simplicial surface, then we obtain on each triangle

$$*d\,\mathrm{id}_{|p}(v) := -Jv \;\forall\, v \in T_pM_h. \tag{4.13}$$

Now we are ready to extend the results on discrete harmonic maps of the previous section to the conjugation of simplicial minimal surfaces. In the following theorem we show that the differential $*d\,\mathrm{id}$ is closed on simplicial minimal surfaces, and that its integral gives the conjugate minimal surface:

Definition 102 *Let M_h be a simplicial minimal surface in S_h (or in S_h^*). Then a* discrete conjugate minimal surface *M_h^* is a solution of Equation 4.13.*

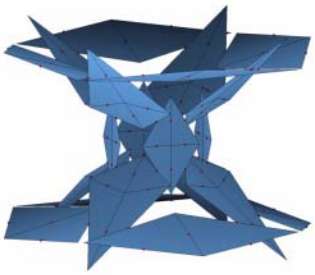

Non-conforming Catenoid.

Conforming Helicoid.

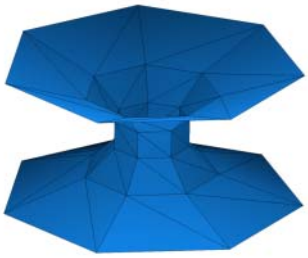

Conforming Catenoid.

Non-conforming Helicoid.

The following theorem justifies this definition and states the general relation between conjugate pairs of discrete minimal surfaces.

Theorem 103 *1. Let $M_h \subset \mathbb{R}^d$ be a discrete minimal surface in S_h. Then there exists a conjugate surface $M_h^* \subset \mathbb{R}^d$ in S_h^* which is critical for the area functional in S_h^*.*
2. Let $M_h \subset \mathbb{R}^d$ be a discrete minimal surface in S_h^*. Then there exists a conjugate surface $M_h^* \subset \mathbb{R}^d$ in S_h which is critical for the area functional in S_h.
3. M_h^* is uniquely determined by M_h up to translation.
4. M_h and M_h^* are isometric and have the same Gauss map in the sense that corresponding triangle are congruent and parallel.
5. Applying the conjugation twice leads to

$$M_h^{**} = -M_h$$

for a suitably chosen origin.

Proof. Since M_h is a critical for the area functional the identity map

$$\mathrm{id} : M_h \to M_h$$

is a discrete harmonic map by Corollary 95. Therefore, Theorem 71 in Chapter 3 proves that there exist conjugate harmonic component functions which give rise to a map on M_h

$$\mathrm{id}^* : M_h \to \mathbb{R}^d.$$

with $M_h^* := \mathrm{id}^* M_h$.
It remains to show that M_h^* is a discrete minimal surface. Here we assume that M_h is in S_h - the case M_h in S_h^* would work with the same words.
We show that M_h^* fulfills the balancing condition. Let $p^* \in M_h^*$ be an interior vertex, then by harmonicity of $\mathrm{id}^* \in S_h^*$ we have

$$\begin{aligned} \frac{d}{dm^*} E_D(\mathrm{id}^*) &= 2(\cot\alpha_{-2}(m^* - m_{-1}^*) + \cot\alpha_{-1}(m^* - m_{-2}^*) \\ &\quad + \cot\alpha_1(m^* - m_2^*) + \cot\alpha_2(m^* - m_1^*)) \\ &= 0 \end{aligned} \tag{4.14}$$

where m^* and m_i^* are the images of id^* of edge midpoints in M_h.
Since on each triangle id^* is a rotation by $\frac{\pi}{2}$, corresponding triangles of M_h and M_h^* are isometric and have the same angles. Therefore, Equation 4.14 also is the criticality condition of the Dirichlet energy

of the identity map of M_h^* which lies in S_h^*. Thus M_h^* is a discrete minimal surface in S_h^*.

The uniqueness follows from the uniqueness of the conjugate harmonic map and its integration constants. □

Summarizing, the theorem shows that a conjugate pair of discrete minimal surfaces does not exist in the space of piecewise linear conforming elements S_h but naturally leads to the space of piecewise linear non-conforming Crouzeix-Raviart elements S_h^*. S_h alone is too rigid to contain the conjugate of a minimal surface too.

In other words, if M_h is be a simplicial minimal surface in S_h respectively in S_h^* then its discrete conjugate minimal surface M_h^* is the image of the conjugate harmonic $\mathrm{id}^* : M_h \to \mathbb{R}^d$ map of the identity map of $\mathrm{id} : M_h \to M_h$, that is, id and id^* fulfill

$$d\,\mathrm{id}^* = *d\,\mathrm{id}\,.$$

The usage of the same domain M_h for both identity maps seems to distinguish M_h from M_h^* but only the conformal structure of the domain surface is relevant for the minimality condition. Therefore, we may instead use M_h^* or, more appropriate, use $\mathrm{id} : M_h \to M_h$ and $\mathrm{id}^* : M_h^* \to M_h^*$.

4.6.2 Numerical Conjugation

In practical applications the conjugation of a simplicial minimal surface by rotating each triangle and reassembling the rotated copies requires that the simplicial minimal surface has been computed very exact. Often, minimal surfaces are computed by solving a variational problem where the numerical method stops before reaching the absolute zero of the gradient. A much more stable procedure has been suggested in [88] to circumvent this difficulty: in a minimization procedure based on the Dirichlet energy there exists an accurately computed harmonic map F_i between the last two compute surfaces M_i and M_{i-1}. Instead of by applying the conjugation to the approximation M_i of the limit minimal surface, it is more stable to compute the harmonic conjugate map

$$F_i^* : M_{i-1} \to M_i^*.$$

The following algorithm summarizes the procedure:

Algorithm 104 *To compute the conjugate M_h^* of the Plateau problem M_h with Dirichlet boundary condition Γ:*

1. Follow the minimization algorithm above to compute a sequence of discrete harmonic maps $F_i : M_i \to M_{i+1}$.

2. Compute the harmonic conjugate F_i^* of $F_i : M_i \to M_{i+1}$.

3. Set $M_h := M_{i+1}$ as numerical approximation of the Plateau solution, and set $M_h^* := F_i^*(M_i)$ as approximation of the conjugate minimal surface.

This algorithm generates a sequence of discrete surfaces $\{M_i\}$ and vector-valued harmonic maps $\{F_i : M_i \to M_{i+1}\}$ which converges to a minimal surface if no degeneration occurs. In order to extend the conjugation technique of the previous sections to the computation of the conjugate of a minimal surface we allow the surfaces M_i to be either all conforming or all non-conforming triangulations. In this case the coordinate functions of each F_i are discrete harmonic functions either in S_h or S_h^*, and the image $F_i^*(M_i)$ of the conjugate harmonic of F_i is a good approximation of the conjugate minimal surface. The two approximations M_h and M_h^* are either a conforming and a non-conforming triangulation, or vice-versa.

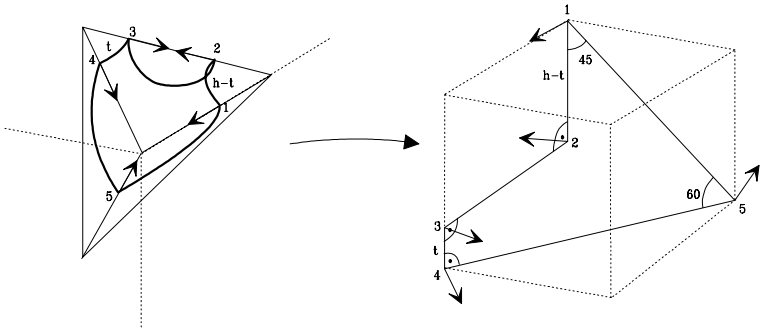

FIGURE 4.3. Transformation of a free-boundary value problem into a family of Dirichlet boundary value problems.

4.7 Discrete Minimal Catenoid

Examples are important building blocks in the development of a mathematical theory. The first smooth minimal surfaces were found already in the 18th century when Lagrange formulated the variational

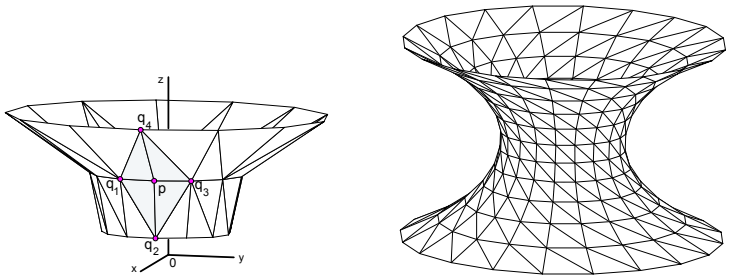

FIGURE 4.4. Discrete catenoid with essential stencil, see Lemma 105

characterization of minimal surfaces. The French geometer and engineer Jean Baptiste Meusnier (1754-1793) recognized the first nontrivial examples of minimal surfaces: the catenoid found by Euler in 1744, also called the chain surface, because it is the surface swept out when one rotates the catenary curve that corresponds to a freely hanging chain about a suitable horizontal line, and the helicoid, or screw surface. Already the discovery of the next examples in 1835 was regarded as so sensational that its discoverer Heinrich Ferdinand Scherk (1798-1885), Professor at Kiel and Bremen, won a prize at the Jablonowski Society at Leipzig in 1831.

The discovery of this discrete minimal catenoid by Polthier and Rossman [95] was driven by a very practical need, namely the provision of an unstable discrete minimal surface for investigations on the index of minimal surfaces. The numerical eigenvalue computations require a very accurate unstable surface as input which is hardly produced by means of minimization methods. Here the explicit formulae allow to create unstable catenoids of arbitrary resolution. The model [94] at the EG-Models journal includes an interactive applet to study the whole family of discrete catenoids.

The strategy for the construction of an explicit formula for embedded complete discrete minimal catenoids is to assume that the vertices lie on congruent planar polygonal meridians and that the meridians placed so that the traces of the surfaces will have dihedral symmetry. Under these assumptions we find that the vertices of a discrete meridian lie equally spaced on a smooth hyperbolic cosine curve. Furthermore, these discrete catenoids will converge uniformly in compact regions to the smooth catenoid as the mesh is made finer.

We begin with a lemma that prepares the construction of the vertical meridian of the discrete minimal catenoid, by successively adding one horizontal ring after another starting from an initial ring. Since our construction will lead to pairwise coplanar triangles, the star of each

individual vertex can be made to consist of four triangles (see Remark 146). We now derive an explicit representation of the position of a vertex surrounded by four such triangles in terms of the other four vertex positions. The center vertex is assumed to be coplanar with each of the two pairs of two opposite vertices, with those two planes becoming the plane of the vertical meridian and the horizontal plane containing a dihedrally symmetric polygonal ring (consisting of edges of the surface). See Figure 4.4.

Lemma 105 *Let a, b, d, e be given real numbers with $b \neq e$ and let θ be a dihedral angle which determine four vertices $p = (d, 0, e)$, $q_1 = (d\cos\theta, -d\sin\theta, e)$, $q_2 = (a, 0, b)$, and $q_3 = (d\cos\theta, d\sin\theta, e)$. Then there exists a choice of other real numbers x and y and a fifth vertex $q_4 = (x, 0, y)$ so that the discrete surface formed by the four triangles (p, q_1, q_2), (p, q_2, q_3), (p, q_3, q_4), and (p, q_4, q_1) is minimal, i.e.*

$$\nabla_p \operatorname{area}(\operatorname{star} p) = 0 \ ,$$

if and only if

$$2ad > \frac{(e-b)^2}{1+\cos\theta} \ .$$

Furthermore, x and y are unique and of the form

$$\begin{aligned} x &= \frac{2(1+\cos\theta)d^3 + (a+2d)(e-b)^2}{2ad(1+\cos\theta) - (e-b)^2}, \\ y &= 2e - b. \end{aligned}$$

Proof. First we note that the assumption $b \neq e$ is necessary. If $b = e$, then one may choose $y = b$, and then there is a free 1-parameter family of choices of x, leading to a trivial planar surface.

For simplicity we apply a vertical translation and a homothety about the origin of $\mathbb{R}^3$ to normalize $d = 1$, $e = 0$, and by doing a reflection if necessary, we may assume $b < 0$. Let $c = \cos\theta$ and $s = \sin\theta$.

We derive conditions for the coordinate components of ∇_p area to vanish. The second component vanishes by symmetry of $\operatorname{star} p$. Using the definitions

$$c_1 := \frac{(a-1)s^2 - b^2(1-c)}{\sqrt{2b^2(1-c) + (a-1)^2 s^2}}, \quad c_2 := \frac{ab+b}{\sqrt{2b^2(1-c) + (a-1)^2 s^2}},$$

the first (resp. third) component of ∇_p area vanishes if

$$c_1 = \frac{y^2(1-c) - (x-1)s^2}{\sqrt{2y^2(1-c) + (x-1)^2 s^2}}, \text{ resp. } c_2 = \frac{-(x-1)y - 2y}{\sqrt{2y^2(1-c) + (x-1)^2 s^2}}. \tag{4.15}$$

Dividing one of these equations by the other we obtain

$$x - 1 = \frac{c_2 y(1-c) + 2c_1}{c_2 s^2 - c_1 y}\, y\,, \tag{4.16}$$

so x is determined by y. It now remains to determine if one can find y so that $c_2 s^2 - c_1 y \neq 0$. If $x-1$ is chosen as in Equation 4.16, then the first minimality condition of Equation 4.15 holds if and only if the second one holds as well. So we only need to insert this value for $x-1$ into the first minimality condition and check for solutions y. When $c_1 \neq 0$, we find that the condition becomes

$$1 = \frac{c_2 s^2 - c_1 y}{|c_2 s^2 - c_1 y|}\frac{y}{|y|} \frac{-(1-c)y^2 - 2s^2}{\sqrt{2(1-c)c_2^2 s^4 + 4c_1^2 s^2 + (2(1-c)c_1^2 + s^2(1-c)^2 c_2^2)y^2}}.$$

Since $-(1-c)y^2 - 2s^2 < 0$, note that this equation can hold only if $c_2 s^2 - c_1 y$ and y have opposite signs, so the equation becomes

$$1 = \frac{(1-c)y^2 + 2s^2}{\sqrt{2(1-c)c_2^2 s^4 + 4c_1^2 s^2 + (2(1-c)c_1^2 + s^2(1-c)^2 c_2^2)y^2}},$$

which simplifies to

$$1 = \frac{\sqrt{(1-c)y^2 + 2s^2}}{\sqrt{(1-c)c_2^2 s^2 + 2c_1^2}}.$$

This implies y^2 is uniquely determined. Inserting the value

$$y = \pm b,$$

one finds that the above equation holds. When $y = b < 0$, we find that $c_2 s^2 - c_1 y < 0$, which is impossible. When $y = -b > 0$, we find that $c_2 s^2 - c_1 y < 0$ if and only if $2a(1+c) > b^2$. And when $y = -b$ and $2a(1+c) > b^2$, we have the minimality condition when

$$x = \frac{2 + 2c + ab^2 + 2b^2}{2a + 2ac - b^2}.$$

Inverting the transformation we did at the beginning of this proof brings us back to the general case where d and e are not necessarily 1 and 0, and the equations for x and y become as stated in the lemma. When $c_1 = 0$, we have $(a-1)(1+c) = b^2$ and $(x-1)(1+c) = y^2$, so, in particular, we have $a > 1$ and therefore $2a(1+c) > b^2$. The right-hand

side of Equation (4.15) implies $y = -b$ and $x = a$. Again, inverting the transformation from the beginning of this proof, we have that x and y must be of the form in the lemma for the case $c_1 = 0$ as well. □

The next lemma provides a necessary and sufficient condition for when two points lie on a scaled cosh curve, a condition that is identical to that of the previous lemma. That these conditions are the same is crucial to the proof of the upcoming theorem.

Lemma 106 *Given two points (a, b) and (d, e) in $\mathbb{R}^2$ with $b \neq e$, and an angle θ with $|\theta| < \pi$, there exists an r so that these two points lie on some vertical translate of the modified* cosh *curve*

$$\gamma(t) = \left(r \cosh\left[\frac{t}{e-b} \operatorname{arccosh}\left(1 + \frac{1}{r^2} \frac{(e-b)^2}{1+\cos\theta} \right) \right], t \right), \quad t \in \mathbb{R},$$

if and only if $2ad > \frac{(e-b)^2}{1+\cos\theta}$.

Proof. Define $\hat{\delta} = \frac{e-b}{\sqrt{1+\cos\theta}}$. Without loss of generality, we may assume $0 < a \leq d$ and $e > 0$, and hence $-e \leq b < e$. If the points (a, b) and (d, e) both lie on the curve $\gamma(t)$, then

$$\operatorname{arccosh}\left(1 + \frac{\hat{\delta}^2}{r^2} \right) = \operatorname{arccosh}\left(\frac{d}{r} \right) - \operatorname{sign}(b) \cdot \operatorname{arccosh}\left(\frac{a}{r} \right),$$

where $\operatorname{sign}(b) = 1$ if $b \geq 0$ and $\operatorname{sign}(b) = -1$ if $b < 0$. Note that if $b = 0$, then a must equal r (and so $(\frac{a}{r}) = 0$). This equation is solvable (for either value of $\operatorname{sign}(b)$) if and only if

$$\left(\frac{d}{r} + \sqrt{\frac{d^2}{r^2} - 1} \right) \left(\frac{a}{r} + \sqrt{\frac{a^2}{r^2} - 1} \right) = 1 + \frac{\hat{\delta}^2}{r^2} + \frac{\hat{\delta}}{r} \sqrt{2 + \frac{\hat{\delta}^2}{r^2}}$$

when $b \leq 0$, or

$$\frac{\frac{d}{r} + \sqrt{\frac{d^2}{r^2} - 1}}{\frac{a}{r} + \sqrt{\frac{a^2}{r^2} - 1}} = 1 + \frac{\hat{\delta}^2}{r^2} + \frac{\hat{\delta}}{r} \sqrt{2 + \frac{\hat{\delta}^2}{r^2}}$$

when $b \geq 0$, for some $r \in (0, a]$. The right-hand side of these two equations has the following properties:

1. It is a nonincreasing function of $r \in (0, a]$.

2. It attains some finite positive value at $r = a$.

3. It is greater than the function $2\hat{\delta}^2/r^2$.

4. It approaches $2\hat{\delta}^2/r^2$ asymptotically as $r \to 0$.

The left-hand sides of these two equations have the following properties:

1. They attain the same finite positive value at $r = a$.

2. The first one is a nonincreasing function of $r \in (0, a]$.

3. The second one is a nondecreasing function of $r \in (0, a]$.

4. The second one attains the value $\frac{d}{a}$ at $r = 0$.

5. The first one is less than the function $4ad/r^2$.

6. The first one approaches $4ad/r^2$ asymptotically as $r \to 0$.

It follows from these properties that one of the two equations above has a solution for some r if and only if $2ad > \hat{\delta}^2$. This completes the proof. □

We now derive an explicit formula for discrete minimal catenoids, by specifying the vertices along a planar polygonal meridian. Then the traces of the surfaces will have dihedral symmetry of order $k \geq 3$. The surfaces are tessellated by planar isosceles trapezoids like a $\mathbb{Z}^2$ grid, and each trapezoid can be triangulated into two triangles by choosing a diagonal of the trapezoid as the interior edge. Either diagonal can be chosen, as this does not affect the minimality of the catenoid, by Remark 146.

The discrete catenoid has two surprising features. First, the vertices of a meridian lie on a scaled smooth cosh curve (just as the profile curve of smooth catenoids lies on the cosh curve), and there is no apriori reason to have expected this. Secondly, the vertical spacing of the vertices along the meridians is constant.

Theorem 107 *There exists a four-parameter family of embedded and complete discrete minimal catenoids $C = C(\theta, \delta, r, z_0)$ with dihedral rotational symmetry and planar meridians. If we assume that the dihedral symmetry axis is the z-axis and that a meridian lies in the xz-plane, then, up to vertical translation, the catenoid is completely described by the following properties:*

1. *The dihedral angle is* $\theta = \frac{2\pi}{k}$, $k \in \mathbb{N}$, $k \geq 3$.
2. *The vertices of the meridian in the* xz*-plane interpolate the smooth* cosh *curve*
$$x(z) = r\cosh\left(\frac{1}{r}az\right),$$
with
$$a = \frac{r}{\delta}\operatorname{arccosh}\left(1 + \frac{1}{r^2}\frac{\delta^2}{1+\cos\theta}\right),$$
where the parameter $r > 0$ *is the waist radius of the interpolated* cosh *curve, and* $\delta > 0$ *is the constant vertical distance between adjacent vertices of the meridian.*
3. *For any given arbitrary initial value* $z_0 \in \mathbb{R}$*, the profile curve has vertices of the form* $(x_j, 0, z_j)$ *with*
$$\begin{aligned} z_j &= z_0 + j\delta \\ x_j &= x(z_j) \end{aligned}$$
where $x(z)$ *is the meridian in item 2 above.*
4. *The planar trapezoids of the catenoid may be triangulated independently of each other (by Remark 146).*

Proof. By Lemma 105, if we have three consecutive vertices (x_{n-1}, z_{n-1}), (x_n, z_n), and (x_{n+1}, z_{n+1}) along the meridian in the xz-plane which satisfy the recursion formula

$$x_{n+1} = \frac{(x_{n-1} + 2x_n)\hat{\delta}^2 + 2x_n^3}{2x_n x_{n-1} - \hat{\delta}^2}, \quad z_{n+1} = z_n + \delta, \tag{4.17}$$

where $\delta = z_n - z_{n-1}$ and $\hat{\delta} = \delta/\sqrt{1+\cos\theta}$. As seen in Lemma 105, the vertical distance between (x_{n-1}, z_{n-1}) and (x_n, z_n) is the same as the vertical distance between (x_n, z_n) and (x_{n+1}, z_{n+1}), so we may consider δ and $\hat{\delta}$ to be constants independent of n.
In order for the surface to exist, Lemma 105 requires that

$$2x_n x_{n-1} > \hat{\delta}^2.$$

This implies that all x_n have the same sign, and we may assume $x_n > 0$ for all n. Therefore the surface is embedded. Also, as the condition $2x_n x_{n-1} > \hat{\delta}^2$ implies

$$2x_{n+1}x_n = \frac{2x_n(x_{n-1} + 2x_n)\hat{\delta}^2 + 4x_n^4}{2x_n x_{n-1} - \hat{\delta}^2} > \frac{2x_n x_{n-1}\hat{\delta}^2}{2x_n x_{n-1} - \hat{\delta}^2} > \hat{\delta}^2,$$

we see, inductively, that x_j is defined for all $j \in \mathbb{Z}$. Hence the surface is complete.

One can easily check that the function $x(z)$ in the theorem also satisfies the recursion formula (4.17), in the sense that if $x_j := x(z_j)$, then these x_j satisfy this recursion formula. It only remains to note that, given two initial points (x_{n-1}, z_{n-1}) and (x_n, z_n) with $z_n > z_{n-1}$, there exists an r so that these two points lie on the curve $x(z)$ with our given δ and θ (up to vertical translation) if and only if $2x_n x_{n-1} > \hat{\delta}^2$, as shown in Lemma 106. □

Remark 108 *If we consider the symmetric example with normalized waist radius $r = 1$, that is if we choose $(x_1, z_1) = (1, 0)$ and $(x_2, z_2) = (1 + \hat{\delta}^2, \delta)$, then the recursion formula in Equation 4.17 implies that*

$$(x_n, z_n) = (1 + \sum_{j=1}^{n-1} 2^{j-1} a_{n-1,j} \hat{\delta}^{2j}, (n-1)\delta), \quad \text{for } n \geq 3,$$

where $a_{n-1,j}$ is defined recursively by $a_{n,m} = 0$ if $m < 0$ or $n < 0$ or $m > n$, $a_{0,0} = 1$, $a_{n,0} = 2$ if $n > 0$, and $a_{n,m} = 2a_{n-1,m} - a_{n-2,m} + a_{n-1,m-1}$ if $n \geq m \geq 1$. Thus

$$a_{n,m} = \begin{pmatrix} n+m \\ 2m \end{pmatrix} + \begin{pmatrix} n+m-1 \\ 2m \end{pmatrix}.$$

These $a_{n,m}$ are closely related to the recently solved refined alternating sign matrix conjecture [22].

Corollary 109 *There exists a two-parameter family of discrete catenoids $C_1(\theta, z_0)$ whose vertices interpolate the smooth minimal catenoid with meridian $x = \cosh z$.*

Proof. The waist radius of the scaled cosh curve must be $r = 1$. Further, we must choose the parameter $a = 1$ which is fulfilled if θ and δ are related by $1 + \cos\theta + \delta^2 = (1 + \cos\theta)\cosh\delta$. The offset parameter z_0 may be chosen arbitrarily leading to a vertical shift of the vertices along the smooth catenoid. Note that if $z_0 = 0$, we obtain a discrete catenoid that is symmetric with respect to a horizontal reflection. □

Corollary 110 *For each fixed r and z_0, the profile curves of the discrete catenoids $C(\theta, \delta, r, z_0)$ approach the profile curve $x = r\cosh\frac{z}{r}$ of a smooth catenoid uniformly in compact sets of $\mathbb{R}^3$ as $\delta, \theta \to 0$.*

Proof. This is a direct consequence of the explicit representation of the meridian. Since

$$\lim_{\delta\to 0}\frac{1}{\delta}\operatorname{arccosh}(1+\frac{1}{r^2}\frac{\delta^2}{1+\cos\theta})=\frac{\sqrt{2}}{r\sqrt{1+\cos\theta}},$$

it follows that the profile curve of the discrete catenoid converges uniformly to the curve

$$x=r\cosh\frac{\sqrt{2}z}{r\sqrt{1+\cos\theta}}$$

as $\delta\to 0$. Then, as $\theta\to 0$ we approach the profile curve $x=r\cosh\frac{z}{r}$. □

4.8 Discrete Minimal Helicoid

We continue with the derivation of explicit discrete helicoids which are a natural second example of a complete, embedded discrete minimal surface. Here we follow the construction of the surface given in [95]. An interactive data set of the model is available at the EG-Models site at [97].

In the smooth setting, there exists an isometric deformation through conjugate surfaces from the catenoid to the helicoid (see, for example, [87]). So, one might first try to make a similar deformation from the discrete catenoids in Theorem 107 to discrete minimal helicoids. But such a deformation is impossible in the space of edge-continuous triangulations. In fact, in order to make an associate family of discrete minimal surfaces, one must allow non-continuous triangle nets having greater flexibility.

Therefore, we adopt a different approach for finding discrete minimal helicoids. The helicoids will be comprised of planar quadrilaterals, each triangulated by four coplanar triangles, see Figures 4.4 and 4.5. Each quadrilateral is the star of a unique vertex, and none of its four boundary edges are vertical or horizontal, and one pair of opposite vertices in its boundary have the same z-coordinate, and the four boundary edges consist of two pairs of adjacent edges so that within each pair the adjacent edges are of equal length.

First we derive an explicit representation for a particular vertex star to be minimal, as this will help us describe helicoids:

Lemma 111 *Let p be a point with a vertex star consisting of four vertices q_1, q_2, q_3, q_4 and four triangles $\triangle_i=(p,q_i,q_{i+1})$, $i\in\{1,2,3,4\}$*

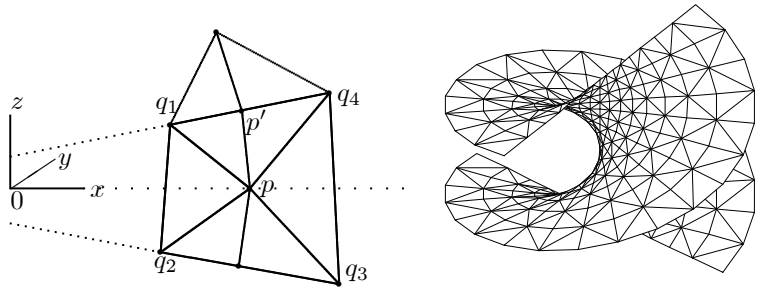

FIGURE 4.5. Essential stencil of the discrete helicoid. $\mathtt{star}(p)$ is the portion considered in Lemma 111, and $\mathtt{star}(p')$ is a planar quadrilateral, like the ones comprising the helicoid in Figure 4.4. Note that the vertex p' can be moved freely inside the planar quadrilateral $\mathtt{star}(p')$ without affecting minimality, by Remark 146. The helicoid on the right uses $x_0 = 0$.

(mod 4). We assume that $p = (u, 0, 0)$, $q_1 = (b\cos\theta, b\sin\theta, 1)$, $q_2 = (b\cos\theta, -b\sin\theta, -1)$, $q_3 = (t\cos\theta, -t\sin\theta, -1)$, $q_4 = (t\cos\theta, t\sin\theta, 1)$ *with real numbers* $b < u < t$ *and* $\theta \in (0, \frac{\pi}{2})$. *If either*

$$t = -b(1 + 2u^2\sin^2\theta) + 2u\sqrt{1 + b^2\sin^2\theta}\sqrt{1 + u^2\sin^2\theta} \quad \textit{or}$$

$$b = -t(1 + 2u^2\sin^2\theta) + 2u\sqrt{1 + t^2\sin^2\theta}\sqrt{1 + u^2\sin^2\theta}\,,$$

then ∇_p area *vanishes.*

Proof. Consider the conormals $J_1 = J(q_2 - q_1)$, $J_2 = J(q_3 - q_2)$, $J_3 = J(q_4 - q_3)$, $J_4 = J(q_1 - q_4)$, where J denotes oriented rotation by angle $\frac{\pi}{2}$ in the triangle $\triangle_j$ containing the edge being rotated. Then

$$J_1 = (2\sqrt{1 + b^2\sin^2\theta}, 0, 0) \quad \text{and} \quad J_3 = (-2\sqrt{1 + t^2\sin^2\theta}, 0, 0)\,.$$

Since

$$\begin{aligned} \langle J_4, (\cos\theta, \sin\theta, 0)\rangle &= 0 \\ det(J_4, (\cos\theta, \sin\theta, 0), (u - b\cos\theta, -b\sin\theta, -1)) &= 0 \\ |J_4|^2 &= (t - b)^2 \end{aligned}$$

we have that the first component of J_4 (and also of J_2) is

$$\frac{u(t - b)\sin^2\theta}{\sqrt{1 + u^2\sin^2\theta}}\,.$$

By symmetry, the second and third components of J_2 and J_4 are equal but opposite in sign, hence the second and third components

of $J_1 + J_2 + J_3 + J_4$ are zero. So for the minimality condition to hold at p, we need that the first component of $J_1 + J_2 + J_3 + J_4$ is also zero, that is, we need

$$\frac{u(t-b)\sin^2\theta}{\sqrt{1+u^2\sin^2\theta}} + \sqrt{1+b^2\sin^2\theta} - \sqrt{1+t^2\sin^2\theta} = 0 \ ,$$

and the solution of this with respect to b or t is as in the lemma. So, for this solution ∇_p area vanishes. □

Theorem 112 *There exists a family of complete embedded discrete minimal helicoids, with the connectivity as shown in Figure 4.4. The vertices, indexed by $i, j \in \mathbb{Z}$, are the points*

$$\frac{r\sinh(x_0 + j\delta)}{\sin\theta}(\cos(i\theta), \sin(i\theta), 0) + (0, 0, ir) \ ,$$

for any given real numbers $\theta \in (0, \frac{\pi}{2})$ and $r, \delta \in \mathbb{R}$.

Note that these surfaces are invariant under the screw motion that combines vertical upward translation of distance $2r$ with rotation about the x_3-axis by an angle of 2θ. The term x_0 determines the offset of the vertices from the $z-$axis (if $x_0 = 0$, then the z-axis is included in the edge set), and δ determines the horizontal spacing of the vertices. The homothety factor is r, which equals the vertical distance between consecutive horizontal lines of edges.

Proof. Without loss of generality, we may assume $r = 1$. So for a given i, the vertices are points on the line $\{s(\cos(i\theta), \sin(i\theta), i) \,|\, s \in \mathbb{R}\}$, for certain values of s. We choose x_0 and δ so that the $(j-2)-$th vertex has s-value $s_{j-2} = \sinh(x_0 + (j-2)\delta)/\sin\theta$ and the $(j-1)-$th vertex has $s-$value $s_{j-1} = \sinh(x_0 + (j-1)\delta)/\sin\theta$. Lemma 111 implies that the $j-$th vertex has $s-$value

$$\begin{aligned} s_j \ &= \ -s_{j-2}(1 + 2s_{j-1}^2\sin^2\theta) + \\ &\quad 2s_{j-1}\sqrt{1+s_{j-2}^2\sin^2\theta}\sqrt{1+s_{j-1}^2\sin^2\theta}, \end{aligned}$$

a recursion formula that is satisfied by

$$s_j = \sinh(x_0 + j\delta)/\sin\theta \ .$$

Lemma 111 implies a similar formula for determining s_{j-3} in terms of s_{j-2} and s_{j-1}, with the same solution. Finally, noting that those vertices whose star is a planar quadrilateral can be freely moved inside that planar quadrilateral without disturbing minimality of the surface, the theorem is proved. □

5

Discrete Constant Mean Curvature Surfaces

Surfaces with constant mean curvature (CMC surfaces) are the mathematical abstraction of physical soap films and soap bubbles. Such surfaces behave like rubber bands which try to contract under their surface tension and thereby to minimize their total surface area under the restriction of enclosing a given amount of volume. The restriction can also be interpreted as a constant difference in pressure on the two sides of the surface – for minimal surfaces the difference is zero. The simplest CMC surface is the sphere, the typical example of a soap bubble. More complicated examples, especially compact ones (i.e. finite and without boundary), are already hard to find and must have self-intersections.

The global condition of "area minimizing under volume constraint" implies a necessary local condition that must be fulfilled at every point: the mean curvature $H = \frac{1}{2}(\kappa_1 + \kappa_2)$, the mean of the two principal curvatures, must be constant on the surface. The differential geometric description of CMC surfaces originates from this local property and therefore defines a class of surfaces which covers more than the set of physically existing soap bubbles. In general, the characterization of "area minimizing under volume constraint" is no longer true from a global point of view, since differential geometric CMC surfaces may have self-intersections and extend to infinity. But locally every small neighbourhood of a point is still area minimizing

while fixing the volume which is enclosed by the cone defined by the neighbourhood's boundary and an arbitrary point in $\mathbb{R}^3$.

There have been a number of approaches to compute CMC surfaces numerically. For example the evolver of Brakke [19] is an efficient tool, see e.g. its application to foam problems in [20]. Other methods apply finite element techniques to the partial differential equation of CMC surfaces. Heil [55] computes CMC tori by making use of an explicit representation in terms of theta functions. In general, direct approaches of minimizing surface area under volume constraint are faced with stability problems. More complicated free boundary value problems are usually instable w.r.t. the variational problem, they degenerate or converge to a solution of a simpler boundary value problem. Different discrete approaches are Bobenko and Pinkall [13] for isothermic surfaces.

Recently the Dorfmeister-Pedit-Wu representation [35] for constant mean curvature surfaces was successfully used to derive new examples [70] by Kilian, McIntosh and Schmitt who also created a powerful experimental laboratory available at GANG.

Our approach differs mainly in two aspects from other algorithms. The first difference is that we do not solve the problem for a CMC surface in $\mathbb{R}^3$ directly, but we start with a corresponding problem for a minimal surface in $\mathbb{S}^3$, the unit sphere in $\mathbb{R}^4$. It is known from differential geometry that there is a 1–1 correspondence between Euclidean CMC surfaces and minimal surfaces in $\mathbb{S}^3$. On the one hand this method converts an unstable problem with Neumann boundary conditions in $\mathbb{R}^3$ into a problem with Dirichlet boundary conditions in $\mathbb{S}^3$ which often is stable. But on the other hand one is faced with the new problem of describing the transformation from a spherical minimal surface to a Euclidean CMC surface, the so-called *conjugation*. The conjugate surface construction has been described and applied in several works and led to the discovery and existence proof of minimal and CMC surfaces in $\mathbb{R}^3$ [67], $\mathbb{S}^3$ [74] [49] [50] and $\mathbb{H}^3$ [91]. It is applied to highly symmetric surfaces where the symmetry lines divide the wanted surface in fundamental patches, thereby reducing the problem to the construction of such a fundamental patch. Our algorithm is designed to cover such problems for CMC surfaces.

The second difference of our approach is the application of *discrete techniques*. Here *discrete* is used in a different sense than in finite element theory: we additionally redefine geometric properties in terms of the discrete surface which allows to operate *exactly* on these data. The conjugate surface construction resisted numerical approaches for a long time because the conjugation was originally defined using sec-

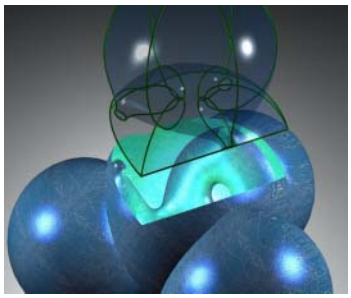
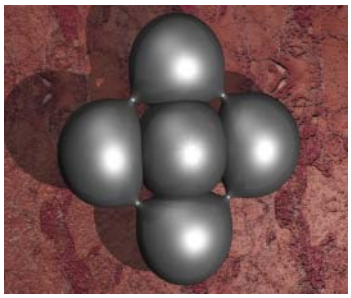

FIGURE 5.1. Compact constant mean curvature surfaces Tetra (left) and Quadro (right) with very low genus.

ond derivatives of the spherical minimal surface which itself is the (inaccurate) result of a numerical algorithm – the accumulative loss of accuracy prohibited an application of standard techniques. But even with the C^1 description of the conjugation (Lemma 117) the application of discrete techniques is the essential point. We extend the concept of discrete surfaces which was introduced for harmonic maps and minimal surfaces Chapters 3 and 4 to both problems, solving the Plateau problem in $\mathbb{S}^3$ and computing the conjugate surface. Especially for the conjugation process our discrete concept provides *exact* results for important geometric properties.

It should be noted that with the algorithm a large number of compact CMC surfaces can be computed for the first time. This algorithm was also used in the recent discovery of compact CMC surfaces with low genus jointly with Große-Brauckmann [50] [51] [52]. Some examples are shown in Figure 5.1.

The conjugate surface algorithm described in this chapter is joint work with Bernd Oberknapp, and the present chapter is an extended version of the publication [86]. The algorithm was implemented by Oberknapp in the mathematical visualization environment GRAPE [112] developed at the Sonderforschungsbereich 256 at the University of Bonn.

5.1 Complete Discrete Examples

We start with a variational characterization of discrete minimal and discrete CMC surfaces. This characterization will allow us to construct

explicit examples of *unstable* discrete CMC surfaces. (Note that merely finding minima for area with respect to a volume constraint would not suffice for this, as that would produce only stable examples.) In Chapter 6 we will use these discrete CMC surfaces for our numerical spectra computations.

In the smooth case, a minimal surface is critical with respect to area for any variation that fixes the boundary, and a CMC surface is critical with respect to area for any variation that preserves volume and fixes the boundary. We wish to define discrete CMC surfaces so that they have the same variational properties for the same types of variations. So we will consider variations $M_h(t)$ of M_h that fix the boundary ∂M_h and that additionally preserve volume in the nonminimal case, which we call *permissible variations*. The condition that makes a discrete surface area-critical for any permissible variation is expressed in the following definition.

Definition 113 *A simplicial surface has* constant mean curvature *(*CMC*) if there exists a constant H so that $\nabla_p \operatorname{area} = H \nabla_p \operatorname{vol}$ for all interior vertices p. If $H = 0$ then it is* minimal.

This definition for discrete minimality is the same as given in Chapter 4. The definition of discrete CMC surfaces differs from [86] which is later used in this chapter, where CMC surfaces are characterized algorithmically using discrete minimal surfaces in S^3 and a conjugation transformation. Compare also [13] for a definition via discrete integrable systems which lacks variational properties.

Discrete Cylinders and Delaunay Surfaces

We start with special examples constructed by Polthier and Rossman [95] namely discrete analogs of cylinders and Delaunay surfaces. Hoffmann [59] constructed discrete CMC surfaces with a quadrilateral mesh and rotational symmetry where CMC is defined as duality of discrete isothermic surfaces while the examples we present here are characterized by a variational property.

Our strategy for constructing these discrete CMC surfaces follows Definition 113 and leads to explicit representations of the vertices: find vertices p so that $\nabla_p area$ is a constant multiple of $\nabla_p vol$. A simple discrete CMC cylinder is obtained by choosing positive reals a and e and an integer $k \geq 3$, and then choosing the vertices to be

$$p_{j,\ell} = (a\cos(2\pi j/k), a\sin(2\pi j/k), e\ell)$$

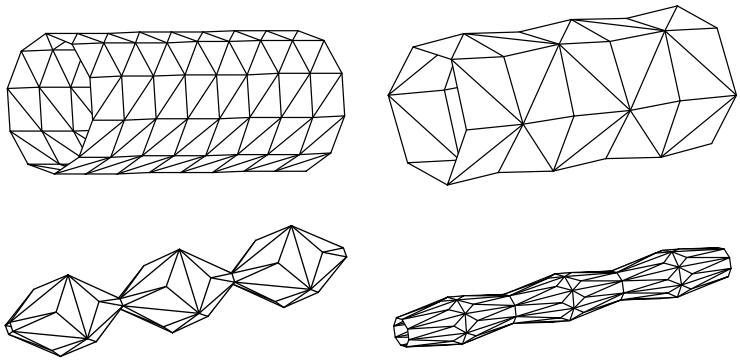

FIGURE 5.2. Discrete analogs of cylinders and Delaunay surfaces.

for $j, \ell \in \mathbb{Z}$. We then make a grid of rectangular faces, and cut the faces by diagonals with endpoints $p_{j,\ell}$ and $p_{j+1,\ell+1}$. This is a discrete CMC surface with $H = a^{-1}(\cos(\pi/k))^{-1}$. It is interesting to note that H is independent of the value of e. See the left-hand side of Figure 5.2.

Another special example is to choose positive reals a, b, e, and an integer $k \geq 3$, and to choose the vertices to be

$$p_{j,\ell} = (a\cos(2\pi j/k), a\sin(2\pi j/k), e\ell) \text{ when } j+\ell \text{ is even, and}$$

$$p_{j,\ell} = (b\cos(2\pi j/k), b\sin(2\pi j/k), e\ell) \text{ when } j+\ell \text{ is odd,}$$

for $j, \ell \in \mathbb{Z}$. We then make a grid of quadrilateral faces, and cut the faces by diagonals with endpoints $p_{j,\ell}$ and $p_{j+1,\ell+1}$ if $j+\ell$ is even, and by diagonals with endpoints $p_{j,\ell+1}$ and $p_{j+1,\ell}$ if $j+\ell$ is odd. By symmetry, it is clear that $\nabla_{p_{j,\ell}} area$ and $\nabla_{p_{j,\ell}} vol$ are parallel at each vertex; and for each value of e, one can then show the existence of values of a and b so that H is the same value at all vertices, using an intermediate value argument. Thus a discrete CMC cylinder is produced. See the second surface in Figure 5.2.

A third example can be produced by taking the vertices to be

$$p_{j,\ell} = (a\cos(2\pi j/k), a\sin(2\pi j/k), e\ell) \text{ when } \ell \text{ is even, and}$$

$$p_{j,\ell} = (b\cos(2\pi j/k), b\sin(2\pi j/k), e\ell) \text{ when } \ell \text{ is odd,}$$

for $j, \ell \in \mathbb{Z}$. We then make a grid of isosceles trapezoidal faces, and put an extra vertex in each of the trapezoidal faces, and connect this extra vertex by edges to each of the four vertices of the surrounding

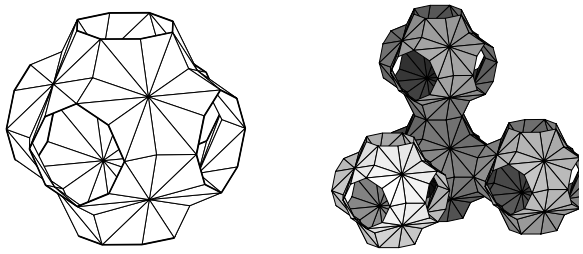

FIGURE 5.3. A triply-periodic discrete minimal surface with the symmetry of the Schwarz *p*-surface. Note that one can easily construct surfaces like this with many triangles if the fundamental domains consist of only a few triangles. There is an even simpler example with Schwarz *p*-surface symmetry whose fundamental piece has only half as many triangles.

trapezoid. Placing the vertices of the surface numerically as symmetric as possible so that Definition 113 is satisfied, surfaces like the last two examples in Figure 5.2 can be produced.

Remark 114 *The 2-dimensional boundaries of the tetrahedron, octahedron, and icosahedron are discrete* CMC *surfaces in our variational characterization in Definition 113, as well as in the sense of Definition 132. The boundaries of the cube and dodecahedron are not discrete surfaces in our sense, as they are not triangulated. However, by adding a vertex to the center of each face and connecting it by edges to each vertex in the boundary of the face, we can make discrete surfaces, and then we can move these face-centered vertices perpendicularly to the faces to adjust the mean curvature.*

5.2 Prerequisites

We start with some necessary differential geometric prerequisites for our algorithm which are well-known in the smooth case except for the C^1 description of the conjugation (Lemma 117). First we recall the $1-1$ correspondence between CMC surfaces in $\mathbb{R}^3$ and minimal surfaces in $\mathbb{S}^3$, and second we discuss consequences of the Lie group structure of $\mathbb{S}^3$.

Let $F : \Omega \to M$ be a minimal surface in $\mathbb{S}^3$ parametrized over a domain $\Omega \subset \mathbb{R}^2$. M is characterized by its metric tensor $g = \langle \partial F, \partial F \rangle$ and its second fundamental form $b = \left\langle \partial^2 F, N \right\rangle$, where $N(p) \in T_{F(p)}\mathbb{S}^3$ is the normal vector of M at a point $F(p)$. Let $S = bg^{-1}$ be the Weingarten operator, then the mean curvature is

$H = \frac{1}{2}\operatorname{trace} S$. The CMC surface $M^* \subset \mathbb{R}^3$ corresponding to M is given by the geometric data

$$\begin{array}{rcl} g^* & = & g \\ S^* & = & JS + \mathrm{id}, \end{array} \tag{5.1}$$

where J_p is the rotation by $\frac{\pi}{2}$ in the oriented tangent space $T_p\Omega$ and id_p the identity map of $T_p\Omega$ at a point $p \in \Omega$. It can easily be proved that the geometric data (g^*, S^*) integrates over Ω to a CMC surface M^* and that M^* is unique up to Euclidean motions [67]. Conversely, every CMC surface in $\mathbb{R}^3$ has a corresponding minimal immersion in $\mathbb{S}^3$.

Remark 115 *For the conjugate surface construction the correspondence of the boundaries of M and M^* is essential (see Section 5.5). If M is bounded by an embedded spherical polygon of great circle arcs then M^* is bounded by geodesic curvature lines (planar symmetry lines of the CMC surface) and vice versa [67]. Since M and M^* are isometric, corresponding boundary arcs have the same lengths and the angles at corresponding vertices – the angles of the spherical polygon and the angles between the planar symmetry lines (the dihedral angles of their symmetry planes) – are identical.*

Remark 116 *The CMC surface $M^* \subset \mathbb{R}^3$ generated by conjugation of a minimal surface $M \subset \mathbb{S}^3$ is NOT the stereographic projection of M into $\mathbb{R}^3$ (stereographic projection is not an isometry). Nevertheless stereographic projection of minimal surfaces in $\mathbb{S}^3$ into $\mathbb{R}^3$ leads to interesting surfaces which are critical points of the Willmore energy in $\mathbb{R}^3$.*

The description (5.1) of the conjugation uses C^2 information of the surface M. For this reason the conjugation resisted numerical approaches for a long time.

We proceed with a more suitable C^1 description of the conjugation process and recall the group representation of $\mathbb{S}^3$. As a model we identify $\mathbb{S}^3$ with the unitary quaternions

$$\mathbb{S}^3 \approx \left\{ x = x_0 + x_1\mathbf{i} + x_2\mathbf{j} + x_3\mathbf{k} \;\middle|\; \sum_{i=0}^{4} x_i^2 = 1 \right\}$$

where $\{\mathbf{i}, \mathbf{j}, \mathbf{k}\}$ are the imaginary units. The quaternionic left multiplication induces a Lie group structure on $\mathbb{S}^3$: every point $p \in \mathbb{S}^3$ defines a map

$$\begin{array}{rcl} p : \mathbb{S}^3 & \to & \mathbb{S}^3 \\ q & \mapsto & pq \end{array}$$

by left multiplication. Its differential map dp also operates by quaternionic left multiplication

$$\begin{aligned} dp : T_q\mathbb{S}^3 &\rightarrow T_{pq}\mathbb{S}^3 \\ v &\mapsto pv. \end{aligned}$$

The geometric effect of the differential map dp on tangent vectors is as follows: let $v \in T_q\mathbb{S}^3$ and γ be the geodesic segment from q to pq with length l. Then pv is obtained by parallel translation of v along γ and left rotation around γ' about an angle l. We call this operation *left translation* of the vector v along γ. The point $id := (1,0,0,0) \in \mathbb{S}^3$ serves as the identity element and will henceforth be called *identity* of $\mathbb{S}^3$.

The Lie algebra of $\mathbb{S}^3$ is identified with the tangent space $T_{id}\mathbb{S}^3$. For every vector $v \in T_p\mathbb{S}^3$ there exists a representative $\mathfrak{v} \in T_{id}\mathbb{S}^3$ in the Lie algebra given by

$$\mathfrak{v} = p^{-1}v$$

where p^{-1} is the inverse element of p.

With this notation at hand we can formulate the following C^1 correspondence.

Lemma 117 *Let $\Omega \subset \mathbb{C}$ be a simply connected domain and $F : \Omega \rightarrow \mathbb{S}^3$ a minimal immersion. We identify $\mathbb{S}^3$ with the unitary quaternions. Then the conjugate* CMC *surface $F^* : \Omega \rightarrow \mathbb{R}^3$ with $H = 1$ is (up to congruence of $\mathbb{R}^3$) given by*

$$F^*(z) := \operatorname{Im} \int_\gamma F^{-1} * dF \tag{5.2}$$

where γ is an arbitrary path in Ω from a fixed point z_0 to z. The map Im *denotes the standard identification of $T_{id}\mathbb{S}^3$ with $\mathbb{R}^3$, resp. the imaginary part of quaternions. $*$ is the Hodge star operator in Ω.*

Proof. Equation (5.2) is the integral representation of the following differential system

$$\begin{aligned} dF^* &= \operatorname{Im} F^{-1} * dF \\ N^* &= \operatorname{Im} F^{-1} N, \end{aligned}$$

where $N \in T\mathbb{S}^3$ is the normal field of F. Since F is minimal in $\mathbb{S}^3$ we have $\Delta_g F = -2F$ and easily obtain that the system is integrable to a smooth surface in $\mathbb{R}^3$.

To prove that F^* is CMC we make use of the identity $\Delta_g F^* = 2HN^*$ for the Laplace-Beltrami operator of any smooth surface in $\mathbb{R}^3$ and

show that $H = 1$ holds. Let F be a conformal immersion with induced metric $g = E\ dw^2$ in Ω with local coordinates $w = (u, v)$. Then $*$ acts by rotation by -90 degrees in the oriented tangent space of $F(\Omega)$ and by using the identities $*F_u = -F_v$, $*F_v = F_u$, $(F^{-1})_u = -F^{-1}F_uF^{-1}$, $F^{-1}F_uF^{-1}F_u = -E\ id$ and $F^{-1}F_uF^{-1}F_v = EF^{-1}N$ we obtain:

$$\begin{aligned}
\Delta_g F^* &= \frac{1}{E}(F^*_{uu} + F^*_{vv}) = \operatorname{Im}\frac{1}{E}((F^{-1}{*}F_u)_u + (F^{-1}{*}F_v)_v) \\
&= \operatorname{Im}\frac{1}{E}(-(F^{-1}F_v)_u + (F^{-1}F_u)_v) \\
&= \operatorname{Im}\frac{1}{E}(F^{-1}F_uF^{-1}F_v - F^{-1}F_{vu} - F^{-1}F_vF^{-1}F_u + F^{-1}F_{uv}) \\
&= \operatorname{Im}\frac{2}{E}F^{-1}F_uF^{-1}F_v = \operatorname{Im} 2F^{-1}N \\
&= 2N^*.
\end{aligned}$$

Therefore F^* is a CMC surface with $H = 1$. □

Remark 118 *Originally, Lawson [74] described the conjugation process via Equations (5.1). Karcher [67] found a C^1 construction using Hopf vector fields to describe the spherical boundary of the accompanying minimal surface in $\mathbb{S}^3$ in terms of the Euclidean boundary of the wanted* CMC *surface – this established the conjugate surface construction as a powerful constructive method (see Section 5.5). Pinkall saw that the C^1 formulation also holds in the interior of the surface.*

The discrete description of formula (5.2) turns out to be ideal for a numerical algorithm, compare Section 5.4.

5.3 Discrete Minimal Surfaces in $\mathbb{S}^3$

We extend the notion of simplicial surfaces to surfaces lying in the unit sphere $\mathbb{S}^3 \subset \mathbb{R}^4$.

Definition 119 *A* simplicial surface in $\mathbb{S}^3$ *is a simplicial surface in $\mathbb{R}^4$ where all vertices lie on the unit sphere $\mathbb{S}^3 \subset \mathbb{R}^4$. Especially, that means, we do not use geodesic triangles in $\mathbb{S}^3$. We denote with $\mathfrak{T}(\mathbb{R}^3)$, $\mathfrak{T}(\mathbb{R}^4)$ and $\mathfrak{T}(\mathbb{S}^3)$ the corresponding classes of simplicial surfaces, and sometimes use $\mathfrak{T}$ as a placeholder for any one of these three classes.*

In Section 5.4 we extent the definition of a discrete surface to non-conforming surfaces.

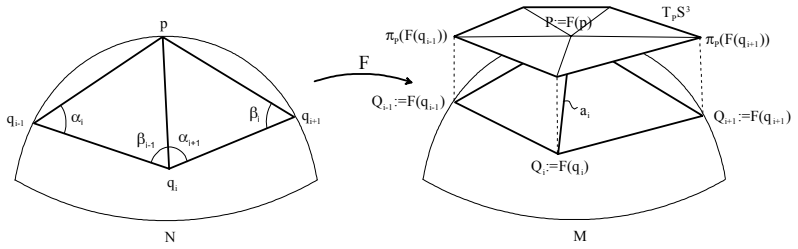

FIGURE 5.4. Notation for the discrete map $F : N \to M$.

Definition 120 *Let $N, M \in \mathfrak{T}$ be two triangulations having the same underlying topological structure, then the pair of surfaces defines a natural* discrete map *$F : N \to M$: if $\{\triangle_i^N\}$ resp. $\{\triangle_i^M\}$ are the set of triangles of N resp. M, then F is defined by* atomic maps *$f_i : \triangle_i^N \to \triangle_i^M$ which map every vertex of $\triangle_i^N$ to its corresponding vertex in $\triangle_i^M$ and extend as linear maps into the interior of $\triangle_i^N$.*

Discrete harmonic maps play an essential part in this algorithm: we obtain minimal surfaces as limit sets of sequences of harmonic maps and also define the discrete conjugation algorithm for harmonic maps. Smooth harmonic maps are characterized by several equivalent criteria, e.g. as solutions of the Laplace equation, as critical points of the Dirichlet energy or by the mean value property. The variational formulation using the Dirichlet energy can be extended to an explicit criterion for discrete surfaces, namely a balancing condition involving weighted edge lengths (compare Corollary 128 for the discrete mean value property).From now on we restrict ourself to discrete maps $F : \mathfrak{T}(\mathbb{S}^3) \to \mathfrak{T}(\mathbb{S}^3)$ to avoid case distinctions. For the Euclidean case $\mathfrak{T}(\mathbb{R}^m)$ we refer to Chapter 4.

Definition 121 *The* Dirichlet energy *of a discrete map $F : N \to M$, $N, M \in \mathfrak{T}(\mathbb{S}^3)$, is defined as the sum of the well-defined Dirichlet energies of its differentiable atomic maps*

$$E_D(F) = \frac{1}{2}\int_N |\nabla F|^2 := \frac{1}{2}\sum_i \int_{\triangle_i^N} |\nabla f_i|^2 .$$

That means, the Dirichlet energy of a map into $\mathfrak{T}(\mathbb{S}^3)$ is defined as its energy as a map into $\mathfrak{T}(\mathbb{R}^4)$.

Remark 122 *Like for smooth surfaces the Dirichlet energy of the identity map* $\mathrm{id} : M \to M$ *of a discrete surface $M \in \mathfrak{T}(\mathbb{S}^3)$ is identical*

to the area of M defined as

$$\text{area}(M) = \sum_{\Delta_i^M \subset M} \text{area}(\Delta_i^M), \tag{5.3}$$

where the area of the atomic triangles Δ_i^M is measured in $\mathbb{R}^4$.

From Chapter 3 we recall Theorem 54 which holds identically for maps $F : \mathfrak{T}(\mathbb{S}^3) \to \mathfrak{T}(\mathbb{S}^3)$:

Theorem 123 *The Dirichlet energy of a discrete map $F : N \to M$, $N, M \in \mathfrak{T}(\mathbb{S}^3)$, is given by*

$$E_D(F) = \frac{1}{2}\int_N |\nabla F|^2 = \frac{1}{4}\sum_{edges\ a_i} (\cot\alpha_i + \cot\beta_i)\,|a_i|^2\,, \tag{5.4}$$

where a_i runs through all edges of M and α_i, β_i denote the two angles in N opposite to $F^{-1}(a_i)$ measured in $\mathbb{R}^4$, see Figure 5.4 for the notation. For edges at the boundary of M one of the two cot *values is missing.*

Definition 124 *A discrete map $F : N \to M$ is* discrete harmonic *if it is a critical point of the Dirichlet energy functional E_D with respect to variations of image points in M. For $M \in \mathfrak{T}(\mathbb{S}^3)$ we restrict the variational directions to be tangential to $\mathbb{S}^3$.*
Further we restrict variational directions of boundary points to respect symmetry properties. This allows to extend harmonic maps as harmonic maps across symmetry arcs of the boundary:

(1) If the boundary is a straight line *in $\mathbb{S}^3$ its vertices are allowed to move on the geodesic of $\mathbb{S}^3$, i.e. on a great circle. This is the only case relevant for the conjugate surface construction, it ensures that the* CMC *surfaces in $\mathbb{R}^3$ will be bounded by planar symmetry arcs.*

(2) If the boundary is planar symmetric *its vertices are allowed to move on a totally geodesic hyperplane of $\mathbb{S}^3$, i.e. on a suitable $\mathbb{S}^2$.*

(3) For all other boundaries the vertices are not allowed to move.

By differentiating equation (5.4) with respect to vertices in image space we obtain a local formula for the critical points of the Dirichlet functional. We restrict ourself to interior vertices of the triangulation to avoid the obvious case distinctions at boundary vertices.

For $p, q \in \mathbb{S}^3$ the map

$$\begin{array}{rcl} \pi_p : \mathbb{S}^3 & \to & T_p\mathbb{S}^3 \\ q & \mapsto & q - \langle q, p\rangle\, p \end{array} \tag{5.5}$$

projects the point q to its part orthogonal to the point p. It can also be interpreted as the projection

$$\begin{array}{rcl} \pi_p : T_p\mathbb{R}^4 & \to & T_p\mathbb{S}^3 \\ q - p & \mapsto & \pi_p(q). \end{array} \tag{5.6}$$

of the vector $q - p \in T_p\mathbb{R}^4$ emanating from p onto its tangential component in $T_p\mathbb{S}^3$.

Theorem 125 (Balancing Condition) *Let $F : N \to M$, $N, M \in \mathfrak{T}(\mathbb{S}^3)$, be a discrete map in $\mathbb{S}^3$. Then F is harmonic iff at every interior point $P \in M$*

$$\frac{1}{2} \sum_{\substack{\text{neighbour} \\ \text{vertices } Q_i \text{ of } P}} (\cot \alpha_i + \cot \beta_i)\ \pi_P(Q_i - P) = 0 \tag{5.7}$$

holds. As above the angles α_i and β_i are measured in the domain N as angles in $\mathbb{R}^4$, see figure 5.4 for the notation.

Proof. The equation follows directly by differentiating Equation (5.4) and taking the tangential part w.r.t. $\mathbb{S}^3$ as defined by (5.5). □

Remark 126 *If one extends a surface with a symmetry arc as boundary curve by reflection then the boundary vertices become interior points of the extended surface. The important result is that Equation (5.7) holds at these points, too. This is an immediate result from the boundary conditions in Definition 124 and justifies the restrictions we imposed there.*

We now state two lemmas showing that our definition of discrete harmonicity preserves similar properties of the continuous case.

Corollary 127 *Let $F : N \to M$, $N, M \in \mathfrak{T}(\mathbb{S}^3)$, be a discrete harmonic map in $\mathbb{S}^3$ and let $\{Q_i\}$ be the set of neighbour points of an interior vertex P in the image of F. If all points Q_i and P lie in a hemisphere of $\mathbb{S}^3$ and all angles $\{\alpha_i, \beta_i\}$ in the parameter domain N are acute, then P lies in the convex hull of the points $\{Q_i\}$ in $\mathbb{S}^3$.*

Proof. Inserting Definition (5.5) of the projection operator π_P we can rearrange the minimality condition (5.7) to

$$P = \sum_i \frac{\cot \alpha_i + \cot \beta_i}{\sum_j \cot \alpha_j + \cot \beta_j} Q_i + \lambda P \tag{5.8}$$

where

$$\lambda = \frac{\sum_i (\cot \alpha_i + \cot \beta_i) \langle Q_i - P, P \rangle}{\sum_i \cot \alpha_i + \cot \beta_i}.$$

Since all angles are assumed to be acute all coefficients are in $[0, 1]$ and Equation (5.8) is a convex combination of the points Q_i plus an additional term λP parallel to P. Therefore P lies in the Euclidean cone spanned by the vertices $\{Q_i\}$ and therefore also in their spherical convex hull. □

The mean value property of smooth harmonic maps is well-known. The following lemma states an equivalent for discrete harmonic maps.

Corollary 128 *Let the points $\{q_i\}$ form a regular n-sided polygon with center p in N, and let $F : N \to M$, $N, M \in \mathfrak{T}(\mathbb{S}^3)$, be a discrete harmonic map. Then $P := F(p)$ is the mean value of the points $Q_i := F(q_i)$ up to some multiple of P*

$$P = \frac{1}{n} Q_i + \lambda P.$$

with λ as in (5.8).

Proof. All angles occurring in Equation (5.8) are identical because the domain polygon is regular. □

Using Theorem 125 we can define discrete minimal surfaces in $\mathbb{S}^3$ by a variational characterization.

Definition 129 (Discrete Minimal Surface in $\mathbb{S}^3$) *A triangulation $M \in \mathfrak{T}(\mathbb{S}^3)$ is a* discrete minimal surface in $\mathbb{S}^3$ *if it is a critical point of the area functional (5.3) w.r.t. variation of its vertices in $\mathbb{S}^3$.*

It can easily be shown that this condition is equivalent to Equation (5.7) with both angles and vertices measured in $M \subset \mathbb{R}^4$.

We now proceed to compute minimal surfaces in $\mathbb{S}^3$ by applying an iteration process as introduced in Dziuk [36] for minimal surfaces in Euclidean space, see also Pinkall and Polthier [88].

In the smooth case it is well-known that the image of a conformal harmonic map is a minimal surface and that the Dirichlet energy of a map is equal to the sum of the area of the image and the so-called conformal energy of the map. We iteratively compute harmonic maps which converge to a conformal harmonic map, i.e. to a minimal surface, in the limit.

Problem: Let Γ be a curve in $\mathbb{S}^3$, then we are looking for a discrete minimal surface with boundary Γ (for simplicity we restrict to a Plateau problem with Dirichlet boundary conditions).

Minimal Surface Construction:

(1) Let $M_0 \in \mathfrak{T}(\mathbb{S}^3)$ be an arbitrary initial surface with boundary $\partial M = \Gamma$.

(2) Let M_i be a surface with boundary Γ, then compute the surface M_{i+1} as the minimizer of

$$E_D(F : M_i \to M_{i+1}) = \min_{\substack{M \in \mathfrak{T}(\mathbb{S}^3) \\ \partial M = \Gamma}} E_D(F : M_i \to M).$$

This defines a map $F_i : M_i \to M_{i+1}$.

(3) As long as $|M_{i+1} - M_i| > \varepsilon$ in some suitable norm continue with step (2) and $i \to i + 1$.

This algorithm generates a sequence of discrete surfaces $\{M_i\}$ and harmonic maps $\{F_i\}$ and leads to a discrete minimal surface M:

Theorem 130 *A subsequence of the discrete surfaces $\{M_i\}$ generated by the above algorithm converges to a discrete minimal surface $M \in \mathfrak{T}(\mathbb{S}^3)$ if no triangles degenerate. The corresponding sequence of harmonic maps $\{F_i\}$ converges to the identity map* $\mathrm{id} : M \to M$.

Proof. With minor modifications the corresponding proof in [88] can directly be extended to $\mathbb{S}^3$. The trick of changing the domain from M_i to M_{i+1} after each step has the same effect as making the new initial map conformal by modifying the domain. But the change of the domain in step (2) generates a true conformal initial map, namely the identity map $\mathrm{id} : M_i \to M_i$. □

Remark 131 *For computing the minimum in step (2) a quadratic problem with non-linear side conditions arising from the restriction of the vertices to $\mathbb{S}^3$ must be solved. The implementation uses a modified a conjugate gradient method which allows minimization along spherical geodesics to solve this problem.*

5.4 Discrete CMC Surfaces via Conjugation

In this section we describe the conjugation process which takes a discrete minimal surface in $\mathbb{S}^3$ (a discrete harmonic map) and computes its corresponding discrete CMC surface in $\mathbb{R}^3$. We reserve the term *conjugation* for that process. In fact, we define conjugation already

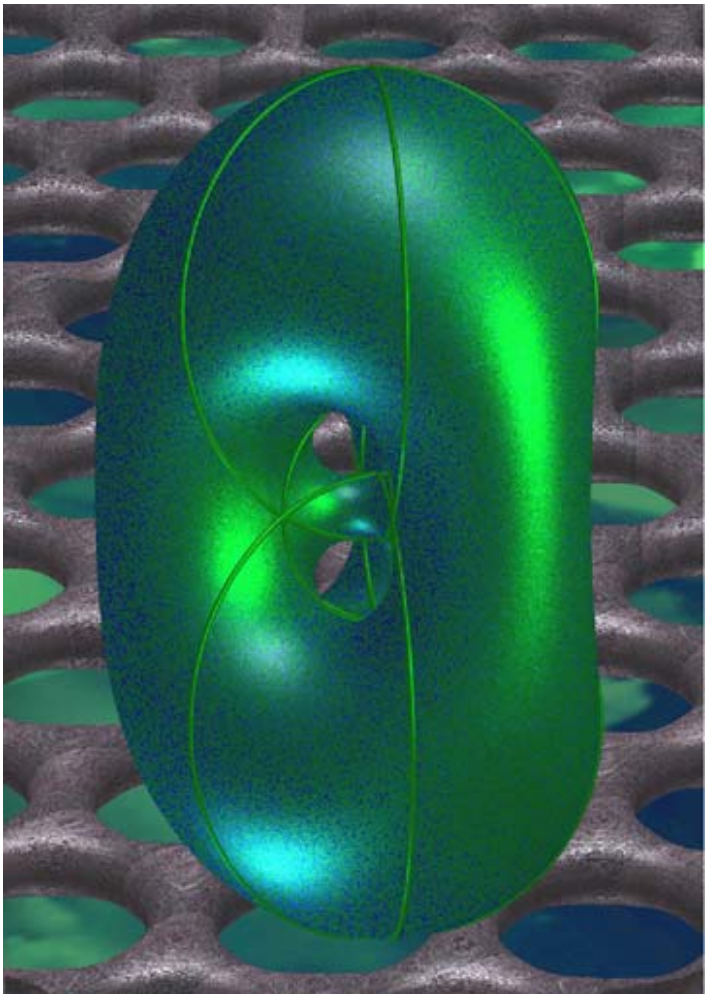

FIGURE 5.5. Lawson's compact minimal surface $\xi_{2,2}$ in $\mathbb{S}^3$ (stereographically projected to $\mathbb{R}^3$) computed with discrete techniques. The symmetry lines on the surface are great circles in $\mathbb{S}^3$, they divide the surface into 18 fundamental quadrilaterals with 60 degree angles. The associated constant mean curvature patch can be reflected to the doubly periodic surface on a hexagonal grid which is shown in the background.

on the level of discrete harmonic maps, which – in contrast to discrete minimal surfaces – can be computed exactly with the methods of the previous section. This allows to conjugate any surface M_{i+1} (respectively discrete harmonic map F_i) computed with the minimization algorithm and avoids numerical difficulties in the conjugation of inaccurate minimal surfaces. Let us start with a definition of a discrete CMC surface.

Definition 132 *Let $M \in \mathfrak{T}(\mathbb{S}^3)$ be a discrete minimal surface and $F : M \to M$ the identity map, then the image of the conjugate map $F^* : M \to M^*$, $M^* \subset \mathbb{R}^3$ defined by Definition 135 is called a* discrete constant mean curvature surface.

Remark 133 *This definition does not solely use a discrete version of the variational characterization of* CMC *surfaces, instead it characterizes discrete* CMC *surfaces by the discrete solution of their corresponding minimal surface problem in $\mathbb{S}^3$ together with a discrete version of Lemma 117.*

With this approach our definition of a discrete CMC *surface lies inbetween a variational characterization of a discrete* CMC *surface in Chapter 6 which poses a condition at every vertex, and an algorithmic definition of discrete* CMC *surfaces by Hoffmann [60] who discretizes the Dorfmeister-Pedit-Wu method.*

When trying to simulate the differentiable conjugation process as described by Lemma 117 several problems occur. Some of these problems can be solved using ideas from Pinkall and Polthier [88] for computing the dual of a Euclidean harmonic map while some others need special considerations of the Lie group structure of $\mathbb{S}^3$.

Let us start with the conjugation of a single atomic map

$$f : \triangle^N \to \triangle^M$$

between two triangles $\triangle^N \subset N$ and $\triangle^M \subset M$, $N, M \in \mathfrak{T}(\mathbb{S}^3)$. According to the definition of the C^1 conjugation in Lemma 117 we will construct an equivalent of

$$f^{-1} * df$$

where f^{-1} is the left translation of the image and $*$ the Hodge star operator on the discrete level.

Instead of defining $*df$ on the whole triangle, we start with the definition of $*df$ at a vertex p of the triangle $\triangle^N$, see Figure 5.6. We use the projection operator

$$\pi_P : T_P\mathbb{R}^4 \to T_P\mathbb{S}^3$$

defined in Definition 5.6 which maps vectors onto the tangent space at $P := f(p)$ to define the dual 1-form $*df_p$ at the point p by

$$*df_p(w) := P^{-1} \cdot \pi_P(df_p J_{\Delta^N} w)$$

where J_{Δ^N} is the rotation by 90° in the domain triangle Δ^N.
In words, we rotate the vector w in Δ^N by 90°, map it to $\triangle^M$, project it onto $T_P\mathbb{S}^3$ and left-translate it to the identity of $\mathbb{S}^3$, i.e. take the representative vector in the Lie-algebra. The definition of $*df_p$ obviously depends on the base point p and we cannot hope to extend $*df_p$ in a sensible way to the whole triangle. But the following lemma shows that $*df_p$ is in some sense independent of the base point, namely if applied to vectors w orthogonal to an edge through p.

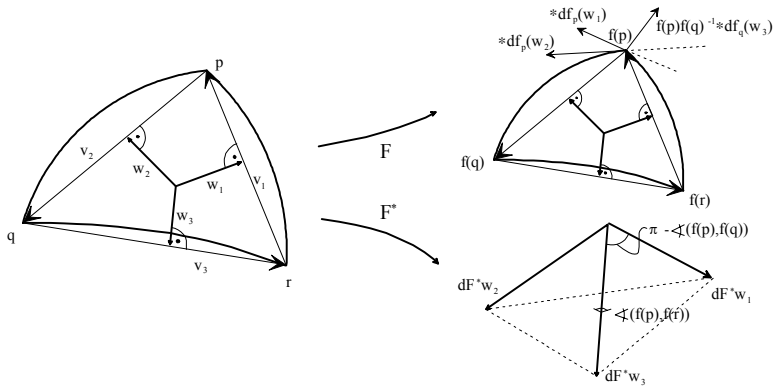

FIGURE 5.6. The dual 1-form $*dF$ is defined on the mid-perpendiculars in every triangle.

Lemma 134 *Let P and Q be two vertices of a triangle $\triangle^M$ joined in the domain by an edge v. Let $w \in T\triangle^N$ be a vector orthogonal to v, i.e. $J_{\Delta^N} w$ is parallel to v, then*

$$*df_q(w) = *df_p(w).$$

Proof. Since $\pi_Q(df_q J_{\Delta^N} w)$ points in the direction of the geodesic joining Q and P left translation by PQ^{-1} from $T_Q\mathbb{S}^3$ to $T_P\mathbb{S}^3$ will parallel translate $\pi_Q(df_q J_{\Delta^N} w)$ to $\pi_P(df_p J_{\Delta^N} w) \in T_P\mathbb{S}^3$. This proves the assertion. □

We could extend the definition of $*df_p$ to the whole triangle by linear extension but this would lead to ambiguities with $*df_q$ and $*df_r$ since

only the application of two of these 1-forms to vectors orthogonal to their common edge gives the same result. Instead we use a case distinction in the following basic definition of the discrete conjugation:

Definition 135 (Discrete Conjugation) *Let $F : N \to M$, $N, M \in \mathfrak{T}(\mathbb{S}^3)$ be a discrete harmonic map. Let $\triangle^N$ be a triangle in N and let v be an edge of Δ^N with endpoint p. Then the 1-form $*dF$ is defined on $T\triangle^N$ on vectors $w \in T\triangle^N$ orthogonal to the edge v by the action of the corresponding atomic dual 1-form. Let $f : \triangle^N \to \triangle^M$ be the corresponding atomic map then we define*

$$*dF(w) := *df_p(w) = P^{-1} \cdot \pi_P(df_p J_{\Delta^N} w). \tag{5.9}$$

In contrast to the Euclidean case of [88], where the dual 1−form of an atomic map could be defined as the smooth dual of the linear atomic map on the whole triangle, we must distinguish which base point we use for each triangle and therefore handle three cases. But we can proceed similar to the Euclidean case and show that our definition of $*dF$ gives a discrete 1−form which is continuous along certain paths and therefore can be integrated.

Lemma 136 *Let γ be the path around a vertex p on the discrete surface N consisting of the mid perpendiculars of the adjacent triangles (cf. Figure 5.7). Then the 1−form $*dF$ is continuous along γ.*

Proof. It is sufficient to prove continuity across a single edge. Let $w_1, w_2 \subset \gamma$ be the two mid perpendiculars corresponding to the edge v of the adjacent triangles Δ_1^N and Δ_2^N. Then a direct trigonometric calculation yields

$$\begin{aligned} w_1 &= \cot\alpha \cdot J_{\Delta_1^N} v \\ w_2 &= \cot\beta \cdot J_{\Delta_2^N} v. \end{aligned}$$

If we apply $*dF$ (in every triangle we apply the dual 1−forms $*df_p$ or $*df_q$ of the atomic map) then we obtain

$$\begin{aligned} *dF(w_1) &= P^{-1} \cdot \pi_P(df_p J_{\Delta_1^N} w_1) = -P^{-1} \cot\alpha \cdot \pi_P(df_p v) \\ *dF(w_2) &= P^{-1} \cdot \pi_P(df_p J_{\Delta_2^N} w_2) = -P^{-1} \cot\beta \cdot \pi_P(df_p v). \end{aligned}$$

Therefore $*dF$ is continuous along paths γ orthogonal to edges.□

The following theorem proves the closedness of $*dF$, consequently the dual graph obtained by integration of $*dF$ is a well-defined discrete surface.

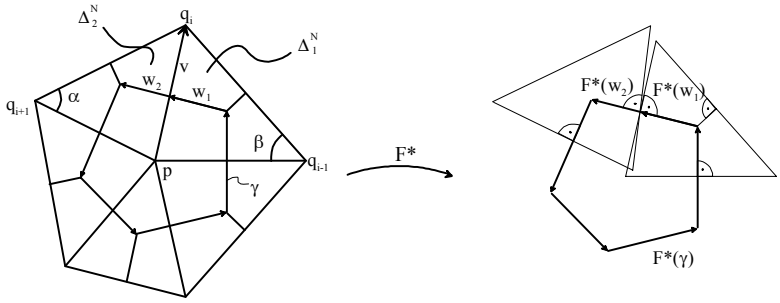

FIGURE 5.7. The dual map $F^* : N \to M^*$ is defined along certain paths γ orthogonal to edges. It associates to every vertex in N a dual cell in M^*.

Theorem 137 *Let $F : N \to M$, $N, M \in \mathfrak{T}(\mathbb{S}^3)$, be a discrete harmonic map into $\mathbb{S}^3$ then the differential $*dF$ is closed along the path on N consisting of the mid perpendiculars of all triangles of N and integrates to a discrete surface in $\mathbb{R}^3$ whose edge graph is dual to the triangulation of N.*

If M is a discrete minimal surface in $\mathbb{S}^3$ and $F : M \to M$ the identity map then the discrete conjugate surface $\int *dF$ is a discrete CMC *surface in $\mathbb{R}^3$.*

Proof. Consider Figure 5.7 and the piecewise linear closed path γ consisting of the mid perpendiculars adjacent to p. We integrate $*dF$ along γ:

$$\begin{aligned} \int_\gamma *dF &= P^{-1} \cdot \int \pi_P(df_p, J\gamma') \\ &= -P^{-1} \cdot \textstyle\sum_i (\cot\alpha_i + \cot\beta_i)\, \pi_P(Q_i - P) \\ &= 0. \end{aligned}$$

It turns out that the closedness condition for $*dF$ is identical to the harmonicity condition (5.7) for F, therefore for discrete harmonic maps Definition 135 defines a continuous closed differential. □

Remark 138 *In practice, we triangulate the obtained dual graph of the Euclidean* CMC *surface by defining an additional center vertex in each cell. Otherwise the continuation of the graph to the interior of the cells would be ambiguous and lead to problems during visualization.*

The following corollary shows the extreme discrete situations in which our algorithm is still applicable, compare also the experiments with

the O,C-TO surface where seven triangles suffice for a successful application of the algorithm.

Corollary 139 *Platonic solids with triangular faces and normalized so that the vertices lie on a great $\mathbb{S}^2$ are discrete minimal surfaces in $\mathbb{S}^3$. Applying our algorithm to these surfaces leads to discrete* CMC *surfaces in $\mathbb{R}^3$ which are the dual Platonic solids (i.e. discrete spheres).*

For example, the algorithm conjugates an octahedron (a discrete minimal surface in $\mathbb{S}^3$) to a cube (a discrete CMC *surface in $\mathbb{R}^3$).*

5.5 Conjugate Surface Construction in $\mathbb{S}^3$

In this section we combine the methods we have developed in the previous sections to the conjugate surface construction which allows us to solve free boundary values problems for CMC surfaces in $\mathbb{R}^3$. We will only state the main facts without proofs since the arguments are of technical nature.

Symmetry properties of CMC surfaces are fundamental for the construction, therefore let us start with the following definition:

Definition 140 *Let M^* be a* CMC *surface with boundary segment δ^*. δ^* is called a* planar symmetry line *if it is a curve lying in a plane P and if M^* can be extended as a* CMC *surface by reflection in P.*

Let P be a (not necessarily convex) polyhedron whose boundary is a collection of planes $\partial P = \{p_i\}$. We want to construct a CMC disk-type patch M^* with free boundary $\Gamma^* = \bigcup \gamma_i^* \subset \bigcup p_j \subset \partial P$ where each arc γ_i^* is a planar symmetry line lying on some p_j. Suppose, there exists a solution M^* with boundary Γ^*, then by Lemma 117 there exists a unique conjugate minimal surface $M \subset \mathbb{S}^3$ with polygonal boundary $\Gamma = \{\gamma_i\}$ where all γ_i are arcs of great circles in $\mathbb{S}^3$ and vice versa (compare Remark 115). This correspondence can be used for a constructive approach, the conjugate surface construction whose basic steps are:

(1) Determine the spherical contour Γ from the original boundary configuration ∂P of M^*.

(2) Compute the corresponding minimal surface $M \subset \mathbb{S}^3$ with boundary Γ.

(3) Conjugate M to a CMC surface $M^* \subset \mathbb{R}^3$.

For determining the contour Γ we need information about ∂P and the boundary curve of the wanted surface [67]. The dihedral angles of adjacent planes p_i, p_{i+1} determine the vertex angles of Γ, see Remark 115, the total rotation of the normal along the boundary curve γ_i^* connecting two vertices is equal to the total rotation of the normal along the corresponding geodesic arc γ_i w.r.t. a left-parallel vector field. Therefore Γ is determined up to the lengths of the boundary arcs $|\gamma_i| = |\gamma_i^*|$. This leaves us with $n-3$ free parameters where n is the number of boundary segments $\{\gamma_i^*\}$ resp. planes in ∂P. Wrong choices of the $n-3$ parameters lead after conjugation to a CMC patch $\widetilde{M^*}$ which is bounded by a set of planes parallel to those of ∂P and not identical to them – the so-called period problem (cf. Figure 5.9). To find the correct values for the parameters the construction can be executed repeatedly using a root finding algorithm.
Assume we have constructed the polygonal contour $\Gamma \subset \mathbb{S}^3$. It is a collection of arcs of spherical geodesics – each arc is part of a great circle. For the accuracy of the discrete conjugate surface construction it is essential to have an *exact* relationship of the boundary data of the numerically computed minimal surface in $\mathbb{S}^3$ with the corresponding data on the final conjugate discrete CMC surface in $\mathbb{R}^3$. The following theorem shows that already the intermediate discrete harmonic maps of the minimization algorithm lead to conjugate discrete surfaces in $\mathbb{R}^3$ which fulfil the boundary properties of the wanted CMC surface exactly – this is one of the most important results of our discrete definitions:

Theorem 141 *Let $\Gamma \subset \mathbb{S}^3$ be an n-sided polygonal boundary contour and $f : N \to M$, $N, M \in \mathfrak{T}(\mathbb{S}^3)$, a discrete harmonic map with the vertices of ∂N and ∂M lying on Γ. If Γ has vertex angles $\{\alpha_i\}_{i\in[1,n]}$ and normal rotation angles $\{\mu_i\}_{i\in[1,n]}$ (compared to a left-parallel vector field), then the conjugate discrete surface M^* has the following properties:*

(1) M^* has the same vertex angles α_i as M at the corresponding boundary vertices.

(2) The total rotation of the normal along the boundary arc γ_i^* of M^* is μ_i.

(3) The boundary arcs of M conjugate exactly to planar symmetry curves of M^* (this allows to extend M^* by reflection).

Remark 142 *Statements about the length of the conjugate boundary curve can only be made in the limit when the discretization approaches zero, then corresponding lengths are identical.*

FIGURE 5.8. Two corresponding isometric fundamental patches for the conjugate surface construction. The picture on the left shows the polygonal contour in $\mathbb{S}^3$ bounding a minimal patch (stereographically projected to $\mathbb{R}^3$), the one on the right the conjugated CMC patch in $\mathbb{R}^3$. It can be extended by reflection at the planar boundaries to a complete CMC surface in $\mathbb{R}^3$, the CMC surface shown in figure 6.2.

Now we can combine our methods from Sections 5.3 and 5.4 to a numerical algorithm, the *discrete conjugate surface construction*. Compare with the Algorithm 104 for minimal surfaces in $\mathbb{R}^3$:

Problem 143 *For a given (not necessarily convex) polyhedron P solve the free boundary value problem for a* CMC *surface in $\mathbb{R}^3$ with n boundary components $\Gamma^* = \{\gamma_i^*\} \subset \partial P$.*

Algorithm 144 (Discrete Conjugate Surface Construction)

(1) Using Equations (5.1) and (5.2) replace the free boundary value problem by a Dirichlet boundary value problem for a minimal surface in $\mathbb{S}^3$ with boundary Γ. Extract from ∂P the information to determine the boundary Γ as a collection of spherical arcs $\{\gamma_i\}$ (up to $n-3$ parameters).

(2) Make a choice for the $n-3$ missing parameters.

(3) Apply the minimization algorithm from Section 5.3 to obtain a sequence of discrete harmonic maps $\{F_i : M_i \to M_{i+1}\}$ such that $\{M_i\}$ converges to a discrete minimal surface $M \subset \mathbb{S}^3$. Since the algorithm stops after some finite number of iterations we obtain a discrete harmonic map $F_n : M_n \to M_{n+1}$ (M_{n+1} should be interpreted as an approximation of the discrete minimal surface M).

(4) Using Theorem 137 compute the discrete conjugate harmonic map $F_n^* : M_n \to M_{n+1}^* \subset \mathbb{R}^3$ where M_{n+1}^* is a discrete approximation of the discrete CMC surface. By Theorem 141 M_{n+1}^* fulfils boundary conditions $\partial\widetilde{P}$ which are identical to the required boundary conditions ∂P of the problem up to parallel displacement of the boundary planes.

(5) If $|\partial P - \partial\widetilde{P}| > \epsilon$ in some norm, start again with step (2) and a different guess for the $n-3$ parameters (in practice a root finding algorithm is used for the subsequent choices of these free parameters). Otherwise stop with a discrete CMC surface M^*.

Remark 145 *A major advantage of our algorithm is the fact, that we have defined the conjugation step (4) for the intermediate discrete harmonic maps and not only for the minimal surface M obtained in the limit in (3) since usually M cannot be computed exactly. Instead, the harmonic maps can be computed* exactly*, and therefore the conjugation algorithm for discrete harmonic maps does not accumulate errors.*

For implementation issues we refer to the original work [86] which also contains experimental results for certain triply periodic CMC surfaces. Applications of this algorithm to the computation of compact CMC surfaces of low genus are described in [52] [50] [51].

5.6 Solving Period Problems

In this section we discuss the solution of the period problem of discrete CMC surfaces, and especially the influence of the discretization and the number of iterations.

As an example we use the CMC companion of A. Schoen's Euclidean minimal surface O,C-TO which has one period to close. Its fundamental patch for the symmetry group is bounded by five symmetry arcs leading to a Plateau problem in $\mathbb{S}^3$ with five geodesic boundary arcs, see Figures 5.8 and 5.9. We consider a sequence of three key-frames, the parameter called "time" controls the size of the handles growing at the centers of the six cubical faces, compare Figures 5.9 and 5.10. To solve the period problem one has to find the time value at which the distance of the handle to the existing symmetry plane formed by the outer boundary arcs becomes zero (if the top of the handle is below the existing symmetry plane the period is negative, if it lies in the existing symmetry plane it is zero, otherwise it is positive). Since

FIGURE 5.9. The three surfaces explain the period problem and graphically show the size of the period values in comparison with the size of the surface. The surfaces are the key-frames at times 0.0, 0.5 and 1.0 in the one-parameter family and correspond to the discretization with 291 triangles per fundamental patch in tables 1 and 2.

the fundamental patch has a second free parameter we get a family of CMC O,C-TO surfaces with varying mean curvature (after rescaling), see Figure 5.11.

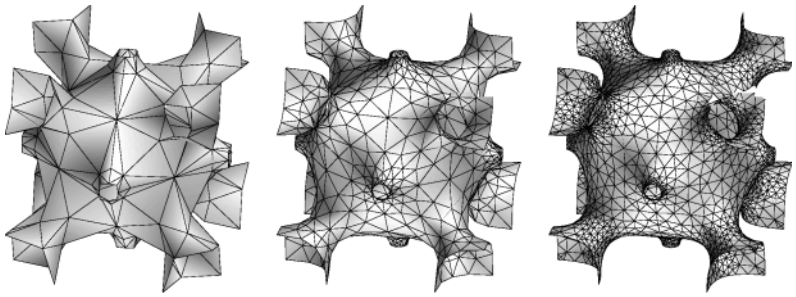

FIGURE 5.10. Discrete CMC versions of A. Schoen's O,C-T surface with 7, 31 and 105 triangles per fundamental patch, the complete cell in a cube consists of 48 fundamental patches. For topological (not numerical) reasons less than 7 triangles seem to be impossible. The algorithm solves a C^1 problem for piecewise linear numerical data, and it is a great advantage of the discrete techniques that such coarse triangulations suffice.

The discrete conjugation algorithm allows us to work with very coarse triangulations to handle the C^1 problem of conjugation (cf. Corollary 139). During the minimization process there appears a degeneracy problem similar to the following example: when approximating a planar circular segment with a polygon, the polygon underestimates the length of the circular segment. When the polygon length is minimized the interior vertices of the polygon tend to move to the fixed end points, leading to a straight line in the limit. This kind of behaviour occurs during minimization in $\mathbb{S}^3$ on those surface parts with non-negative Gaussian curvature, i.e. spherical or cylindrical parts. If

the surface is in principle stable, interactive local refinement depending on curvature terms can be used to eliminate these problems (at least for computing discrete harmonic maps). It should be mentioned that we use several methods to obtain smoother triangulations. This leads to very good initial triangulations for the minimization.

It turns out that the numerical minimization algorithm converges rapidly during the first steps of the iteration and then slows down (after some steps the surface vertices merely move tangential to minimize energy). Already the first iterates may be conjugated to give qualitatively and quantitatively good discrete CMC surfaces. Surely, the area of the spherical patch depends on the triangulation because we approximate with Euclidean triangles. But it turns out that the period depends very little on the discretization. The resulting surface in Figure 5.10 is qualitatively correct even for the coarsest example.

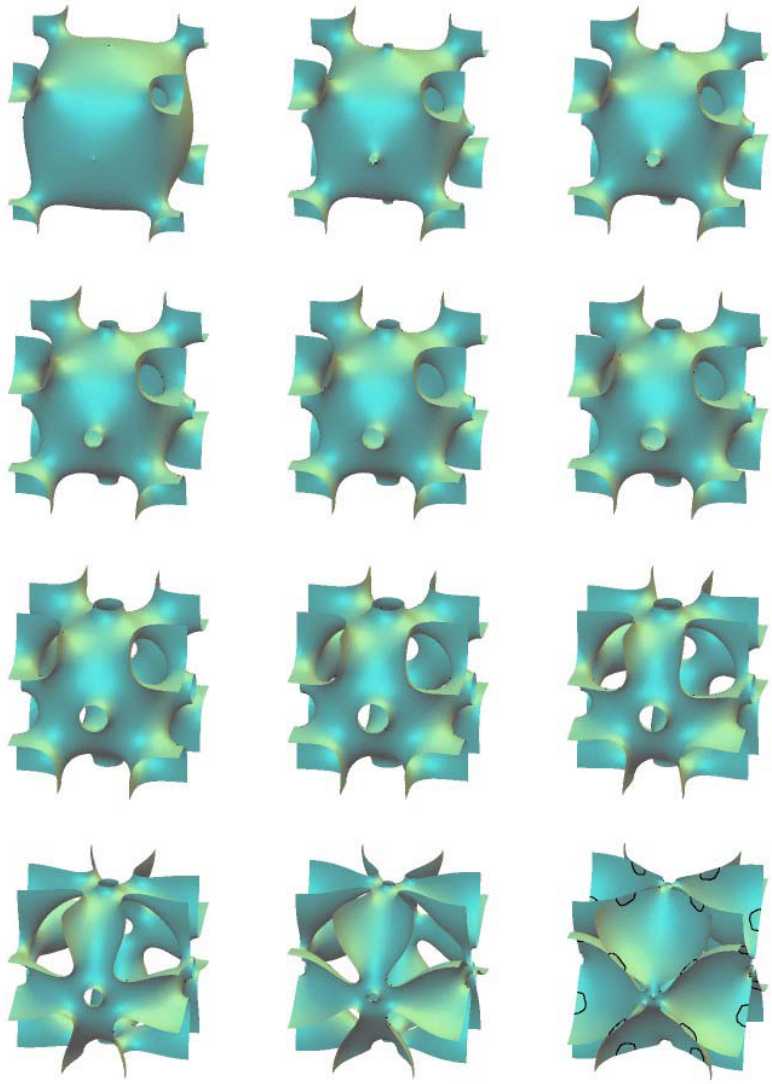

FIGURE 5.11. Discrete constant mean curvature companions of A. Schoen's O,C-TO minimal surface. The surface has two free parameters, one controls the distance (which is zero for this sequence) from the top of the handles at the centers of the cubical faces to the outer symmetry planes. The remaining parameter controls – after rescaling the surfaces – the mean curvature. At both ends of the sequence it is almost one. The O,C-TO minimal surface with zero mean curvature would be in the middle.

6

Second Variation of Discrete CMC Surfaces

Discrete CMC surfaces have both interesting differences from and similarities with smooth ones. For example, they are different in that smooth minimal graphs in $\mathbb{R}^3$ over a bounded domain are stable, whereas discrete minimal graphs can be highly unstable. We will explore properties like this in Section 6.1.

Discrete surfaces have finite dimensional spaces of admissible variations, therefore the study of linear differential operators on the variation spaces reduces to the linear algebra of matrices. This advantage over smooth surfaces with their infinite dimensional variation spaces makes linear operators easier to handle in the discrete case.

This suggests that a useful procedure for studying the spectra of the linear Jacobi operator in the second variation formula of smooth CMC surfaces is to consider the corresponding spectra of discrete CMC approximating surfaces. Although similar to the finite element method in numerical analysis, here the finite element approximations will have geometric and variational meaning in their own right.

As an example, consider how one finds the index (the number of negative points in the spectrum) of a smooth minimal surface. The standard approach is to replace the metric of the surface with the metric obtained by pulling back the spherical metric via the Gauss map. This approach can yield the index: for example, the indexes of a complete catenoid and a complete Enneper surface are 1 ([43]), the

index of a complete Jorge-Meeks n-noid is $2n-3$ ([83], [80]) and the index of a complete genus k Costa-Hoffman-Meeks surface is $2k+3$ for every $k \leq 37$ ([85], [84]). However, this approach does not yield the eigenvalues and eigenfunctions on compact portions of the original minimal surfaces, as the metric has been changed. It would be interesting to know the eigenfunctions associated to negative eigenvalues since these represent the directions of variations that reduce area. The above procedure of approximating by discrete surfaces can provide this information.

In Sections 6.3 and 6.4 we establish some tools for studying the spectrum of discrete CMC surfaces. Then we test the above procedure on two standard cases – a (minimal) rectangle, and a portion of a smooth minimal catenoid bounded by two circles. In these two cases we know the spectra of the smooth surfaces (Section 6.2), and we know the discrete minimal surfaces as well (Chapter 4), so we can check that the above procedure produces good approximations for the eigenvalues and smooth eigenfunctions (Section 6.5), which indeed must be the case, by the theory of the finite element method [21], [44]. With these successful tests, in Section 6.5 we go on to consider cases where we do not apriori know what the smooth eigenfunctions should be, such as the Jorge-Meeks $3-$noid and the genus 1 Costa surface.

We note that the above procedure can also be implemented using discrete approximating surfaces which are found only numerically and not explicitly, such as surfaces found by the method in [88]. And in fact, we use this method to find approximating surfaces for the $3-$noid and Enneper surface and Costa surface.

We note also that Ken Brakke's surface evolver software [19] is an efficient tool for numerical index calculations using the same discrete Ansatz. Our main emphasis here is to provide explicit formulations for the discrete Jacobi operator and other geometric properties of discrete surfaces.

6.1 Non-Uniqueness of Discrete Minimal Disks

Uniqueness of a bounded minimal surface with a given boundary ensures that it is stable. For smooth minimal surfaces, uniqueness can sometimes be decided using the maximum principle of elliptic equations, which ensures that the minimal surface is contained in the convex hull of its boundary, and, if the boundary has a $1-1$ projection to a convex planar curve, then it is unique for that boundary and is a minimal graph. The maximum principle also shows that any

minimal graph is unique even when the projection of its boundary is not convex. More generally, stability still holds when the surface merely has a Gauß map image contained in a hemisphere, as shown in [9] (although their proof employs tools other than the maximum principle).

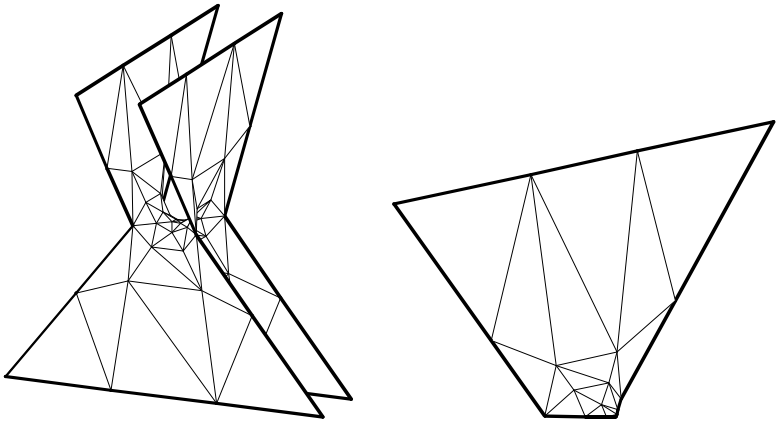

FIGURE 6.1. The left figure is unstable, even though it is locally a graph over a horizontal plane in the sense that the third coordinate of the normal vector to the surface is never zero. The right figure is one of the four congruent pieces of the first figure which are all stable.

However, such statements do not hold for discrete minimal surfaces. Consider the minimal surface shown in the margin figure in Section 4.4 whose height function has a local maximum at an interior vertex. This example does not lie in the convex hull of its boundary and thereby disproves the general existence of a discrete version of the maximum principle. Also, the three surfaces in Figure 6.2 are all minimal graphs over an annular domain with the same boundary contours and the same simplicial structure, and yet they are not the same surfaces, hence graphs with given simplicial structure are not unique. And the left-hand surface in Figure 6.1 is a surface whose Gauß map is contained in a hemisphere but which is unstable (this surface is not a graph) – another example of this property is the first annular surface in Figure 6.1, which is also unstable. (We define stability of discrete CMC surfaces in Section 6.3).

The influence of the discretization on nonuniqueness, like as in the annular examples of Figure 6.2, can also be observed in a more trivial way for a discrete minimal graph over a simply connected convex domain. The two surfaces in Figure 6.3 have the same trace, i.e. they

are identical as geometric surfaces, but they are different as discrete surfaces. Interior vertices may be freely added and moved inside the middle planar square without affecting minimality. We also note the following:

Remark 146 *If M_h is a discrete minimal surface that contains a simply-connected discrete subsurface M_h' that lies in a plane, then it follows easily from Equation 4.3 that the discrete minimality of M_h is independent of the choice of triangulation of the trace of M_h'.*

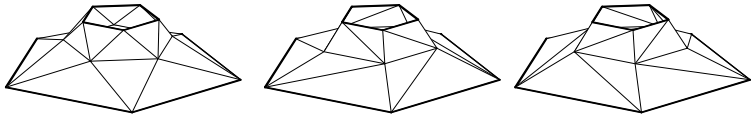

FIGURE 6.2. The leftmost annular graph is unstable, even though it is a graph over an annular polygonal region in a horizontal plane; it has area-reducing variations that can deform to either of the other two stable minimal surfaces on the right, which have the same simplicial structure.

In contrast to existence of these counterexamples we believe that some properties of smooth minimal surfaces remain true in the discrete setting. We say that a discrete surface is a disk if it is homeomorphic to a simply connected domain.

Conjecture 147 *Let $M_h \subset \mathbb{R}^3$ be a discrete minimal disk whose boundary projects injectively to a convex planar polygonal curve, then M_h is a graph over that plane.*

We were able to prove this conjecture with the extra assumption that all the triangles of the surface are acute, using the fact that the maximum principle (a height function cannot attain a strict interior maximum) actually does hold when all triangles are acute.

One can ask if a discrete minimal surface M_h with given simplicial structure and boundary is unique if it has a $1-1$ perpendicular or central projection to a convex polygonal domain in a plane. The placement of the vertices need not be unique, as we saw in Remark 146, however, one can consider if there is uniqueness in the sense that the trace of M_h in $\mathbb{R}^3$ is unique:

Conjecture 148 *Let $\Gamma \subset \mathbb{R}^3$ be a polygonal curve that either $\mathcal{A}$: projects injectively to a convex planar polygonal curve, or $\mathcal{B}$: has a 1-1 central projection from a point $p \in \mathbb{R}^3$ to a convex planar polygonal curve. Let K be a given abstract simplicial disk, and let $\gamma : \partial K \to \Gamma$ be*

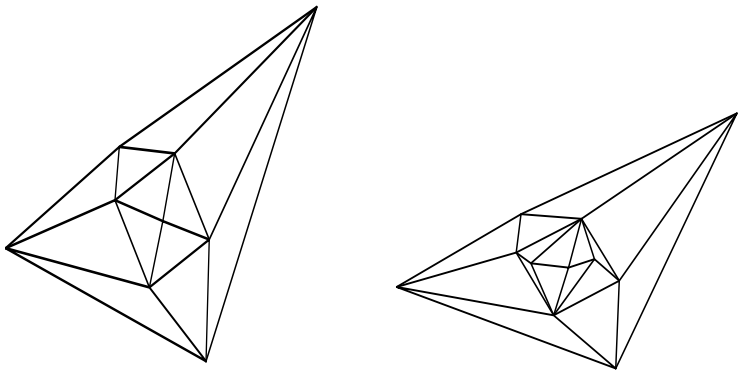

FIGURE 6.3. Two minimal meshes having the same geometric shape.

a given piecewise linear map. If M_h is a discrete minimal surface that is a geometric realization of K so that the map $\partial K \to \partial M_h$ equals γ, then the trace of M_h in $\mathbb{R}^3$ is uniquely determined. Furthermore, M_h is a graph in the case $\mathcal{A}$, and M_h is contained in the cone of Γ over p in the case $\mathcal{B}$.

We have the following weaker form of Conjecture 148, which follows from Corollary 155 of Section 6.3 in the case that there is only one interior vertex:

Conjecture 149 *If a discrete minimal surface is a graph over a convex polygonal domain, then it is stable.*

6.2 Jacobi Operator for Smooth CMC Surfaces

We now begin the study of the spectra of the second variation of CMC surfaces, and in this section we consider smooth surfaces. In particular, here we explicitly determine the eigenvalues and eigenfunctions of the Jacobi operator for portions of smooth catenoids, which will have applications to Section 6.5. Also, here we state the well-known connection between the second variation and the Jacobi operator in the smooth case, which motivates the computations we do for the discrete case in Sections 6.3 and 6.4.

Let $\Phi : M \to \mathbb{R}^3$ be an immersion of a compact 2-dimensional surface M. Let $\vec{N}$ be a unit normal vector field on $\Phi(M)$. Let $\Phi(t)$ be a smooth variation of immersions for $t \in (-\epsilon, \epsilon)$ so that $\Phi(0) = \Phi$ and

$\Phi(t)|_{\partial M} = \Phi(0)|_{\partial M}$ for all $t \in (-\epsilon, \epsilon)$. Let $\vec{\mathcal{U}}(t)$ be the variation vector field on $\Phi(t)$. We can assume, by reparametrizing $\Phi(t)$ for nonzero t if necessary, that the corresponding variation vector field at $t = 0$ is $\vec{\mathcal{U}}(0) = u\vec{N}$, with $u \in C^\infty(M)$ and $u|_{\partial M} = 0$. Let $a(t)$ be the area of $\Phi(t)(M)$ and H be the mean curvature of $\Phi(M)$. The first variational formula is

$$a'(0) := \frac{d}{dt}a(t)\bigg|_{t=0} = -\int_M \langle nH\vec{N}, u\vec{N}\rangle dA,$$

where $\langle , \rangle$ and dA are the metric and area form on M induced by the immersion Φ. We now assume H is constant, so $a'(0) = -nH\int_M u dA$. Let $V(t)$ be the volume of $\Phi(t)(M)$, then $V'(0) = \int_M u dA$. The variation is *volume preserving* if $\int_M \langle \vec{\mathcal{U}}(t), \vec{N}(t)\rangle dA(t) = 0$ for all $t \in (-\epsilon, \epsilon)$. In particular, $\int_M u dA = 0$ when $t = 0$, so $a'(0) = 0$ and $\Phi(M)$ is critical for area amongst all volume preserving variations.

The second variation formula for volume preserving variations $\Phi(t)$ is

$$a''(0) := \frac{d^2}{dt^2}a(t)\bigg|_{t=0} = \int_M \{|\nabla u|^2 - (4H^2 - 2K)u^2\}dA = \int_M uLudA,$$

where K is the Gaussian curvature on M induced by Φ, and

$$L = -\triangle - 4H^2 + 2K \tag{6.1}$$

is the Jacobi operator with Laplace-Beltrami operator $\triangle$.

There are two ways that the index of a smooth CMC surface can be defined: the geometric definition for $\operatorname{ind} M = \operatorname{ind}\Phi(M)$ is the maximum possible dimension of a subspace $\mathcal{S}$ of volume-preserving variation functions $u \in C_0^\infty(M)$ for which $a''(0) < 0$ for all nonzero $u \in \mathcal{S}$. The analytic definition for $\operatorname{ind}_U M$ is the number of negative eigenvalues of the operator L, which equals the maximum possible dimension of a subspace $\mathcal{S}_U$ of (not necessarily volume-preserving) variation functions $u \in C_0^\infty(M)$ for which $\int_M uLudA < 0$ for all nonzero $u \in \mathcal{S}_U$. The subscript U stands for "U-nconstrained index". We have $\operatorname{ind}_U M \geq \operatorname{ind} M \geq \operatorname{ind}_U M - 1$, see [30]. As it is geometrically more natural, we want to compute $\operatorname{ind} M$. But $\operatorname{ind}_U M$ is more accessible to computation than $\operatorname{ind} M$, and they differ only by at most 1.

In the case that we are considering minimal surfaces, as in Section 6.5, the volume constraint is not necessary, and hence $\operatorname{ind} M = \operatorname{ind}_U M$.

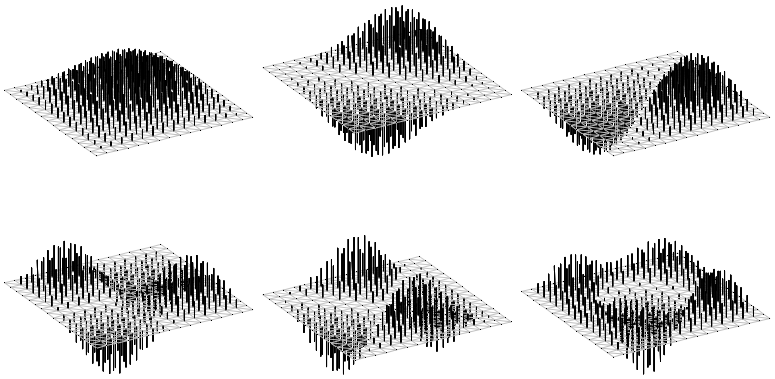

FIGURE 6.4. The eigenvectors of the discrete square with $n = 15$ associated to the first six positive eigenvalues described in section 7.1. Note that these eigenvectors closely resemble linear combinations of eigenfunctions of the Laplacian on the smooth square in section 4.1, for example the first two resemble $\sin(x)\sin(y)$ and $\sin(x)\sin(2y) - \sin(2x)\sin(y)$ and the last resembles $\sin(3x)\sin(y) + \sin(x)\sin(3y)$.

Eigenvectors of L for Rectangles

Consider the minimal rectangle

$$M = \{(x, y, 0) \in \mathbb{R}^3 \,|\, 0 \leq x \leq x_0, 0 \leq y \leq y_0\}$$

with natural coordinates $(x, y) \in \mathbb{R}^2$, and consider functions on M with Dirichlet boundary conditions. Then $L = -\triangle$ with eigenvalues and eigenfunctions

$$\lambda_{m,n} = \frac{m^2\pi^2}{x_0^2} + \frac{n^2\pi^2}{y_0^2}, \quad \phi_{m,n} = \frac{2}{\sqrt{x_0 y_0}} \sin\frac{m\pi x}{x_0} \sin\frac{n\pi y}{y_0}$$

for $(m, n) \in \mathbb{Z}^+ \times \mathbb{Z}^+$. Hence $\operatorname{ind} M = 0$.

Eigenvectors of L for Catenoids

The catenoid is given as a conformal map

$$\Phi : (x, y) \in \Omega \to (\cos x \cosh y, \sin x \cosh y, y) \in \mathbb{R}^3,$$

with $\Omega = S^1 \times [y_0, y_1]$. The metric, the Laplace-Beltrami operator and the Gauss curvature are given by

$$ds^2 = \cosh^2 y \cdot (dx^2 + dy^2), \quad \triangle = \frac{\frac{\partial^2}{\partial^2 x} + \frac{\partial^2}{\partial^2 y}}{\cosh^2(y)}, \quad K = -\cosh^{-4} y.$$

We put Dirichlet boundary conditions on the two boundary curves of Ω.

Lemma 150 *The catenoid Φ has an L^2-basis of eigenfunctions for its Jacobi operator $L = -\triangle + 2K$ of the form*

$$\phi_m = \sin(mx)f(y) \quad or \quad \phi_m = \cos(mx)f(y)$$

for $m \in \mathbb{N} \cup \{0\}$. The function f is a solution of the 2nd-order ordinary differential equation

$$f_{yy} = (m^2 - \lambda \cosh^2 y - 2\cosh^{-2} y)f, \tag{6.2}$$

with eigenvalue $\lambda \in \mathbb{R}$ of L and Dirichlet boundary conditions $f(y_0) = f(y_1) = 0$.
Therefore, the eigenvalues λ and eigenfunctions of L are determined by the solutions of Equation 6.2 with $f(y_0) = f(y_1) = 0$.

Proof. It is well known that L, with respect to the Dirichlet boundary condition, has a discrete spectrum in $\mathbb{R}$, and that, for all $\lambda \in \mathbb{R}$, $\ker(L - \lambda)$ is a finite dimensional space of smooth functions. Furthermore, an orthonormal basis of the L^2 space over Ω (with respect to ds^2) can be obtained as a set of smooth eigenfunctions of L satisfying the Dirichlet boundary condition.
Define the symmetric operator $D = i\frac{\partial}{\partial x}$. To see that D is symmetric, for functions u and v that are 2π-periodic in x we have

$$\langle \frac{\partial}{\partial x}u, v\rangle_{L^2} + \langle u, \frac{\partial}{\partial x}v\rangle_{L^2} = \int_\Omega (u_x\overline{v} + u\overline{v}_x)\cosh^2 y dxdy = 0,$$

which implies that the operator $\frac{\partial}{\partial x}$ is skew symmetric, and so D is symmetric.
Note that $DL = LD$, so $D : \ker(L - \lambda) \to \ker(L - \lambda)$. Since D is symmetric, it has a basis of eigenfunctions in each finite dimensional space $\ker(L - \lambda)$. So we can choose a set of functions that is simultaneously an L^2-basis of eigenfunctions for both D and L. Since the eigenfunctions of D must be of the form $e^{mxi}f(y)$ with $m \in \mathbb{Z}$, the first part of the lemma follows.
Applying L to an eigenfunction $\phi_m = \sin(mx)f(y)$ we obtain

$$\begin{aligned} L(\phi_m) &= \frac{m^2\sin(mx)f(y)}{\cosh^2 y} - \frac{\sin(mx)f_{yy}(y)}{\cosh^2 y} - \frac{2\sin(mx)f(y)}{\cosh^4 y} \\ &= \lambda \sin(mx)f(y) \end{aligned}$$

and a similar computation holds for an eigenfunction $\cos(mx)f(y)$. Hence f satisfies Equation 6.2. $\square$

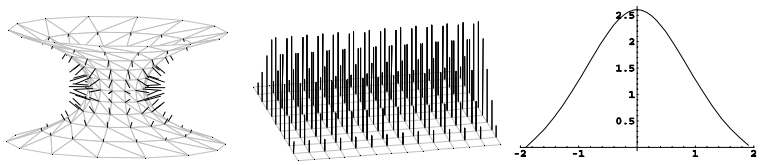

FIGURE 6.5. On the left is the eigenvector associated to the negative eigenvalue $\lambda_0 \approx -0.542$ of an unstable discrete catenoid. In the middle we have also shown this $\mathbb{R}^{3n}$-vector field on the domain grid (where each $\mathbb{R}^3$-vector is vertical with length equal to that of the corresponding $\mathbb{R}^3$-vector in the $\mathbb{R}^{3n}$-eigenvector field on the discrete catenoid), to show the close resemblance to the eigenfunction on the right for the smooth case. The function $f(y)$ (computed numerically) on the right is the eigenfunction when $m = 0$ for the catenoid $\Phi(\mathcal{R})$ in Section 4 with $y_1 = -y_0 = 1.91$. The corresponding eigenvalue is $\lambda \approx -0.54$, and all other eigenvalues are positive.

6.3 Second Variation of Area

We now consider the spectra of the second variation for discrete CMC surfaces $M_h(t)$ as in Definition 79, and start with a reminder on stability.

Definition 151 *A discrete minimal or* CMC *surface M_h is* stable *if* $\text{area}''(0) \geq 0$ *for any permissible, that means, volume preserving and boundary fixing variation.*

We begin with a technical and explicit computation of the second variation in this section.

Lemma 152 *For a compact discrete* CMC *H surface M_h with vertex set $\mathcal{V}$,*

$$\frac{d^2}{d^2t}\,\text{area}\,M_h\Big|_{t=0} = \sum_{p\in\mathcal{V}} \langle p', (\nabla_p\,\text{area})' - H(\nabla_p\,\text{vol})'\rangle$$

for any permissible variation.

Proof. Differentiating Equation 4.4 and using Definition 113, we have

$$\text{area}''(0) = \sum_{p\in\mathcal{V}} \langle p'', H\nabla_p\,\text{vol}\rangle + \sum_{p\in\mathcal{V}} \langle p', (\nabla_p\,\text{area})'\rangle.$$

For a minimal discrete surface, the first term on the right hand side vanishes. For a discrete CMC surface with $H \neq 0$, the variation $p(t)$

is volume preserving for all t, so by Equation 4.6 we have

$$\sum_{p\in\mathcal{V}}\langle p', \nabla_p \operatorname{vol}\rangle = 0 \;\forall t \Longrightarrow \sum_{p\in\mathcal{V}}\langle p'', \nabla_p \operatorname{vol}\rangle + \langle p', (\nabla_p \operatorname{vol})'\rangle = 0,$$

which proves the lemma. □

For any permissible variation as in Equation 4.1 with $\vec{v} \in \mathbb{R}^{3n}$ as in Equation 4.2, the second variation $\operatorname{area}''(0)$ is a bilinear form which can be represented by a symmetric $3n \times 3n$ matrix Q, so that $\vec{v}^t Q \vec{v}$ equals $\operatorname{area}''(0)$. We now decompose $\operatorname{area}''(0)$ into the sum of two terms

$$\begin{aligned} \vec{v}^t Q^a \vec{v} &: = \sum_{p\in\mathcal{V}}\langle v_p, (\nabla_p \operatorname{area})'\rangle \\ -H\vec{v}^t Q^V \vec{v} &: = -H\sum_{p\in\mathcal{V}}\langle v_p, (\nabla_p \operatorname{vol})'\rangle \end{aligned} \tag{6.3}$$

for any permissible variation with variation vector field $\vec{v}$. In the next two propositions we determine the components of the matrices Q^a and Q^V satisfying Equation 6.3, thus giving us the components of $Q = Q^a - HQ^V$.

Proposition 153 *The Hessian of the area function from S_h to $\mathbb{R}$ is a symmetric bilinear form with $3n \times 3n$ matrix representation Q^a, with respect to the basis $\{\psi_{p_j}\}$ of S_h. Q^a can be considered as an $n \times n$ grid with a 3×3 entry $Q^a_{i,j}$ for each pair of interior vertices $p_i, p_j \in \mathcal{V}_{int}$ of M_h, so that*

$$\vec{v}^t Q^a \vec{v} = \sum_{p\in\mathcal{V}}\langle v_p, (\nabla_p \operatorname{area})'\rangle$$

for the variation vector field $\vec{v}$ of any permissible variation. The entry $Q^a_{i,j}$ is 0 if the vertices p_i, p_j are not adjacent, and is

$$Q^a_{i,j} = \frac{1}{2}\sum_{\substack{T=(p_i,p_j,r)\in star(\overline{p_ip_j}),\\ \vec{e}_{ij}:=p_i-p_j}} \frac{\vec{e}_{ij}\cdot J^t(\vec{e}_{ij}) - J(\vec{e}_{ij})\cdot \vec{e}^t_{ij}}{|\vec{e}_{ij}|^2} - \cot\theta_T \vec{N}_T \cdot \vec{N}^t_T$$

for p_i and p_j adjacent and unequal, where θ_T is the interior angle of the triangle $T = (p_i, p_j, r)$ at r, and is

$$Q^a_{i,i} = \frac{1}{4}\sum_{T=(p_i,q,r)\in \operatorname{star}(p_i)} \frac{|r-q|^2}{\operatorname{area} T}\vec{N}_T\vec{N}^t_T$$

when the vertices are both equal to p_i. Here, $\vec{N}_T$ (or just $\vec{N}$) denotes the oriented unit normal vector of the triangle $T = (p, q, r)$.

Proof. For notating area and volume, we shall now frequently use "a" and "V" instead of area and vol, for brevity. We will also use $|T|$ or $|(p,q,r)|$ to signify the area of a triangle $T=(p,q,r)$. If $\vec{v}$ and $\vec{w}$ are variation vector fields for any pair of permissible variations, we can define a bilinear form

$$
\begin{aligned}
&Q^a(\vec{v},\vec{w}) := \\
&\frac{1}{2}\sum_{T\in M_h} -\langle v_p\times w_r - v_r\times w_p + v_q\times w_p - v_p\times w_q + v_r\times w_q - v_q\times w_r, \vec{N}\rangle \\
&\qquad + \frac{1}{2|T|}\langle v_p\times(r-q)+v_q\times(p-r)+v_r\times(q-p), \\
&\qquad\quad w_p\times(r-q)+w_q\times(p-r)+w_r\times(q-p)\rangle \\
&\qquad - \frac{1}{2|T|}\langle v_p\times(r-q)+v_q\times(p-r)+v_r\times(q-p),\vec{N}\rangle\cdot \\
&\qquad\qquad \langle w_p\times(r-q)+w_q\times(p-r)+w_r\times(q-p),\vec{N}\rangle.
\end{aligned}
$$

Using $\vec{N}' = \frac{(q-p)\times(r'-p')+(q'-p')\times(r-p)}{2|T|} - \frac{\vec{N}}{2|T|}\langle (q-p)\times(r'-p') + (q'-p')\times(r-p), \vec{N}\rangle$, it follows that $Q^a(\vec{v},\vec{v}) = \sum_{p\in\mathcal{V}}\langle v_p, (\nabla_p a)'\rangle$. Q^a is clearly bilinear, and the last two terms of Q^a are obviously symmetric in $\vec{v}$ and $\vec{w}$. The first term is also symmetric in $\vec{v}$ and $\vec{w}$, since $v_p\times w_r - v_r\times w_p = w_p\times v_r - w_r\times v_p$, $v_q\times w_p - v_p\times w_q = w_q\times v_p - w_p\times v_q$, and $v_r\times w_q - v_q\times w_r = w_r\times v_q - w_q\times v_r$.

It only remains to determine an explicit form for Q^a. For a given interior vertex p, suppose $\vec{v}$ and $\vec{w}$ are nonzero only at p, that is, that $\vec{v}^t = (0^t,...,0^t,v_p^t,0^t,...,0^t)$ and $\vec{w}^t = (0^t,...,0^t,w_p^t,0^t,...,0^t)$. Then using the notation $T=(p,q,r)$ in each triangle we have

$$
\begin{aligned}
&Q^a(\vec{v},\vec{w}) = Q^a_{pp}(v_p,w_p) = \\
&\qquad = \sum_{T\in\mathrm{star}(p)}\frac{1}{4|T|}(\langle v_p\times(r-q), w_p\times(r-q)\rangle - \\
&\qquad\qquad \langle v_p\times(r-q),\vec{N}\rangle\langle w_p\times(r-q),\vec{N}\rangle) \\
&= \sum_{T\in\mathrm{star}(p)}\frac{1}{4|T|}v_p^t(|r-q|^2 I - (r-q)(r-q)^t - ((r-q)\times\vec{N})((r-q)\times\vec{N})^t)w_p \\
&\qquad = \sum_{T\in\mathrm{star}(p)}\frac{|r-q|^2}{4|T|}v_p^t(\vec{N}\vec{N}^t)w_p\ ,
\end{aligned}
$$

hence Q^a_{pp} is of the form in the proposition.

Now suppose $\vec{v}^t = (0^t,...,0^t,v_p^t,0^t,...,0^t)$ and $\vec{w}^t = (0^t,...,0^t,w_q^t,0^t,...,0^t)$ for some given unequal interior vertices p and q. If p and q are not connected by some edge of the surface, then clearly $Q^a(\vec{v},\vec{w})=0$, so assume that p and q are adjacent. Note that $\mathrm{star}(\overline{pq})$ then contains two triangles (p,q,r_j) for $j=1,2$ and precisely one of them is properly oriented. Noting also that

the normal vector $\vec{N}$ of a triangle changes sign when the orientation of the triangle is reversed, we have the following equation:

$$Q^a(\vec{v},\vec{w}) = Q^a_{pq}(v_p, w_q) = \frac{1}{2}\sum_{T=(p,q,r_k),k=1,2} \langle v_p \times w_q, \vec{N}\rangle +$$

$$\frac{1}{2|T|}(\langle v_p \times (r_k - q), w_q \times (p - r_k)\rangle - \langle v_p \times (r_k - q), \vec{N}\rangle\langle w_q \times (p - r_k), \vec{N}\rangle) =$$

$$\sum_{k=1}^{2} \frac{1}{4|T|} v_p^t \left((p-r_k)(q-r_k)^t - (q-r_k)(p-r_k)^t - \langle p - r_k, q - r_k\rangle \vec{N}\vec{N}^t \right) w_q.$$

For a triangle (p, q, r), one can check that

$$(p-r)(q-r)^t - (q-r)(p-r)^t = \frac{2|(p,q,r)|}{|p-q|^2}\left((p-q)(J(p-q))^t - J(p-q)(p-q)^t\right),$$

so Q^a_{pq} is as in the proposition. □

Proposition 154 *The Hessian of the volume function from S_h to $\mathbb{R}$ is a symmetric bilinear form with $3n \times 3n$ matrix representation Q^V, with respect to the basis $\{\psi_{p_j}\}$ of S_h. Q^V has a 3×3 entry $Q^V_{i,j}$ for each pair of vertices $p_i, p_j \in \mathcal{V}_{int}$ of M_h, so that*

$$\vec{v}^t Q^V \vec{v} = \sum_{p\in\mathcal{V}} \langle v_p, (\nabla_p \operatorname{vol})'\rangle$$

for the variation vector field $\vec{v}$ of any permissible variation. We have $Q^V_{i,i} = 0$, and $Q^V_{i,j} = 0$ when the vertices p_i and p_j are not adjacent, and

$$Q^V_{i,j} = \frac{1}{6}\begin{pmatrix} 0 & r_{2,3} - r_{1,3} & r_{1,2} - r_{2,2} \\ r_{1,3} - r_{2,3} & 0 & r_{2,1} - r_{1,1} \\ r_{2,2} - r_{1,2} & r_{1,1} - r_{2,1} & 0 \end{pmatrix}$$

for adjacent unequal p_i and p_j, where (p_i, p_j, r_k) are the two triangles in $\operatorname{star}\overline{p_i p_j}$ and $r_k = (r_{k,1}, r_{k,2}, r_{k,3})$ for $k = 1, 2$, and (p_i, p_j, r_2) is properly oriented and (p_i, p_j, r_1) is not.

Proof. We have

$$\begin{aligned}\sum_{p\in\mathcal{V}} \langle p', (\nabla_p V)'\rangle &= \sum_{p\in\mathcal{V}_{int}} \langle v_p, \frac{1}{6}\sum_{(p,q,r)\in \operatorname{star}(p)} (q \times r)'\rangle \\ &= \frac{1}{6}\sum_{p\in\mathcal{V}_{int}} \left(\sum_{q\in \operatorname{star} p, q\neq p} \langle v_p \times v_q, r_2 - r_1\rangle \right)\end{aligned}$$

where (p, q, r_2) is the properly oriented triangle in $\operatorname{star}\overline{pq}$, and (p, q, r_1) is the non-properly oriented triangle in $\operatorname{star}\overline{pq}$. Thus we have

$$\sum_{p\in\mathcal{V}}\langle p', (\nabla_p V)'\rangle = \sum_{p\in\mathcal{V}_{int}}\left(\sum_{q\in\operatorname{star} p, q\neq p} v_p^t(Q^V_{pq})v_q\right),$$

where Q^V_{pq} is a 3×3 matrix defined as in the proposition. Thus $Q^V_{pp} = 0$, and the fact that Q^V_{pq} is skew-symmetric in p and q implies Q^V is symmetric. □

Corollary 155 *If a discrete* CMC *surface M_h has only one interior vertex, then it is stable.*

Proof. The single interior vertex is denoted by p_1, and $\operatorname{star} p_1 = M_h$. Then $Q^a = Q^a_{1,1}$ and $Q^V = Q^V_{1,1}$ are 3×3 matrices. By Propositions 153 and 154, $Q^V = 0$ and for any vector $u_p \in \mathbb{R}^3$ at p we have that $u_p^t Q^a u_p$ equals

$$\begin{aligned}\frac{1}{4}\sum_{T=(p,q,r)\in M_h}\frac{|r-q|^2}{\operatorname{area} T}u_p^t\vec{N}\vec{N}^t u_p &= \frac{1}{4}\sum_{T=(p,q,r)\in M_h}\frac{|r-q|^2}{\operatorname{area} T}\langle u_p, \vec{N}\rangle^2\\ &\geq 0,\end{aligned}$$

so $\operatorname{area}''(0) \geq 0$ for all permissible variations. □

6.4 Jacobi Operator for Discrete CMC Surfaces

Since we know the second variation matrix Q explicitly from Section 6.3, we are now able to find the discrete Jacobi operator for compact discrete CMC surfaces M_h, analogous to L in the smooth case (see Equation 6.1). In this section, we find the correct matrix for the discrete Jacobi operator; this matrix has the eigenvalues and eigenfunctions of the second variation of M_h.

We begin with an explicit form for the L^2 inner product on S_h with respect to the basis $\{\psi_{p_1}, .., \psi_{p_n}\}$.

Lemma 156 *The L^2 norm*

$$\langle u, v\rangle_{L^2} := \int_{M_h}\langle u, v\rangle dA = \sum_{T\subset M_h}\int_T \langle u|_T, v|_T\rangle dA$$

on M_h for $u, v \in S_h$ has the positive definite $3n\times3n$ matrix representation

$$S = (\langle\psi_{p_i}, \psi_{p_j}\rangle_{L^2} I_{3\times3})_{i,j=1}^n,$$

so that $\langle u, v\rangle_{L^2} = \vec{u}^t S\vec{v}$*, where* $\vec{u}, \vec{v} \in \mathbb{R}^{3n}$ *are the vector fields associated to* u, v*.* S *consists of* 3×3 *blocks* $S_{i,j}$ *in an* $n \times n$ *grid with*

$$S_{j,j} = \sum_{T \in \operatorname{star} p_j} \frac{\operatorname{area} T}{6} \cdot \mathrm{id}_{3\times 3}, \quad \textit{resp.} \quad S_{i,j} = \sum_{T \in \operatorname{star}(\overline{p_i p_j})} \frac{\operatorname{area} T}{12} \cdot \mathrm{id}_{3\times 3}$$

when p_i *and* p_j *are adjacent, and* $S_{i,j} = 0$ *when* p_i *and* p_j *are not adjacent.*

Proof. Noting that, for each triangle $T \subset M_h$,

$$\int_T \psi_p^2 dA = \frac{\operatorname{area} T}{6}, \quad \int_T \psi_p \psi_q dA = \frac{\operatorname{area} T}{12}$$

for any distinct vertices p and q of T, we have that, for any two functions $u, v \in S_h$, $\langle u, v\rangle_{L^2}$ equals

$$\sum_{p_j \in \mathcal{V}_{int}} (\langle u_{p_j}, v_{p_j}\rangle \sum_{T \in \operatorname{star} p_j} \frac{\operatorname{area} T}{6} + \sum_{\substack{p_i \in \mathcal{V}_{int} \cap \\ \operatorname{star} p_j}} \langle u_{p_j}, v_{p_i}\rangle \sum_{T \in \operatorname{star} \overline{p_i p_j}} \frac{\operatorname{area} T}{12}).$$

Hence the 3×3 blocks $S_{i,j}$ are as in the lemma. □

We now define the discrete Jacobi operator $L_h : S_h \to S_h$ associated to the second variation formula for the surface - recall Equations 4.1 and 4.2.

Definition 157 *For* $v \in S_h$ *with associated vector field* $\vec{v}$*, we define the* discrete Jacobi operator $L_h v$ *on* v *to be the function in* S_h *associated to the vector field* $S^{-1}Q\vec{v}$*.*

$L_h(S_h) \subset S_h$, so we can consider the eigenvalue problem for L_h. We also desire L_h to be linear and symmetric, that is, $\int_{M_h} u^t L_h v = \int_{M_h} v^t L_h u$ for all $u, v \in S_h$. With these properties, the above choice of L_h is canonical:

Proposition 158 $L_h : S_h \to S_h$ *is the unique linear operator so that* $\int_{M_h} u^t L_h v dA$ *is symmetric in* u *and* v *and*

$$\int_{M_h} v^t L_h v dA = \vec{v}^t Q \vec{v}$$

for all $v \in S_h$*.*

Proof. The map L_h is clearly linear, and

$$\int_{M_h} u^t L_h v dA = \langle u, L_h v\rangle_{L^2} = \vec{u}^t S(S^{-1}Q\vec{v}) = \vec{u}^t Q\vec{v}$$

for all $u, v \in S_h$. Hence, since Q is symmetric, $\int_{M_h} u^t L_h v dA$ is symmetric in u and v.
Uniqueness of L_h with the above properties follows from the following:

$$\begin{aligned} & \int_{M_h} u^t L_h v dA \\ = \; & \frac{1}{2}\left(\int_{M_h} (u+v)^t L_h (u+v) dA - \int_{M_h} u^t L_h u dA - \int_{M_h} v^t L_h v dA\right) \\ = \; & \frac{1}{2}\left((\vec{u}+\vec{v})^t Q(\vec{u}+\vec{v}) - \vec{u}^t Q\vec{u} - \vec{v}^t Q\vec{v}\right). \end{aligned}$$

Hence $\int_{M_h} u^t L_h v dA$ is uniquely determined for all $u \in S_h$, so $L_h v$ is uniquely determined for each $v \in S_h$. □
Since $S^{-1}Q$ is self-adjoint with respect to the L^2 inner product on S_h, all the eigenvalues of $S^{-1}Q$ are real.

Definition 159 *The* spectrum *of the second variation of $M_h(t)$ at $t = 0$ is the set of eigenvalues of $S^{-1}Q$.*

Remark 160 *Another way to see that $S^{-1}Q$ is the correct discrete Jacobi operator is to consider the Rayleigh quotient*

$$\frac{\vec{v}^t Q\vec{v}}{\langle v, v\rangle_{L^2}} = \frac{\vec{v}^t S(S^{-1}Q\vec{v})}{\vec{v}^t S\vec{v}}.$$

The standard minmax procedure for producing eigenvalues from the Rayleigh quotient will produce the eigenvalues of $S^{-1}Q$.

6.5 Approximating Smooth Spectra

Using our explicit form for $S^{-1}Q$ of the discrete Jacobi operator L_h, we can now implement the procedure described in the second half of the introduction.
If a sequence of compact CMC discrete surfaces $\{M_h\}_{i=1}^{\infty}$ converges (in the Sobolev H^1 norm as graphs over the limiting surface) to a smooth compact CMC surface $\Phi : M \to \mathbb{R}^3$, then standard estimates from the theory of finite elements (see, for example, [21] or [44]) imply that the eigenvalues and eigenvectors (piecewise linearly extended to functions) of the operators L_h of the M_{hj} converge to the eigenvalues and eigenfunctions of the Jacobi operator L of Φ (convergence is in the L^2 norm for the eigenfunctions).

For the first two examples here – a planar square and rotationally symmetric portion of a catenoid – we know the approximating discrete minimal surfaces exactly, and we know the eigenvalues and eigenfunctions of L for the smooth minimal surfaces exactly, so we can check that convergence of the eigenvalues and eigenfunctions does indeed occur.

In the final two examples – symmetric portions of a trinoid and a Costa surface – the spectra of the smooth minimal surfaces is unknown, so we see estimates for the eigenvalues and eigenfunctions for the first time. Our experiments confirm the known values 3 and 5 respectively for the indexes of these unstable surfaces, and additionally show us the directions of variations that reduce area. Thus we have approximations for maximal spaces of variation vector fields on the smooth minimal surfaces for which the associated variations reduce area. (For the approximating discrete surfaces in these examples, we do not have an explicit form; however, the theory of finite elements applies and we can still expect convergence of the eigenvalues and eigenfunctions in L^2 norm, if we choose the discrete approximations so that they converge in H^1 norm to the smooth minimal surfaces.)

Spectrum of the Flat Minimal Square

Considering the square $M = \{0 \leq x \leq \pi, 0 \leq y \leq \pi\}$ included in $\mathbb{R}^3$ as a smooth minimal surface, the eigenvalues and eigenfunctions of L are $\mu_{m,n} = m^2 + n^2$ and $\phi_{m,n} = \frac{2}{\pi}\sin(mx)\sin(ny)$ for $m, n \in \mathbb{Z}^+$ (Section 6.2).

Now we consider the discrete minimal surface M_h that is M with a regular square $n \times n$ grid. In each subsquare of dimension $\frac{\pi}{n} \times \frac{\pi}{n}$, we draw an edge from the lower left corner to the upper right corner, producing a discrete minimal surface with $2n^2$ congruent triangles with angles $\frac{\pi}{4}$, $\frac{\pi}{4}$, and $\frac{\pi}{2}$.

For this M_h, $S^{-1}Q$ has no negative eigenvalues, as expected, since the smooth minimal square is stable. However, we must take tangential motions into account in the discrete case, and we find that (when writing the eigenvalues in increasing order) the first two-thirds of the eigenvalues are 0 and their associated eigenvectors are entirely tangent to the surface. The final one-third of the eigenvalues are positive, with eigenvectors that are exactly perpendicular to the surface. Examples of these perpendicular vector fields are shown in Figure 6.4 for $n = 15$. Note, there are 196 interior vertices, and so there are 588 eigenvalues λ_j of $S^{-1}Q$ and $\lambda_0 = ... = \lambda_{391} = 0$ and $\lambda_j > 0$ when $j \in [392, 587]$. The eigenvectors shown in these figures and their eigen-

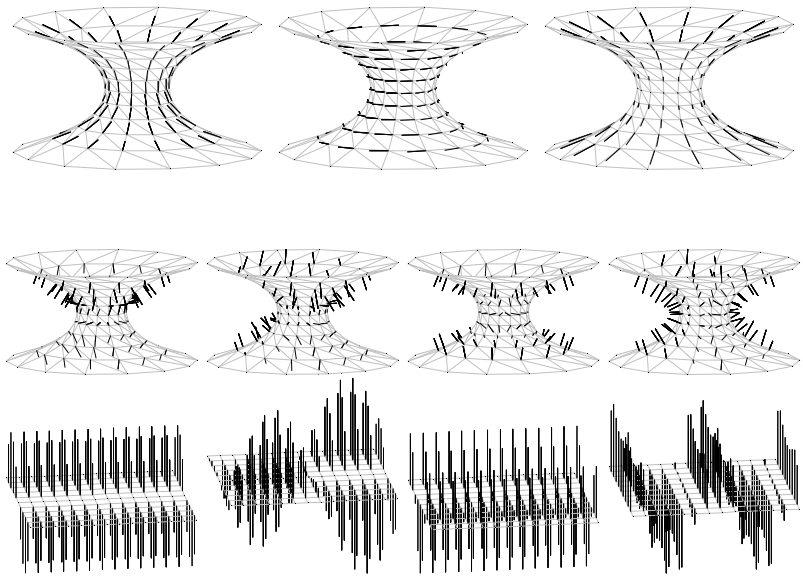

FIGURE 6.6. Two-thirds of the eigenvectors are approximately tangential to the surface. For example, in the first row we show the $\mathbb{R}^{3n}$-eigenvector fields associated to the eigenvalues λ_1, λ_2, and λ_3 (whose values are just slightly greater than 0). One-third of the eigenvectors are approximately perpendicular to the surface, and the second row shows such eigenvector fields, associated to the eigenvalues λ_{147}, λ_{171}, λ_{204}, and λ_{210}. The final row shows projected versions of the eigenvectors in the second row, for use in comparing with the eigenfunctions of the smooth case considered in section 4. These projected versions are made just as in Figure 6.5.

values are close to those of the smooth operator L of M. We have $\lambda_{392} = 2.022 \approx \mu_{1,1}$, $\lambda_{393} = 5.094 \approx \mu_{1,2}$, $\lambda_{394} = 5.148 \approx \mu_{2,1}$, $\lambda_{395} = 8.347 \approx \mu_{2,2}$, $\lambda_{396} = 10.434 \approx \mu_{1,3}$, $\lambda_{397} = 10.445 \approx \mu_{3,1}$.

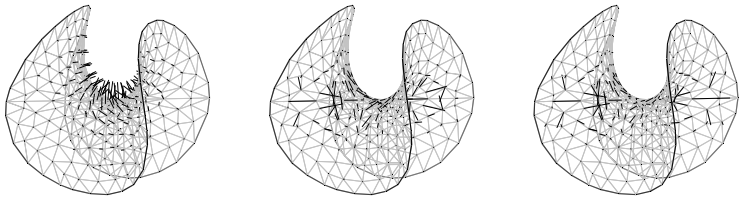

FIGURE 6.7. The first eigenvector field for a discrete approximation of a compact portion of an Enneper surface (left). The associated first eigenvalue is negative and is the only negative eigenvalue that is not approximately zero, corresponding to the fact that the smooth Enneper surface has index 1. Those other negative (approximately zero) eigenvalues have corresponding eigenvector fields that appear roughly tangent to the surface.

Spectrum of the Discrete Minimal Catenoid

By Corollary 110, we know that the discrete minimal catenoids converge to smooth catenoids as the meshes are made finer. Hence the eigenvalues and eigenvectors of the discrete catenoids converge to the eigenvalues and eigenfunctions of the smooth catenoid. For the discrete catenoids with relatively fine meshes, we find that two-thirds of the eigenvectors are approximately tangent to the surface, and the remaining ones are approximately perpendicular. The approximately perpendicular ones - considered as functions which are multiplied by unit normal vectors - and their eigenvalues converge to the eigenfunctions and eigenvalues of the smooth catenoid which are computed in Section 6.2.

Consider the example shown in the Figures 6.5 and 6.6. Here the catenoid has $9 \times 14 = 126$ interior vertices, so the matrix $S^{-1}Q$ has dimension 378×378. The first eigenvalue of this matrix is $\lambda_0 \approx -0.542$ and $\lambda_j > 0$ for all $j \in [1, 377]$, as expected, since the smooth complete catenoid has index 1 [43]. Note that λ_0 is very close to the negative eigenvalue for the smooth case, described in the caption of Figure 6.5. The closest matching smooth catenoid portion satisfies $y_1 = -y_0 = 1.91$. The first eigenfunction in the discrete case, see also Figure 6.5, is also very close to the first eigenfunction in the smooth case.

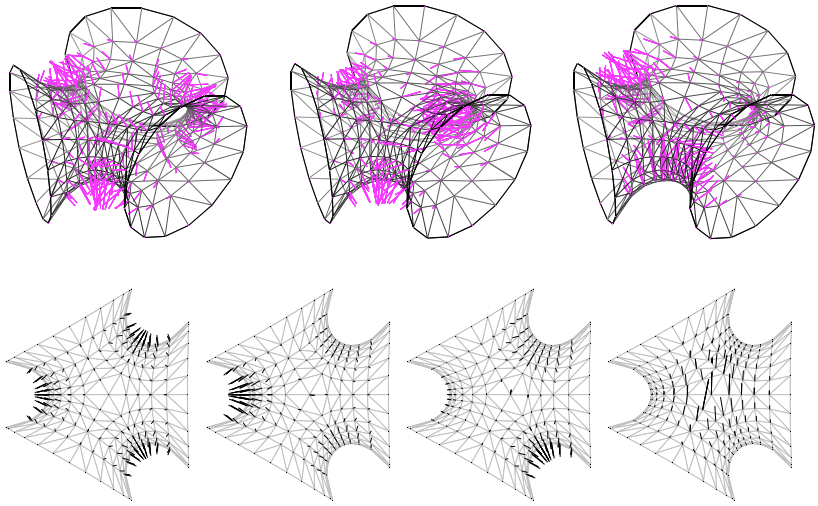

FIGURE 6.8. Variation vector fields for three area-reducing variations of a discrete approximation of a compact portion of a trinoid. The lower row has overhead views of these variation vector fields, as well as an overhead view of the variation vector field associated to the fourth (and first positive) eigenvalue.

Spectrum of the Discrete Minimal Trinoids and Costa Surface

Since the trinoid has index 3, we find that approximating discrete surfaces with relatively fine meshes have 3 negative eigenvalues. And we can look at the corresponding eigenvector fields, which estimate the eigenfunctions in the smooth case, shown in Figure 6.8. For the approximating discrete trinoid in Figure 6.8, the first four eigenvalues are approximately -3.79, -1.31, -1.31, 0.014, so we indeed have 3 negative eigenvalues and the second eigenvalue has multiplicity 2.

Similarly, the genus 1 Costa surface has index 5, and approximating discrete surfaces with relatively fine meshes have 5 negative eigenvalues. See Figure 6.9.

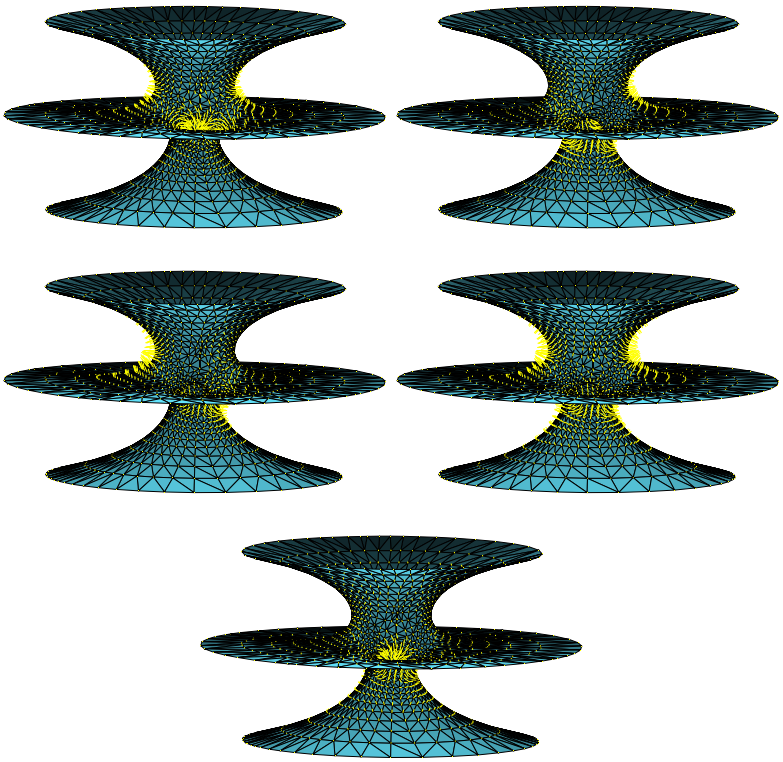

FIGURE 6.9. The first five eigenvector fields (whose corresponding eigenvalues are the five negative ones) for a discrete approximation of a compact portion of a genus 1 Costa surface.

7

Singularities of Discrete Vector Fields

Singularities of vector fields are among the most important features of flows. They determine the physical behavior of flows and allow one to characterize the flow topology [56][57]. The most prominent singularities are sinks, sources, and vortices. Higher order singularities often appear in magnetic fields. All these singularities must be detected and analyzed in order to understand the physical behavior of a flow. Although feature analysis is an important area, only a few technical tools are available for the detection of singularities and their visualization.

Methods for direct vortex detection are often based on the assumption that there are regions with high amounts of rotation or of pressure extrema. See, for example, Banks and Singer [7] for an overview of possible quantities to investigate. The deficiencies of first-order approximations have been widely recognized, and, for example, higher-order methods try to overcome this problem [106]. The detection and visualization of higher-order singularities is an active research area where rather heavy mathematical methods have been employed [110].

The Jacobian $\nabla\xi$ of a differentiable vector field ξ in $\mathbb{R}^2$ and $\mathbb{R}^3$ can be decomposed in a stretching tensor S and a vorticity matrix Ω. The eigenvalues of the diagonal matrix S correspond to the compressibility of the flow, and the off-diagonal entries of the anti-symmetric matrix

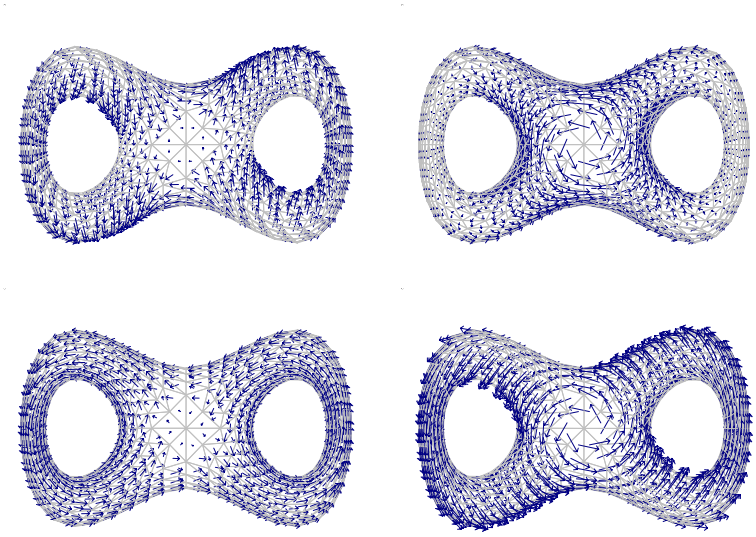

FIGURE 7.1. Decomposition of the vector field obtained as tangential component of the tangent field of a rotation of 3-space. Original field (bottom right), rotation-free component (upper left) and divergence-free component (upper right). The harmonic component (bottom left) belongs to an incompressible, rotation-free component around the handles of the pretzel.

Ω are the components of the rotation vector. This matrix decomposition has classically been used also for discrete vector fields where the Jacobian is approximated by discrete difference techniques. The quality of this approach depends on the quality of the underlying grid and the accuracy of the vector field.

Another class of methods follows a geometric approach where geometric properties of streamlines and pathlines are investigated and put in relation to properties of the flow [108][109]. Tittgemeyer et al. [116] use a contraction mapping to detect singularities of displacement fields in magnetic resonance imaging. This helps in the understanding of pathological processes in a brain. Their method is applicable to any higher order singularities but fails to detect some critical points like centers of rotation or balanced saddle points.

Our approach uses a discrete version of the Helmholtz-Hodge decomposition of discrete vector fields. We choose a global variational approach to compute the decomposition of a discrete vector field which seems to be a novel approach to the detection and analysis of singularities of discrete vector fields. We compute two potential functions

related to different components of the flow, namely to a rotation-free and to a divergence-free component. A remaining harmonic component is also discussed. The potential functions are computed by a global variational approach where certain energy functionals are minimized in the set of scalar-valued functions. The detection and analysis of vector field singularities is then transferred to the much simpler study of the critical points of the scalar valued potential functions. In contrast to local methods, our approach avoids the approximation problem of the Jacobian matrix or higher order tensors. Further, the method is rather stable with respect to local deficiencies of the vector field arising from numerical approximation errors or from sampling inaccuracies.

Although the Helmholtz decomposition [58] of smooth fields into a curl-free and divergence-free part is well-known in fluid dynamics [26], we have not found any application to the study of singularities of discrete vector fields. Discrete differential forms were introduced in differential geometry by Whitney [119] who invented the so-called Whitney forms. Whitney forms were brought to a new life in the pioneering work on discrete Hodge decompositions in computational electromagnetism by Bossavit [17][16] who applied them to the solution of boundary value problems. For simplicial complexes K Eckmann [39] developed a combinatorial Hodge theory. Dodziuk [34] showed that if K is a smooth triangulation of a compact oriented Riemann manifold X then the combinatorial Hodge theory is an approximation of the Hodge theory of forms on X by choosing a suitable inner product on K.

Our discretization method has contact with weak derivatives used in finite element theory where the formal application of partial integration is used to shift the differentiation operation to differentiable test functions. In fact, the integrands of our discrete differential operators div_h and rot_h can be obtained from $\nabla\xi$ by formal partial integration with test functions. In contrast, our focus here is to emphasize the geometric interpretation of the discrete differentials, and to relate them with the discrete curvature and Hodge operators which played a role in Section 4.

We apply our method to several test cases with artificial and simulated flows which are accurately analyzed. The simulated flow in the Bay of Gdansk reproduces similar results of Post and Sadarjoen [108], who employed different geometric methods.

7.1 Setup

In the following sections we extend the discussion on discrete differential operators to vector fields and differential forms on simplicial surfaces. Among the simplest operators are the discrete divergence and rotation operators which naturally continue the discussion on differential properties of simplicial maps in chapters 3 and 4. For example, the discrete Hodge $*-$operator defined on gradient fields in the chapters on discrete conjugate harmonic maps and minimal surfaces extends to discrete differential forms and plays a rôle in the Hodge-Helmholtz decomposition. A practical application of the discrete setup to fluid dynamics is given at the end of the chapter where we use the Hodge decomposition to locate and study singularities of noisy vector fields.

In the following let M_h be a simplicial surface immersed in $\mathbb{R}^n$. Let S_h be the space of piecewise linear continuous functions, and S_h^* the space of piecewise linear functions which are edge midpoint continuous. We denote with $\{\varphi_i\}$ the set of vertex-based Lagrange basis functions of S_h, and with $\{\psi_i\}$ the set of edge-based basis functions of S_h^*.

We use the following space of vector fields on M_h

$$\Lambda_h^1 := \left\{ v \mid v_{|T} \text{ is a constant, tangential vector on each triangle} \right\}$$

which will later be considered in the wider setup of discrete differential forms. As common practice in the finite element context, the subindex h distinguishes this set from smooth concepts.

On each oriented triangle, we define the operator J that rotates each vector by an angle $\frac{\pi}{2}$. For example, let c be an edge of the oriented boundary of a triangle, then $Jc = -\nu$ is in opposite direction of the outer normal of the triangle at c. The operator J is a special form of the Hodge star operator.

We recall some basic relation. Let T be a triangle with vertices $\{p_1, p_2, p_3\}$ and counterclock-wise oriented edges $\{c_1, c_2, c_3\}$ with $c_i = p_{i-1} - p_{i+1}$. Let $u \in S_h$ be a piecewise linear function with function values $u_i = u(p_i)$ then its gradient has the following representation

$$\nabla u_{|T} = \frac{1}{2 \operatorname{area} T} \sum_{i=1}^{3} u_i J c_i.$$

The following scalar products with triangle edges describe the total rotation respectively the total flow through an edge:

$$\begin{aligned} \langle \nabla u, c_j \rangle &= u_{j-1} - u_{j+1} && (7.1) \\ \langle \nabla u, Jc_j \rangle &= \cot \alpha_{j+1}(u_j - u_{j-1}) + \cot \alpha_{j-1}(u_j - u_{j+1}). && (7.2) \end{aligned}$$

7.2 Discrete Rotation

The rotation rot of a differentiable vector field on a smooth surfaces is at each point p a vector normal to the surface whose length measures the angular momentum of the flow. On a planar Euclidean domain with local coordinates (x, y), the rotation of a differentiable vector field $v = (v_1, v_2)$ is given by $\operatorname{rot} v = (0, 0, v_{2|x} - v_{1|y})$. In the discrete version of this differential operators, the (total) discrete rotation, we neglect the vectorial aspect and consider the rotation as scalar value given by the normal component.

In the following we use a simplicial domain M_h which contains its boundary. The boundary is assume to be counter-clockwise parametrized. If $p \in \partial M_h$ is a vertex on the boundary then $\operatorname{star} p$ consists of all triangles containing p. If $m \in \partial M_h$ is the midpoint of an edge c then $\partial \operatorname{star} m$ does contain the edge c as well.

Definition 161 *Let $v \in \Lambda_h^1$ be a piecewise constant vector field on a simplicial surface M_h. Then the (total)* discrete rotation $\operatorname{rot} v$ *is a function in S_h given by*

$$\operatorname{rot}_h v(p) := \frac{1}{2} \oint_{\partial \operatorname{star} p} v = \frac{1}{2} \sum_{i=1}^{k} \langle v, c_i \rangle$$

where c_i are the edges of the oriented boundary of the star of $p \in M_h$. Additionally, the discrete rotation $\operatorname{rot}^* v$ *at the midpoint m of each edge c is a function in S_h^* given by*

$$\operatorname{rot}_h^* v(m) := \oint_{\partial \operatorname{star} c(m)} v$$

where $\partial \operatorname{star} m$ is the oriented boundary of the triangles adjacent to edge c.

If the rotation of a vector field is positive on each edge of the link of a vertex then the vector field rotates counter clock-wise around this vertex. Note that rot_h^* vanishes along the boundary.

Lemma 162 *Let p be a vertex of a simplicial surface M_h with emanating edges $\{c_1, ..., c_k\}$ with edge midpoints m_i. Then*

$$2 \operatorname{rot}_h v(p) = \sum_{i=1}^{k} \operatorname{rot}_h^* v(m_i).$$

Note, that $\operatorname{rot}_h^* v = 0$ at all edge midpoints implies $\operatorname{rot}_h v = 0$ on all vertices. The converse is not true in general.

Rotation-free vector fields are be characterized by the existence of a discrete potential.

Theorem 163 *Let M_h be a simply connected simplicial surface with a piecewise constant vector field v. Then $v = \nabla u$ is gradient of a function $u \in S_h$ if and only if*

$$\operatorname{rot}_h^* v(m) = 0 \quad \forall \text{ edge midpoints } m,$$

respectively, $v = \nabla u^*$ is gradient of a function in $u^* \in S_h^*$ if and only if

$$\operatorname{rot}_h v(p) = 0 \quad \forall \text{ interior vertices } p.$$

Further, for a vertex $q \in \partial M_h$ the value $\operatorname{rot}_h \nabla u^*(q)$ is the difference of $u^*(q)$ at the two adjacent boundary triangles.

Proof. 1.) " $\Rightarrow$ ": Assume the orientation of the common edge $c = T_1 \cap T_2$ of two triangles leads to a positive orientation of ∂T_1. Then we obtain from the definition of rot_h^*

$$\operatorname{rot}_h^* v(m) = -\left\langle v_{|T_1}, c \right\rangle + \left\langle v_{|T_2}, c \right\rangle.$$

Let T_1 be a triangle with vertices $\{p_1, p_2, p_3\}$ and edges $c_j = p_{j-1} - p_{j+1}$. Assume $v = \nabla u_h$ is the gradient of a piecewise linear function $u_h \in S_h$. Let $u_j = u_h(p_j)$ be the function values at the vertices of T_1 then

$$\langle \nabla u_h, c_j \rangle = u_{j-1} - u_{j+1}.$$

The sum of the two scalar products $\langle \nabla u_h, c \rangle$ at the common edge of two adjacent triangles cancels because of the continuity of u_h and the reversed orientation of c in the second triangle.

" $\Leftarrow$ ": We construct a vertex spanning tree of M_h and oriented its edges towards the root of the tree. Since v is rotation-free the scalar product of v with each oriented edge c_j is unique, and we denote it with $v_j := \langle v, c_j \rangle$. Now we construct a function u_h by assigning

$u_h(r) := 0$ at the root of the spanning tree, and integrate along the edges of the spanning tree such that

$$u_h(p_{j_2}) - u_h(p_{j_1}) = v_j$$

if $c_j = p_{j_2} - p_{j_1}$. This leads to a function $u_h \in S_h$. On each triangle T we have $\nabla u_{|T} = v_{|T}$ since by construction we have $\langle \nabla u_h, c_j \rangle = u_h(p_{j_2}) - u_h(p_{j_1}) = v_j$ on each edge c_j.
We now show that the function u_h is independent of the choice of the spanning tree. It is sufficient to show that the integration is path independent on each triangle (which is clear) and around the link of each vertex. Around a vertex p denote the vertices of its oriented link with $\{q_1, ..., q_s\}$. Since we have the edge differences $u(p) - u(q_j) = v_j$ it follows that

$$\begin{aligned} \sum_{j=1}^{s} u(q_j) - u(q_{j+1}) &= \sum_{j=1}^{s} u(q_j) - u(p) + u(p) - u(q_{j+1}) \\ &= \sum_{j=1}^{s} -v_j + v_{j+1} = 0. \end{aligned}$$

The function u_h solely depends on v and the integration constant $u_h(r)$.
2.) The second assumption follows from a similar calculation which we only sketch here.
" $\Rightarrow$ ": If v is gradient of a function $u^* \in S_h^*$ then the assumption follows since at all interior vertices p we have

$$\begin{aligned} \oint_{\gamma_p} \nabla u^* &= \sum_{j=1}^{n} \langle \nabla u^*, m_j - m_{j-1} \rangle \\ &= \sum_{j=1}^{n} u^*(m_j) - u^*(m_{j-1}) = 0 \end{aligned}$$

where γ_p is a polygon connecting the midpoints m_j of all edges emanating from p.
" $\Leftarrow$ " By assumption, the path integral of v along any closed curve γ crossing edges at their midpoints vanishes. Since v integrates to a linear function on each triangle, we obtain a well-defined function $u_h^* \in S_h^*$ similar to the procedure in 1.) by

$$u_h^*(p) := \oint_{\gamma} v$$

where γ is any path from a base point $r \in M_h$ to p which crosses edges at their midpoints.

3.) The statement on the height difference of u^* at a boundary vertex q follows directly from the evaluation of $\operatorname{rot}_h \nabla u^*(q)$. □

The above theorem does not hold for non-simply connected surfaces since integration along closed curves, which are not $0-$homotop, may lead to periods. Also note, that from $S_h \subset S_h^*$ follows $0 = \operatorname{rot}_h \nabla u = \operatorname{rot}_h^* \nabla u$ for any $u \in S_h$.

The next lemma derives a vector field on a simplicial surface M_h which has a given rotation along each edge.

Lemma 164 *Let T be a triangle with oriented edges $\{c_1, c_2, c_3\}$. Any given set of edge weights $\{v_1, v_2, v_3\}$, $v_i \in \mathbb{R}$ with $v_1 + v_2 + v_3 = 0$ uniquely determines a vector v*

$$v = \sum_{i=1}^{3} v_i \frac{\cot \alpha_i}{2 \operatorname{area} T} c_i$$

with rotation $\langle v, c_j \rangle = v_j$ at the edge c_j.

Proof. A simple calculation shows that v has the given rotation

$$\begin{aligned}
& \langle v, c_j \rangle \\
= \; & \frac{v_{j-1} \cot \alpha_{j-1} \langle c_{j-1}, c_j \rangle + v_j \cot \alpha_j |c_j|^2 + v_{j+1} \cot \alpha_{j+1} \langle c_{j+1}, c_j \rangle}{2 \operatorname{area} T} \\
= \; & -v_{j-1} \cot \alpha_{j-1} \cot \alpha_{j+1} + v_j \cot \alpha_j (\cot \alpha_{j-1} + \cot \alpha_{j+1}) \\
& -v_{j+1} \cot \alpha_{j-1} \cot \alpha_{j+1} \\
= \; & v_j \left(\cot \alpha_{j-1} \cot \alpha_{j+1} + \cot \alpha_j (\cot \alpha_{j-1} + \cot \alpha_{j+1}) \right) \\
= \; & v_j .
\end{aligned}$$

□

If v is the gradient field of a function $u \in S_h$ then the weights v_i are the difference of u evaluated at the endpoints of edge c_i. v is integrable if these coefficients agree at the common edge of adjacent triangles.

7.3 Discrete Divergence

In the smooth case the divergence div of a field is a real-valued function measuring at each point p on a surface the amount of flow generated in an infinitesimal region around p. On a planar Euclidean

domain with local coordinates (x, y), the divergence of a differentiable vector field $v = (v_1, v_2)$ is given by $\operatorname{div} v = v_{1|x} + v_{2|y}$. The discrete version of this differential operators, the (total) discrete divergence, is obtained by a similar physical reasoning, that means we define the discrete divergence as the amount of flow generated inside the $\operatorname{star} p$ of a vertex p which is the total amount flowing through the boundary of $\operatorname{star} p$.

At a boundary vertex p the discrete divergence must take into account the flow through the two boundary edges as well as divergence generated at all other edges emanating from p since the divergence at these interior edges has only been considered by half at interior vertices. The following definition also fulfills the formal integration by parts relation 7.3:

Definition 165 *Let $v \in \Lambda_h^1$ be a piecewise constant vector field on a simplicial surface M_h. Then the (total)* discrete divergence $\operatorname{div}_h : \Lambda_h^1 \to S_h$ *of v is a function in S_h given by*

$$\operatorname{div}_h v(p) = \frac{1}{2} \int_{\partial \operatorname{star} p} \langle v, \nu \rangle \, ds$$

where ν is the exterior normal along the oriented boundary of the star of $p \in M_h$. If $p \in \partial M_h$ then $\operatorname{star} p$ consists of all triangles containing p.

Additionally, we define the divergence operator $\operatorname{div}_h^* : \Lambda_h^1 \to S_h^*$ based at the midpoint m of an edge c

$$\operatorname{div}_h^* v(m) = \int_{\partial \operatorname{star} c} \langle v, \nu \rangle \, ds$$

where $\partial \operatorname{star} m$ is the oriented boundary of the triangles adjacent to edge c. If $m \in \partial M_h$ then $\partial \operatorname{star} m$ does not contain the edge c.

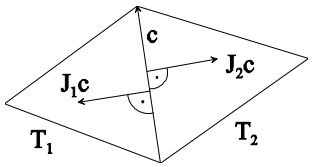

Divergence at the midpoint of an edge.

Note, the divergence div_h^* at an edge c common to two triangles T_1 and T_2 may equivalently be defined by $\operatorname{div}_h^* v(m) = \langle v, Jc_1 \rangle_{|T_1} + \langle v, Jc_2 \rangle_{|T_2}$ where the common edge has opposite orientation $c_1 = -c_2$ in each triangle. Let $\varphi_p \in S_h$ denote the basis Lagrange function associate to each vertex p of M_h. Then formally, the discrete divergence can obtained by applying Green's integration by parts

$$\begin{aligned} \operatorname{div}_h v(p) \quad &: \quad = \int_{\operatorname{star} p} \text{" } \operatorname{div} v \text{"} \cdot \varphi_p dx \qquad (7.3) \\ &= \quad - \int_{\operatorname{star} p} \left\langle v, \nabla \varphi_p \right\rangle dx + \int_{\partial \operatorname{star} p} \langle v, \nu \rangle \, \varphi_p ds \end{aligned}$$

although Green's formula does not hold in the discrete setting since v and φ_p are not differentiable on $\operatorname{star} p$. On the right hand side the boundary integral vanishes since $\varphi_p = 0$ along $\partial \operatorname{star} p$ such that we obtain the same equation for $\operatorname{div}_h v(p)$ as in definition above.

The normalization of the divergence operator gives the following equalities known from the smooth case:

Lemma 166 *The gradient vector field of a potential $u_h \in S_h$ on a simplicial surface M_h fulfills*

$$\operatorname{div}_h \nabla u_h = \Delta_h u_h \tag{7.4}$$

using the discrete Laplace operator Δ_h of Definition 3.18. Similarly, the gradient vector field of a potential $u_h^* \in S_h^*$ on M_h fulfills

$$\operatorname{div}_h^* \nabla u_h^* = \Delta_h u_h^*. \tag{7.5}$$

Proof. If p is an interior vertex of M_h then the Definition 3.18 of the discrete Laplacian gives

$$\begin{aligned} \operatorname{div}_h \nabla u_h(p) &= \frac{1}{2} \int_{\partial \operatorname{star} p} \langle \nabla u_h, \nu \rangle \, ds \\ &= -\int_{\operatorname{star} p} \left\langle \nabla u_h, \nabla \varphi_p \right\rangle dx = \Delta_h u_h(p) \end{aligned} \tag{7.6}$$

using $\nabla \varphi_p = J c_p / (2 \operatorname{area} T)$ on each triangle T with edge c_p opposite to p.

The edge-based divergence relates similarly to the Laplacian of a function $u^* \in S_h^*$. Let m be the midpoint of an edge c shared by two triangles T_1 and T_2 of $\operatorname{star} m$. Then

$$\begin{aligned} \operatorname{div}_h^* \nabla u_h^*(m) &= \int_{\partial \operatorname{star} m} \langle \nabla u_h^*, \nu \rangle \, ds \\ &= -\int_{\operatorname{star} m} \langle \nabla u_h^*, \nabla \psi_m \rangle \, dx = \Delta_h u^*(m) \end{aligned}$$

where T_1 and T_2 are the two triangles with common edge c_m. □

Lemma 167 *The discrete rotation and divergence of a vector field $v \in \Lambda_h^1$ on a simplicial surface M_h relate by*

$$\operatorname{rot}_h Jv(p) = \operatorname{div}_h v(p),$$

respectively,

$$\operatorname{rot}_h^* Jv(m) = \operatorname{div}_h^* v(m)$$

where p is a vertex and m is the midpoint an edge of M_h.

Proof. The two relations of rot and div follow directly from the definitions 165 and 161 of the differential operators. □

For practical applications, we compute the explicit formula for the discrete divergence operator in terms of triangle quantities. Note the similarity with the formula of the discrete Laplace operator where the influence of the domain metric solely appears in the cotangens factor.

Theorem 168 *Let $v \in \Lambda_h^1$ be a piecewise constant vector field on a simplicial surface M_h. Then the discrete divergence* div_h *of v is given at each vertex p by*

$$\operatorname{div}_h v(p) = -\frac{1}{2}\sum_{i=1}^{s} \langle v, Jc_i \rangle = \frac{1}{2}\sum_{i=1}^{k} (\cot \alpha_i + \cot \beta_i) \langle v, a_i \rangle \qquad (7.7)$$

where J denotes the rotation of a vector by $\frac{\pi}{2}$ in each triangle, k the number of directed edges a_i emanating from p, and the edges c_i form the closed cycle of $\partial \operatorname{star} p$ in counter clockwise order. In the two triangles adjacent to an edge a_i we denote the vertex angles at the vertices opposite to a_i with α_i, β_i.

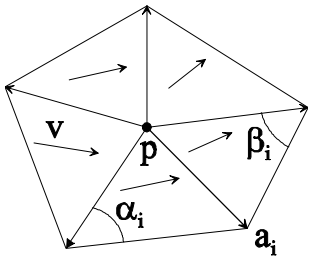

Divergence at a vertex p.

Proof. By definition Jc rotates an edge such that it points into the triangle, i.e. $Jc = -\nu$ is in opposite direction of the outer normal of the triangle at c. Therefore, the representation of the discrete divergence operator follows from the representation of

$$Jc = \cot \alpha a + \cot \beta b$$

in each triangle with edges $c = a - b$, and sorting the terms around $\operatorname{star} p$ by edges. □

The discrete version of the Gauß integration theorem relates the divergence of a domain to the flow through its boundary.

Theorem 169 *Let M_h be a simplicial surface with boundary ∂M_h and piecewise constant vector field v. Then*

$$\sum_{p \in M_h} \operatorname{div}_h v(p) = \int_{\partial M_h} \langle v, \nu \rangle \qquad (7.8)$$

where ν is the exterior normal along ∂M_h. Further, we have

$$\sum_{m \in M_h} \operatorname{div}_h^* v(m) = \int_{\partial M_h} \langle v, \nu \rangle \qquad (7.9)$$

where m runs through the midpoints of all edge of M_h.

Proof. The total divergence

$$\sum_{p\in M_h} \operatorname{div}_h v(p) = \sum_{p\in \mathring{M}_h} \frac{1}{2}\int_{\partial \operatorname{star} p} \langle v,\nu\rangle \, ds + \sum_{p\in \partial M_h} \frac{1}{2}\int_{\partial \operatorname{star} p} \langle v,\nu\rangle \, dx,$$

each interior edge appears two times, once for each adjacent triangle. Since $\partial \operatorname{star} p$ of a boundary vertex p includes the two edges adjacent to p, each boundary edge appears three times. On each triangle, the sum of the contributions $\langle v,\nu\rangle$ of all three edges of a triangle vanishes, which consumes two interior edges and one boundary edge. The remaining two boundary edges sum up to the boundary integral.

In the case of div_h^*, we sort the sum of the edge divergences by boundary edges, which vanishes, and by interior edges.

$$\begin{aligned}\sum_{p\in M_h} \operatorname{div}_h v(p) &= \frac{1}{2}\sum_{i=1}^{\#\text{int edges}} \langle v, Jc_i\rangle_{|T_{i_1}} + \langle v, Jc_i\rangle_{|T_{i_2}} \\ &= -\sum_{b=1}^{\#\text{bnd edges}} \langle v, Jc_b\rangle_{|T_b}\end{aligned}$$

The last equation follows since the total divergence on each triangle vanishes. □

The divergence at vertices and edges is related by the following lemma.

Lemma 170 *Let p be a vertex of simplicial surface M_h with emanating edges $\{c_1,...,c_k\}$ with edge midpoints m_i. Then*

$$2\operatorname{div}_h v(p) = \sum_{i=1}^{k} \operatorname{div}_h^* v(m_i).$$

Proof. On a single triangle we have $\operatorname{div}_h^* v(m_3) = -\operatorname{div}_h^* v(m_1) - \operatorname{div}_h^* v(m_2)$. Therefore, the right-hand side of the assumed equation is equal to

$$\int_{\partial \operatorname{star} p} \langle v,\nu\rangle$$

as assumed. □

Divergence-free vector fields can be characterized by the existence of a discrete 2−form which is another justification of the discrete definition of div_h. Here we formulate the statement without the usage of differential forms which are introduced in the next section.

Theorem 171 *Let v be a piecewise constant vector field on a simply connected simplicial surface M_h. Then*

$$\operatorname{div}_h v(p) = 0 \quad \forall \text{ interior vertices } p$$

if and only if there exists a function $u^* \in S_h^*$ with $v = J\nabla u^*$. Respectively,

$$\operatorname{div}_h^* v(m) = 0 \quad \forall \text{ edge midpoints } m$$

if and only if there exists a function $u \in S_h$ with $v = J\nabla u$. In both cases, the function is unique up to an integration constant.

Proof. Using the relation between the discrete rotation and divergence of Lemma 167 the statement follows directly from the integrability conditions proven in Theorem 163. □

7.4 Hodge Decomposition of Vector Fields

On each triangle we have a well-defined volume form ω from the induced metric of the triangle which can be expressed as $\omega = dx \wedge dy$ in local coordinates (x, y) of the triangle, and a one-form v which can expressed as $v_1 dx + v_2 dy$.

Definition 172 *The spaces of* discrete differential forms *on a simplicial surface M_h are defined piecewise per triangle T:*

$$\begin{aligned}
\Lambda_h^0 &: = \left\{u : M_h \to \mathbb{R} \mid u \text{ is continuous and } u_{|T} \text{ linear}\right\} \cong S_h \\
\Lambda_h^1 &: = \left\{v \mid v_{|T} \text{ is a constant, tangential vector}\right\} \\
\Lambda_h^2 &: = \left\{ \begin{array}{c} w \mid \text{on each simply connected region } D \\ w_{|D} = u\omega \text{ with a function } u \in \Lambda^0 \end{array} \right\}.
\end{aligned}$$

Additionally, we define the spaces $\Lambda^{0,*} \supset \Lambda^0$ and $\Lambda^{2,*} \supset \Lambda^2$ having functional representatives in S_h^*.

The space Λ_h^1 is the space of discrete vector fields on a polyhedral surface which are tangential and constant on each triangle. In the following we try avoid too much formalism and, sometimes, identify a $2-$form $w = u\omega$ with its function u without explicitly listing the volume form ω. Similarly, we identify vectors with $1-$forms.

On each oriented triangle, we define the operator J that rotates each vector by an angle $\frac{\pi}{2}$. For example, let c be an edge of the oriented boundary of a triangle, then $Jc = -\nu$ is in opposite direction of the outer normal of the triangle at c. The operator J is a special form of the Hodge star operator $* : \Lambda_h^i \to \Lambda_h^{n-i}$.

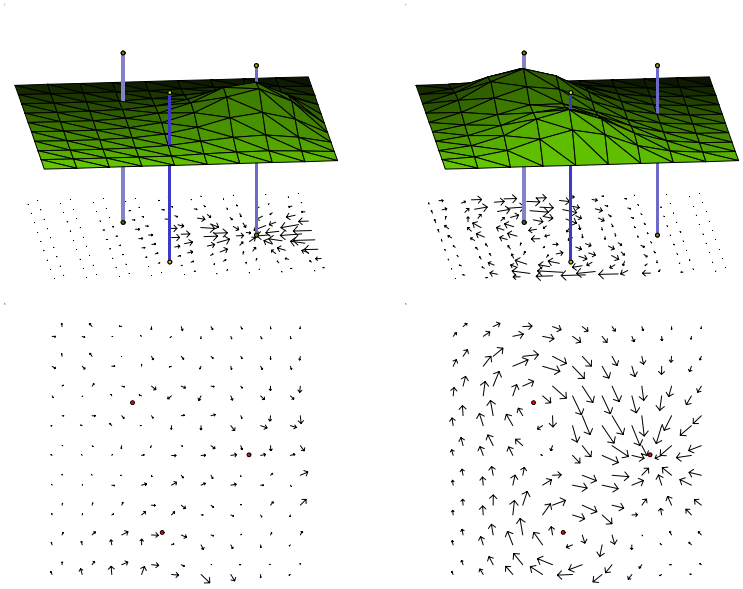

FIGURE 7.2. Test vector field (bottom right) decomposed in rotation-free (upper left), divergence-free (upper right) and harmonic component (bottom left). The three lines indicate the centers of the original potentials.

Definition 173 *On a simplicial surface M_h the Hodge operator $*$ is a map*

$$* : \Lambda_h^i \to \Lambda_h^{n-i}$$

such that locally

$$\begin{aligned} *u &= u\omega \quad \forall u \in \Lambda_h^0 \text{ respectively } \Lambda_h^{0,*} \\ *v &= Jv \quad \forall v \in \Lambda_h^1 \\ *(u\omega) &= u \quad \forall (u\omega) \in \Lambda_h^2 \text{ respectively } \Lambda_h^{2,*}. \end{aligned}$$

The gradient operator ∇ used in S_h^* generalizes to two differential operators d and δ on differential forms. We use rot_h^* respectively div_h in order to synchronize with the integrability condition of discrete vector fields in the following sequences.

Definition 174 *The* differential operator $d : \Lambda_h^0 \to \Lambda_h^1 = \Lambda_h^{1,*} \to \Lambda_h^{2,*}$ *on a simplicial surface M_h is defined by*

$$\begin{aligned} du &= \nabla u \quad \forall u \in \Lambda_h^0 \\ dv &= \mathrm{rot}_h^* v \quad \forall v \in \Lambda_h^1 \\ d(u\omega) &= 0 \quad \forall (u\omega) \in \Lambda_h^{2,*}. \end{aligned}$$

The co-differential operator δ *is defined by* $\delta := *d* : \Lambda_h^{2,*} \to \Lambda_h^{1,*} = \Lambda_h^1 \to \Lambda_h^0$, *that is*

$$\begin{aligned} \delta u &: = 0 \quad \forall u \in \Lambda_h^0 \\ \delta v &: = \operatorname{div}_h v \quad \forall v \in \Lambda_h^1 \\ \delta(u\omega) &: = J\nabla u \quad \forall (u\omega) \in \Lambda_h^{2,*}. \end{aligned}$$

Both operators are similarly defined on $\Lambda_h^{0,*}$ *respectively* Λ_h^2 *using* rot_h *respectively* div_h^*.

We remind that in the smooth situation for vector field $v = (v_1, v_2)$, we have $dv = (v_{2_{|x}} - v_{1_{|y}})dxdy$ and $\delta v = v_{1_{|x}} + v_{2_{|y}}$ on a planar Euclidean domain with coordinates (x, y).

Lemma 175 *Let* $u \in \Lambda^0$ *and* $w \in \Lambda^2$ *then*

$$d^2u(m) = 0 \text{ and } \delta^2 w(m) = 0 \text{ at each edge midpoint } m \in M_h,$$

respectively, if $u \in \Lambda^{0,*}$ *and* $w \in \Lambda^{2,*}$ *then*

$$d^2u(p) = 0 \text{ and } \delta^2 w(p) = 0 \text{ at each interior vertex } p \in M_h,$$

Proof. Direct consequence of the corollaries of the previous section. □

We now state a Hodge-type decomposition of 1−forms, respectively vector fields, on simplicial surfaces in a rotation-free, divergence-free, and a harmonic field.

Theorem 176 *Let* M_h *be a simplicial surface. Then any tangential vector field* $\xi \in \Lambda^1(M_h)$ *has a unique decomposition*

$$\xi = du + \delta(w\omega) + v \tag{7.10}$$

with $u \in \Lambda^0$, $w\omega \in \Lambda^2$ *and harmonic component* $v \in \Lambda^1$ *with* $\operatorname{div}_h v = \operatorname{rot}_h v = 0$ *respectively* $dv = 0$, $\delta v = 0$. *Uniqueness of the decomposition follows from the normalization*

$$\int_{M_h} u = 0, \ \int_{M_h} w\omega = 0.$$

Since u *and* w *are potential functions,* du *is rotation-free and* $\delta(w\omega)$ *is divergence-free.*

Proof. First, we derive the potential $u \in \Lambda^0$ of the rotation-free component of a given vector field ξ. We define the following quadratic functional F for functions in S_h

$$F(u) := \int_{M_h} \left(|\nabla u|^2 - 2 \langle \nabla u, \xi \rangle \right) \tag{7.11}$$

which associates a real-valued energy to each function u_h. A quadratic functional has a unique minimizer which we denote with $u \in S_h$. As a minimizer, u is a critical point of the functional which fulfills at each vertex p the following minimality condition

$$0 \stackrel{!}{=} \frac{d}{du_p} F(u) = 2 \int_{\operatorname{star} p} \left\langle \nabla u - \xi, \nabla \varphi_p \right\rangle \tag{7.12}$$

where $\varphi_p \in S_h$ is the Lagrange basis function corresponding to vertex p. Formally, u solves the Poisson equation $\operatorname{div}_h \nabla u = \operatorname{div}_h \xi$ respectively $\Delta_h u = \delta \xi$.

To obtain the divergence-free component we define a similar functional

$$G(w) := \int_{M_h} \left(|\delta(w\omega)|^2 - 2 \langle \delta(w\omega), \xi \rangle \right) \tag{7.13}$$

and compute the potential $w \in S_h$ as its unique minimizer which solves

$$0 \stackrel{!}{=} \frac{d}{dw_p} G(w) = 2 \int_{\operatorname{star} p} \left\langle \delta(w\omega) - \xi, J \nabla \varphi_p \right\rangle . \tag{7.14}$$

Formally, w solves $\operatorname{rot}_h J \nabla (w\omega) = \operatorname{rot}_h \xi$ resp. $\Delta_h w = d\xi$.

The harmonic remainder is defined as $v := \xi - \nabla u - J \nabla w$. Using the above relations and the fact that for a $2-$form $w\omega \in \Lambda^2_h$ we have $\operatorname{div}^*_h \delta(w\omega) = 0$ which implies $\operatorname{div}_h \delta(w\omega) = 0$, one easily verifies

$$\operatorname{div}_h v(p) = \operatorname{div}_h (\xi - \nabla u) - \operatorname{div}_h \delta(w\omega) = 0.$$

And using the fact that for a function $u \in \Lambda^1_h$ we have $\operatorname{rot}^*_h \nabla u = 0$ which implies $\operatorname{rot}_h \nabla u = 0$, we obtain

$$\operatorname{rot}_h v(p) = \operatorname{rot}_h (\xi - \delta(w\omega)) - \operatorname{rot}_h \nabla u = 0.$$

□

7.5 Detecting Vector Field Singularities

7.5.1 Decomposition Algorithm

For arbitrary tangential piecewise-constant vector fields on a simplicial (planar or curved) surface M_h we now apply the discrete

Helmholtz-Hodge decomposition introduced in the previous sections to split a given vector field in a rotation-free, a divergence-free, and a remaining harmonic component. The first component is the gradient field of a potential u, and the second component is the cogradient field of a second potential w. The decomposition is obtained by directly computing the potentials as minimizers of certain energy functionals. In the proof of the decomposition theorem we state the functionals.

The steps for a practical decomposition of a vector field are now straightforward. Assume, we want to compute the rotation-free component of a given vector field ξ on a simplicial surface M_h with boundary. We begin with an arbitrary initial function $u_0 \in S_h$ with zero-boundary values and arbitrary function values at the finite set of interior vertices of M_h. Then we apply a standard conjugate gradient method to minimize the energy functional F by modifying the interior function values of u_0. As a result we obtain the unique minimizer u of F. The same approach using the functional G is performed to compute the second potential w.

The evaluation of the gradient of the functional F can be made rather efficient using the explicit representation of the discrete divergence operator given in Equation 7.7:

$$\frac{d}{du_p}F(u) = \sum_{i=1}^{k} (\cot \alpha_i + \cot \beta_i) \langle \nabla u - \xi, a_i \rangle .$$

Since the cotangens values belong to the triangulation and its nonlinear computation can be done once before the conjugate gradient method starts. Precomputing the scalar products of the vector field ξ with the edges a_i is also possible. During runtime of the conjugate gradient method it computes repeatedly per vertex the k scalar products $\langle \nabla u, a_i \rangle$ and k scalar multiplications and one addition.

The vector field components of ξ are easily derived by differentiating the potentials. For efficiency, one does not need to store the three vector field components explicitly since they are explicitly determined by the scalar-valued potential functions u and w. Further, if one is interested only, say, in identifying the vortices of a vector field ξ, then it suffices to calculate w and to avoid the calculation of the full decomposition.

The Jacobian $\nabla\xi$ of a smooth vector field ξ in $\mathbb{R}^2$ or on a surface allows decomposition in a stretching tensor S and a vorticity matrix Ω

$$\nabla\xi = \frac{1}{2}(\nabla\xi + \nabla\xi^t) + \frac{1}{2}(\nabla\xi - \nabla\xi^t) =: S + \Omega$$

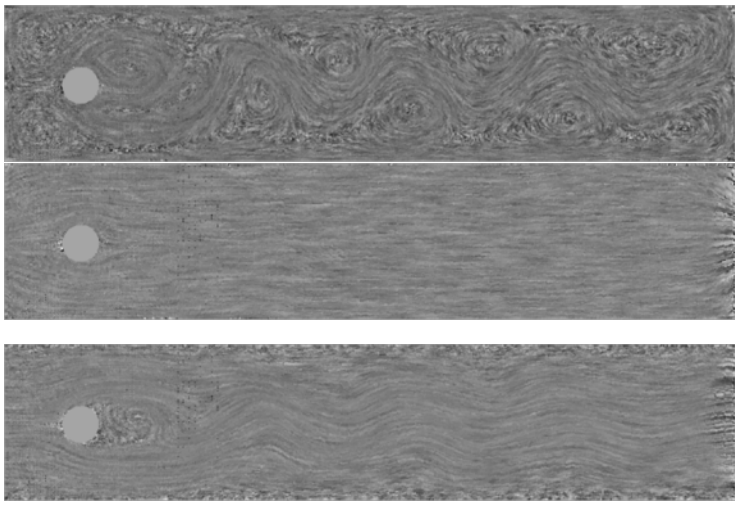

FIGURE 7.3. Incompressible flow around a cylinder (bottom) with vanishing rotation-free component. Divergence-free component (top) and harmonic component (middle) show expected behavior.

to analyze the physical properties of the flow. The eigenvalues of the diagonal matrix S correspond to the compressibility of the flow, and the off-diagonal entries of the anti-symmetric matrix Ω are the components of the rotation vector. For example, local methods for vortex identification and feature analysis of discrete vector fields often try to approximate the Jacobian by discrete differences or by higher-order interpolation of the vector field. This approach often suffers from numerical or measured inaccuracies of the vector field which make it a delicate task to extract higher order data such as the Jacobian or even higher order differential tensors. Compare the first approaches in direction of detecting higher-order singularities done by Scheuermann et al. in [111].

In this section we suggest a global approach to detect and analyze singularities of a vector field on a simplicial surface M_h by studying the critical points of the potential functions obtained from the Helmholtz-Hodge decomposition presented in the previous sections.

We start to locate first-order sinks and sources of a given vector field ξ:

- Calculate the potential u whose gradient is the rotation-free component of ξ by minimizing the functional 7.11.

- Locate the local maxima and minima of the scalar valued function u over the two-dimensional surface. This can be done automatically with another minimization routine, or by studying the graph of u manually.

Our approach is global in the sense that u is rather independent of small variations of the vector field which might have been introduced by numerical errors in the simulation, during the measurement, or by deficiency from a bad triangle mesh. This global approach is mainly due to the use of integrated values during the minimization of the functional.

A similar algorithm determines first-order vortices of the vector field ξ:

- Calculate the potential w by minimizing the functional 7.13.
- Locate the local maxima and minima of the potential w on the surface M_h.

Higher-order singularities correspond to higher-order critical points of the corresponding functions u respectively w. Since the smoothing effect of the global variation removes high frequencies of the vector field one might calculate higher-order approximations of the potential and use a Newton method to find the zeros of the derivative. Note, this higher-order approximation is performed on scalar data rather than on vector fields as in [110], and therefore, avoids using machineries like Clifford algebras. Figure 7.6 shows the associated potentials of a vector field singularity of index 3 and the clearly detectable critical points in the potentials.

It would be interesting to compare the original vector field with the vector field obtained from compositing the gradient fields of the two smoothed potentials and the original harmonic component. This reconstructed vector field should contain much less higher frequencies. Leeuw and van Liere [29] proposed a hierarchical ordering of flow features to reduce the complexity and suppress high-frequency patterns.

The figures show a number of experiments where the methods above are used for vortex identification and the detection of sources. Currently, in both algorithms step two is performed manually.

7.5.2 Examples

The first example in Figure 7.2 is an artificial vector field. We denote a *co-gradient field* a gradient field which has been rotated by 90°

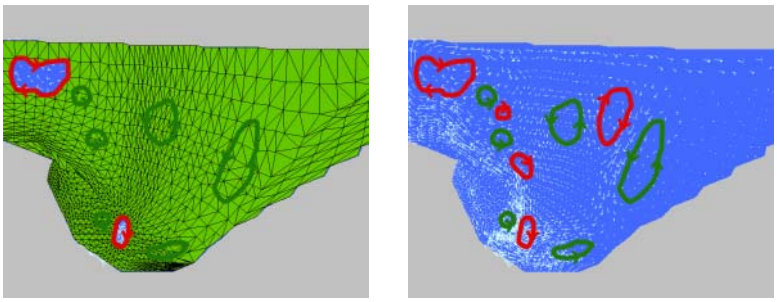

FIGURE 7.4. Bay of Gdansk with potential of divergence-free component (green mesh) clipped at a certain height to locate vortices. Major vortices located in flow (right) rotating clockwise (red) and counter-clockwise (green).

degrees. The field is the sum of a gradient vector field and two co-gradient fields. Application of the Hodge decomposition leads to two potentials u and w with gradient ∇u and co-gradient $J\nabla w$ shown in the upper two images on the left and right. The location of the original, generating potentials are indicated by dots. The algorithm detects the singularities and clearly separates the source from the two vortices. The centers of the potentials may be varied at interactive speed since on a smaller grid the decomposition is done in real-time as shown at the web site [92].

It should be noted that our algorithm correctly reconstructs the positions of the extrema of the original potential. In the combined vector field these positions may seem to deviate from these centers, although the potentials are correctly reconstructed. Obviously, the summation of both vector field components leads to a misleading transition of the visible vortex centers and the potential in the combined flow.

In Figure 7.3 the decomposition is applied to an incompressible flow around a cylinder from a CFD simulation. The rotation-free component of the incompressible flow vanishes as expected. The divergence-free component is tangential at the boundary because of the zero-boundary condition used in the decomposition algorithm. The harmonic component shows the incompressible, non-rotational part of the flow.

The flow in the Bay of Gdansk in Figures 7.5 and 7.4, a coastal region in Poland, is data from a simulation performed at WL | Delft Hydraulics using a curvilinear grid of $43 * 28 * 20$ nodes. The goal of the simulation was to investigate the flow patterns induced by wind and several inflows. In [108] Sadarjoen and Post derive geometric quantities from curvature properties of streamlines to find vortex cores

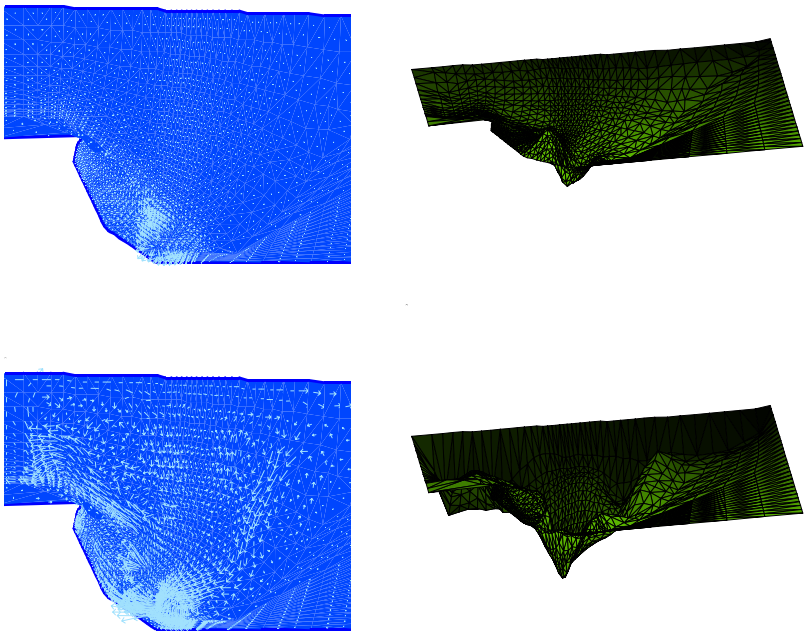

FIGURE 7.5. Decomposition of horizontal section of flow in Bay of Gdansk. Rotation-free component (top) with potential, and divergence-free component (bottom)

and analyze their qualitative behaviour. We computed the potentials of the gradient and co-gradient components and easily recovered the vortices and magnitudes by moving horizontal clip planes through the graph of the potential functions.

The harmonic component of a vector field corresponds to an incompressible, irrotational flow. On compact surfaces this harmonic component represents the non-integrable flows around the handles of the surface. The artificial vector field in Figure 7.1 is obtained from the restriction of the tangent field of a rotation of 3−space onto the pretzel. Around each handle we see a well-distinguished harmonic flow. There are also two sinks and two sources at the upper side and the lower side.

The example in Figure 7.6 shows a typical higher order singularity of index 3 which has a representation

$$\begin{aligned} v : \mathbb{R}^2 &\rightarrow \mathbb{R}^2 \\ z &\mapsto z^3 \end{aligned}$$

with a local complex coordinate z. Both potentials show a singularity of higher order at 0. Clipping the potential at the singularity with a horizontal plane separates the neighbourhood of the graph in 3 components.

Acknowledgment

The numerical flows were contributed by different sources. The simulation data of the Bay of Gdansk with courtesy WL|Delft Hydraulics and the help of Frits Post and Ari Sadarjoen. The flow around a cylinder by Michael Hinze at Technische Universität Berlin. Eike Preuß helped with the numerical computations and visualizations in JavaView [92].

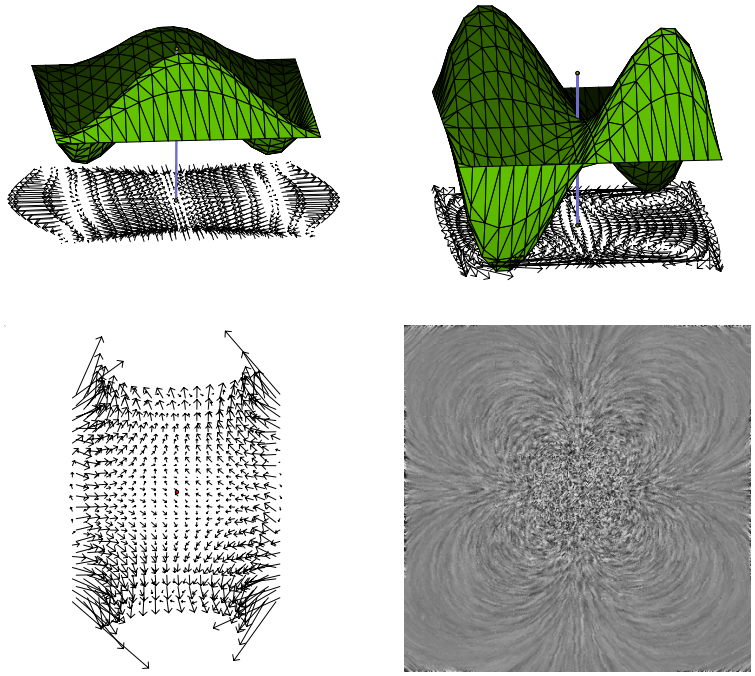

FIGURE 7.6. Higher-order singularity of vector field with index=3 (bottom right). Rotation-free (upper left) and divergence-free (upper right) components show critical point of higher order at singularity.

8

Interpolation of Adaptive Triangulations

Surfaces in animation often change their shape in time. If there is no functional description of the deformation available, one often uses the keyframe technique to describe the animation. Here a surface is stored at a finite set of key-times, and in-between surfaces are computed by interpolating between adjacent keyframes. In the special case that all keyframe surfaces have the same underlying simplicial complex, the interpolation task reduces to the simple linear interpolation between corresponding pairs of vertices, or interpolation of higher polynomial order if more keyframes are considered.

The interpolation task becomes more delicate if the keyframe surfaces are allowed to have different underlying simplicial complexes. In our discussion we restrict all surfaces of an animation to be topologically equivalent, i.e. they have the same genus and boundary curves. Nevertheless, our task remains to interpolate between topologically equivalent – but differently discretized – surfaces. Such surfaces occur naturally, in numerics when an initial surface evolves by minimizing an energy functional and it is adaptively refined and coarsened after each time step. These surfaces also arise in flow visualization, where an initial test ball is inserted in the flow and after some time-steps the ball strongly deforms, requiring an adaptive change of its mesh. In both cases one obtains a new keyframe object after each time-step,

and interpolation between keys with different meshes is required for slow-motion playback.

In this chapter we solve the interpolation problem between adaptively refined triangulations by imposing the following two constraints: firstly, the bisection scheme in each hierarchy follows the rules of Rivara [105] and, secondly, a certain correspondence between the root elements of all hierarchies is required. These assumptions are rather weak, especially since it is only the second constraint which requires an adjustment between different hierarchies. After this initial adjustment, each keyframe hierarchy may be locally refined and coarsened depending only on its own error criteria without any reference to the other hierarchies of the family. The compatibility of different meshes follows from the Rivara bisection method. This chapter is a minor extension of [47] which is joint work with Friedrich and Schmies.

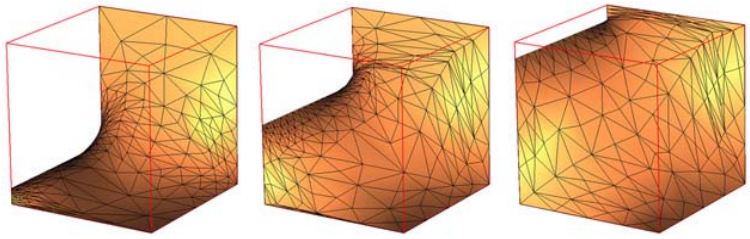

FIGURE 8.1. Parameter-dependent boundary value problem. Each geometry was adaptively refined without spoiling the interpolation property.

Instead of using the Rivara bisection method, one might try to use a $4-1$ split as subdivision rule. After a local refinement the $4-1$ split must be accompanied by a process called conformal closure to remove hanging vertices, for example, by introducing so-called green edges [6]. These green edges are responsible for case distinctions and require further subdivisions when interpolating between different hierarchies. These tasks can be handled, but the effort increases when interpolating in multi-parameter families.

8.1 Bisection Method of Rivara

Refinement and coarsening algorithms have a long tradition in numerics and computer graphics, and some can be used to generate hierarchical data representations where each child triangle is combinatorially a subset of its parent. Since we consider curved surfaces in

$\mathbb{R}^3$, it is essential to maintain the distinction between the simplicial combinatorics and the geometric realization: if we bisect a triangle to obtain two children, then combinatorially the two children are considered as subsets of its parent, but in the geometric realization the children need not be part of its parent triangle.

There exist different types of hierarchical triangulations, and a good overview and formal concept are given in DeFloriani and Puppo [31]. The concept of vertex-based hierarchies is described in detail in Hoppe's papers [61] and [62]. In numerics, it is essential to ensure stability of a sequence of triangulations or a hierarchical triangulation, i.e. to bound the angles inside all triangles uniformly from below. In visualization, small angles may also disturb the visual perception since they sometimes allow, the element normals to vary heavily in the neighbourhood of such a degenerate triangle. In some cases, long thin triangles may be appropriate, for example, to describe cylindrical shapes.

The bisection algorithm of Rivara [105] addresses the problem of how to locally refine a conforming triangulation to a new conforming triangulation and, additionally, of how to ensure that all angles in subsequently refined triangulations are greater than or equal to half of the smallest angle in the original triangulation. The method leads to nested triangulations and allows smooth transition between different levels of detail. In his original formulation, Rivara bisects a triangle exactly at the longest edge. Bänsch [8] generalized the method by introducing a formal refinement edge. In each triangle a single edge is marked as *refinement edge,* i.e. if the triangle is refined, then it is refined by bisecting its refinement edge, and the two child triangles inherit a refinement edge in the manner shown in Figure 8.2. In the simplicial complex an additional vertex is inserted at the midpoint of the refinement edge.

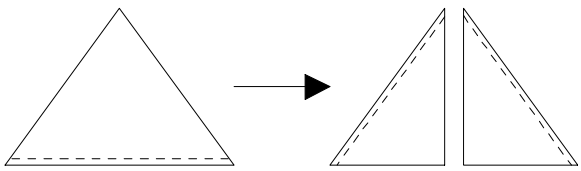

FIGURE 8.2. The Rivara bisection method refines a triangle exactly at its refinement edge. Each child inherits a refinement edge as shown.

Formally, the Rivara algorithm assumes that in a conforming triangulation T each triangle has an arbitrary edge marked as refinement edge.

Algorithm 177 (A) *Let T_0 be a conforming triangulation with a subset of triangles $S \subset T_0$ marked for refinement, usually according to some local error criteria, then the* Rivara Bisection Method *consists of the following steps:*

1. All marked triangles S are bisected according to the Rivara bisection rule. This produces a (possibly empty) new set of non-conforming triangles.

2. Mark all non-conforming triangles for refinement; the set is again denoted with S.

3. If S is not empty, then go to 1. Otherwise, there are no marked triangles and the algorithm stops. The new triangulation is T_{k+1}.

When the algorithm stops the new triangulation is conforming. As shown in [8] the algorithm stops after a finite number of steps since in one pass it inserts at most a single vertex on each edge. This is a fairly rough upper estimate for theoretical purposes – and one can construct such badly behaved examples – but, in practice, the subdivision has only local influence on the triangulation, see [8], [105]. The sequence $\{T_k\}$ is stable, i.e. all triangle angles are bounded from below by half the minimum triangle edges of the first triangulation T_1.

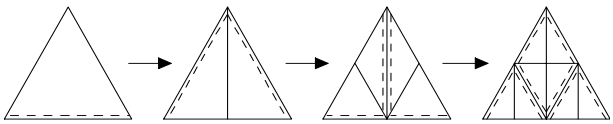

FIGURE 8.3. Successive applications of the Rivara algorithm introduce new vertices matching those retrieved by 4-1 splits.

The method using 4-1 splits, where each parent triangle is decomposed into four similar children, leads to non-conforming vertices if applied locally. Bank and Sherman [6] introduced so-called *green triangles* which join a non-conforming vertex with the opposite vertex of the non-conforming triangle, but this approach leads to non-nested triangulations over the green triangles. Rheinbold and Mesztenyi [104]

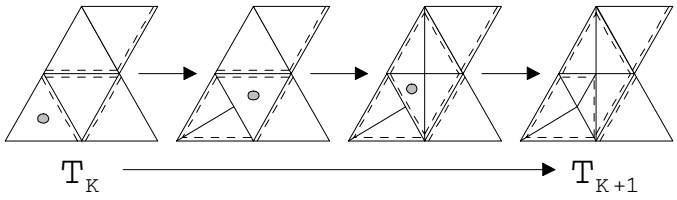

FIGURE 8.4. A single step of the Rivara bisection method with refinement edges and marked triangles.

work with non-conforming grids and, in order to maintain the continuity of the surface over the non-conforming points, they impose the condition that the geometric vertex over each non-conforming point is equal to the values interpolated from the nearby conforming points. However, the appearance of the non-conforming vertices complicates further geometrical or numerical computations because of the additional constraints.

The Rivara method (A) is a formalized version of the rule "bisect a triangle at its longest edge," where the method has its origin. We will later use the algorithm to ensure the interpolation property between hierarchies. Further, this algorithm bounds all triangle angles away from zero and therefore it guarantees numerical stability. We also note the following close connection: after applying the Rivara bisection method twice the same vertices as in a 4-1 split of triangles have been introduced (compare Figure 8.3). Therefore, the Rivara method does not differ too much from the well-used 4-1 rule, but merely eliminates the case distinctions occurring in connection with the conformal closure.

8.2 Triangle Hierarchy

A *triangle hierarchy* is a hierarchical structure of triangular elements where each element has a reference to one *parent* element, to one *child*, and to a *sibling*. The sibling is a child of the same parent and the children shall be produced by subdivision of the parent. Elements with no parents are called *root elements*, and elements with no children are *leaf elements*. We assume that the geometric vertices of a hierarchy are given in a global vertex array, and each triangle is determined by three vertex indices. Vertices and elements usually have color and material properties, or carry texture coordinates. Elements may have references to neighbour elements.

Similar to the situation with meshes, it is essential to maintain the distinction between the topological, i.e. combinatorial, structure of the hierarchy and the geometric shape. For example, when bisecting a parent triangle, from the topological viewpoint we identify the two children with subsets of the parent triangle. But in the geometric view, the additional geometric vertex introduced during bisection (possibly as the midpoint of an edge) may deviate from its original position on the parent edge after a further numerical process.

The main value of this distinction for interpolation different hierarchies is the existence of a unique relationship between each additional geometric vertex and a topological point in the parent triangle (as given explicitly by the level maps below).

For our interpolation property of a sequence of key hierarchies, it is essential that each hierarchy is generated using the Rivara bisection algorithm (A). In the implementation, we use a fixed numbering of the three vertex indices of each of the two child triangles (consider Figure 8.5). If the parent Δ_p is determined by three indices $\{i, j, k\}$ which refer to the vertices $v[i]$, $v[j]$, and $v[k]$ in the global vertex array v, then we assume the two child triangles to reference vertices $\{l, k, i\}$ and $\{l, i, j\}$ in this specific order, where $v[l]$ is the new vertex inserted during bisection. The specific ordering of the vertices in the children simplifies the location of each child triangle within its parent in the topological mesh. Additionally, the refinement edge of the children is always opposite to the first vertex and, therefore, the information is implicitly given by the vertex ordering. The refinement rule is then reformulated to 'refine a leaf triangle at the edge opposite to its first vertex'. Further, the second and third vertex refer to parent vertices and are therefore implicitly given and do not need to be explicitly referenced. Both observations save memory, but the latter requires recursive calls to obtain the two vertex indices from one of its ancestral triangles. Only the root elements must have references to three vertices in the global vertex array.

For smooth level-of-detail interpolation, it is important to observe that the new geometric vertex on a refined edge can be uniquely associated with the topological midpoint of the original edge in the simplicial complex. Let Δ_p be a parent triangle with two children, Δ_1 and Δ_2, generated by Rivara bisection. Let us work with barycentric coordinates and represent each point p of a triangle by its barycentric coordinate (b_1, b_2, b_3) with respect to the triangle vertices $\{v_1, v_2, v_3\}$. Explicitly, if $p = b_1 v_1 + b_2 v_2 + b_3 v_3$, we use the notation $p_b = (b_1, b_2, b_3)$ for its barycentric representation. Then we can describe the parent-

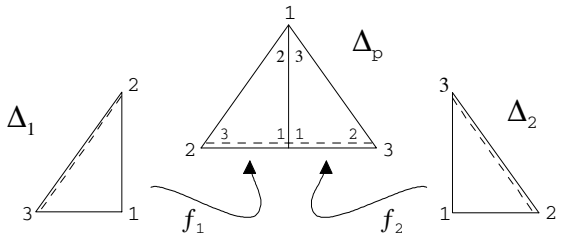

FIGURE 8.5. The refinement edge used in the Rivara bisection method can be implicitly stored to be opposite to vertex 1.

child relationship by two linear maps $f_i : \Delta_i \to \Delta_p$ given by

$$f_1(b_1, b_2, b_3) = \begin{pmatrix} 0 & 1 & 0 \\ \frac{1}{2} & 0 & 1 \\ \frac{1}{2} & 0 & 0 \end{pmatrix} \begin{pmatrix} b_1 \\ b_2 \\ b_3 \end{pmatrix} \tag{8.1}$$

and

$$f_2(b_1, b_2, b_3) = \begin{pmatrix} 0 & 0 & 1 \\ \frac{1}{2} & 0 & 0 \\ \frac{1}{2} & 1 & 0 \end{pmatrix} \begin{pmatrix} b_1 \\ b_2 \\ b_3 \end{pmatrix}$$

which relate every point in a child triangle to a point in its parent. This relationship is only on the combinatorial level of the hierarchy connectivity, and it does not mean that, for a geometric point $p \in \Delta_i$, we have $f_i(p) = p$.

We observe that we can now relate each triangle Δ_n of the hierarchy on level n with a subset of one of the root elements Δ_1 by a recursive application of level functions f, namely $f^{(n-1)}(\Delta_n) := f \circ ... \circ f(\Delta_n) \subset \Delta_1$. The computational cost is reduced when using barycentric coordinates - since only division by two and addition are used in each composition. When the composite level function $f^{(i)}(\Delta_n)$ has been computed, it is applied to the geometric (x, y, z) coordinate representation of points. The level maps are also used in the computation of the local texture coordinate of a triangle, which are implicitly given via the texture coordinates of the root triangles.

Generation of Hierarchies

In practice, hierarchies are generated by two different approaches: One starts with a high resolution data set and iteratively coarsens the geometry to produce a hierarchy. This 'bottom up' approach is successfully used by Hoppe [61], [62] in the progressive mesh concept

to obtain a vertex-based hierarchy by successive vertex-split and edge-collapse steps. As shown by Hoppe, different sections of one hierarchy can be interpolated, so-called geomorphs. The handling of arbitrary initial data sets is flexible, but this restricts the compatibility of two hierarchies obtained from similar initial geometries and reduces the possibility of interpolating between different hierarchies.

Generating a hierarchy 'top down' from a given coarse triangulation is ideal for element based approaches. One sets the triangles of the initial triangulation as root elements of a hierarchy, and successively refines according to some error criteria. For example, in the numerics of a boundary value problem for a partial differential equation one starts with a rough approximation of the solution and then refines/coarsens the geometry depending on a local numerical error.

Eck et al. [38] produce, from a given fine resolution mesh, a new element-based hierarchy for usage in multiresolution analysis. Their approach should also apply in generating hierarchies based on the Rivara bisection method since they already solved the major task of distributing vertices equidistantly on the surface.

8.3 Interpolating Different Hierarchies

Animation in computer graphics can be classified by image-based, see Stekettee and Badler [114], and geometry-based methods. Geometry-based methods split further into keyframe animations and into functional (resp. algorithmic) animations. For an overview we refer to the book [76] and its detailed bibliography.

We concentrate on the problem of interpolation between keyframe geometries and propose (in Section 8.3) some constraints on the geometries. The constraints guarantee a smooth interpolation without the need to remesh during the interpolation process, and then further ensure the freedom for local grid modifications separately on each keyframe. This means that the refinement and coarsening process can be applied to a single keyframe without disturbing the interpolation property.

Finally, our constraints efficiently allow higher order spline interpolation and interpolation in a multi-parameter family of geometries shown in section 8.4.

Review of Keyframe Interpolation

The keyframe technique is a common and old technique in animation. The animator specifies, say n, key geometries G_i at certain time steps t_i, $i \in \{1, ..., n\}$. If there exists an interpolation method between each two successive pairs G_i and G_{i+1}, then a smooth animation is obtained by generating the geometry at time $t \in [t_i, t_{i+1}]$ on the fly by interpolating between key geometries G_i and G_{i+1}.

Any geometry mesh can be used in a keyframe animation if there exists an interpolation method, see Burtnyk and Wein [23], [24] for general shape interpolation techniques. In the simplest case, all key geometries have the same combinatorial mesh and differ only in their vertices. In this case the interpolation object at time t uses the same topological mesh and has vertices $v_j(t) \in \mathbb{R}^3$, $j \in \{1, ..., m\}$. They are given by linear combinations

$$v_j(t) = (1 - t)v_j^i + tv_j^{i+1} \tag{8.2}$$

where v_j^i is the j-th vertex of G_i. Here, one can include more key geometries in the interpolation scheme and use polynomial interpolation of higher order in t.

In many applications the animated geometry varies heavily in time, and one would like to make local adaptions of the mesh on each keyframe geometry based on some local error criteria. But this spoils the simple interpolation technique above.

In [98], Polthier and Rumpf require at each time step t_i two topological meshes whose geometric realizations are of the same geometric shape. One connectivity is used to interpolate with the previous keyframe, and the other connectivity for interpolation with the next keyframe. In effect, they associate one connectivity per time interval $[t_i, t_{i+1}]$, and require two geometric realizations at each time step. Besides the additional storage requirement of two geometric realizations, this approach does not allow further modifications of keyframes since both geometric realizations must be modified in the identical way.

Interpolation Constraints for Hierarchies

We now specify constraints on the key hierarchies that, firstly, guarantee a smooth interpolation without the need to remesh during the interpolation process, and, secondly, ensure the freedom for local grid modifications separately on each keyframe.

Condition 178 (B) *A family of triangle hierarchies F must fulfill:*

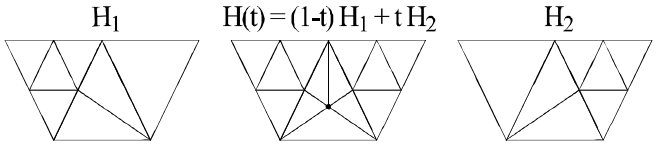

FIGURE 8.6. Drawback of the red-green subdivision method. If the green elements of a $4-1$ split in H_1 and H_2 overlap then not only the union but further subdivision is required during interpolation. This additional depth is avoided in our method.

1. *The simplicial complex of the root triangles of each hierarchy is the same for all hierarchies in F, i.e. for each pair of hierarchies $G, H \in F$ there exists a bijective simplicial map ϕ_{GH} between the set of root triangles.*
2. *Each root triangle has a refinement edge, and the simplicial map ϕ_{GH} maps each refinement edge to a refinement edge, i.e. the root triangles of all hierarchies are marked in the same way.*
3. *Each hierarchy is refined using the Rivara Algorithm (A).*

The root triangles can be interpreted as charts of each hierarchy, and condition 1. requires a bijective correspondence between the charts of different hierarchies. Conditions 2. and 3. ensure that hierarchies are automatically refined in a synchronized way without further restricting the refinement process in each hierarchy. Each hierarchy can be refined according to its own error criteria without *a posteriori* synchronization with the other key hierarchies. Once one has agreed to use the Rivara bisection method, it only remains to ensure properties 1. and 2. for the family F in an initial synchronization step.

The Rivara bisection algorithm depends only on the initial choice of the refinement edges in the root elements. The subsequent position of the refinement edge in each child and further descendants is predetermined by the algorithm. Therefore we have

Theorem 179 *If two hierarchies G and H fulfill the interpolation constraints (B) then both of their topological simplicial complexes are a subcomplex of the same infinite complex obtained by infinitely refining the simplicial complex of the root triangles, see Figure 8.7.*

Of course, the geometric representations of G and H are usually not identical since their geometric vertices differ.

In scientific computing a close connection between numerical computations and visualization is desirable. Since the Rivara method is

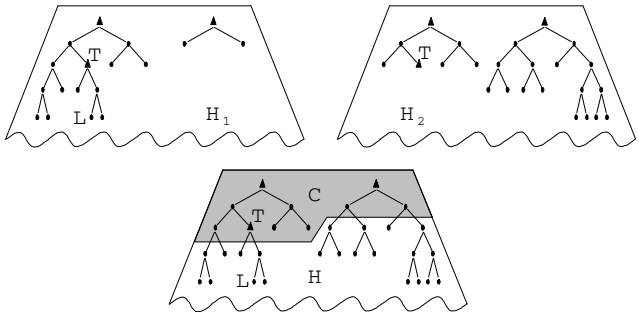

FIGURE 8.7. Two hierarchies fulfilling the interpolation constraints (B) are subsets of the same infinite hierarchy. The interpolation hierarchy H is the union of H_1 and H_2.

a suitable tool in both fields, hierarchies generated with the Rivara bisection method allow smooth transition of data between numerical and visualization methods.

Interpolating between Hierarchies

We prove the interpolation property between hierarchies fulfilling the interpolation constraints (B) in a general form which, includes standard keyframe animation with a time parameter t described in Section 8.3. Additionally, it covers higher order spline interpolation and interpolation in a multi-parameter family of hierarchies which we will apply in Section 8.4.

Theorem 180 *Let $F = \{H_1, H_2, ..\}$ be a family of hierarchies which fulfill the interpolation constraints (B) and let $b = \{b_1, b_2, ..\}$, $b_i \in \mathbb{R}$, be a set of weights. Then there exists an interpolated hierarchy*

$$H(b) = \sum_i b_i H_i \tag{8.3}$$

which depends smoothly on b, and its underlying simplicial hierarchy is the union of the simplicial hierarchies of each H_i. Further, the interpolated hierarchy H depends smoothly on b and fulfills the same interpolation constraints as the elements of F.

Proof: For the proof we restrict ourselves to two hierarchies H_1 and H_2 and show how to interpolate between both. First we recall the existence of a bijective simplicial map ϕ between the two simplicial complexes formed by the root elements. Since ϕ extends to a bijective map between the refinement edges of the root triangles, the Rivara

algorithm ensures that the different simplicial hierarchical complexes of H_1 and H_2 are subcomplexes of a theoretically infinite hierarchy which is obtained by infinitely refining the simplicial complex of the root triangles, see Theorem 179 and Figure 8.7.

It follows that interpolation between the common hierarchical subcomplex C of H_1 and H_2 can be done by simply interpolating corresponding geometric vertices.

Now assume H_1 is locally more refined than H_2. Then there exists a situation, as shown in Figure 8.8, where a topological leaf triangle T of the common subhierarchy C is a leaf triangle of the complex of H_2 but not a leaf triangle of H_1 (since H_1 is more refined). Of course, T has different geometric realizations in H_1 and H_2.

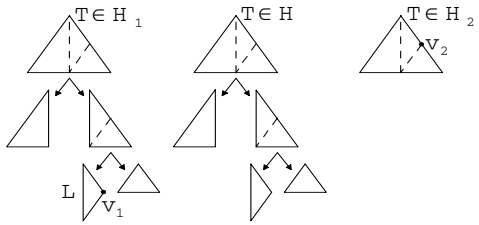

FIGURE 8.8. The central step when interpolating between two hierarchies.

All children and further descendants of T in H_1 are associated with a unique position in T via the level maps defined in Equation 8.1. The topological subtree generated by T in H_1 can be projected via the level maps onto T and then associated with geometric positions of T in H_2. Here we make essential use of the distinction between topological and geometric realizations. The level maps operate on the topological realization and give for each geometric vertex v_1 in a leaf triangle L in H_1 the topological, i.e. barycentric, position b_2 in T. From the barycentric coordinates b_2, with respect to the vertices of T in H_2, one can immediately compute the geometric position v_2.□

For the practical interpolation between a geometric leaf triangle L of H_1 and the corresponding subset of the geometric realization of T in H_2, we need to compute the barycentric coordinates of each vertex of L with respect to T. Let v_1 be one vertex of L with barycentric coordinates b_1 in L. Then we compose a level map f for the transition of L to T and use f to compute the barycentric coordinates b_2 of v_1 with respect to T:

$$b_2 = f(b_1).$$

By weighting the three vertices of the geometric realization of the triangle T in H_2 with b_2, we obtain the geometric position of v_2. Now we can interpolate between $v_1 \in H_1$ and $v_2 \in H_2$

$$v(t) = (1-t)\, v_1 + t v_2.$$

Applying the same procedure to the other two vertices of L gives the interpolation for L.

It is remarkable that the interpolation hierarchy is not more refined than the union of its keyframe hierarchies.

The interpolation hierarchy fulfills the same interpolation constraints as the keyframes. This is relevant in the following section for higher order interpolation and for further numerical or graphical processing, e.g. the interpolation hierarchy can immediately be used as a new keyframe. Additionally, each subhierarchy of a hierarchy in F fulfills the interpolation constraints (B) as soon as its leaf triangles form a conforming triangulation. This allows for smooth level-of-detail transitions within a single hierarchy and, by Theorem 180, between different levels-of-detail of different hierarchies of F.

8.4 Applications

Higher Order Spline Interpolation

The interpolation property of Theorem 180 immediately allows higher order interpolation in a keyframe animation. Let H_i,..,H_{i+n} be $n+1$ successive keyframe hierarchies fulfilling the interpolation constraints (B), then

$$H(t) = \sum_{i=0}^{n} B_{i,n}(t) H_i$$

is a polynomial hierarchy interpolant of degree n where $B_{i,n}(t)$ are the Bernstein polynomials.

The computation of the interpolation hierarchy follows the same lines explained in the linear case. First, the union of all $n+1$ hierarchies is generated, which will be the hierarchical combinatorics of $H(t)$. The combinatorics of $H(t)$ will not change as long as the same set of hierarchies H_i is used as control points. The second step is the interpolation step where each vertex v of $H(t)$ is located within the hierarchies H_i. If the vertex does not exist in one of the H_i, for example, if H_i is too coarse in the corresponding region, then a representative in one of the leaf triangles of H_i is located. Finally, the

position of v is computed by a weighted sum of the v_i

$$v(t) = \sum_{i=0}^{n} B_{i,n}(t) v_i.$$

Multi-Parameter Families of Hierarchies

The idea of smooth interpolation in a set of hierarchies can be pursued to the interpolation in a two- or multi-parameter family of hierarchies (as shown in Figure 8.12). The vertices of the discretized parameter domain, a square with four triangles and five vertices, represent five keyframe hierarchies at different resolutions and are shown in the lower part: an icosahedron, a bone, a cushion, a star, and a sphere in the midpoint of the domain. Each vertex of the domain represents a key hierarchy, and the set of keyframe hierarchies fulfills the interpolation property (B). This allows a barycentric interpolation in each domain triangle between the three key hierarchies at the vertices of each triangle. Let H_1, H_2, and H_3 denote the key hierarchies at the vertices of a domain triangle, and let $b = (b_1, b_2, b_3)$ be the barycentric coordinate of the point in the domain triangle. Then the interpolation hierarchy is given by

$$H(b) = b_1 H_1 + b_2 H_2 + b_3 H_3. \tag{8.5}$$

Similar to the 1-dimensional case, with time parameter t, the combinatorial structure of the interpolation hierarchy $H(b)$ is the topological union of all its three key hierarchies.

Multiparameter families of hierarchies occur frequently in geometrical and numerical problems depending on more than one parameter. But even when studying one-parameter families, the inclusion of a view-dependent rendering may be considered to be a 2−parameter family.

For numerical purposes the interpretation of the parameter domain of a, say, two-parameter family as a triangulation has significant further implications. Similar to the approximation of a smooth surface by a triangulation, the triangulated domain may approximate a smooth family of surfaces. One may use an adaptive refinement of the parameter domain, i.e. an automatic process which inserts a new key hierarchy in the domain, if the interpolation hierarchy does not satisfy a given error threshold.

View-Dependent Rendering

The hierarchical data structure are effectively used to render a camera flight through a scene while continuously adjusting the resolution

of the displayed geometries. For simplicity, assume there is a single geometry which is given as a static triangle-based hierarchy satisfying condition A, although the geometry might also change in time in which case it must be given as a set of keyframe hierarchies satisfies the interpolation constraints B.

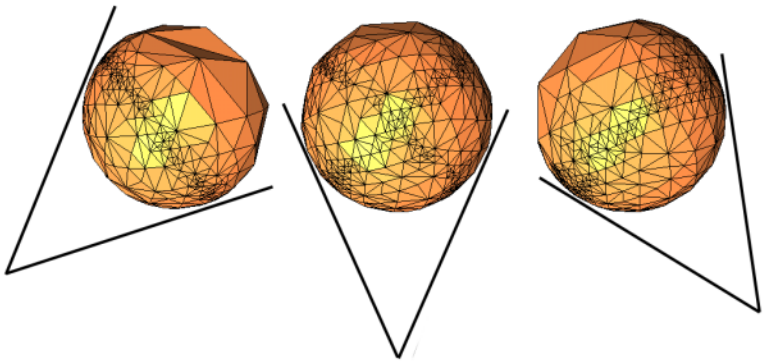

FIGURE 8.9. Left and right image show view-dependent representations of a sphere depending on the indicated camera position. The middle image shows the sphere at an intermediate time. Its rendered mesh has been obtained by interpolating the two view-dependent meshes of the adjacent keyframes, thereby avoiding a new view-dependence computation.

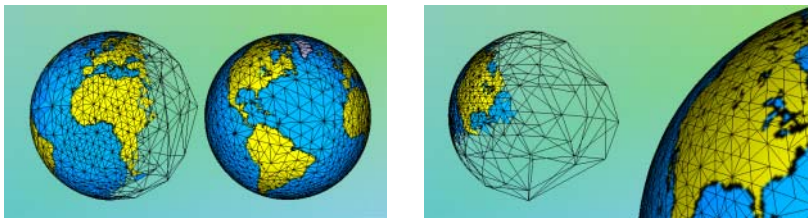

FIGURE 8.10. View-dependent representation of a geometry extracted on the fly from a hierarchical representation. Left image shows the coarse resolution on the invisible back side of the model as seen on the right.

Let t be the time in an interactive fly-through or of an animation of the geometry. We perform the view-dependent extraction of the geometry only at certain discrete timesteps $\{t_1, t_2, ...\}$ of the time interval which are (by a factor of, say 5) less than the number of actual shown frames. A frame generated at time t, where t lies in an open interval (t_i, t_{i+1}) between two timesteps, renders the geometry obtained by interpolating the view-dependent keyframe sections

at times t_i and t_{i+1}. Theorem 180 ensures that the interpolation is continuous over the whole time line since the view-dependent extraction of a subhierarchy at each timestep is the same as a coarsening step of the hierarchy. Such local modifications on a single key hierarchy are allowed by the assumption of the theorem. They do not spoil the original interpolation property. In practice, the proportion of the number of frames to the number of timesteps is between 5 and 10, and it depends on the amount of camera movement. Figure 8.9 gives a good impression for timesteps further apart. Nevertheless, the interpolation property holds for each choice.

In view-dependent computations, at each frame each vertex or triangle of the hierarchy is assigned a level of detail error. If this level of detail error depends continuously on the position of the camera and the geometry then it is possible to generate a section which is continuous in time.

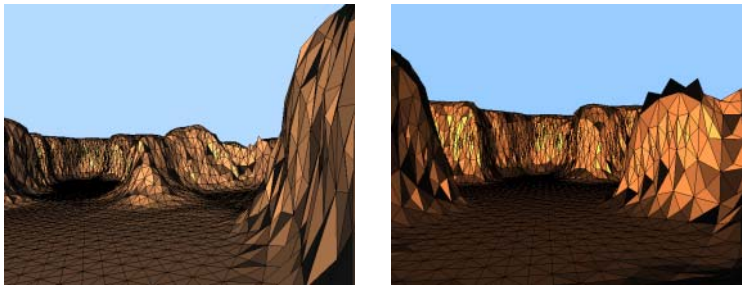

FIGURE 8.11. Interpolation between view-dependent keyframe representations $H(t_1)$ and $H(t_2)$ at times t_1 resp. t_2 of an animated scene. Since the view-dependence computation has been performed on the keyframe representations, the interpolated representation H(t) can be rendered directly. This approach avoids the view-dependence computations at every frame.

It is important to note that computing the interpolation between the two hierarchy levels above and below the current view-dependence threshold can be avoided in our method. This leads to a further essential speed-up for the view-dependence computation. In our method we accelerated the view-dependence computation of the keyframe subhierarchies by using the floating point view threshold as a boolean value: if the threshold is between the error values of two levels then we simply take the upper level and do not interpolate between the upper and next lower level. Such interpolation is the basis in the continuous level of detail concept but can be avoid here. Therefore, we do not employ the continuity feature with respect to the level of de-

tail in the hierarchy when generating a view-dependent keyframe. In fact, this introduces a minor error term, but it leads to a significant acceleration of the view-dependent extractions since no interpolation between level of details must be computed, triangles are just assigned a visibility flag.

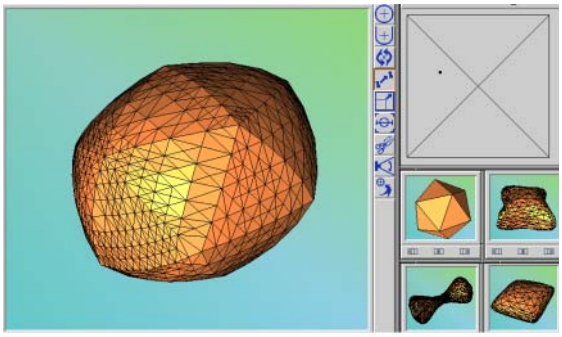

FIGURE 8.12. Interpolation between a two-dimensional set of keyframe hierarchies. The vertices of the parameter domain represent the four hierarchies on the bottom right and a sphere at the midpoint. All hierarchies have a different combinatorics, but fulfill the interpolation constraints (A) and (B). This allows for a continuous interpolation when varying the position in the parameter domain.

References

[1] A. D. Aleksandrov and V. A. Zalgaller. *Intrinsic Geometry of Surfaces*, volume 15 of *Translation of Mathematical Monographs*. AMS, 1967.

[2] S. B. Alexander and R. L. Bishop. Comparison theorems for curves of bounded geodesic curvature in metric spaces of curvature bounded above. *Diff. Geom. Appl.*, 6(1):67–86, 1996.

[3] C. Allendoerfer and A. Weil. The Gauss-Bonnet theorem for riemannian polyhedra. *Trans. Amer. Math. Soc.*, 53:101–129, 1943.

[4] T. Banchoff. Critical points and curvature for embedded polyhedra. *J. Diff. Geom*, 1:245–256, 1967.

[5] T. Banchoff. Critical points and curvature for embedded polyhedra ii. *Progress in Math.*, 32:34–55, 1983.

[6] R. E. Bank and A. H. Sherman. The use of adaptive grid refinement for badly behaved elliptic partial differential equations. *Advances in Computer Methods for Partial Differential Equations*, 3:33–39, 1979.

[7] D. Banks and B. Singer. A predictor-corrector technique for visualizing unsteady flow. *IEEE Transactions on Visualization and Computer Graphics*, 1(2):151–163, June 1995.

[8] E. Bänsch. Local mesh refinement in 2 and 3 dimensions. *IMPACT of Computing in Science and Engineering*, 3:181–191, 1991.

[9] J. L. Barbosa and M. d. Carmo. Stability of minimal surfaces and eigenvalues of the laplacian. *Math. Z.*, 173:13–28, 1980.

[10] H. Battke, D. Stalling, and H.-C. Hege. Fast line integral convolution for arbitrary surfaces in 3d. In H.-C. Hege and K. Polthier, editors, *Visualization and Mathematics*, pages 181–195. Springer Verlag, Heidelberg, 1997.

[11] B. Baumgart. Winged-edge polyhedron representation. Technical Report STAN-CS-320, Stanford University, 1972.

[12] E. D. Bloch. *A First Course in Geometric Topology and Differential Geometry*. Birkhäuser Verlag, 1997.

[13] A. Bobenko and U. Pinkall. Discrete isothermic surfaces. *J. reine angew. Math.*, 475:187–208, 1996.

[14] A. Bobenko and U. Pinkall. Discretization of surfaces and integrable systems. In A. Bobenko and R. Seiler, editors, *Discrete Integrable Geometry and Physics*. Clarendon Press, Oxford, 1999.

[15] A. Bobenko and B. Springborn. Variational principles for circle patterns and koebe's theorem. Technical report, Sfb288, 2001.

[16] A. Bossavit. Mixed finite elements and the complex of whitney forms. In J. Whiteman, editor, *The Mathematics of Finite Elements and Applications VI*, pages 137–144. Academic Press, 1988.

[17] A. Bossavit. *Computational Electromagnetism*. Academic Press, Boston, 1998.

[18] K. Brakke. *Surface Evolver Manual v2.14*, 1999. `http://www.susqu.edu/facstaff/b/brakke/evolver`.

[19] K. A. Brakke. The surface evolver. *Exp. Math.*, 1(2):141–165, 1992.

[20] K. A. Brakke and J. M. Sullivan. Using symmetry features of the surface evolver to study foams. In H.-C. Hege and K. Polthier, editors, *Visualization and Mathematics*, pages 95–117. Springer Verlag, Heidelberg, 1997.

[21] S. C. Brenner and L. R. Scott. *The Mathematical Theory of Finite Element Methods*. Springer Verlag, 1994.

[22] D. Bressoud and J. Propp. How the alternating sign matrix conjecture was solved. *Notices of the AMS*, 46(6):637–646, 1999.

[23] N. Burtnyk and M. Wein. Computer generated key-frame animation. *J. Soc. Motion Picture and Television Engineers*, 80:149–153, 1971.

[24] N. Burtnyk and M. Wein. Interactive skeleton techniques for enhancing motion dynamics in key frame animation. *Communications ACM*, 19(10):564–569, 1976.

[25] M. P. D. Carmo. *Differential Geometry of Curves and Surfaces*. Prentice-Hall, 1976.

[26] A. J. Chorin and J. E. Marsden. *A Mathematical Introduction to Fluid Mechanics*. Springer Verlag, 1998.

[27] P. Ciarlet. *The Finite Element Method for Elliptic Problems*. North-Holland, 1978.

[28] M. de Berg, M. van Kreveld, M. Overmars, and O. Schwarzkopf. *Computational Geometry*. Springer Verlag, 1997.

[29] W. C. de Leeuv and R. van Liere. Visualization of global flow structures using multiple levels of topology. In E. Gröller, H. Löffelmann, and W. Ribarsky, editors, *Data Visualization '99*, pages 45 – 52. Springer Verlag, 1999.

[30] L. de Lima and W. Rossman. On the index of constant mean curvature 1 surfaces in hyperbolic space. *Indiana Math. J.*, 47(2):685–723, 1998.

[31] L. DeFloriani and E. Puppo. Hierarchical triangulation for multiresolution surface description. *ACM Transactions on Graphics*, 14(4):363–411, October 1995.

[32] U. Dierkes, S. Hildebrandt, A. Küster, and O. Wohlrab. *Minimal Surfaces*, volume 1 of *Grundlehren der Mathematik*. Springer Verlag, 1992.

[33] E. Dijkstra. A note on two problems in connection with graphs. *Numer. Math.*, 1:269–271, 1959.

[34] J. Dodziuk. Finite-difference approach to the hodge theory of harmonic forms. *Amer. J. of Math.*, 98(1):79–104, 1976.

[35] J. Dorfmeister, F. Pedit, and H. Wu. Weierstrass type representation of harmonic maps into symmetric spaces. *Com. Anal. Geom.*, 6:633–667, 1998.

[36] G. Dziuk. An algorithm for evolutionary surfaces. *Numer. Math.*, 58:603–611, 1991.

[37] G. Dziuk and J. E. Hutchinson. Finite element approximations and the Dirichlet problem for surfaces of prescribed mean curvature. In H.-C. Hege and K. Polthier, editors, *Mathematical Visualization*, pages 73–87. Springer-Verlag, Heidelberg, 1998.

[38] M. Eck, T. DeRose, T. Duchamp, H. Hoppe, M. Lounsbery, and W. Stuetzle. Multiresolution analysis of arbitrary meshes. *Computer Graphics (SIGGRAPH '95 Proceedings)*, pages 173–182, August 1995.

[39] B. Eckmann. Harmonische funktionen und randwertaufgaben in einem komplex. *Commentarii Math. Helvetici*, 17:240–245, 1944–45.

[40] H. Edelsbrunner, D. Kirkpatrick, and R. Seidel. On the shape of a set of points in the plane. *IEEE Transactions on Information Theory*, 29(4):551–559, 1983.

[41] H. Edelsbrunner and E. P. Mücke. Three dimensional alpha shapes. *ACM Transactions on Graphics*, 13:43–72, 1994.

[42] G. Farin. *Curves and Surfaces for CAGD.* Academic Press, 1993.

[43] D. Fischer-Colbrie. On complete minimal surfaces with finite morse index in three manifolds. *Invent. Math.*, 82:121–132, 1985.

[44] G. Fix and G. Strang. *An analysis of the finite element method.* Prentice-Hall, 1973.

[45] M. S. Floater. Parametrization and smooth approximation of surface triangulations. *Computer Aided Geometric Design*, 14:231–250, 1997.

[46] A. Fournier and W. Reeves. A simple model of ocean waves. *ACM Siggraph 86*, pages 75–84, 1986.

[47] A. Friedrich, K. Polthier, and M. Schmies. Interpolating triangle hierarchies. In D. Ebert, H. Rushmeier, and H. Hagen, editors, *Proceedings Visualization '98*, pages 391–396. IEEE Computer Society Press, October 1998.

[48] M. Gromov. *Metric structures for Riemannian and non-Riemannian spaces*, volume 152 of *Progress in Mathematics*. Springer-Verlag, 1999.

[49] K. Große-Brauckmann. New surfaces of constant mean curvature. *Math. Zeit.*, 214:527–565, 1993.

[50] K. Große-Brauckmann and K. Polthier. Numerical examples of compact surfaces of constant mean curvature. In B. Chow, R. Gulliver, S. Levy, and J. Sullivan, editors, *Elliptic and Parabolic Methods in Geometry*, pages 23–46, Wellesley (MA), 1996. AK Peters.

[51] K. Große-Brauckmann and K. Polthier. Compact constant mean curvature surfaces with low genus. *Experimental Mathematics*, 6(1):13–32, 1997.

[52] K. Große-Brauckmann and K. Polthier. Constant mean curvature surfaces derived from Delaunay's and Wente's examples. In H.-C. Hege and K. Polthier, editors, *Visualization and Mathematics*, pages 119–134. Springer Verlag, Heidelberg, 1997.

[53] C. Gunn, A. Ortmann, U. Pinkall, K. Polthier, and U. Schwarz. Oorange - a visualization environment for mathematical experiments. In H.-C. Hege and K. Polthier, editors, *Visualization and Mathematics*, pages 249–265. Springer Verlag, Heidelberg, 1997.

[54] I. Guskov, K. Vidimce, W. Sweldens, and P. Schröder. Normal meshes. In *Computer Graphics Proceedings (Siggraph '00)*, pages 95–102, 2000.

[55] M. Heil. Numerical tools for the study of finite gap solutions of integrable systems. Master's thesis, Technical University of Berlin, Berlin, 1995.

[56] J. Helman and L. Hesselink. Representation and display of vector field topology in fluid flow data sets. *IEEE Computer*, 22(8):27–36, August 1989.

[57] J. Helman and L. Hesselink. Visualizing vector field topology in fluid flows. *IEEE Computer Graphics & Applications*, 11(3):36–46, 1991.

[58] H. Helmholtz. Über Integrale der Hydrodynamischen Gleichungen. *J. Reine Angew. Math.*, 55:25–55, 1858.

[59] T. Hoffmann. Discrete rotational CMC surfaces and the elliptic billiard. In H.-C. Hege and K. Polthier, editors, *Mathematical Visualization*, pages 117–124. Springer-Verlag, Heidelberg, 1998.

[60] T. Hoffmann. Discrete H-surfaces and discrete holomorphic maps. In A. Bobenko and R. Seiler, editors, *Discrete Integrable Geometry and Physics*. Oxford Press, 1999.

[61] H. Hoppe. Progressive meshes. *Computer Graphics (SIGGRAPH '96 Proceedings)*, pages 99–108, August 1996.

[62] H. Hoppe. View-dependent refinement of progressive meshes. In *Computer Graphics (SIGGRAPH '97 Proceedings)*, pages 189–198, August 1997.

[63] L. Hsu, R. Kusner, and J. Sullivan. Minimizing the squared mean curvature integral for surfaces in space forms. *Experimental Mathematics*, 1(3):191–207, 1992.

[64] K. Hurdal, P. L. Bowers, K. Stephenson, D. W. L. Sumners, K. Rehm, K. Schaper, and D. A. Rottenberg. Quasi-conformally flat mapping the human cerebellum. In C. Taylor and A. Colchester, editors, *Medical Image Computing and Computer-Assisted Intervention - MICCAI'99*, volume 1679 of *Lecture Notes in Computer Science*, pages 279–286. Springer Verlag, 1999.

[65] J. E. Hutchinson. Computing conformal maps and minimal surfaces. *Proc. Centr. Math. Anal., Canberra*, 26:140–161, 1991.

[66] H. Karcher. Construction of minimal surfaces. *Surveys in Geometry, University of Tokyo*, pages 1–96, 1989.

[67] H. Karcher. The triply periodic minimal surfaces of A. Schoen and their constant mean curvature compagnions. *Man. Math.*, 64:291–357, 1989.

[68] H. Karcher and K. Polthier. Construction of triply periodic minimal surfaces. In J. Klinowski and A. L. Mackay, editors, *Curved Surfaces in Chemical Structures*, volume 354 (1715) of *A*, pages 2077–2104. The Royal Society, London, Great Britain, phil. trans. r. soc. lond. edition, September 1996.

[69] Z. Karni and C. Gotsman. Spectral compression of mesh geometry. In *Computer Graphics Proceedings (Siggraph '00)*, pages 279–286. ACM SIGGRAPH, 2000.

[70] M. Kilian, I. McIntosh, and N. Schmitt. New constant mean curvature surfaces. *Exp. Math.*, 9(4):595–611, 2000.

[71] C. L. Lawson. Transforming triangulations. *Discrete Math.*, 3:365–372, 1972.

[72] C. L. Lawson. Software for C^1 surface interpolation. In J. R. Rice, editor, *Math. Software III*, pages 161–194. Academic Press, 1977.

[73] H. Lawson. *Lectures on Minimal Submanifolds.* Publish or Perish Press, 1971.

[74] H. B. Lawson. Complete minimal surfaces in S^3. *Ann. of Math.*, 92:335–374, 1992.

[75] H. Lee, L. Kim, M. Meyer, and M. Desbrun. Meshes on fire. In N. Magnenat-Thalmann and D. Thalmann, editors, *Computer Animation and Simulation 2001*, Computer Science. Springer Verlag, 2001. Proceedings of the Eurographics Workshop.

[76] N. Magnenat-Thalmann and D. Thalmann. *Computer Animation.* Computer Science Workbench. Springer Verlag, second edition, 1985.

[77] N. Max. Carla's island. ACM Siggraph 81 Video Review, 1981. Animation.

[78] J. S. B. Mitchell, D. M. Mount, and C. H. Papadimitriou. The discrete geodesic problem. *SIAM J. Comput.*, 16(4):647–668, 1987.

[79] E. Moise. *Geometric Topology in Dimensions 2 and 3.* Springer Verlag, New York, 1977.

[80] S. Montiel and A. Ros. Schrödinger operators associated to a holomorphic map. In *Global Differential Geometry and Global Analysis*, volume 1481 of *Lect. Notes in Math.*, pages 147–174. Springer Verlag, 1991.

[81] S. Müller, M. Struwe, and V. Sverak. Harmonic maps on planar lattices. Technical Report 17, MPI Leipzig, 1997.

[82] J. R. Munkres. *Elements of Algebraic Topology*. Addison Wesley, 1984.

[83] S. Nayatani. Lower bounds for the Morse index of complete minimal surfaces in Euclidean 3-space. *Osaka J. Math.*, 27:453–464, 1990.

[84] S. Nayatani. Morse index of complete minimal surfaces. In M. Rassias, editor, *The Problem of Plateau*, pages 181–189. World Scientific, 1992.

[85] S. Nayatani. Morse index and gauß maps of complete minimal surfaces in Euclidean 3-space. *Comment. Math. Helv.*, 68:511–537, 1993.

[86] B. Oberknapp and K. Polthier. An algorithm for discrete constant mean curvature surfaces. In H.-C. Hege and K. Polthier, editors, *Visualization and Mathematics*, pages 141–161. Springer Verlag, Heidelberg, 1997.

[87] R. Osserman. *A Survey of Minimal Surfaces*. Dover, 1986.

[88] U. Pinkall and K. Polthier. Computing discrete minimal surfaces and their conjugates. *Experim. Math.*, 2(1):15–36, 1993.

[89] A. V. Pogorelov. Quasigeodesic lines on a convex surface. *Amer. Math. Soc. Transl.*, I. Ser. 6(72):430–473, 1952.

[90] E. Polak. *Computational Methods in Optimization*. Academic Press, 1971.

[91] K. Polthier. Geometric a priori estimates for hyperbolic minimal surfaces. *Bonner Mathematische Schriften*, 263, 1994.

[92] K. Polthier, S. Khadem-Al-Charieh, E. Preuß, and U. Reitebuch. JavaView Homepage, 1998–2002. `http://www.javaview.de/`.

[93] K. Polthier, S. Khadem-Al-Charieh, E. Preuß, and U. Reitebuch. Publication of interactive visualizations with JavaView. In J. Borwein, M. H. Morales, K. Polthier, and J. F. Rodrigues, editors, *Multimedia Tools for Communicating Mathematics*. Springer Verlag, 2002. `http://www.javaview.de`.

[94] K. Polthier and W. Rossman. Discrete catenoid. *Electronic Geometry Models*, 2000. `http://www.eg-models.de/2000.05.002/`.

[95] K. Polthier and W. Rossman. Index of discrete constant mean curvature surfaces. Report 484, SFB 288, TU-Berlin, 2000. To appear in: J. Reine Angew. Math.

[96] K. Polthier and W. Rossman. Counterexample to the maximum principle for discrete minimal surfaces. *Electronic Geometry Models*, 2001. `http://www.eg-models.de/2000.11.040/`.

[97] K. Polthier and W. Rossman. Discrete minimal helicoid. *Electronic Geometry Models*, 2001. `http://www.eg-models.de/2001.01.046/`.

[98] K. Polthier and M. Rumpf. A concept for time-dependent processes. In M. Göbel, H. Müller, and B. Urban, editors, *Visualization in Scientific Computing*, pages 137–153. Springer Verlag, 1995.

[99] K. Polthier and M. Schmies. Straightest geodesics on polyhedral surfaces. In H.-C. Hege and K. Polthier, editors, *Mathematical Visualization*, pages 135–150. Springer Verlag, Heidelberg, 1998.

[100] K. Polthier and M. Schmies. Geodesic flow on polyhedral surfaces. In E. Gröller and H. Löffelmann, editors, *Data Visualization*. Springer Verlag, 1999.

[101] K. Polthier, M. Schmies, M. Steffens, and C. Teitzel. Geodesics and waves. Siggraph'97 Video Review 120 and VideoMath Festival at ICM'98, 1997. Video, 4:40 min.

[102] W. H. Press, S. A. Teukolsky, W. T. Vetterling, and B. P. Flannery. *Numerical Recipies in C: The Art of Scientific Computing*. Cambridge University Press, 1993. `http://www.nr.com/`.

[103] Y. G. Reshetnyak. *Geometry IV*, volume 70 of *Encyclopaedia of Mathematical Sciences*, chapter 1. Two-Dimensional Manifolds of Bounded Curvature, pages 3–164. Springer Verlag, 1993.

[104] W. C. Rheinboldt and C. K. Mesztenyi. On a data structure for adaptive finite element mesh refinements. *ACM Transactions on Mathematical Software*, 6:166–187, 1980.

[105] M. Rivara. Algorithms for refining triangular grids suitable for adaptive and multigrid techniques. *International J. for Numerical Methods in Engineering*, 20:745–756, 1984.

[106] M. Roth and R. Peikert. A higher-order method for finding vortex core lines. In D. Ebert, H. Hagen, and H. Rushmeier, editors, *Proc. Visualization '98*, pages 143 – 150. IEEE Computer Society Press, 1998.

[107] M. Rudin. An unshallable triangulation of a tetrahedron. *Bull. Amer. Math. Soc.*, 64:90–91, 1958.

[108] I. A. Sadarjoen and F. H. Post. Geometric methods for vortex extraction. In E. Gröller, H. Löffelmann, and W. Ribarsky, editors, *Data Visualization '99*, pages 53 – 62. Springer Verlag, 1999.

[109] I. A. Sadarjoen, F. H. Post, B. Ma, D. Banks, and H. Pagendarm. Selective visualization of vortices in hydrodynamic flows. In D. Ebert, H. Hagen, and H. Rushmeier, editors, *Proc. Visualization '98*, pages 419 – 423. IEEE Computer Society Press, 1998.

[110] G. Scheuermann, H. Hagen, and H. Krüger. Clifford algebra in vector field visualization. In H.-C. Hege and K. Polthier, editors, *Mathematical Visualization*, pages 343–351. Springer-Verlag, Heidelberg, 1998.

[111] G. Scheuermann, H. Hagen, H. Krüger, M. Menzel, and A. Rockwood. Visualization of higher order singularities in vector fields. In R. Yagel and H. Hagen, editors, *Proc. Visualization '97*, pages 67–74. IEEE Computer Society, 1997.

[112] Sfb256. GRAPE *Manual*. Sonderforschungsbereich 256, University of Bonn, Sept. 1995. `http://www-sfb256.iam.uni-bonn.de/grape/main.html`.

[113] M. Sharir and A. Schorr. On shortest paths in polyhedral space. *SIAM J. Comput.*, 15(1):193–215, 1986.

[114] S. N. Steketee and N. I. Badler. Parametric keyframe interpolation incorporating kinetic adjustment and phrasing control.

Computer Graphics (SIGGRAPH '85 Proceedings), pages 255–262, 1985.

[115] G. Taubin and J. Rossignac. Geometric compression through topological surgery. *ACM Transactions on Graphics*, 17(2):84–115, 1998.

[116] M. Tittgemeyer, G. Wollny, and F. Kruggel. Visualising deformation fields computed by non-linear image registration. *Computing and Visualization in Science*, 2002. to appear.

[117] T. Tsuchiya. Discrete solutions of the Plateau problem and its convergence. *Math. of Comp.*, 49:157–165, 1987.

[118] D. F. Watson. Computing the n-dimensional delaunay tessellation with application to voronoi polytopes. *Comp. J.*, 24:167–172, 1981.

[119] H. Whitney. *Geometric Integration Theory*. Princeton University Press, 1957.

[120] G. M. Ziegler. *Lectures on Polytopes*. Springer Verlag, 1998. 2nd ed.